Feasibility Studies on the Application of Relativistic Electron Beams from a Laser Plasma Wakefield Accelerator in Radiotherapy

by

Anna Subiel

Thesis submitted for the degree of
Doctor of Philosophy in Physics

Physics Department, University of Strathclyde

Supervisors:
Prof. Dino A. Jaroszynski
Dr. Gregor H. Welsh

2014

Signed:
Date:

Abstract

Very high energy electrons (VHEEs) (100-250 MeV) have the potential of becoming an alternative modality in radiotherapy because of their improved dosimetry properties compared with X-ray photons, which could confer possible radiobiological benefits. The rapid development of ultra-compact laser-plasma wakefield accelerators (LWFAs) is now providing a potential low cost device for VHEE radiotherapy. These beams have characteristics unlike any other beams currently used for radiotherapy: femotosecond radiation pulses, small field size and energies that exceed electron energies currently used in clinical applications.

A set of Monte Carlo (MC) calculations have been performed to study dosimetric properties of VHEEs propagating in water. To assess radiation protection and safety handling issues, the generation of neutrons, induced activity and equivalent doses have been evaluated.

A dosimetry system, consisting of EBT2 Gafchromic® film and EPSON Expression 10000XL scanner, for VHEEs has been established. EBT2 Gafchromic film turns out to be a robust dosimeter with a minor energy-dependent response over a broad range of beam energies and modalities, and can be successfully used for dosimetry of very high energy electron beams. The dosimetric measurements have been carried out using three different accelerators: a 20 MeV clinical LINAC, a 165 MeV conventional LINAC and a 135 MeV laser-plasma wakefield accelerator. The measurements have been compared with Monte Carlo simulations using the FLUKA code. Additionally, the set of dose measurements employing IBA CC04 ionisation chamber has been presented.

Dosimetric measurements have been complemented by preliminary cancer cell irradiation studies to determine the toxicity and dose response to LWFA VHEEs of two lung cancer cell lines (A549 and H460). The efficacy of VHEEs on *in vitro* tumour cells has been assessed by clonogenic assay and γ-H2AX assay employing immunofluorescence detection of signalling molecules has been deployed to indicate DNA double-strand breaks and repair.

Acknowledgements

The completion of my PhD career will not be possible without the help of the following:

- Prof. Dino Jaroszynski, for accepting me as his student and letting me to carry out work on fascinating research project, for giving me the freedom to follow my initiative, for helping me in exploring my research interests and for reviewing this work.
- Dr. Gregor Welsh, for courageous enough to be my second supervisor, for supporting me in every step of my PhD, for the valuable discussions and experimental advice in improving this project.
- Dr. Annette Sorensen for training me in carrying out biological analysis in tissue culture environment, for valuable discussions on radiobiology, for reviewing chapter 6 of this thesis and for courtesy of sharing radiobiological results on VHEE irradiation.
- Dr. Marie Boyd for welcoming me in the Strathclyde Institute of Pharmacy and Biomedical Sciences, where all radiobiological studies presented in this work have been carried out and for many fascinating discussions on radiobiology.
- Dr. Silvia Cipiccia for her advice on performing experiments and numerical calculations presented in this work.
- Dr. Vadim Moskvin for long discussions on experimental results and invaluable advice on numerical calculations.
- Prof. Philip Evans and Dr. Mike Partridge for sharing their expertise in many aspects of medical physics discussed during meetings and Skype calls.
- Dr. Enrico Brunetti for solving many mysterious problems with my office computer and valuable advice on MC calculations and data analysis.
- Dr. Riju Issac for giving me the initial training in ALPHA-X laboratory.
- Dr. Gregor Welsh, Dr. Silvia Cipiccia, David Robredo Gil for spending many hours in the laboratory and supporting me during experimental campaigns
- My dear friends and colleagues: John Farmer, Constantin Aniculaesei, Grace Manahan, Silvia Cipiccia, Maria Pia Anania, Yevgen Kravets, Gregor Welsh, David Roboredo Gil, Adam Noble, Mark Wiggins, Enrico Brunetti, Gregory Vieux, Peter Grant, Cristian Ciocarlan, David Grant, Paul Farrell for being my everyday

companions and who provided an enjoyable atmosphere in which to conduct my PhD.

- David Clark and Tom McCanny for the technical support.
- SPARC team who helped in the experiment in INFN Laboratories in Frascasti.
- My colleagues from the group, who are not mentioned by name, for the fruitful discussions and entertaining chats during many events.
- My wonderful family, my mom, dad and Kasia, for their constant support during my whole life and my dear Ines for giving me motivation throughout the PhD.

My sincerest gratitude to all.

Role of the author

The idea of developing VHEE therapy at the University of Strathclyde was initiated by Prof. Dino Jaroszynski. The Monte Carlo calculations presented in this thesis were designed and carried out by the author. The experiments were performed by the author with the help of Dr. Gregor Welsh, Dr. Silvia Cipiccia, David Roboredo Gil and Dr. Annette Sorensen (in ALPHA-X laboratory), Prof. Philip Evans, Dr. Mike Partridge (at the Royal County Surrey Hospital) and Dr. Gregor Welsh and experimental team in INFN in Frascati (in SPARC Laboratory). The author has established dosimetry system for VHEEs and was responsible for the design, set-up, data collection and analysis during all of the dosimtery experiments. The collected data in ALPHA-X laboratory during radiobiological experiment were analysed by Dr. Annette Sorensen. The author has carried out the radiobiological studies on 225 kV X-ray source.

List of Publications

1. A. Subiel, V. Moskvin, G. H. Welsh, S. Cipiccia, D. Reboredo, P. Evans, M. Partridge, C. DesRosiers, M. P. Anania, A. Cianchi, A. Mostacci, E. Chiadroni, D. Di Giovenale, F. Villa, R. Pompili, M. Ferrario, M. Belleveglia, G. Di Pirro, G. Gatti, C. Vaccarezza, B. Seitz, R. C. Isaac, E. Brunetti, S. M. Wiggins, B. Ersfeld, M. R. Islam, M. S. Mendonca, A. Sorensen, M. Boyd and D. A. Jaroszynski, *Dosimetry of Very High Energy Electrons (VHEE) for radiotherapy application: EBT2 film measurements and Monte Carlo simulations with FLUKA code*, Physics in Medicine in Biology (2014) – *accepted*

2. V. Moskvin, A. Subiel, C. DesRosiers, M. Wiggins, M. Maryanski, M. Mendonca, M. Boyd, A. Sorensen, S. Cipiccia, R. Issac, G. Welsh, E. Brunetti, C. Aniculaesei, D. Jaroszynski, *Characterization of the Very High Energy Electrons, 150 - 250 MeV (VHEE) Beam Generated by ALPHA-X Laser Wakefield Accelerator Beam Line for Utilization in Monte Carlo Simulation for Biomedical Experiment Planning*, Medical Engineering and Physics Vol 39, No. 6, pp. 3813-3814 (2012)

3. S. M. Wiggins, J. G. Gallacher, H-P. Schlenvoigt, H. Schwoerer, G. H. Welsh, R. C. Issac, E. Brunetti, G. Vieux, R. P. Shanks, S. Cipiccia, M. P. Anania, G. Manahan, C. Aniculaesei, A. Subiel, D. W. Grant, A. J. W. Reitsma, B. Ersfeld, M. R. Islam, D. A. Jaroszynski, *Laser-driven radiation sources in the ALPHA-X project* , SPIE 8075, Harnessing Relativistic Plasma Waves as Novel Radiation Sources from Terahertz to X-Rays and Beyond II, 80750O (2011)

Table of Content

1. Introduction

Cancer remains a leading global cause of death. The International Agency for Research on Cancer (IARC) recently estimated that 8.2 million deaths worldwide are due to cancer with 14.1 million new cases per year being reported worldwide [1]. A significant proportion of this burden is borne by developing countries, where as much as 63% of cancer deaths have been reported [1-3]. Cancer is a multigenic and multicellular disease that can arise in all cell types and organs with a multi-factorial etiology. If uncontrolled cell growth or metastatic spread occurs it will result in the death of the individual [4]. In the past decade considerable progress towards the treatment and understanding of the earlier evidence of cancer [5, 6] together with advances in early detection and in the various treatment modalities, which have resulted in many cancers becoming curable [7].

The discovery of X-rays by Wilhelm Conrad Röntgen in 1895 is acknowledged as the start of radiation research. The discovery of artificial ionising radiation led to the discovery of natural radioactivity by Henri Becquerel less than a year later [8]. Applications of the new phenomenon were quickly established. The first radiography of a part of the human body is an X-ray image of the hand of Roentgen's wife in December 1895 [8]. In January, 1896, six weeks after Roentgen published his results, Emil Grubbe treated breast cancer with X-rays [9]. It is one hundred years since Marie Curie won a second Nobel Prize for her research into radium, establishing her position as a pioneer in the field of radiation therapy.

For over eleven decades, radiation therapy has developed into a recognised medical specialty. Radiation oncology is a discipline in which various health and science professionals from numerous disciplines work together. Along with surgery and chemotherapy, radiation therapy remains one of the main methods used in cancer treatment, as a highly cost-effective single treatment accounting for 5% of the total cost of cancer care [10]. Furthermore, approximately 50% of all cancer patients receive radiation therapy during the course of their illness [11, 12]. Estimates show that radiation therapy contributes around 40% towards curative treatment [13]. Rapid progress in this field continues to be boosted by advances in imaging techniques, computerised treatment planning systems, radiation treatment machines (with improved X-ray production and treatment delivery) in addition to improved understanding of the radiobiology of radiation therapy [9].

Energy deposited by ionizing radiation can either directly kill cancer cells or cause genetic changes that result in the death of cancer cells. Radiation can be given both with the intent of cure and as a very effective palliative treatment to relieve symptoms caused by the cancer.

Ionising radiation damages genetic material (deoxyribonucleic acid, DNA) of cells, blocking their ability to divide and proliferate [14]. Radiation damages both cancer and normal (healthy) cells. Therefore, the goal of radiation therapy is to maximize the radiation dose to cancer cells while minimising exposure to normal cells, adjacent to the cancer cells or in the path of the radiation. Normal cells usually repair themselves at a faster rate and retain normal function compared with cancer cells. In general, cancer cells are not as efficient as normal cells in repairing the damage caused by radiation [11].

Three methods of delivering radiation to the location of the cancer are used. External beam radiation is delivered from outside the body by aiming a high-energy beam (photons, protons or particle radiation) at the location of the tumour. This is the most common approach in a clinical setting [15]. Internal radiation or brachytherapy is delivered from within the body by radioactive sources, that are sealed in catheters or seeds implanted directly into the tumour site. This is used particularly in the routine treatment of gynecological and prostate malignancies in addition to situations where local retreatment is required. And the third method of delivering radiation, targeted radionuclide therapy, uses a molecule labeled with a radionuclide to deliver a toxic level of radiation to disease sites [16].

1.1. Current status of radiotherapy

The main goal of radiotherapy is the concentration of energy deposition, in the terminology of radiation research referred to as dose, in the tumour and the sparing of healthy tissue. Radiotherapy aims to irradiate the tumour with sufficient dose to achieve local tumour control (i.e. arrest cancer growth) while minimizing the dose to adjacent sensitive organs to avoid complication (e.g. induction of secondary tumours) in normal tissues. As tumour control probability (TCP) and normal tissue complication probability

(NTCP) increase with increasing dose, there is a dose range (the so called *therapeutic window*) where the probability for tumour control without complications is a maximum (Figure 1). Biological models in radiotherapy aim to predict these TCP and NTCP values at the stage of treatment planning to optimize the treatment of the individual patient. The balance between tumour control, on one hand, and avoidance of radiation damage on the other should be ensured.

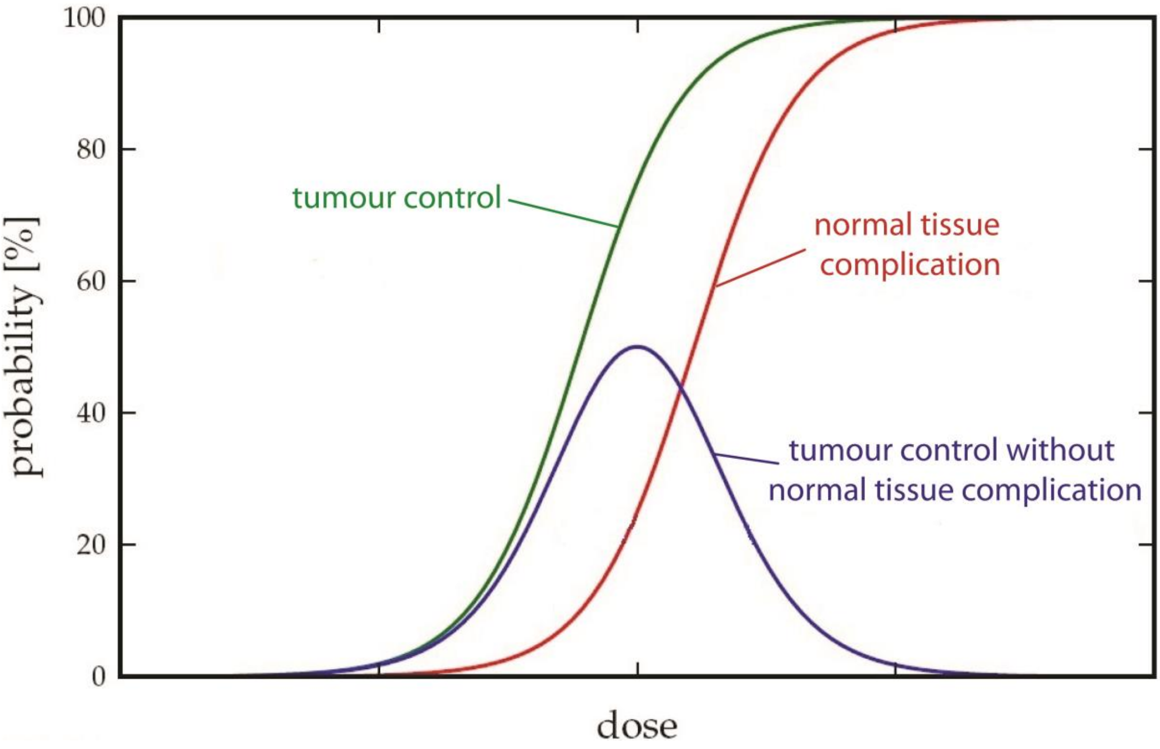

Figure 1. Dependence of TCP and NTCP on dose. The probability of tumour control without normal issue complications receives its maximum in the so-called *therapeutic window* [17].

Photons are the most commonly applied radiation therapy. They are generated through b*remstrahlung* of decelerated electrons that have been accelerated by a linear accelerator (LINAC). This will be discussed further in section 4.2.5.

Figure 2 shows the depth dose deposition profiles for currently available radiotherapy modalities, i.e. photons, electrons and protons.

The black curve in Figure 2 represents the dose distribution along the central beam axis for a 16 MeV photon beam in water. The maximum dose, and the maximum energy deposition is positioned just below the surface of the phantom. This is a disadvantage if the tumour is located deeper than the dose maximum for photon beams. To minimise the dose outside the tumour and maximise it in its volume the target is irradiated from different angles, so that the fields overlap in the tumour volume. This creates a higher dose in the target with lower dose deposition in healthy tissue. By using the state of the art technique of intensity modulated radiotherapy (IMRT) the radiation dose can be conformed more precisely to the three-dimensional (3D) shape of the tumour by intensity modulation of the radiation beam in multiple small volumes. Because the ratio of normal tissue dose to tumour dose is reduced to a minimum in IMRT, higher and more effective radiation doses can be delivered safely to tumours, with fewer side effects compared with conventional radiotherapy techniques.

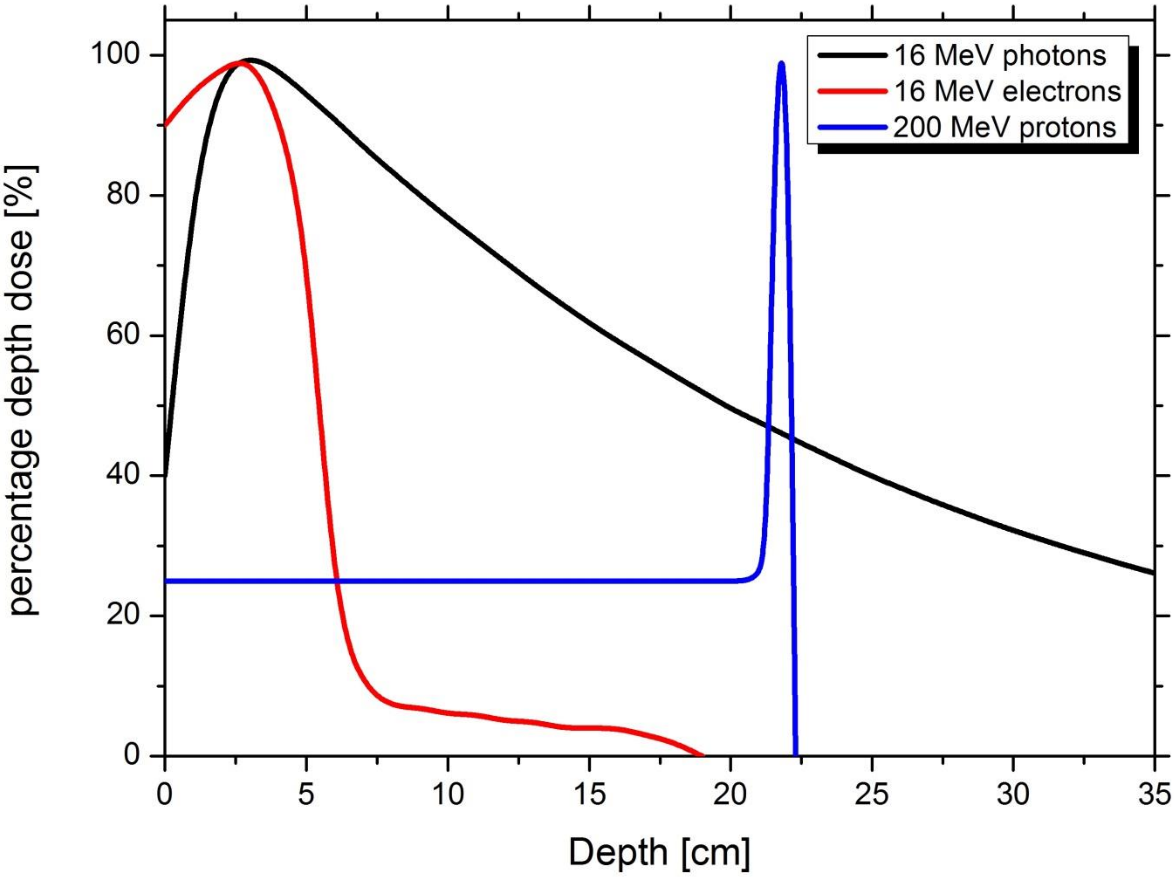

Figure 2. Comparison of on-axis monoenergetic depth dose distributions in water of current radiotherapy modalities (photons, electrons and protons). The curves have been calculated using a Monte Carlo method and are normalized to their maximum dose for each modality.

The depth dose profile for electron beams currently used in radiotherapy is represented in Figure 2 by the red curve. Electron beams have a finite range of propagation in tissue, after which the dose falls off rapidly. Therefore, this modality spares dose deposition at deeper located healthy tissue. The depth of the treatment is determined by the particle energy. However, currently only energies up to 20-30 MeV range are available, which allows for treatment of tumours located at a depth of 4-5 cm. Thus, electron beam therapy is only used in the treatment of superficial tumours such as skin cancer (e.g. melanoma), diseases of the limbs (e.g. lymphoma), nodal irradiation, but can be also used to boost the radiation dose to the surgical bed after a mastectomy or lumpectomy.

Proton and heavy ion beams are a newer form of particle beam radiation therapy used to treat cancer. They have distinct depth dose profiles compared with photons or electrons. The percentage depth dose profile (PDD) is represented by the blue curve in Figure 2. Protons have a finite range and can offer better dose distribution due to their unique absorption profiles in tissue, because they deposit most of their energy just before they come to rest, which results in maximum destruction at the tumour site, while minimising the damage to healthy tissues along their path. This feature is known as *Bragg peak*. Based on this inverse dose profile, Wilson [18] suggested the use of energetic protons for radiotherapy in 1946, before accelerators were able to deliver particle beams at the required energies. The extent of the Bragg peak for a monoenergetic beam can be as small as 1 mm. The tumours treated by radiotherapy are always large, often of the order of a few centimeters. Current imaging modalities in radiotherapy have a detection resolution of the order of 1 mm for magnetic resonance imaging (MRI) and around 2 mm for high resolution computed tomography (CT) [19]. Proton and heavy ion radiotherapy give flexibility in the treatment of larger tumours. With the variation of the initial particle energy and therefore the penetration depth, the location of the Bragg peak can be shifted. A superposition of several Bragg peaks, a so called *spread-out Bragg peak* (SOBP), can be used to cover an extended volume with a homogeneous dose.

Figure 3 shows the concept of the SOBP (orange curve), which consists of the superposition of many single Bragg peaks (red curves) of monoenergetic beams. The figure also shows that the ratio of the maximum energy deposition to the energy deposition in the entrance region is lower than for the monoenergetic case. The total integral dose to normal tissue in a treatment with protons is up to a factor of two lower than with IMRT [20]. However, the dose conformity of proton fields can be matched by IMRT in most cases. Better results than with IMRT can be achieved using proton beams if the target volume is in the vicinity of critical organs or complex shaped dose distributions are required [21]. The risk of secondary cancer is also believed to be lower for protons than for photon treatment [22]. Therefore, proton and heavy ion beams have particular clinical use for pediatric tumours and adult tumours located near critical structures, such as the spinal cord and skull base tumours, where maximal normal tissue sparing is crucial [23].

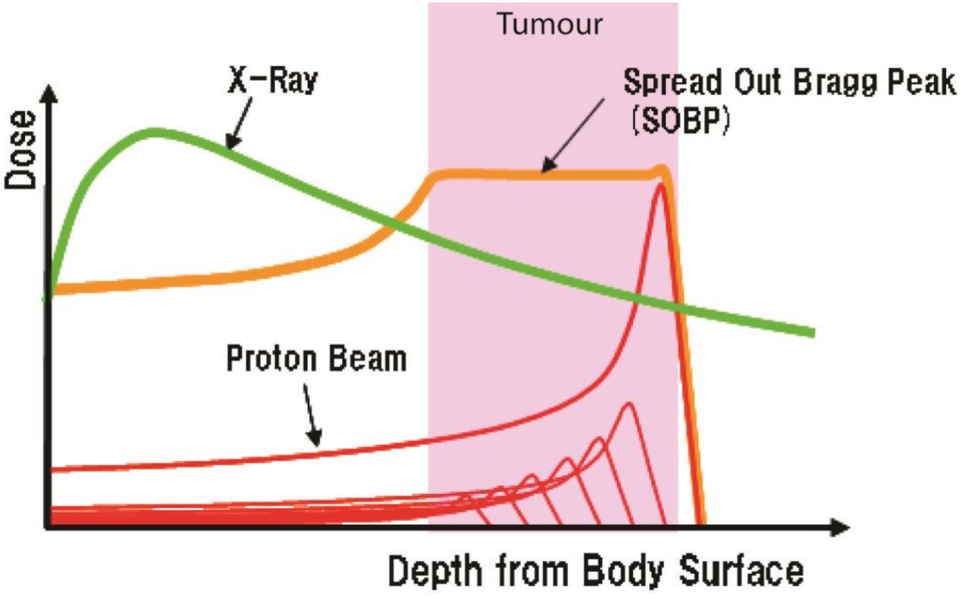

Figure 3. The concept of spread-out Bragg peak [24].

Ions are heavier than protons, which has the advantage of less scattering and a higher ionisation density. This manifests in a narrower Bragg peak and a higher peak to entrance dose ratio. The use of heavier ions and especially carbon ions has been suggested by Wilson [18]. However, as seen in Figure 4 behind the Bragg peak of carbon ions dose is deposited due to generated products of nuclear fragmentation [25].

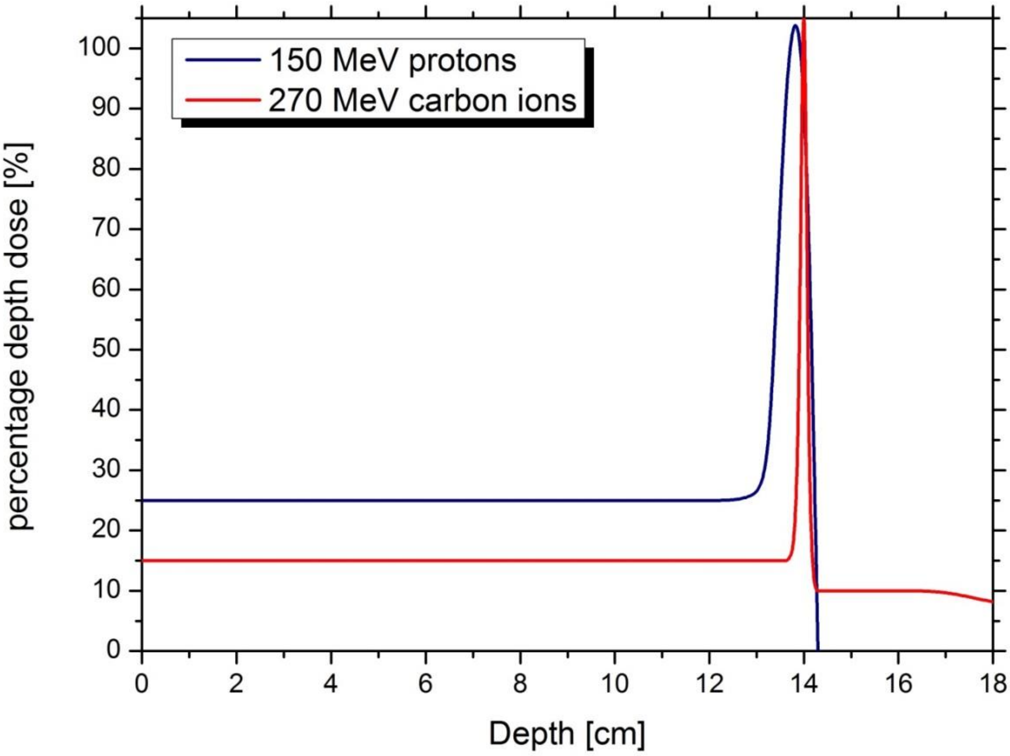

Figure 4. Comparison of depth dose deposition for monoenergetic protons and carbon ions.

The dose advantage of carbon ions over protons vanishes with superposition of several energies to produce a SOBP. However, due to less scattering, a smaller penumbra than with protons in deep seated tumours can be achieved [26].

The main rationale for the employment of carbon ions is the additional biological effect [27]. A physical dose applied with carbon ions can result in a higher biological effect compared with the same dose applied with protons or photons. This effect is not constant over the whole particle range but is enhanced towards the end of the particle trajectory, in the Bragg peak. An increased physical dose in the peak, due to the higher linear energy transfer (LET) in that region, enhances the biological effect in that region. This allows the application of higher effective doses to the target region with same or less effective dose to the surrounding healthy tissue. Thus a higher probability of tumour control with the same or lower probability of side effects (i.e. normal tissue complications) can be achieved.

The relative biological effectiveness (RBE) is the ratio between the physical and biological effective dose, which is an important factor in patient treatment. It is, however, not related to a single physical quantity. For treatment, it is calculated using models that take into account the energy deposition pattern of ions [28]. The question of which treatment is the best can only be answered by comparing the results of clinical trials. There is still no clear evidence whether carbon ions are superior to protons [29] or if radiation therapy with particles have any benefit over photon therapy [30].

It is known that particle radiation has a higher LET and higher biological effectiveness than photons. Therefore, these forms of radiation may be more effective for radioresistant cancers, such as sarcomas, renal cell carcinomas, melanomas and glioblastoma [31]. However, equipment for producing heavy particles is considerably more expensive than for photons. The decreasing costs of cyclotrons may result in a wider use of proton beam therapy in the future [32]. According to estimates in 2010, the cost ratio of particle versus photon/electron treatment is 4.8 [33]. Currently, there are 48 operating proton and ion centres worldwide, where a total of 100,000 patients have been treated.

1.2. Very high energy electrons – a new modality in radiotherapy

Given the expense of procuring and installing radiotherapy machines, which is around £3 million each, the cost of increasing capacity for cancer treatment requires a significant investment, also for operation and machine maintenance [34]. Therefore, there is a pressing need for less expensive and more effective radiation therapy.

An alternative modality, proposed over a decade ago, in 2000, by DesRosiers *et al*. [35], is very high energy electron (VHEE) therapy that uses electron beams over 100 MeV. The depth-dose characteristic for VHEEs is shown in Figure 5 together with conventional radiotherapy modalities, for comparison. The study shows that high energy electrons in the range of 150 MeV exhibit maximum dose deposition deep in tissue, therefore would be suitable for the treatment of deep-seated tumours. Moreover, the dose profile for VHEEs has a very similar outline (up to the Bragg peak) compared with the depth dose deposition in SOBP of proton beams. However, the exit dose is still high.

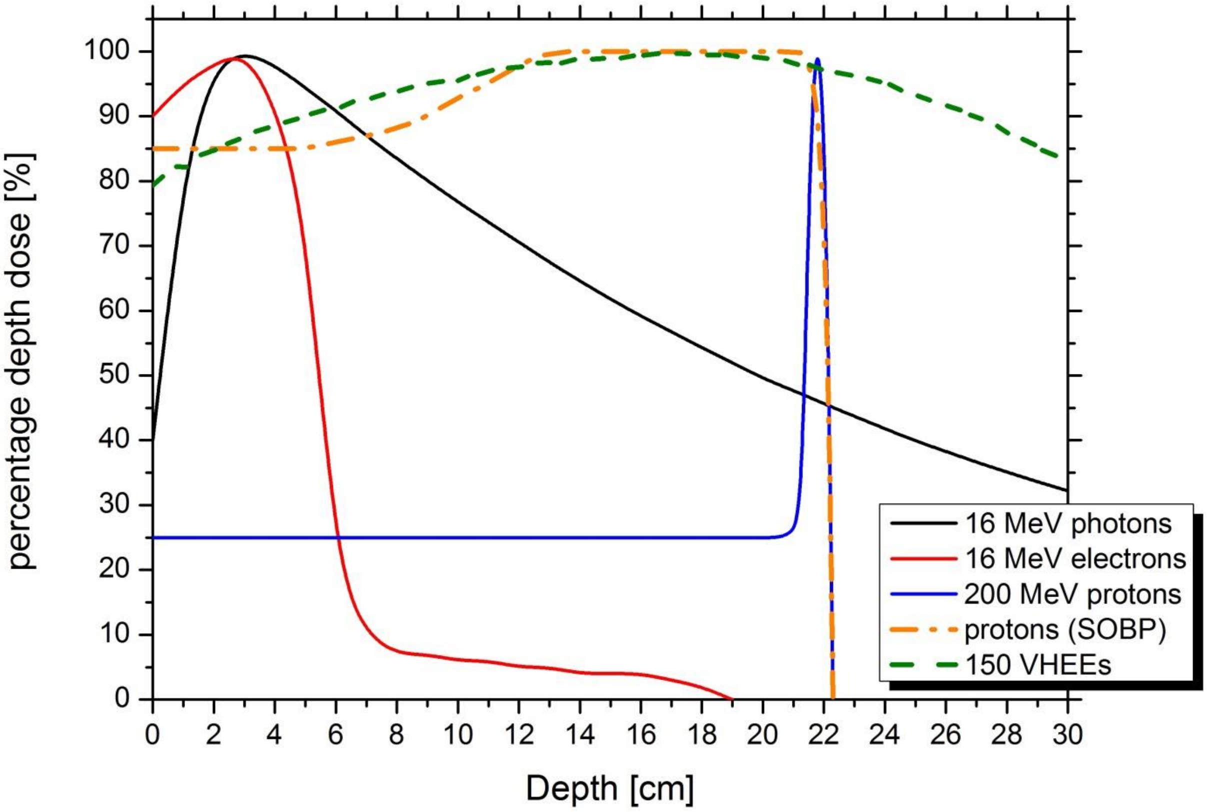

Figure 5. Comparison of depth dose deposition for conventional modalities and VHEEs (the dashed green curve).

Previous theoretical studies using the PENELOPE code [36] have shown the potential of 150–250 MeV VHEE beams [35, 37]. The effective range of such beams can exceed 40 cm and, moreover, lateral scattering of high-energy electrons in tissue is sufficiently small for intensity modulated radiotherapy (IMRT) treatment of deep seated tumours [38, 39].

Furthermore, the potential clinical advantage of electron beams with energies exceeding 100 MeV have been studied for lung cancer [40] and prostate cancer treatment [41].

Figure 6 illustrates the effect of an air cavity (embedded in tissue) on the dose distribution of 15 MeV photon and 200 MeV electron beams, using the MC simulations carried out by DesRosiers *et al.* [41]. The VHEE beam is superior to photon dose deposition in tissue with varying density, while for 15 MeV photons a significant dose perturbation occurs. This can lead to overdosage of healthy tissue and underdosage of the targeted lesion in radiation therapy. Moreover, it should be noted that the sophistication of the algorithms required to predict this effect in photon beam treatment requires computational time that are not practical in clinical settings. Because there is no perturbation due to presence of air cavity for the very high energy 200 MeV beams, simplified algorithms can be used for accurate dose prediction.

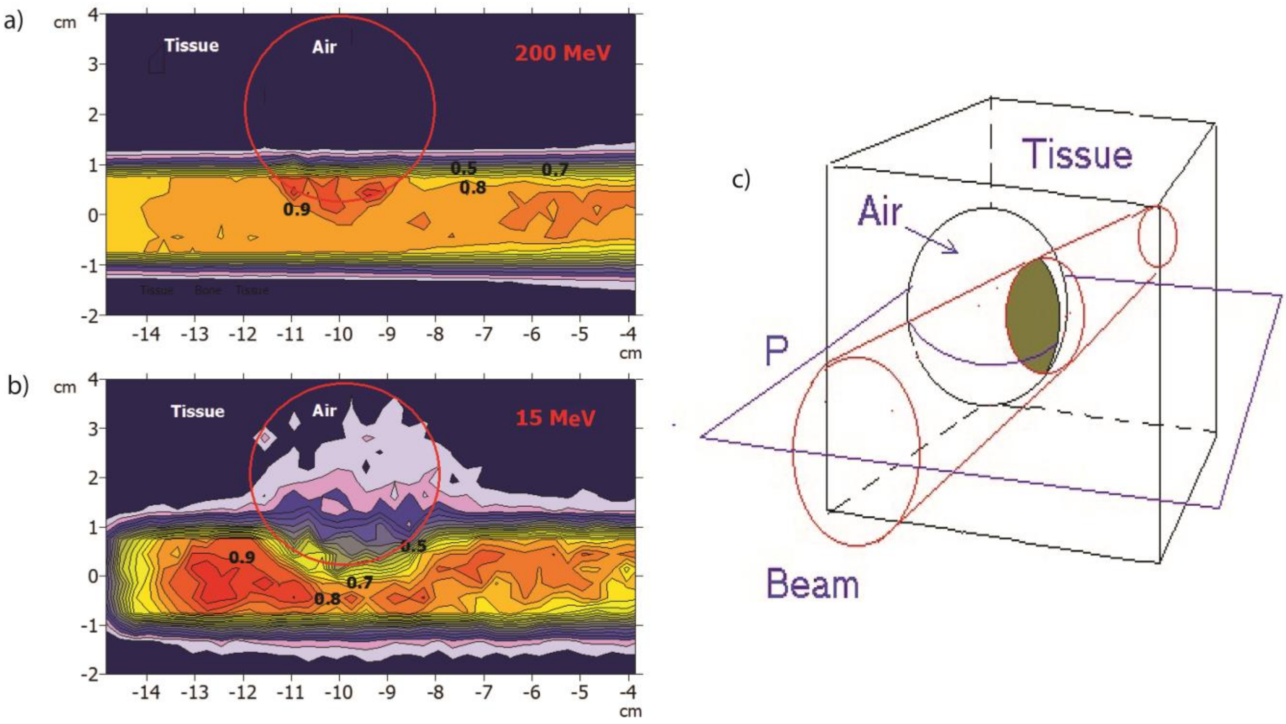

Figure 6. 2D dose distributions based on PENELOPE calculations of (a) 200 MeV electron beam and (b) 15 MeV photon for an air cavity embedded in tissue. (c) depicts simulation setup [41].

Previous studies have shown that electron beams with energies above 100 MeV can achieve a very good dose conformation, comparable with or even exceeding those of current photon modalities, while offering significantly better dose sparing of healthy tissue

[42]. Advantages of VHEE beams include the possibility of irradiating the target volume from several different directions simultaneously, a small penumbra and higher dose rates.

Conventional VHEE LINACs are large devices due to their limited accelerating gradient (<100 MV/m), imposed by electrical breakdown of their radio frequency (RF) cavities. Their large size (many meters in length) and high cost have limited the development of LINAC-based VHEE applications.

Over the past three decades, advances in laser technology have made it possible to focus light to unprecedented intensity levels, triggering new fields of research in laser-based particle acceleration and high brightness light sources. This progress has not been confined to large central facilities, making the technology widely available to other research groups across the globe. The physics of this field is characterised by extreme conditions, where light and matter are linked through highly nonlinear electrodynamical and plasma processes. Ordinary matter, whether solid, liquid or gas, is rapidly ionised when subjected to high-intensity radiation. This initially occurs via field ionisation. Ionised electrons oscillate with a characteristic frequency. The space-charge separation creates high electrostatic fields that can be used to accelerate charged particles and produce short-wavelength radiation. The laser-plasma accelerator, is a very compact accelerator with accelerating gradients exceeding 100 GV/m such that energies in the 100-250 MeV range can be obtained from a mm-scale accelerator [43-45]. Electron beams from LWFAs have unique properties: ultra-short pulse duration (1-3 fs)[46], low energy spread ($\delta E/E<1\%$) [47], low transverse emittance ($\varepsilon_n < 1\ \pi$ mm mrad) and high peak current (> 1 kA) [48]. Their compactness and their high quality electron beams makes them an attractive candidate for VHEE radiotherapy [38]. Furthermore, the cost of a LWFA , is of the orders 2 million pounds [41], which is considerably lower than both proton radiotherapy and current state of the art intensity-modulated radiotherapy (IMRT).

1.3. The need for dosimetry

The successful application of radiotherapy requires precise beam delivery, regardless of the radiation type. A 5-7 % deviation in dose has an impact on clinical outcome [49, 50], e.g. for head and neck cancer, a 5 % under dosage reduces the tumour control probability by 15 % while, a 5 % higher dose increases the risk of side effects [51].

Precise beam delivery, however, relies on the capability of measuring dose, i.e. dosimetry.

The standard dosimetry used in modern radiotherapy is air-filled ionisation chambers. These are reliable for use with photon and ion beams. Due to their size and the need of a power supply, they are not always suitable for measurement of complex radiation fields used, for example, in intensity modulated radiotherapy or beams with a small size. Solid state detectors provide a higher signal per volume due to their higher density. This enables smaller detectors and thus dosimetry with a higher spatial resolution. However, solid state detectors exhibit saturation effects due to higher signal density [52]. Very high energy electrons have characteristics unlike any other radiotherapy beam. The radiation pulses (particularly from LWFAs) are very short (pico- or femtosecond duration), and their energies are one order of magnitude higher than from conventional electron sources. Therefore, dosimetric characterisation of these beams and choice of the most appropriate detector for dosimetry can be challenging.

1.4. Thesis Objectives

This thesis aims to investigate the possibility of using very high energy electron beams generated by LWFAs as a new modality in radiotherapy.

The work focuses on investigating dosimetry of VHEE beams for radiotherapy applications. Monte Carlo simulations are presented to investigate the capabilities of the method to predict dose deposition in tissue and demonstrate their potential in planning of experiments and the assessment of radiation safety. Dosimetric measurements of LINAC and laser-wakefield – accelerated VHEEs are presented. In addition, preliminary radiobiological studies on the response of cancer cells irradiated to LWFA VHEEs are reported.

The second chapter briefly discusses the theoretical foundations of LWFA. Different configurations of LWFA and nonlinear operation, which have the potential of generating high-quality electrons are given.

The third chapter describes the ALPHA-X laboratory, at the University of Strathclyde, the laser, the beam transport system and the electron beam diagnostic systems that are used to characterise the beam for the experiments on LWFA VHEEs presented here.

Chapter four presents Monte Carlo data on dosimetry of VHEEs and compares the results with low energy electrons commonly used in radiotherapy. Aspects of radiation safety, production of secondaries and potential difference of radiobiological effectiveness (RBE) due to the difference in LET and bunch length for VHEE beams are discussed.

In chapter five, dosimtery measurements of electron beams are given. The calibration of the dosimeter, EBT2 Gafchromic film, for dose measurements of LWFA- and LINAC-accelerated very high energy electron beams with extensive characterization of the detector is described. A comparison of film dose measurements with ionization chamber measurements is also presented.

Chapter six discusses the biological effects of VHEE produced by a laser-plasma wakefield-accelerated accelerator in *in vitro* cancer cell models. Preliminary pilot studies on cell toxicity exposed to LWFA VHEEs and the kinetics of DSBs following VHEE irradiation are presented.

In the seventh and last chapter, the results are discussed and future perspectives and challenges for LWFA sources are outlined.

2. Principles of Laser-Plasma Accelerators

Laser-driven plasma-based accelerators were first proposed in 1979 by Tajima and Dawson [53]. Dawson was responsible for many of the early developments in this field, including the plasma beat wave accelerator, the plasma wakefield accelerator, and the photon accelerator. He was also one of the early pioneers of particle-in-cell (PIC) simulations of plasma [54], which are widely used in the study of plasma-based accelerators. In the past three decades the field of plasma-based accelerators has grown into a world-wide research effort with ongoing experimental programmes worldwide, including Europe, Asia and the US. Much of this growth is due to the development of chirped- pulse amplification (CPA) laser technology, pioneered by Mourou *et al.* [55], making available compact sources of intense, high-power, ultrashort laser pulses.

Laser-plasma accelerator experiments prior to 2004 demonstrated acceleration gradients 100 GV/m, accelerated electron energies 100 MeV, and accelerated charge 1 nC. However, the breakthrough happened in 2004 when three groups simultaneously reported the seminal studies on laser plasma accelerated electrons in the so called *Dream Beam* papers [43-45], which included the project led by the University of Strathclyde. They demonstrated the production of high-quality electron bunches with small energy spread of approximately a few percent and low divergence of a few milliradians.

The majority of experiments reported in this thesis are based on the laser-plasma wakefield accelerator (LWFA). Understanding the physics behind laser-plasma interaction helps to improve the quality of the accelerated electron beams. This chapter gives a brief overview of laser and plasma properties and the theoretical foundation of laser-plasma acceleration

2.1. Propagation of EM waves

An electromagnetic wave is a field that propagates in space and consists of both an electric and a magnetic components. The propagation of the wave in a medium is described by Maxwell equations [56]:

$$\begin{cases} \vec{\nabla}\cdot\vec{E} = \dfrac{\rho}{\varepsilon_0} \ , \qquad \vec{\nabla}\cdot\vec{B} = 0, \\ \vec{\nabla}\times\vec{E} = -\dfrac{\partial\vec{B}}{\partial t} \ , \qquad \vec{\nabla}\cdot\vec{B} = \dfrac{1}{c^2}\dfrac{\partial\vec{E}}{\partial t} + \mu_0\vec{j}, \end{cases} \tag{2.1}$$

where $\vec{E}, \vec{B}, \rho, \vec{j}$ denotes the electric and magnetic fields, the electric charge and current density, respectively. ε_0 and μ_0 are the permittivity and permeability of vacuum and c is the speed of light. The operator $\vec{\nabla}$ is the spatial partial derivative operator.

From equations (2.1), we can derive the equation of propagation of electric and magnetic fields. For propagation in vacuum (i.e., $\rho = 0$ and $\vec{j} = 0$) we obtain the following expression:

$$\nabla^2\vec{E}(\vec{x},t) - \frac{1}{c^2}\frac{\partial^2\vec{E}}{\partial^2 t}(\vec{x},t) = \vec{0}, \tag{2.2}$$

which in the frequency domain can be written as:

$$\nabla^2\vec{E}(\vec{x},\omega) - \frac{\omega^2}{c^2}\vec{E}(\vec{x},\omega) = \vec{0}. \tag{2.3}$$

In the more general case of propagation in an isotropic medium we can introduce η – the refractive index – incorporating the response of the medium to obtain:

$$\nabla^2\vec{E}(\vec{x},\omega) - \frac{\omega^2}{c^2}\eta^2(\omega)\vec{E}(\vec{x},\omega) = \vec{0}. \tag{2.4}$$

2.2. Laser parameters

A laser is producing an electromagnetic wave that can be described using scalar and vector potentials defined in equation (2.5):

$$\begin{cases} \vec{E} = -\vec{\nabla}\Phi - \dfrac{\partial \vec{A}}{\partial t}, \\ \vec{B} = \vec{\nabla} \times \vec{A}. \end{cases} \tag{2.5}$$

It is useful to define a normalised vector potential $\vec{a}$, as:

$$\vec{a} = \frac{e\vec{A}}{m_e c}, \qquad a_0 = \frac{eA_0}{m_e c} \simeq \frac{eE_l}{\omega m_e c}, \tag{2.6}$$

where e is the electron charge, m_e its mass, ω and E_l are the laser angular frequency and electric field peak amplitude, respectively.

Ultra-short laser pulses delivered by laser systems have broad spectra which contain many Fourier components. In a linear, non-dispersive medium, this spectrum (for particular laser) can be described in approximation by a Gaussian envelope. In the same way, the spatial profile of the laser pulse at the focal plane can also be represented by a Gaussian function. The electric field has the following form, for a linearly polarised pulse:

$$\vec{E}(r,z,t) = \frac{E}{2} f(r,z) g(t,z) e^{[-i(k_0 z - \omega_0 t]\vec{e}_x} + \vec{c}c. \tag{2.7}$$

The field (2.7) is composed of a carrying envelope with wave number k_0 and frequency ω_0 and spatial and temporal information in $f\ (r,\ z)$ and $g(t)$, respectively. The following gaussian expressions (2.8) verify the equation of propagation of the electric field in vacuum in the paraxial approximation. These expressions reproduce accurately the electric field of the laser when the focusing optics have small aperture [57]:

$$f(r,z) = \frac{w_0}{w(z)} e^{\left(-\frac{r^2}{w^2(z)} - i\frac{k_0 r^2}{2R(z)}\right)} e^{i\phi(z)}, \qquad g(t,z) = e^{-2ln2\left(\frac{t-\frac{z}{c}}{\tau_0}\right)^2}, \tag{2.8}$$

where τ_0 is the pulse duration at full width at half maximum (FWHM), w_0 is the waist of the focal spot (the radius at $1/e$ of the electric field in the focal plane $z = 0$). $\phi(z)$ is the

Gouy phase and functions $w(z)$ and $R(z)$ represent the radius at *1/e* of the electric field and the radius of curvature of the wave front respectively and are expressed by equation :

$$\begin{gathered} w(z) = w_0\left(1+\frac{z^2}{Z_r^2}\right)^{1/2}, \\ R(z) = z\left(1+\frac{Z_r^2}{z^2}\right), \end{gathered} \tag{2.9}$$

where $Z_r = \frac{\pi w_0^2}{\lambda_0}$ is the Rayleigh length. This parameter represents the length over which the laser intensity on axis drops by a factor of 2 compared with the intensity in the focal plane.

The following relation exists between the maximum intensity I_0 and the power P :

$$\mathrm{I}_0 = \frac{2P}{\pi w_0^2}. \tag{2.10}$$

For a linearly polarised Gaussian beam, the normalised vector potential a_0 is related to the laser peak intensity I_0 by the following expression [58]:

$$a_0^2 = \left(\frac{e^2}{2\pi^2\varepsilon_0 m_e^2 c^5}\right)\lambda^2 I_0 \simeq 7.3\times10^{-19}[\lambda(\mu m)]^2 I_0\left(\frac{W}{cm^2}\right). \tag{2.11}$$

When $a_0 = p/mc$ (i.e. the ratio of the transverse momentum to *mc*) exceeds unity, the oscillations of an electron in the laser field become relativistic.

2.3. Plasma waves

For initially uniform, non-collisional plasma in which electrons are displaced from the equilibrium position, the restoring force of the ions drives them towards an equilibrium position. For the time scale corresponding to the electron motion the ion motion can be neglected due to its inertia. This results in an oscillation around the equilibrium position at a frequency known as the electron plasma frequency, ω_p, expressed by equation (2.12):

$$\omega_p = \left(\frac{n_e e^2}{m_e \varepsilon_0}\right)^{1/2}, \tag{2.12}$$

where n_e is the unperturbed electron density.

If one assumes a perfect gas, a homogeneous plasma has an electron velocity distribution $f_e(v_e)$ that obeys the Maxwell-Boltzmann relation at thermodynamic equilibrium:

$$\mathrm{f}_e(v_e) = \left(\frac{m_e}{2\pi k_B T_e}\right)^{\frac{3}{2}} e^{\left(-\frac{1}{2}\frac{m_e v_e^2}{k_B T_e}\right)}, \tag{2.13}$$

where k_B is the Boltzmann's constant, T_e is the temperature of the electron gas. The average thermal velocity of the electrons for this distribution is $v_{te} = \sqrt{k_B T_e / m_e}$.

2.4. Laser-plasma interactions

Laser pulses with intensities of 10^{18}-10^{20} W/cm^2 yield electric fields of the order of 10^{10}-10^{11} V/cm. Therefore, matter interacting with a high intensity laser pulse is partially or fully ionised by the leading edge of the laser pulse and the high intensity part of the pulse interacts with plasma.

A free electron in an alternating electric field $\vec{E} = E_0 \hat{e}_x \cos(\omega t - kz)$ with frequency ω oscillating with a classical quiver velocity amplitude expressed as:

$$v_{osc,class} = \frac{eE}{m_0 \omega}. \tag{2.14}$$

When $v_{osc,class} \rightarrow c$ the electron becomes relativistic.

The amplitudes of the electric and the magnetic field components and the intensity can be expressed formally in terms of the normalized vector potential, a_0:

$$E_0 = \frac{a_0}{\lambda[\mu\mathrm{m}]} \cdot 32.2 \frac{\mathrm{GV}}{\mathrm{cm}}, \tag{2.15}$$

$$B_0 = \frac{E_0}{c} = \frac{a_0}{\lambda[\mu\mathrm{m}]} \cdot 107\ \mathrm{MG}\,, \tag{2.16}$$

$$I_0 = \frac{\varepsilon_0 c}{2} E_0^2 = \frac{a_0^2}{\lambda^2[\mu\mathrm{m}^2]} \cdot 1.37 \cdot 10^{18}\,\frac{\mathrm{W}}{\mathrm{cm}^2}\,, \tag{2.17}$$

Because the dynamics of an electron in high amplitude fields has to be described relativistically the relativistic (Lorentz) factor needs to be employed:

$$\gamma = \left(1 + \frac{p^2}{m^2c^2}\right)^{1/2}\,. \tag{2.18}$$

Particularly, the momentum of the electron is given by $\vec{p} = \gamma m \vec{v}$. The fully relativistic equations of motion of an electron oscillating in a plane electro-magnetic wave can be solved exactly [78, 88, 89]. While in the case of low amplitude the momentum of the oscillation is perpendicular to the laser direction, at high field amplitudes the orbits reveal a more complicated geometry. Therefore, in addition, a momentum component parallel to the direction of the laser pulse is observed. As an example, we can consider an electron under the influence of a super-intense, linearly polarized laser field, $\vec{E} = E_0 \hat{e}_y \sin(\omega t - kz)$, propagating in *z*-direction. The momenta in the laboratory frame are given by

$$p_x = 0\,, p_y = a_0 \cos\psi\,, p_z = \frac{a_0^2}{4}(1 + \cos 2\psi). \tag{2.19}$$

As above, the phase factor is $\psi = \omega t - kz$. The electron is pushed parallel to the propagation direction of the laser and carries a *z*-momentum, p_z, that is pulsing with twice the laser frequency. The average drift velocity, v_D, is here given by:

$$\frac{v_D}{c} = \frac{a_0^2}{4 + a_0^2}\,. \tag{2.20}$$

To illustrate the relativistic dynamic of an electron placed in a super-intense electro-magnetic wave, the relativistic equation of motion of an electron needs to be solved numerically. The orbits observed in the laboratory frame and in the co-moving frame are illustrated in Figure 7.

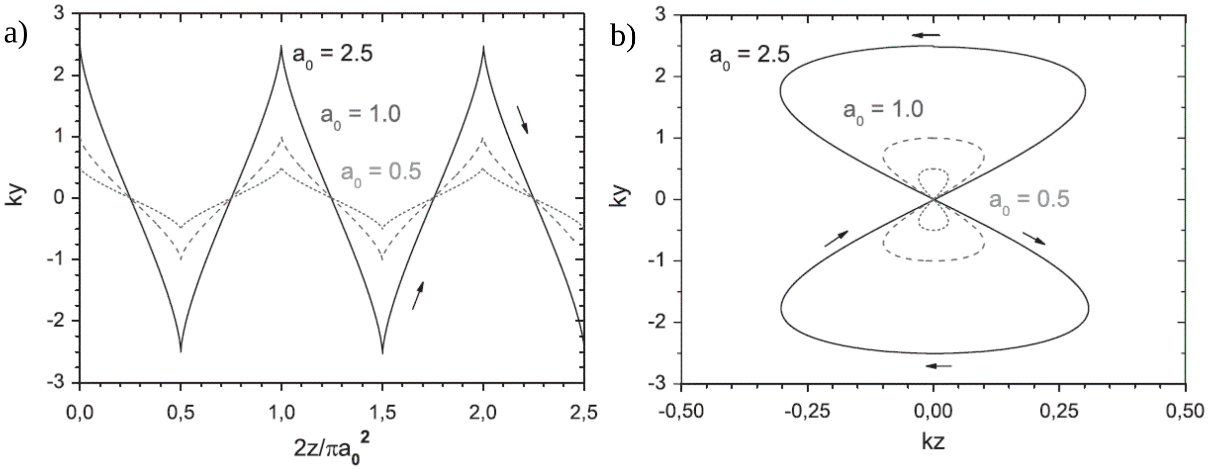

Figure 7. (a) Orbits of a free electron oscillating in a linearly polarised plane wave as observed in the laboratory rest frame for different normalised amplitudes, a_0. (b) Same orbits as seen in a co-moving average rest frame. Here typically a *figure of eight* motion is observed. The normalised amplitudes correspond to laser intensities of $5\cdot10^{17}$ W/cm^2, $2\cdot10^{18}$ W/cm^2 and $1.4\cdot10^{19}$ W/cm^2 at a wavelength of λ= 800 nm [59].

In the co-moving frame moving with the averaged centre of velocity, the periodic motion of the electron is seen as a *figure-of-eight* track (Figure 7(b)) . Consequently, a super-intense, ultra-short pulse (in the form of a plane wave) will accelerate an electron both transversally and longitudinally. As the electron is overtaken by the pulse, it is decelerated again.

2.5. Basic concept of Laser Plasma Wakefield Acceleration

Propagation of electromagnetic waves in plasma

To investigate laser-plasma interactions, the collective behavior of electrons/cm^3 needs to be considered. A plasma does not consist of the electrons alone but is usually described as a composition of an electron- and ion-fluid, with electron and ion density

$$n_e = Zn_i, \tag{2.21}$$

where *Z* is the charge state of the ions. The Coulomb potential of a single ion with charge *Ze* is shielded by surrounding electrons and therefore modified to

$$\Phi_{ion}(r) = \frac{Ze}{4\pi\varepsilon_0 r} e^{-\frac{t}{\lambda_D}}, \tag{2.22}$$

where λ_D is the Debye length:

$$\lambda_D = \sqrt{\frac{\varepsilon_0 T_e}{n_e e^2}}, \tag{2.23}$$

where T_e is the plasma temperature. The modification of the ion Coulomb potential by its surrounding electrons is known as Debye shielding, which states that on scales larger than the Debye length the plasma can be considered quasi neutral.

Small-scale density deviations in a plasma lead to electrostatic forces due to space charge separation. Therefore, electron and ion sheets will oscillate at frequencies determined by their densities and mass. For ions the frequency $\omega_{p,i}$ is defined by:

$$\omega_{p,i} = \sqrt{\frac{n_i (Ze)^2}{\varepsilon_0 m_i}} = \omega_{p,e} \sqrt{\frac{Z m_e}{m_i}}. \tag{2.24}$$

For a monochromatic electromagnetic wave traveling through an unmagnetised, cold plasma, the dispersion relation that describes the dependence of the wave frequency, ω, on the wave number, k has following form:

$$\omega^2 = c^2 k^2 + \omega_p^2, \tag{2.25}$$

where $k = \frac{\omega\left(1 - \frac{\omega_p^2}{\omega^2}\right)^{1/2}}{c}$.

Waves with frequencies $\omega < \omega_p$ are reflected at the boundary because wave number k becomes imaginary, and the plasma is *overdense*, while for $\omega > \omega_p$, waves propagate and the plasma is *underdense*. Therefore, we can define a critical density as:

$$n_c \left[\frac{1}{cm^3}\right] = \frac{m_e \omega^2}{4\pi e^2} \simeq \frac{1.12 \times 10^{21}}{\lambda^2 [\mu m^2]}. \tag{2.26}$$

For laser wakefield acceleration, plasma sources usually have densities in the range between 10^{17}-10^{19} cm^{-3}, and therefore the plasma is underdense.

The phase, v_p, and group, v_g, velocities for transverse electromagnetic fields in plasma are:

$$\begin{aligned} v_p &= \frac{\omega}{k} = \frac{c}{\eta_p}, \\ v_g &= \frac{\partial \omega}{\partial k} = c\eta_p, \end{aligned} \tag{2.27}$$

where $\eta_p = \left(1 - \frac{\omega_p^2}{\omega^2}\right) = \left(1 - \frac{n_e}{n_{cr}}\right)$ is the refractive index. For underdense plasma, the refractive index is always < 1, thus the phase velocity of an electromagnetic wave is > c, while the group velocity is always < c.

Dephasing length

Electrons from the plasma can surf the waves formed during propagation of a high intensity laser pulse in plasma and be accelerated to velocities approaching the speed of light, to a higher velocity than that of the plasma wave (Figure 8). Electrons trapped on the plasma wave are accelerated until they outrun the wave. This distance is called the dephasing length (L_{deph}). The plasma wave travels with the phase velocity, v_p, equal to group velocity, v_g, of the laser pulse in the plasma medium. Under the assumption that the plasma wave travels at a normalized velocity $\frac{v_e}{c}$, the electrons will overtake the plasma wave after $t = \lambda_p / \left[2c\left(\frac{v_e}{c} - \frac{v_g}{c}\right)\right]$, because $\frac{v_e}{c} \rightarrow 1$ and $\frac{v_g}{c} = \sqrt{1 - n_p/n_c} \approx 1 - n_p/2n_c$ in the underdense plasma.

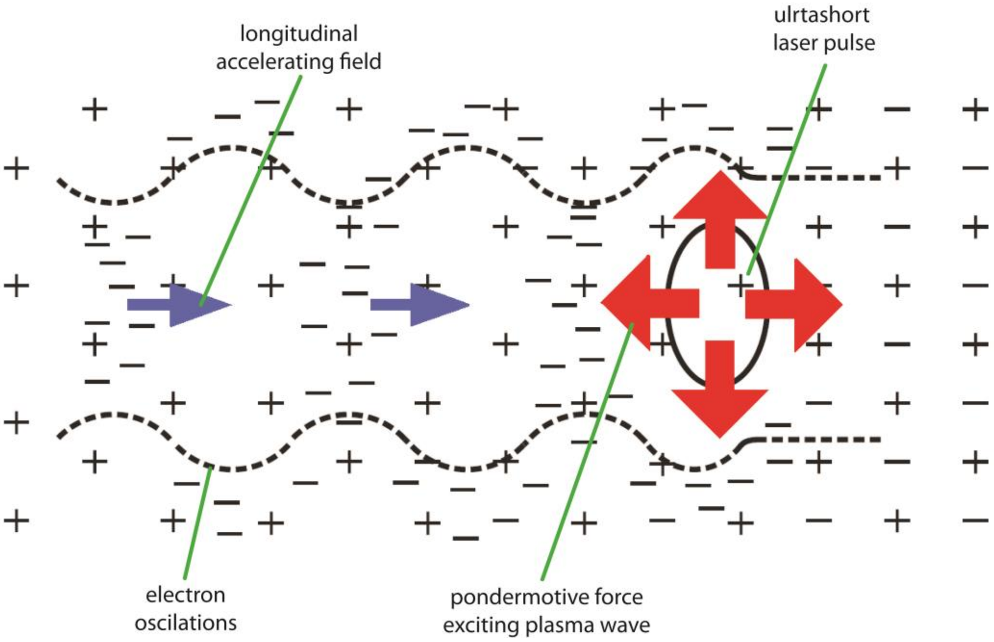

Figure 8. The schematic of plasma electron oscillations excited by the laser pulse. The pondermotive force of a laser pulse pushes electrons (-) aside leaving heavier ions (+) immobile. The plasma electron displacement creates a strong longitudinal accelerating field capable of accelerating charged particles (electrons).

The ponderomotive force

The light pressure of the laser pulse due to its intensity gradient gives rise to pondermotive force, F_p. This force can be derived using electron fluid momentum:

$$\frac{d\vec{p}}{dt} = -e\left[\vec{E} + \frac{(\vec{v} \times \vec{B})}{c}\right], \tag{2.28}$$

in the cold fluid limit as described in reference [58]. In the linear limit, i.e. for $|a_o| \ll 1$, the dominant term of the solution of equation (2.28) is a quiver momentum $\vec{p}_q = m_e c\vec{a}$, as indicated by $\frac{\partial p_q}{\partial t} = -e\vec{E}$. Letting $\vec{p} = \vec{p}_q + \delta\vec{p}$, the second order motion is given by:

$$\frac{d\delta\vec{p}}{dt} = -\left(\frac{\vec{p}_q}{m_e} \cdot \nabla\right)\vec{p}_q - \vec{p}_q \times (c\nabla \times \vec{a}) = -m_e c^2 \nabla \frac{a^2}{2} = \vec{F}_p. \tag{2.29}$$

Therefore, equation (2.29) is the 3-dimensinal pondermotive force in the linear limit. This force can be also seen as the radiation pressure, i.e. the gradient of the electromagnetic energy density.

At the focus of a “relativistic laser pulse”, i.e. for irradiances above $I{\cdot}\lambda^2 \approx 10^{18}$ W·cm^2, an electron will be expelled from regions of high intensity towards lower intensity in a similar way to the non-relativistic case. Differences in the dynamics arise from the relativistic mass increase at high quiver velocities and the non-vanishing B-component in the Lorentz force. A relativistic generalisation of the ponderomotive force has been derived in [60, 61] and is given by:

$$F_p = -\frac{e^2}{2\gamma m_e}\nabla A^2 == -\frac{m_e c^2}{2\gamma}\nabla {a_0}^2. \tag{2.30}$$

The relativistic ponderomotive force is responsible for the average electron motion observed in the laboratory frame and can be written as the negative gradient of a relativistic ponderomotive potential,

$$U_p = -\frac{m_e c^2}{4\bar{\gamma}} a_0^2. \tag{2.31}$$

Critical power

The pondermotive force, *F_p*, is responsible for expelling electrons from the laser path producing a local reduction in the electron density [62]. This effect together with the increase of the relativistic mass due to the electrons' quivering motion depend on the normalised vector potential in the strong EM field of the laser resulting in an increase of the refractive index, which in turns leads to laser self-focusing in the plasma. This effect occurs just above the critical power (defined in equation (2.32)) when the self-focusing rate is balanced by natural diffraction of the laser pulse[62],

$$P_c = 17\frac{\omega_0^2}{\omega_p^2}[PW]. \tag{2.32}$$

Depletion length

A laser pulse propagating through plasma loses its energy to the plasma wave. The distance over which the laser pulse energy is depleted in known as the depletion length, L_{depl}. To estimate the depletion length it is necessary to calculate the length over which the energy deposited in the plasma is equal to energy of the laser pulse. For the LWFA the depletion length is given by equation (2.33):

$$L_{depl} = \frac{\omega_0^2}{\omega_p^2} \lambda_p a_0^{-2} \tag{2.33}$$

Wavebreaking

The plasma-oscillation amplitude is limited by wavebreaking, which occurs when the velocity of plasma electrons exceed the phase velocity of the plasma wave. This concept is important because it gives the limit of the electric field obtainable in the plasma wave and because electrons that exceed the phase velocity of the plasma wave can be trapped and accelerated. The velocity of an electron in a cold linear wave is $\frac{e}{m_e \omega_p} E_0$. The maximum electron velocity is equal to the phase velocity of the plasma wave, which is equal to the group velocity of the laser pulse, v_g. The maximum electric field is reached when the electron velocity is equal to the group velocity of the laser pulse and the maximum electric field is given by [63]:

$$E_{max} = \frac{m_e v_g \omega_p}{e}. \tag{2.34}$$

Using Poisson's equations and assuming the oscillations are harmonic it is possible to derive the maximum electric field, E_0, assuming that the phase velocity of the plasma wave approaches the speed of light: $E_0 = \frac{c v_g \omega_p}{e}$. The critical longitudinal attainable field, E_{WB}, is equal to electric field of the laser pulse, $E_L \approx E_0$. When this limit is reached, the wave steepens and crest forms and falls through. This wave-breaking limit is valid only for the cold non-relativistic case. Nevertheless, the wave breaks when the electrons have a velocity approaching phase velocity of the plasma wave, therefore when electrons are fully relativistic. It has been shown in the 1 D cold relativistic wavebreaking limit for plasma waves with relativistic phase factor, γ_p, that the maximum amplitude of the plasma wave is given by the so called relativistic wave-breaking field [64, 65]:

$$E_{WB} = E_0 \sqrt{2(\gamma_p - 1)}. \tag{2.35}$$

2.6. Configurations of Laser-Plasmas Accelerators

There are four types of laser-plasma accelerators: laser wakefield accelerator (LWFA), the plasma beat-wave accelerator (PBWA), self-modulated laser-wakefield accelerator (SM-LWFA) and resonant laser pulse train (Figure 9).

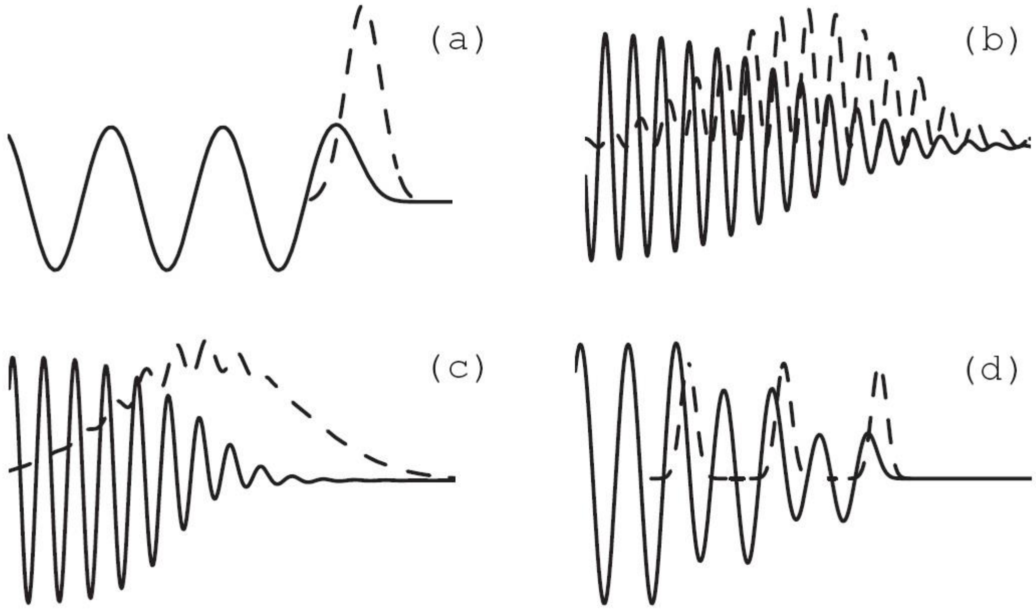

Figure 9. Schematic of laser-plasma accelerators: (a) LWFA, (b) PBWA, (c) self-modulated (SM) LWFA, and (d) resonant laser pulse train. Shown are the excited plasma wave potentials (solid lines) and right-moving laser intensity envelopes (dashed lines) [58].

2.6.1. Laser wakefield acceleration (LWFA)

The wakefield is driven most efficiently when the laser pulse length, L, is of the order of the plasma period, λ_p. This scheme of acceleration was first proposed by Tajima and Dawson in 1979 [53]. When an intense laser pulse propagates through underdense plasma, $(\lambda/\lambda_p)^2 \ll 1$, the pondermotive force, F_p, of the laser pulse envelope expels electrons from the region of the laser pulse propagation. If the length scale, L_z, of the axial gradient in the pulse profile is approximately equal to plasma wavelength ($L_z \approx \lambda_p$) then F_p excites wakefields with a phase velocity $\approx v_g$ of the laser pulse (Figure 9(a)).

2.6.2. Plasma beat wave accelerator (PBWA)

The PBWA and LWFA was first proposed by Tajima and Dawson [53] as an alternative to ultrashort and ultrahigh laser technology. In the plasma beat wave accelerator the laser pulses of frequencies ω_1 and ω_2 are used to resonantly excite the plasma wave. This is done by adjusting the laser pulse frequencies so that $\Delta\omega \equiv \omega_1 - \omega_2 \cong \omega_p$. When this relation is satisfied large amplitude plasma waves can be generated. However, plasma inhomegenities and laser-plasma instabilities are an important limitation factor for this regime of operation. For instance, the electric field increases with the growth of plasma waves, therefore the velocities of plasma electrons can approach the speed of light and increase their effective mass resulting in red-shifting of plasma frequency and losing resonance. Another limitation of the PBWA scheme is laser diffraction and pump depletion dephasing (this is also a limitation of LWFA). Laser diffractions could be overcome by using plasma waveguides while pump depletion can be avoided by employing more powerful lasers.

2.6.3. Self-modulated laser wakefield accelerator (SM-LWFA)

It is possible for a single laser pulse to break into a train of short pulses, each having a length of the order of the plasma length, λ_p. The break up of a long pulse to shorter pulses is associated with the formation of large plasma wave amplitude. This process is called self-modulation [66]. Self-modulation occurs from the plasma wave producing periodic regions of enhanced focusing and diffraction [67]. The SM-LWFA is a hybrid mechanism combining the laser plasma wakefield acceleration and forward Raman scattering. Forward Raman scattering is the resonant decay of the incoming laser wave (with frequency ω_0) into a plasma wave (with frequency ω_p) and two electromagnetic waves with frequencies $\omega_0 \pm \omega_p$. The plasma wave is resonantly driven by the pondermotive force associated with the incident and the scattered waves. The plasma wave results in the modulation of the refractive index $n = \left(1 - \omega_p^2/\omega_0^2\right)^{1/2}$. If the laser pulse is longer than λ_p the laser pulse propagating through plasma experiences refractive index modulations that result in focusing, defocusing and modulation of the phase and group velocities, which lead to amplitude modulations. The regime of SM-LWFA strongly depends on the power of the laser and increases drastically when the laser power exceeds the critical power of self-focusing [62]. The disadvantage of SM-LWFA compared with LWFA, is a higher electron density and, therefore, a lower laser group velocity, which results in shorter dephasing length and lower electron energy. Due to continuous electron trapping over the short dephasing length the accelerated electron beam exhibits broad energy spread and a high dark current component [58]. Therefore, the electron beam quality in self-modulated regime is another drawback.

2.6.4. *Resonant laser pulse train*

As discussed in the above section, for the plasma beat wave wakefield accelerator

- the laser beat wave acts in effect as a series of short laser pulses
- the growth of the plasma wave creases the plasma wave, which leads to loss of resonance with respect to the laser beat pulses
- the period of the beat laser pulses can be optimised to maximise the plasma wave amplitude

These general principles can be extended to describe plasma wave generation by a series of short laser pulses. For instance, the resonant laser-plasma accelerator uses an optimised train of short laser pulses to drive the plasma wave, in which the width of each pulse and the spacing between pulses is independently controlled. The resonance with plasma wave and saturation of plasma wave (by resonant detuning) can be maintained with the optimisation of the short laser pulses train and the spacing between these pulses [68, 69]. The number of pulses is optimised when the pulse widths and spacings are chosen to maximise the amplitude of the plasma wave. In the nonlinear regime ($a_0^2 \gg 1$) the resonance can only be maintained by optimising both pulse widths and spacing of each individual pulses.

2.7. The Bubble Regime

Theoretical work based on 3D PIC simulations have shown the existence of a robust acceleration mechanism known as the bubble regime [70]. In this regime, the dimensions of the focused laser match the bubble dimensions in longitudinal and also transverse directions. If the laser energy contained in this volume is high enough, the ponderomotive force of the laser efficiently radially expels electrons from its propagation path, forming an evacuated cavity that is positively charged (oval red region in Figure 10), surrounded by a high density electron sheath. Behind the bubble, electronic trajectories intersect each other. A few electrons are injected into the cavity and are accelerated along the laser axis.

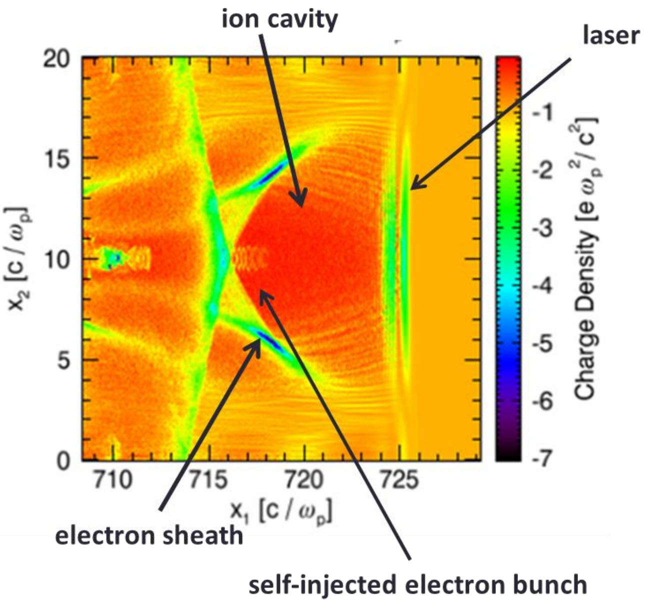

Figure 10. Ion cavity simulated in OSIRIS [71] showing three density regions: ion cavity behind the laser pulse, high density electron sheath and self-injected electrons [72].

The electric field required to enter the bubble regime is estimated from the cold-relativistic model that holds for low plasma temperature. Wave breaking gives rise to an abundance of self-trapping electrons inside the bubble. This oval structure following the laser pulse appears to be very stable and not influenced by laser depletion due to energy transfer to the electrons. The radius, R, of the bubble can be estimated by equating the electrostatic restoring force to the pondermotive force at the surface of the bubble:

$$k_pR \cong F_p \sim k_p\nabla\frac{a_0^2}{\gamma} \cong \frac{a_0}{k_pR}. \tag{2.36}$$

Based on 3D PIC simulations of reference [73] a condition governing the laser spot size variation over the self-guided distance is found:

$$k_pR = 2\sqrt{a_0}. \tag{2.37}$$

To calculate the electric field experienced by electrons inside the bubble, the cavity can be modeled as a sphere moving along the *z*-axis. From Gauss' law the electric potential inside the cavity is:

$$\Phi = \frac{en_e}{\varepsilon_0}\left(\frac{R^2 - r^2}{6}\right), \tag{2.38}$$

where $r^2 = x^2 + y^2 + \xi^2$ and $\xi = z - v_g t$ is the co-moving coordinate along the direction of propagation of the laser pulse [74]. Thus the contribution from the bubble's electrostatic field is:

$$\vec{F}_b = -e\nabla\Phi = -\frac{e^2 n_e}{\varepsilon_0}\nabla\left(\frac{x^2 + y^2 + \xi^2}{6}\right) = -\frac{\omega_p^2}{3}m_e\vec{r}. \tag{2.39}$$

Because part of the bubble is filled by the laser pulse, the electric field of the pulse can be experienced by the accelerating electrons within the cavity.

Electron acceleration in the bubble regime

Electron acceleration lasts until electrons outrun the wave. The dephasing length, L_{deph}, can be calculated as the time required to cross the radius of the cavity, *R*. For highly relativistic electrons with velocities approaching the speed of light and for the phase velocity $v_p \cong c\left(1 - 3\omega_p^2/2\omega_0^2\right)$, the dephasing length is given by [73]:

$$L_{deph} \cong \frac{c}{c - v_\phi} \cong \frac{2}{3}\frac{\omega_0^2}{\omega_p^2}R. \tag{2.40}$$

Generally, the energy gained in acceleration length, L_{acc}, is:

$$\Delta E = eE_{WF}L_{acc}, \tag{2.41}$$

where E_{WF} is the average wakefield experienced by electrons accelerated along length L_{acc}.

Scaling laws

Theoretical studies of the bubble regime, supported by numerous 3D PIC simulations have shown the existence of scaling laws relating the laser, plasma and electron parameters. According to Lu *et al.* [73], the bubble generation is optimised when the plasma density, laser spot size and laser intensity satisfy the condition (in the limit of $a_0 \gg 2$):

$$k_p R \cong k_p w_0 \cong 2\sqrt{a_0}. \tag{2.42}$$

This condition is obtained by balancing the ponderomotive force creating the bubble and the force from the ion channel. The bubble radius, R, is approximately equal to the laser spot size, w_0. This is an indication that that the generation of the bubble strongly depends on the evolution of the laser properties (the spot size, the pulse duration and spectrum). This condition is derived under the assumption that the laser power is larger than the critical power for self-guiding and it has been shown in [75] that for short pulses, relativistic self-guiding is possible when $P > P_c$. This is mainly due to the depletion of the laser front edge before it starts to diffract, while the laser back edge is guided in the ion cavity.

As a consequence of pump depletion, the dephasing length must match the pump depletion length to obtain the maximum electron energy. Because the bubble is roughly a sphere and the electrons are either self-injected or externally injected at the rear, the electrons travel a relative distance R before they dephase. The peak useful accelerating field $eE_{z,max}/mc\omega_p = \sqrt{a_0}$ and because the wakefield is roughly linear, the average field is half of the peak: $eE_{z,max}/2mc\omega_p = \sqrt{a_0}/2$. For $2 < a_0 < 4$, the approximate equation for the energy gain is [73]:

$$\Delta E^{Lu} \cong m_e c^2 \left(\frac{P}{m^2 c^5 e^{-2}}\right)^{3/2} \left(\frac{n_c}{n_p}\right)^{3/2}. \tag{2.43}$$

Pukhov *et al.* [76] showed for ultra-relativistic laser plasmas ($a_o \gg 1$) the scaling law for energy gain using similarity theory is,

$$\Delta E^{Pukhov} \cong 0.16 m_e c^2 \frac{c\tau}{w_0} \left(\frac{P}{m^2 c^5 e^{-2}}\right)^{3/2} \left(\frac{n_c}{n_p}\right)^{3/2}. \tag{2.44}$$

Equation (2.44) strongly depends on the laser properties, while equation (2.43) emphasises the scaling with the plasma density. The difference is a consequence of the regime considered by Lu *et al.*[73], where the acceleration length is limited by pump depletion increasing the laser etching velocity. This results in a plasma wave with a phase velocity less than the laser group velocity, therefore the acceleration stops even before the electrons reach the dephasing length. Pukhov, on the other hand, considered ultrarelativistic regimes where laser etching does not occur, and the plasma wave moves at the laser group velocity.

3. The ALPHA-X laboratory

Experiments on dosimetry and the radiobiological response of LWFA VHEEs have been carried out at the ALPHA-X (Advanced Laser-Plasma High-Energy Accelerators towards X-rays) laboratory at the University of Strathclyde. The accelerator is driven by high power, ultra-short laser pulses from the Terahertz to Optical Pulsed Source (TOPS) laser system [77]. The laser system, plasma source (gas jet) and diagnostic systems are described in the following sections.

3.1. The TOPS laser system

The laser system layout in the ALPHA-X laboratory is shown in Figure 11.

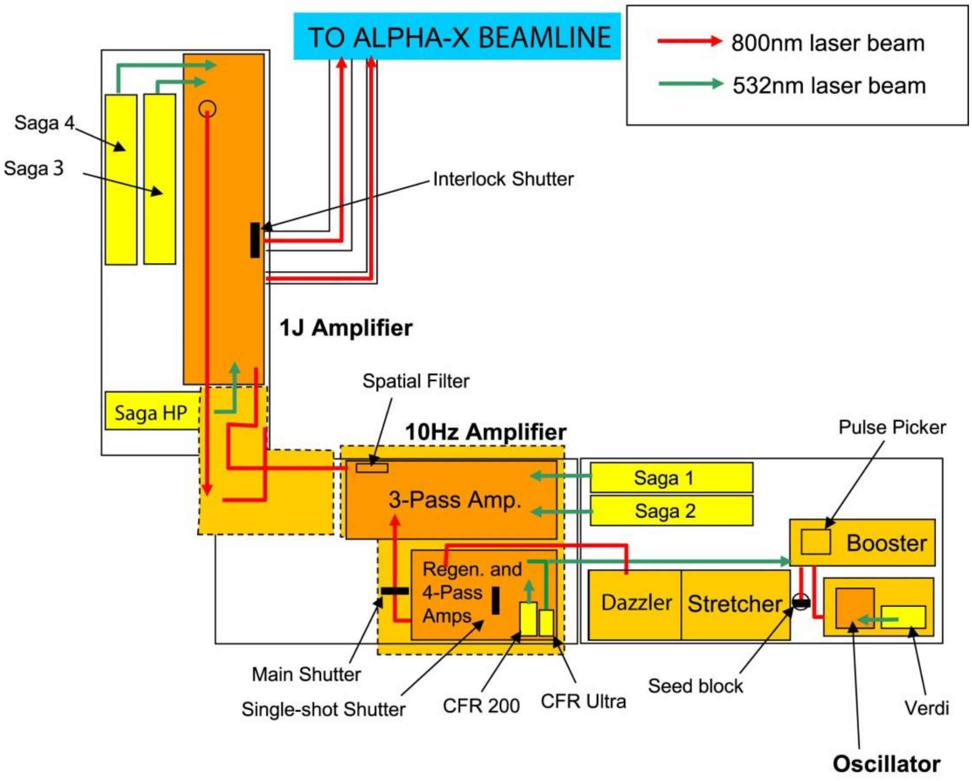

Figure 11. Schematic diagram of the TOPS laser system.

The Ti:sapphire oscillator generates ~20 fs, 9 nJ pulses at repetition rate of a 75 MHz. The crystal has a gain bandwidth from 700-1000 nm, with a 800 nm central wavelength. The TOPS system utilizes chirped pulse amplification. To amplify the laser pulse to very high intensities, the oscillator pulse is stretched to avoid optical damage after amplification. The stretcher introduces dispersion by delaying high frequency components relative to low energy components, which generate a chirp. The TOPS stretcher negatively chirps the pulse to a duration of ~250 ps using a single reflective grating in combination with concave and convex mirrors. Spherical mirrors are used instead of lenses to avoid dispersion. A Pockels cell (pulse picker) reduces the repetition rate of the laser system to 10 Hz. The stretched pulse is first amplified in a regenerative amplifer resonator cavity by a Ti:sapphire crystal, used as a gain medium. The regenerative amplifier uses a fast acting Pockels cell to allow transmission of the laser at a 10 Hz repetition rate. The Pockels cell, acting as a wave plate, rotates the polarisation of the laser allowing the beam to pass through a thin film polarizer and then enter the cavity. After the laser pulse has made a number of passes through the amplifier the Pockels cell again rotates the polarisation allowing the laser beam to be ejected from the cavity. The TOPS regenerative amplifier has an output energy of about 1 mJ. A Pockels cell (the pulse cleaner) is placed immediately after the regenerative amplifier to remove nanosecond pre-pulses before the second stage of amplification in a multipass amplifier. The beam passes through a Ti:sapphire crystal five times to reach an output energy of 20-25 mJ.

The two final amplification stages are based on multi-pass amplifiers. The first amplifier is pumped by two Nd:YAG lasers (Saga1 and Saga2) with a combined energy of 1 J. After three passes, the output energy is typically 250-330 mJ. A spatial filter is placed between the two amplifiers to remove low spatial frequency components that could cause damage to the crystal in the last amplifier. The second amplifier is pumped by three Nd:YAG lasers (Saga 3, Saga 4 and Saga HP). The last amplification crystal (Ti:sapphire) is cryogenically cooled to prevent thermal lensing. The laser final energy can reach up to 1.6 J. On the exit of the last amplifier, the laser beam is expanded to ~4 cm diameter prior to pulse compression. The TOPS compressor (with transmission efficiency of ~70 %) uses parallel gratings that reduce the pulse duration to about 35 fs. Neglecting dispersion from the amplifiers, the pulse should be completely recompressed by a compressor with an identical grating to that of the stretcher so that complete compensation of path lengths occurs. However, additional dispersion is added by the amplifier and it is essential to compensate for this. Therefore, an acousto-optic dispersive filter (Dazzler in Figure 11) is installed after the stretcher to fine tune the group delay dispersion for the non-ideal conjugation between the stretcher and compressor.

The 800 nm laser passes from the compressor to the accelerator chamber through a vacuum beam line. The accelerator chamber is located inside a one meter thick concrete walled bunker designed to contain any radiation produced in the acceleration process.

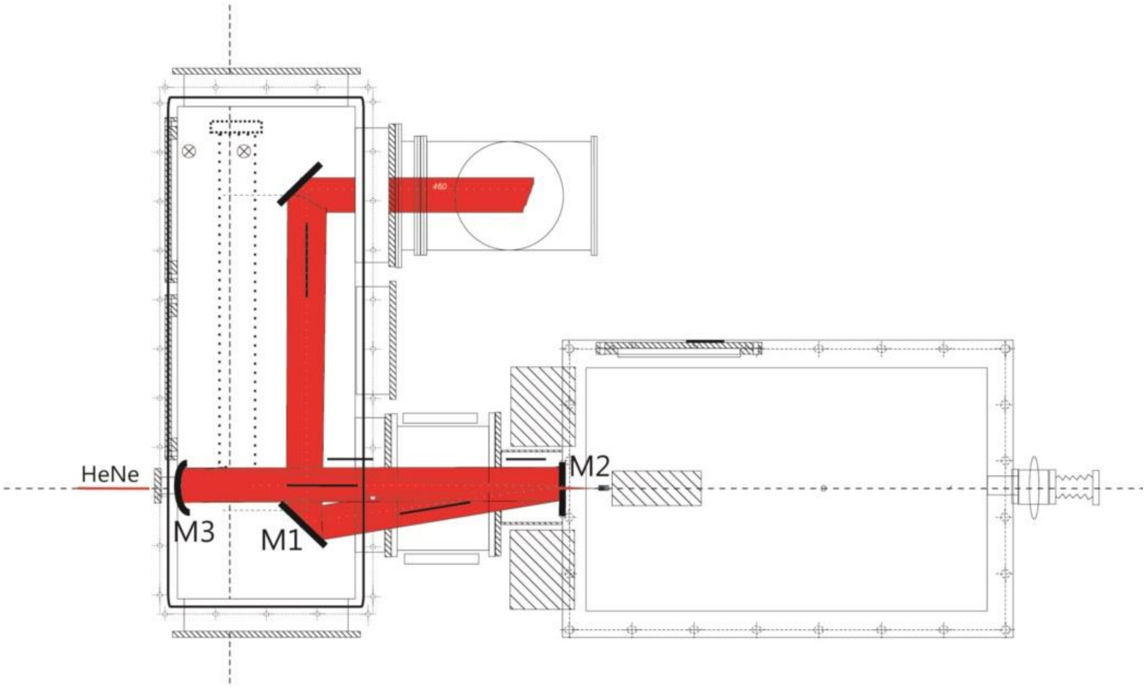

Figure 12. The ALPHA-X focusing chamber.

The laser enters the accelerator chamber from the compressor and is directed to the focussing optics by mirror M1. The focusing optics consists of an on axis spherical (M3) mirror (with focal length, f = 75 cm) focused through the mirror with a hole, M2. The laser is reflected onto the spherical mirror by M2, which then focuses the laser back through M2 to the gas jet position. The electron beam axis is defined by an alignment helium neon laser beam, which travels along electron beam axis and enters through the rear of the spherical mirror, shown by the dotted line in Figure 12. The 800 nm laser beam is centred on all mirrors and aligned with the HeNe laser beam on the spherical mirror and screen positioned on a beam axis. This ensures that the laser is co-aligned with the beam line axis. Fine alignment of the spherical mirror is very important in producing an aberration-free laser spot, because the nonlinear processes necessary to reach the bubble regime require extremely high intensity gradients, therefore the alignment of laser transport system before each experiment is crucial. For laser wakefield acceleration experiments, it is important that the laser meets essential requirements, such as high peak power, good contrast ratio (preferably > 10^6), aberration-free focal spot and symmetric broad spectrum; i.e. a smooth laser pulse.

By the time the laser pulse arrives at the interaction area, it undergoes some losses. 10 % of the laser beam intensity is lost between the last amplifier and the compressor. A further 30 % of the beam is lost in the compressor and another 10 % is lost as it progresses to the spherical mirror. Therefore, typically, the laser energy on target is around 0.9 J.

3.2. Experimental setup in ALPHA-X laboratory

The ALPHA-X laser-wakefield accelerator beam line has been used to conduct experiments studying the dosimetric and radiobiological properties of VHE electron beams. A high power Ti:sapphire laser pulse (described in section 3.1) is focused with an F/18 spherical mirror to a spot size of 40 μm ($1/e^2$ diameter) just inside the leading edge of the gas jet, giving a maximum peak intensity $I = 2\times10^{18}$ Wcm^{-2}, corresponding to a normalised vector potential $a_0 \approx 1$. The plasma source and the diagnostic systems used for characterisation of the emitted relativistic electron beams are described in the next sections.

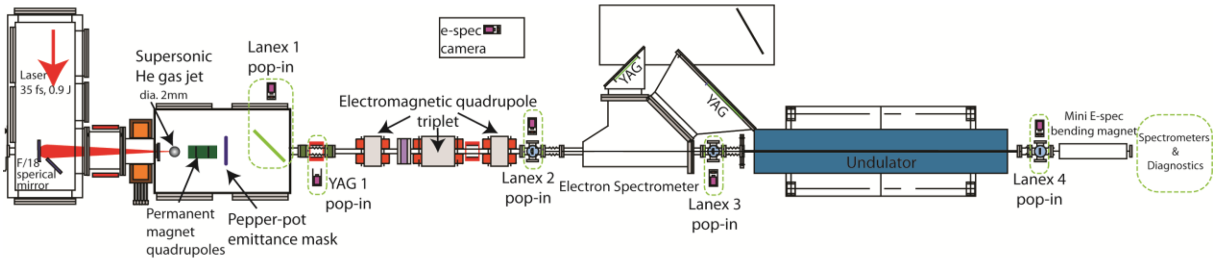

Figure 13. A detailed schematic of the ALPHA-X laser wakefield accelerator, showing the positioning of the gas jet relative to the key detection systems.

3.2.1. *Gas jet*

The laser-wakefield acceleration experiments use a gas target as a plasma source. All of the experiments with LWFA presented in this thesis use supersonic gas jet targets produced by gas nozzles with different geometrical designs. The target of the experiment is an underdense plasma created from helium. The gas is injected by a supersonic gas jet pulsed in synchronism with the laser. The nozzle is connected to a pulsed gas valve and is open for 2 to 3 ms.

The threshold intensity for ionisation is of the order of 10^{15} W/cm^2, therefore the front of the laser completely ionises the gas target, creating plasma, which is exposed to the full laser irradiance. The plasma density is dictated by the profile of the gas generated by the particular nozzle.

Nozzle used in the experiments, designed by C. Aniculaesei [78] and manufactured in the Departmental Mechanical Workshop, is an axisymmetric conical de Laval design, shown in Figure 14. The throat of this nozzle and the exit has a diameter of 0.50 mm and 2.8 mm, respectively.

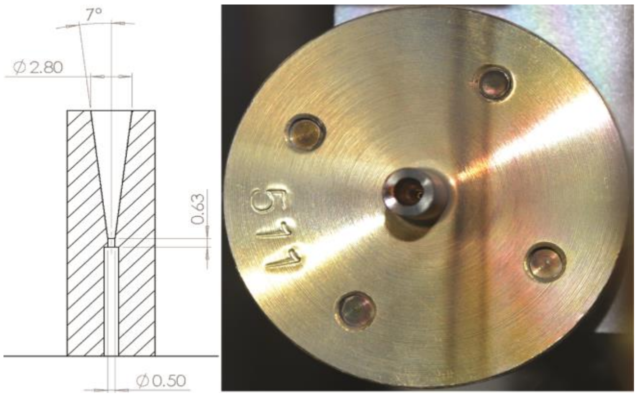

Figure 14. De Laval design nozzle used in the experiments.

These types of nozzles produce density profiles with an approximately constant central region between the rising and falling density ramps. The length of the central region can vary between ~ 0.5 and 5 mm, depending on the exit diameter of the nozzle. Further information can be found in [78]. Plasma densities from the He gas jets for 20-40 bar give a density of the order of 10^{19} cm^{-3}.

3.2.1.1. Interferometry

Measuring the structure of supersonic gas jets is not a trivial task. The density of the gas in the supersonic jets is relatively low, even at the centre it can be as low as 10^{18} cm^{-3}, and due to the small dimensions of the jets only a short interaction length is available for any characterization method. Furthermore, commonly used neutral gases, especially noble gases, are transparent up to very short optical wavelengths and have an index of refraction very close to 1. For the laser plasma experiments the nozzles are operated with helium, with an index of refraction the closest to unity of all gases. It is evident that measuring the structure of these supersonic gas jets is challenging. However, with a sufficiently sensitive imaging technique, such as one based on interferometry, where even slightest differences in optical path lengths can be detected, quantitative optical imaging of helium gas jets is possible. Interferometric characterizations of gas jets using helium have been reported for densities of 10^{19} to 10^{20} cm^{-3} for 1 to 2 mm diameter gas jets[79].

The index of refraction η of a gas is proportional to the particle density n and depends on the probe wavelength. This dependence is described by the Lorentz-Lorenz equation (3.1) [80, 81], with α the polarizability of the gas atoms and ε_0 the permittivity of free space.

$$\frac{\eta(\lambda)^2 - 1}{\eta(\lambda)^2 + 2} = \frac{\alpha(\lambda)}{3\varepsilon_0} n. \tag{3.1}$$

When $\eta \approx 1$ (as in a case for He) this can be approximated by:

$$n \approx \frac{2\varepsilon_0}{\alpha(\lambda)} [\eta(\lambda) - 1]. \tag{3.2}$$

Using reference values of the refractive index [82] the atomic polarizability of a gas can be calculated. By applying the Lorentz-Lorenz equation an interferometric measurement of the refractive index distribution of the supersonic gas jet allows determination of the density structure of the gas jet.

3.2.1.2. Gas jet interferometry

The interferometer set-up in ALPHA-X laboratory used for characterizing the supersonic gas jet is shown in Figure 15. The probe beam for the interferometer is picked off by a 90:10 beam splitter before the last amplifier of the TOPS laser. The 25 mJ 800 nm beam is transmitted to the ALPHA-X interaction area chamber, where the gas nozzle is located. The diameter of the beam is reduced to 6 mm using a telescope and split into the two arms of a Mach-Zehnder interferometer. One arm of the interferometer remains in the ambient with a precise adjustable delay line to much the propagation distance to the gas jet with the pump beam, while the other arm entered a vacuum chamber and traversed the gas jet. Both arms are recombined at a small angle to create an interference pattern which is imaged onto a CCD camera. The nozzle is mounted inside the vacuum chamber to obtain a supersonic outflow. To reduce the gas load on the vacuum pumps and maintain an average pressure below 10^{-4} mbar inside the vacuum chamber the nozzle is maintained by a pulsed valve with a 0.33 Hz repetition rate. The interferograms of the generated plasma are recorded by the CCD camera.

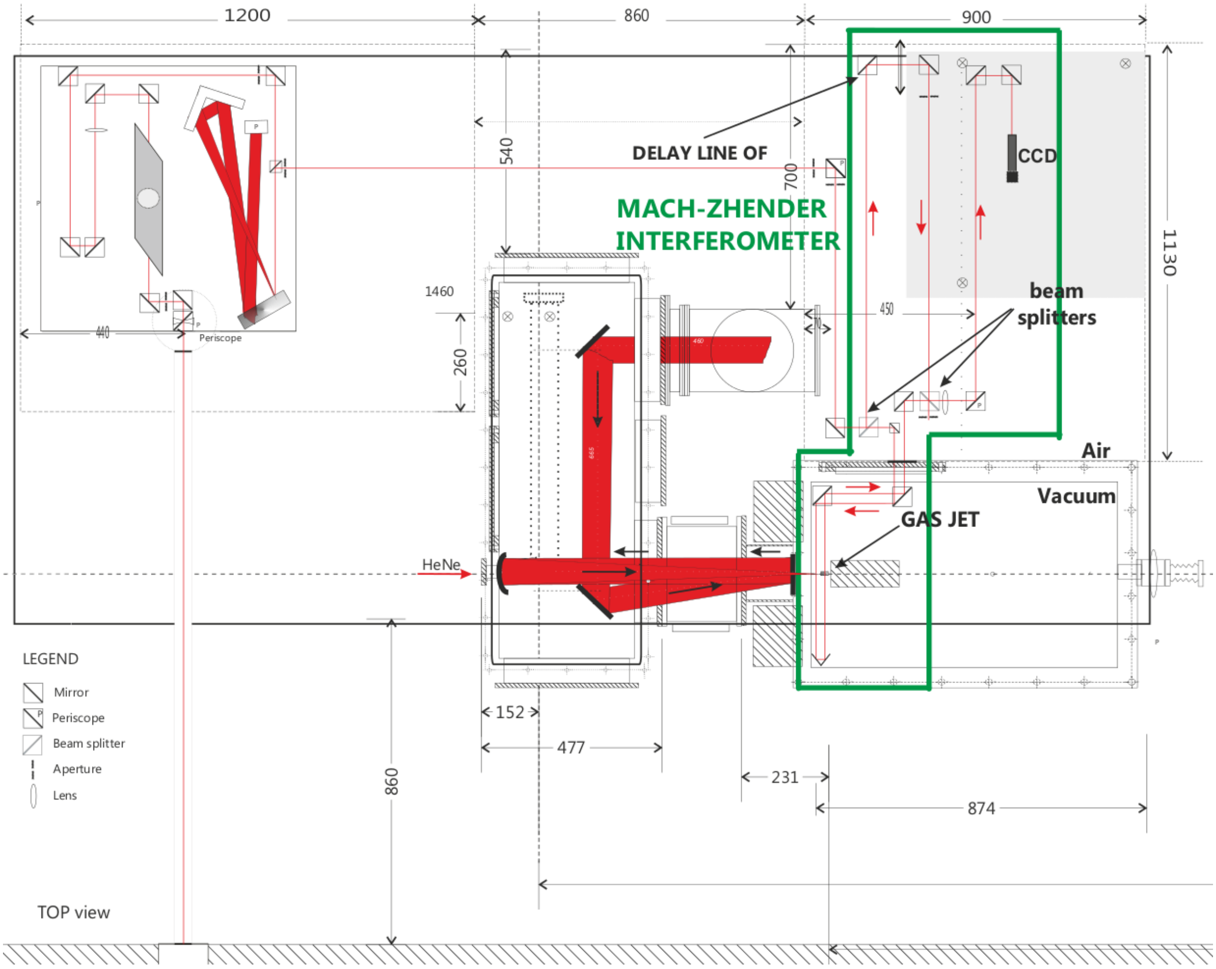

Figure 15. Detailed set-up of the Mach-Zehnder interferometer in the ALPHA-X lab. One arm of the interferometer enters the vacuum chamber and passes through the gas jet, the other arm transverses through the ambient.

From the captured interferograms, the phase information is obtained by making a use of Fourier transformations. The intensity $I(y, z)$ of a fringe pattern in the z-direction (laser propagation direction) can be described using equation (3.3). $I_{BG}(y, z)$ represents the background intensity and $I_0(y, z)$ the variations in the visibility of the fringes. These intensity fluctuations are assumed to vary slowly compared with the modulation introduced by the carrier frequency ν_0, which is well satisfied in the experiments due to the low gas index and thickness of the jet. $\Phi(y,z)$ is the local fringe phase, which is retrieved from the fringe pattern because it is related to the particle density of the gas.

$$I(y,z) = I_{BG}(y,z) + I_0(y,z)\cos\big(2\pi\upsilon_0 z + \Phi(y,z)\big). \tag{3.3}$$

It is convenient to rewrite the expression for the intensity of the fringe pattern using Euler's formula [83], introducing $I'_0(y,z)$ defined according to equation (3.5) [84]

$$I(y,z) = I_{BG}(y,z) + I'_0(y,z)e^{i2\pi\upsilon_0 z} + \overline{I'_0}(y,z)e^{-i2\pi\upsilon_0 z}, \tag{3.4}$$

$$I'_0(y,z) = \frac{1}{2}I_0(y,z)e^{i\phi(y,z)}. \tag{3.5}$$

Fourier transforming (3.4) with respect to z results in the spectrum of the fringe pattern intensity (3.6).

$$\hat{I}(y,\upsilon) = \hat{I}_{BG}(y,\upsilon) + \widehat{I'}_0(y,\upsilon-\upsilon_0) + \widehat{I'}_0(y,\upsilon+\upsilon_0). \tag{3.6}$$

Next to the slowly-varying background $\hat{I}_{BG}(y,\upsilon)$ it consists of two spectra separated from the zero frequency spectrum by the carrier frequency ν_0. After selecting one of these spectra $I'_0(y,\upsilon-\upsilon_0)$ and translating it by $+\nu_0$ one can apply the inverse Fourier transform to obtain $I'_0(y,z)$(3.5). In this process the slowly-varying background $I_{BG}(y,z)$ is essentially filtered out. Finally the phase information modulo 2π can be extracted using equation (3.7) and (3.8) and subsequently can be unwrapped. Intensity fluctuations of the fringes $I_0(y,z)$ are cancelled out in this stage.

$$\phi(y,z) = arctan\left(\frac{\overline{I'_0(y,z)}}{I'_0(y,z)}\right). \tag{3.7}$$

The step of selecting the $\widehat{I'}_0(y,\upsilon-\upsilon_0)$ spectrum means essentially filtering out of all spatial frequency components of the interferogram that are not related to the phase shift resulting from the gas jet. In this filtering process one has to take care that all information of the gas jet is preserved.

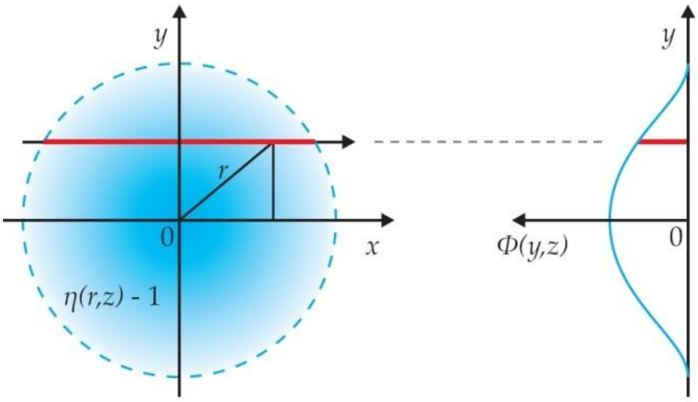

Figure 16. Schematic representation of the measurement of an axisymmetric distribution (blue) of relative refractive index $\eta(r, z) - 1$. At large distances the distribution converges to zero. The accumulated phase shift of a light ray traversing the distribution will be the integral of the relative refractive index along the path travelled through the distribution (red) [85].

To obtain the refractive index distribution and thus the density distribution inside gas jet from the phase images, additional calculations are needed. To deduce the relation between the measured phase-shift and the density of the gas jet one can consider the geometry shown in Figure 16, where a ray of light propagates in the positive x-direction through an axisymmetric gas jet, positioned at the origin in the x, y-plane. The axis of symmetry of the jet is along the z-axis, perpendicular to the x, y-plane. The relative refractive index of the gas is assumed to drop to zero at large distances from the origin. The amount of gas encounter results in a projection of the refractive index $\eta(r, z)$ -1 of the gas jet onto the y, z-plane. Calculating the accumulated phase-shift Φ of the light results in equation (3.8), which is known as the Abel transform [86]

$$\Phi(y,z) = \frac{2\pi}{\lambda} 2 \int_y^\infty \frac{(\eta(\lambda,r,z)-1)r}{\sqrt{r^2-y^2}} dr. \tag{3.8}$$

Inverting the Abel transform allows one to retrieve the index of refraction of the gas jet from a measured phase-shift

$$\eta(\lambda,r,z) - 1 = \frac{\lambda}{2\pi}\frac{-1}{\pi}\int_r^\infty \frac{d\phi(y,z)}{dy}\frac{1}{\sqrt{y^2-r^2}} dy. \tag{3.9}$$

The particle density profile of the gas jet is then obtained by making use of the Lorentz-Lorenz equation (3.2)

$$n(r,z) = \frac{-\epsilon_0 \lambda}{\pi^2 \alpha(\lambda)} \int_r^\infty \frac{d\phi(y,z)}{dy} \frac{1}{\sqrt{y^2 - r^2}} dy. \qquad (3.10)$$

The plasma density can be varied by changing the backing gas pressure or the distance between the nozzle exit and the laser beam. Captured interferograms of plasma channel are analysed with a MATLAB program, written by Paolo Tomassini [87], utilizing the phase map extraction with Fourier analysis, which after few more steps (described above) retrieve density of the plasma with the inverse Abel transform. Figure 17 shows the variation in plasma density profiles for different heights from the nozzle exit, at a constant backing pressure of 20 bar at various distance of the pump laser with respect to exit of the gas jet. Typically, experiments are performed with a backing gas pressure of between 20 and 35 bar, and the laser focus is positioned between 1.5 and 3 mm above the nozzle exit. For these parameters, the laser beam creates a relativistic plasma channel with a density of ~1-1.5×10^{19} cm^{-3}.

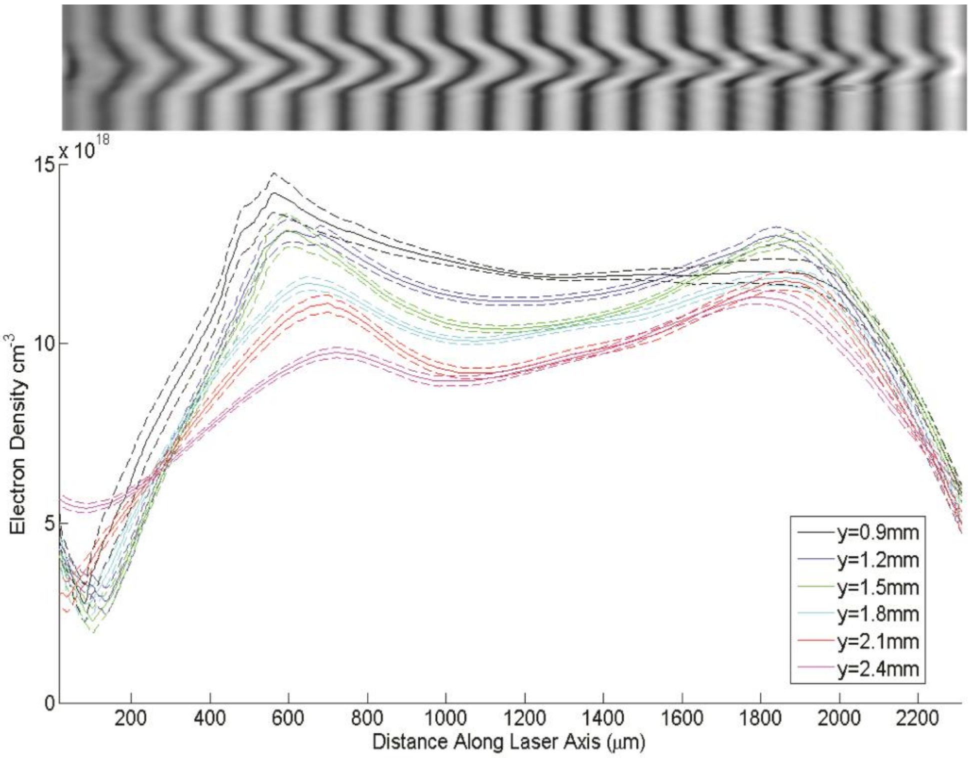

Figure 17. Electron density profiles for increasing distance between gas jet exit and pump laser axis for the nozzle used in the experiments, averaged over ±1 SD (standard deviation) along the vertical axis. All profiles have been obtained for 20 bar backing pressure and 3 ms of valve opening time. The inset is a sample interferogram of the imaged plasma channel for the studied gas nozzle. The laser propagates from left to right (courtesy of David Grant).

3.2.2. Beam profile monitors

Lanex screen

Scintillation screens are used to monitor the transverse properties of the electron beam downstream along the beam line as shown in Figure 13.

The Lanex (KODAK) screen is a thallium doped caesium iodide (CsI:Tl) grown in a columnar "needle-like" structure. The structure of Lanex screen reduces scattering and can provide good resolution as each column of CsI acts as a light pipe channelling the visible light to the CCD sensor. During experiments the quality of the electron beam has been optimised by inspecting the quality of the electron beams detected downstream on Lanex1 (Figure 13), located 64 cm from the gas jet and tilted 45° horizontally with respect to the beamline cetral axis. Images are recorded with a CCD camera. 1 pixel corresponds to 38 and 30 μm along the x and y axes, respectively. Measurements of the electron beam lateral profile do not provide any information on beam energy. It is possible for the high energy components to be concentrated at the core of the beam on top of a large halo made of low energy electrons. This high divergence, low energy component would be quickly lost while propagating through the beamline, especially if transport (PMQ quadrupoles) is used (Figure 18). The shot to shot pointing stability for ALPHA-X beam during experiments presented in this work is less than 10 mrad and the rms divergence typically is between 3 and 8 mrad, for hundreds of consecutive laser shots.

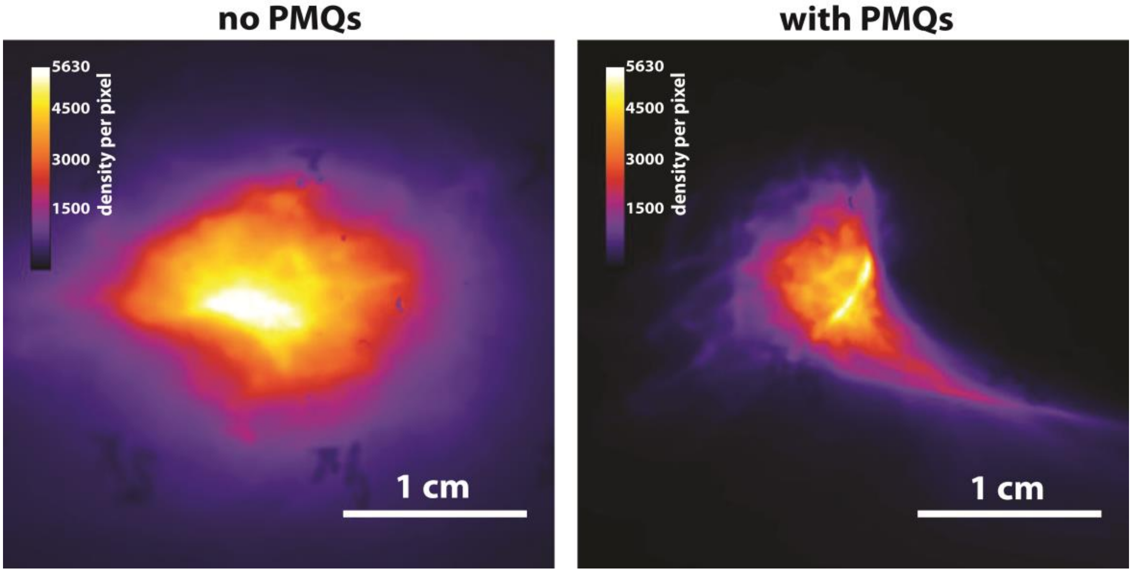

Figure 18. Images of 100 accumulated consecutive electron beam shots captured on Lanex 1 located 64 cm after the gas nozzle. The images compare electron beam without (left) and with (right) transport using quadrupole magnets (i.e. permanent quadrupoles –PMQs).

DynAMITe

Detectors for biomedical imaging applications require good spatial resolution, low noise and high dynamic range.

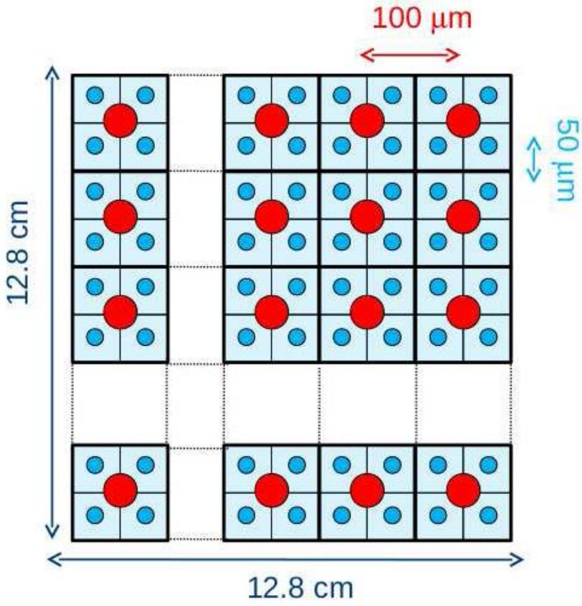

Figure 19. A schematic of the pixel array arrangement. Red circles represent the large size diodes placed at 100 µm pitch, referred as pixels. Cyan circles represent the small size diodes placed at 50 µm pitch - sub-pixels [88].

Dynamic range Adjustable for Medical Imaging Technology or DynAMITe sensor (Figure 19) is an Active Pixel Sensor (APS) that has been constructed using a 0.18 µm CMOS process by employing a reticule stitching technique [89] with a total active area of 12.8 × 12.8 cm^2. The pixel array is designed to produce two imagers in one by using different size light-converting elements meshed into the same pixel matrix. The detector consists of a fine-pitch grid of diodes superimposed on a set of a large-pitch grid diodes. Thus each cell of the DynAMITe matrix is fitted with multiple diodes: four diodes of small 50 µm (side) size, referred to as a sub-pixel, and one diode of 100 µm size (side), referred to as a pixel. The whole matrix comprises 1260 × 1280 pixels and 2520 × 2560 sub-pixels (Figure 19). Only after the sub-pixels reach near saturation, do the pixel diodes start collecting significant amount of charge, so offering a higher dynamic range due to their larger collecting area compared with the sub-pixels [88]. An example lateral profiles of electron and X-rays, generated in ALPHA-X laboratory, captured on various detectors are shown in Figure 20.

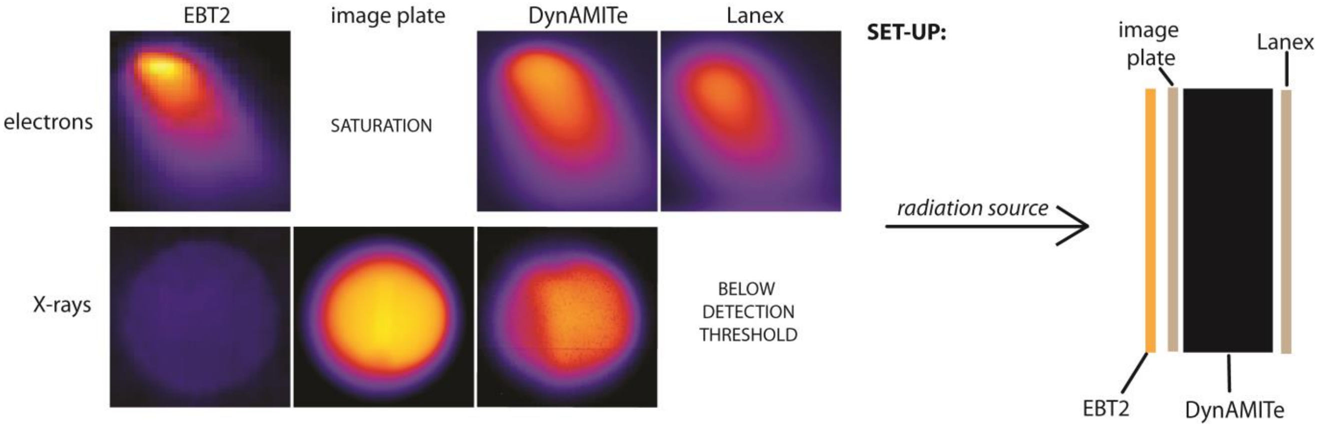

Figure 20. False-colour images of electron and X-ray beams generated in ALPHA-X captured on Gafchromic EBT2 film, image plate, DynAMITe sensor and Lanex screen.

All of the profiles in Figure 20 have been recorded simultaneously on 4 specified detectors, therefore the beam captured on the last monitor in the set-up (i.e. Lanex screen) sufferes the largest scattering due to prior propagation through detectors positioned in front. Both, EBT2 film and image plate, require post-exposure digitalization and are included here just for comparison. The resolution and detection efficiency of electrons for DynAMITe and Lanex screen are comparable. Nevertheless, DynAMITe exhibits superior sensitivity to X-rays and therefore would be better choice for monitoring the profile of photon beams. Image plate detector and Gafchromic EBT2 film are characterized in chapter 5.2.1.

3.2.3. Charge measurements

The image plate is a two dimensional detector of ionizing radiation. A Fuji Biological Analysis System (BAS) IPs have been used, which consist of a photostimulable phosphor layer (barium fluoro-halogenite doped with europium 2+ ions, BaFX:Eu2+) coated on a polyester support layer [90]. The image plate is coated with a Mylar protective layer on the top surface and a magnetic base layer that is used to mount the sample into the reader. When the active phosphor absorbs an X-ray photon, it promotes electrons from Eu2+ ions into a metastable state where they remain trapped in lattice defects. These defects are intentionally introduced during the manufacturing process. The trapped states decay in time depending on temperature and the exact chemical composition of the IP. They can also decay if illuminated by light at 632.8 nm, which is how they are read out in a scanning system to extract their stored data. As the metastable state decays, blue light at 400 nm is emitted and then detected using a photomultiplier tube, in a process known as photo-stimulated luminescence (PSL) or optically stimulated luminescence (OSL). The information stored on the IP can then be completely erased (i.e., all the Eu2+ ions return to the ground state) through further optical illumination to white light, and thus allowing the IP to be reused to take further data [91].

Because the IP scanner digitizes the plate readout using a logarithmic amplifier [92], the measured pixel data are first converted between this logarithmic value, also known as the quantum level (QL), to a linear PSL scale with the following equation

$$PSL = \left(\frac{R}{100}\right)^2 \times \frac{400}{S} \times 10^{L\left(\frac{QL}{G}-\frac{1}{2}\right)}, \tag{3.11}$$

where R = 50 is the scanning resolution (in μm) , S = 1000 is the sensitivity, L = 5 is the latitude and G = 65 535 is the gradation of the 16 bit image. These parameters may not be the same for different scanning systems and these values have been established for the FUJI FLA7000 scanner used in these studies. It is important to establish the appropriate correction factor due to fading time. The fade rates of the Fuji BAS IPs are measured as a function of time from 5 minutes to 5 hours, at 20°C by Meadowcroft *et al.* [90] and these coefficient are used for the analysis.

The absolute calibration of the image plate has been carried out by Tanaka et al. [93] and extended to higher energies by Nakanii et al. [94]. In these studies a LINAC accelerator of various energies with known charge has been used to calibrate the image plate. Fading of the image plate signal has been found to stabilise after 45 minutes, which is when the calibration is performed. The sensitivity of the image plate is found to be stable across small electron beam energies at high energies (> 10 MeV) and a calibration value of 0.0064 PSL/electron for 100 MeV electrons.

Image plate charge measurement in the ALPHA-X beamline is routinely performed during all experiments. It is found that measurements with image plates after propagation several centimeters in air are difficult to analyse due to capture on an image plate of low energy bremsstrahlung photons, generated by VHEEs in air, which form a background in the scanned image. Image plates suffer from different response for varying photon spectra [95], therefore the evaluation of the true background correction in such experimental setup is impossible. One would need to have a precise measurement of the photon flux and its spectra. This problem vanishes when the measurement is performed in vacuum or just after a vacuum window. Therefore, charge measurements with IPs have been performed just after the Mylar window, located after electron spectrometer shown in Figure 13.

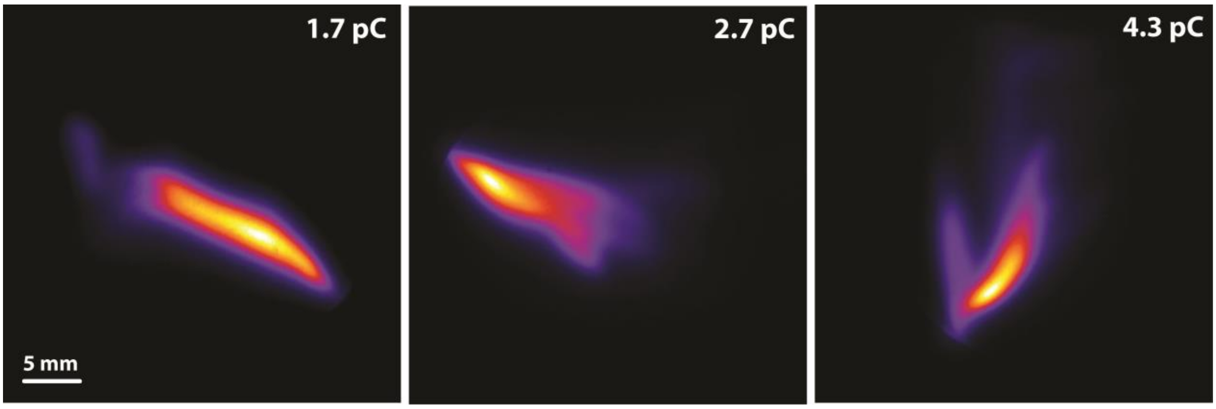

Figure 21. Three samples of 10 consecutive electron shots recorded on image plate. The measured charge per shot (in pC) is given in an upper right corner.

Figure 21 shows three samples of 10 consecutive electron shots captured on an image plate. During experiments presented in this work the electron beam charge varies between 1 and 10 pC per shot depending on the accelerator operation.

3.2.4. Transport system – electromagnetic quadrupoles

To maintain the high quality electron beams produced in laser wakefield accelerators it is necessary to utilise a transport system to deliver the electrons to the interaction area where measurement or detection takes place. The beam transport system on the ALPHA-X beam line consists of magnetic quadrupoles and beam steering coils. The electron beam is manipulated through its interaction with an electromagnetic field and experience the Lorentz force:

$$\vec{F}_l = m\frac{d\vec{v}}{dt} = -e\left[\vec{E}(d\vec{r}) + \vec{v} \times \vec{B}(\vec{r})\right]. \tag{3.12}$$

As magnetic fields are utilised in the transport system only the $\vec{v} \times \vec{B}$ force interacts with the electron beam. The direction of this force is at the right angle to vector of velocity and the magnetic fields. This is most simply demonstrated by the steering (or dipole) magnets, which apply a magnetic field across the beam line. Figure 22 (a) shows the principle of operation of a steering magnet. With fields lines from bottom to top and the electron beam moves towards the page and the particles are deflected to the left hand side. One steering coil is mounted in each of the three electromagnetic quadrupoles in alternating directions. The current can be reversed in each of the coils to allow steering in both the positive and negative directions.

The quadrupoles work in a similar manner as the dipole steering magnet, they are constructed of four rather than the two dipole steering magnets, producing a quadrupole field, where the two north poles are facing south poles (Figure 22 (b)). Such a configuration bends from the north to the south poles creating a sweeping force influencing electrons transport. This force compresses the beam on one axis and elongates it on the other. The following second and third quadrupoles located afterwards alter the field direction resulting in an overall focusing effect along both axes.

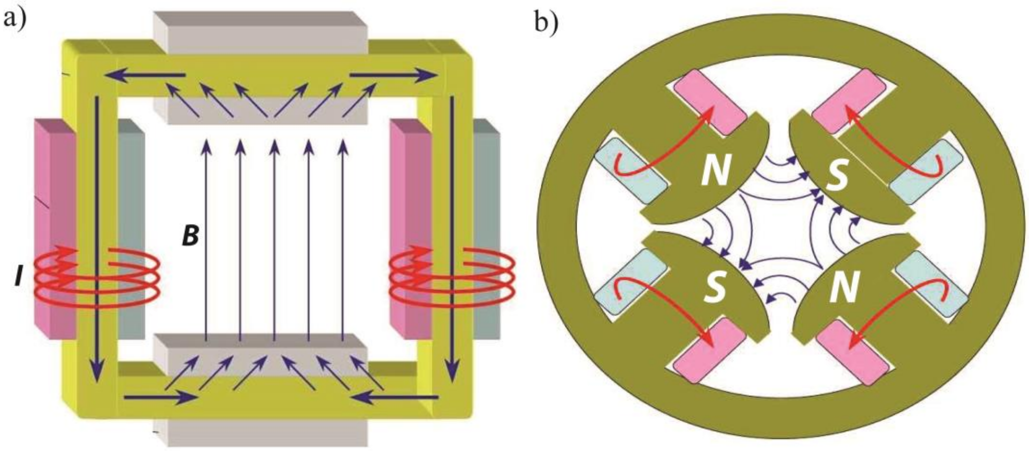

Figure 22. Schematic diagrams of operation principles for (a) steering dipole magnets and (b) electromagnetic quadrupoles [96].

Two sets of magnetic quadrupole triplets are installed in the ALPHA-X beam line (see Figure 13). The first, permanent magnetic field quadrupoles (PMQs), are mounted just few centimeters from the accelerator (gas nozzle), which can be utilised due to their compactness. This allows the electron beam to be collimated immediately after the accelerator to reduce its divergence. The aperture of permanent quadrupoles is 6 mm. The drift distances between the PMQs can be adjusted between 1.5 and 5 cm to optimise transport at different energies. As shown in Figure 23, the triplet of quadrupoles also reduce the background halo, effectively removing the low energy components of the electron beam and improves the pointing stability (in comparison with configuration without collimation). However, the spatial profiles may be slightly distorted owing to the large energy spreads and the energy dependence of the PMQs focusing strength.

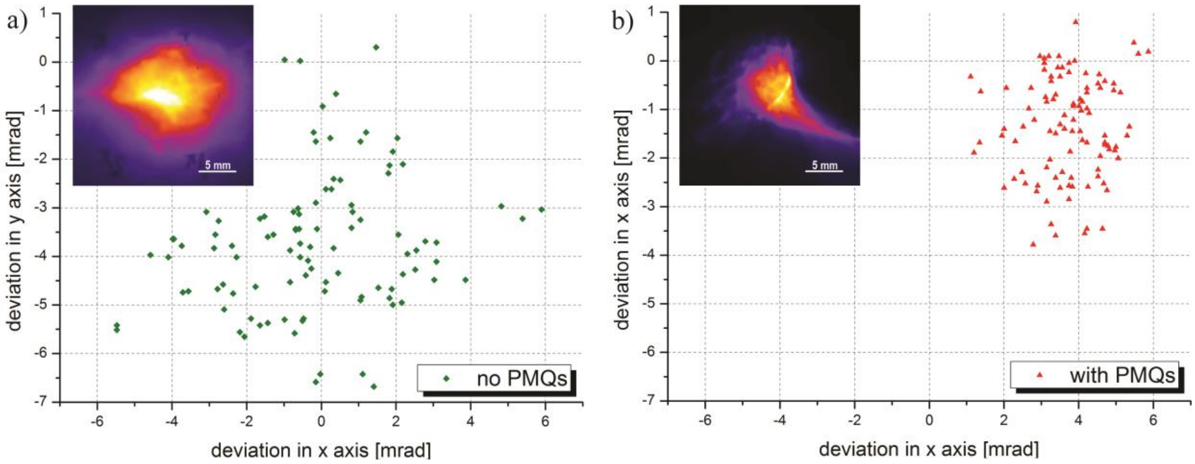

Figure 23. Shot to shot electron beam pointing fuctuations of the ALPHA-X electron beam obtained for 100 consecutive laser shots on the Lanex1 without (a) and with (b) electromagnetic guiding. Inset shows the false-colour image of the accumulated electron beam over all shots.

The second triplet set of quadrupoles – dynamic electromagnetic quadrupoles - are mounted after the accelerator chamber and in front of the electron spectrometer, as shown in Figure 13. The magnetic fields in these quads are controlled by the current passing through their coils and can be fully adjusted to suit the requirements of the electron beam. The dynamic electromagnetic quadrupoles are used to optimise electron beam transport for electron spectrometer measurements.

3.2.5. Energy measurements

The electron energy is measured using an electron spectrometer designed by Allan Gillespie and constructed by SigmaPhi [47], which consists of a steering electromagnet. The electromagnets can be turned on to bend the electrons out of the beam line. Electron deflection depends on its velocity, and therefore by measuring the deflection, the electron trajectory and the energy spectrum can be determined. When a collimated electron beam enters the spectrometer the different path lengths through the spectrometer cause different trajectories for each side of the beam causing the beam to focus at some distance after the spectrometer. Vertical focusing, on the other hand, arises from the electrons passing at an angle to the fringe fields at the entrance to the spectrometer causing the electrons to pass through a curved magnetic field. These curved magnetic fields result in both a horizontal and vertical force to act on the electrons to focus the beam.

For an electron of energy E_0 and relativistic mass γm_0 being deflected into a circular orbit by a magnetic field of strength $B(I)$, the orbit radius r is given by:

$$r = \frac{\gamma m_0 c}{eB} \cong \frac{3.34 E_0[MeV]}{B[T]}, \tag{3.13}$$

thus

$$E_0[MeV] = \frac{r[mm]B[T]}{3.34}. \tag{3.14}$$

The maximum magnetic field of the spectrometer of 1.7 T allows the measurement of electron energy up to 600 MeV with a resolution of 1 - 10%. The low energy, high resolution, part of the spectrometer bends the electron through a larger angle and thus has a larger dispersion and a higher resolution (0.1%), but is limited to a maximum energy of 100 MeV. The spectrometer utilises the Browne-Buechner design [97] to focus the electrons in both the horizontal and vertical planes over a wide energy range. Electrons are detected on Ce:YAG crystals and imaged by a 14 bit Grasshoper CCD camera. The Ce:YAG crystal is a cerium doped yttrium-aluminium-garnet crystal, which emits in the green under scintillation [98]. This high resolution crystal used in the electron spectra measurements was a 100 μm thick and had a 10 μm resolution.

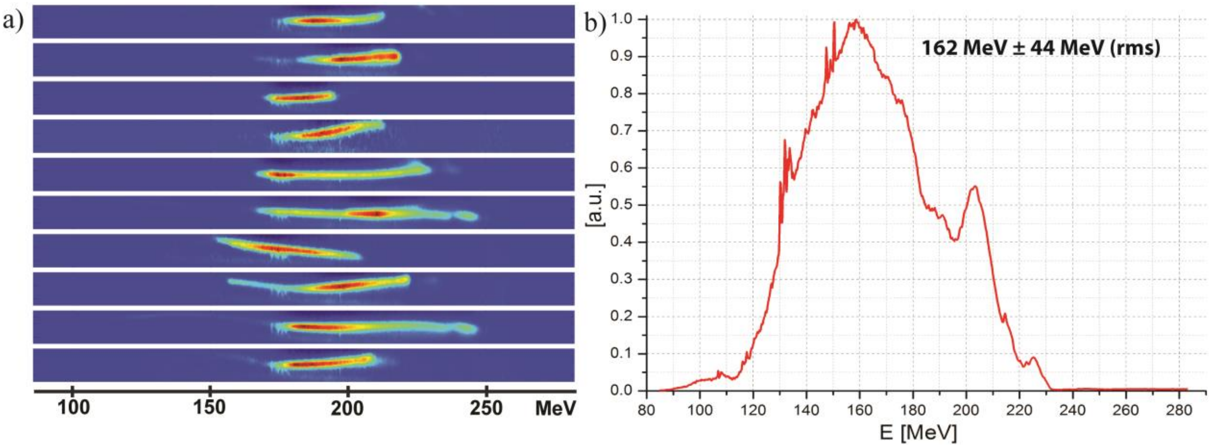

Figure 24. Sample of consecutive electron beam shots captured on YAG screen (a) and accumulated energy spectra over 200 shots (b) for a typical electron beam used in the experiments.

Figure 24 shows 10 consecutive electron shots captured on the YAG screen and a typical averaged energy spectrum accumulated over 200 shots during experiments of ALPHA-X beam for the experiments reported in this thesis.

4. Monte Carlo simulations

Deterministic and Monte Carlo (MC) methods [99] are two approaches of numerical modelling. Deterministic methods involve solution of differential equations of motion for the system. The equation, cast in an approximate form, permits calculation of the incremental change in the variables. The accuracy of the deterministic method is limited by how well the equation approximates physical reality and by the necessity of defining spatial or temporal grid points.

The Monte Carlo method involves calculating the average or probable behaviour of a system by observing the outcome of a large number of trials that simulate the physical events responsible for the behaviour. MC calculations make explicit use of random numbers. It is well suited to the study of stochastic processes, particularly processes of radiation transport – motion or radiation (e.g. photons, neutrons, charged particles) through matter. However, they also require a deterministic approach, e.g. for the implementation of the electric and magnetic fields.

Repetitions of a Monte Carlo calculation yield only approximately the same answer, whereas repetitions of a calculation based on a deterministic method (for the fixed initial conditions) yield exactly the same answer. That difference is due to the random nature of Monte Carlo calculations.

All modelling presented in that work is based on Monte Carlo methods.

4.1. Introduction to Monte Carlo simulation tools

4.1.1. A Brief History of the Monte Carlo Method

Before the Monte Carlo method was developed, uncertainties in the simulations were estimated using statistical sampling or by testing a previously understood deterministic problem. Monte Carlo simulations invert this approach, solving problems using a probabilistic analog.

The early variants of MC have been established in the second half of the 18th century by Buffon [100], performing experiments dropping a needle in a haphazard manner on a board marked with parallel lines to infer probability that the needle will intersect one of those lines. The subsequent experiments allowed him to make an accurate estimation of the value of π. Following this procedure Hall used MC methods to calculate π [101].

In early 20th century, a number of simple Monte Carlo studies has been conducted. Most of these had rather didactic character and were rarely used for research or discovery. In 1908 Student (W.S. Gosset) used experimental sampling to help him towards his discovery of the distribution of the correlation coefficient [102].

The real use of MC methods goes back to early 1940s marked the beginning of the modern history of Monte Carlo when scientists at Los Alamos systematically used them as a research tool in their work on developing nuclear weapons [103]. Stanislaw Ulam was the first one to realize the potential of using computers to automate the statistical sampling process [104]. Together with John von Neuman and Nicolas Metropolis, he developed algorithms and explored the means to convert non-random problems into random forms so that statistical sampling can be used for their solution [105]. The method is called after the famous casino in Monaco, because of a roulette, a simple random number generator. One of the first published papers on this topic was by Metropolis and Ulam in 1949 [99].

The rapid development in computer technology has increased the applicability and accuracy of the Monte Carlo method and is now used routinely in diverse fields, such as economics, physics and chemistry as a powerful numerical technique. It is easy to solve equations of interaction between two atoms or molecules and get an exact solution for a specific problem while in the case of large systems, where the number of particles involved in a problem is large, solving the problem in a deterministic way becomes impossible due to the large number of equations and variables that are needed to study the problem. MC methods are stochastic (random) techniques in which random numbers and probability statistics are used to examine scientific problems in a probabilistic fashion.

4.1.2. Monte Carlo transport codes

MC particle transport codes are used to simulate interactions and transport of particles in media. From the knowledge of the physics of the elementary collision processes, analog (or “event by event”) MC simulations explicitly create, track and range out a number of primary particles, and secondary particles that are created in the interactions.

Apart from their wide application in basic research, they are also of increasing importance in applied fields such as medical physics. The main strength of MC simulations lies in their accuracy and the possibility of making calculations for arbitrary geometries where analytical calculations might be too complex or experimental measurements unfeasible. However, the accuracy of the results of any MC simulation is, in general, as good as the physical models behind them, which are, in turn, as good as the experimental data from which they are derived. For this reason, an adequate configuration of the simulation program, if possible based on experimental measurements, is always needed.

4.1.2.1. GEANT4

The software package Geant4 [106, 107] was developed by RD44, a world-wide collaboration of about 100 scientists participating in more than 10 experiments in Europe, Russia, Japan, Canada and the United States. Since 1999 the production service, user support and development of Geant4 have been managed by the international Geant4 Collaboration [108].

Geant4 is a MC-based, C++ toolkit for simulating the passage of particles through matter. Geant4 provides a complete set of tools for all areas of detector simulation: geometry, tracking, detector response, run, event and track management, visualization and user interface. The multi-disciplinary nature of the toolkit requires that it supply an abundant set of physics processes to handle diverse interactions of particles with matter over a wide energy range. For many physical processes a choice of different models is available.

A large set of utilities is provided, including a powerful set of random number generators. Other features, including a set of physics units and constants, interfaces to event generators, and object persistency solutions, complete the toolkit. Geant4 exploits advanced software engineering techniques and object-oriented technology to achieve transparency of the physics implementation and hence provide the possibility of validating the physics results [106].

4.1.2.2. FLUKA

FLUKA [109-111] is a general purpose MC transport and interaction code originally created at CERN for high-energy physics.

The history of FLUKA spans more than 40 years. It is possible to distinguish three different generations of "FLUKA" codes along the years, which can be roughly identified as the FLUKA of the '70s the FLUKA of the '80s , and the FLUKA of today.

These codes stem from the same root and every new "generation" originates from the previous one. However, each new "generation" represents not only an improvement of the existing program, but a quantum jump in the code physics, design and goals. The same name "FLUKA" has been preserved as a reminder of this historical development - mainly in homage to J. Ranft who was involved in it as an author and mentor from the beginning until the present days - but the present code is completely different from the versions that were released before 1990, and in particular from the second generation, FLUKA87 [112].

Major changes and additions have improved the physical models used, the code structure, the tracking strategy and scoring[1]. Important additions, such as a wider range of biasing possibilities and specialised tools for calorimeter simulation, have extended the field of its possible applications.

FLUKA code is written in Fortran, and can simulate the interaction and propagation in matter of about 60 different particles, including photons, electrons, neutrinos, muons, hadrons and all of the corresponding antiparticles. The set of particle types in FLUKA with the transport limits is presented in Table 1.

Table 1. Transport of particles in magnetic and electric fields in FLUKA [109].

Particle type	**Transport limits (primary particles)**	**Transport limits (secondary particles)**
Charged hadrons	10 keV – 10 PeV	1 keV – 10 PeV
Neutrons	thermal – 10 PeV	thermal – 10 PeV
Muons	10 keV – 1 PeV	1 keV – 1 PeV
Electrons	10 keV – 1 PeV	1 keV – 1 PeV
Photons	1 keV – 1 PeV	100 eV – 1 PeV
Heavy ions	< 10 PeV/n	< 10 PeV/n

---

[1] 'Scoring' is a common term in MC simulations which means the statistical estimation of value. Each MC code has own terminology which historically was built around it. For example, MCNP/MCNPX users use the term "tally", which is a synonym of "score".

The highest priority in the design and development of FLUKA has always been the implementation and improvement of proper, modern and updated physical models. FLUKA is based, as far as possible, on original and well tested microscopic models. All the reactions and the reaction types are checked against experimental data. As a result, final predictions are obtained with a minimal set of free parameters fixed for all energy/target/projectile combinations. Therefore, results in complex cases, and properties and scaling laws, arise naturally from the underlying physical models. Extrapolations are provided where no experimental data are directly available [113]. Various visualization and debugging tools are also available. For most applications, no programming is required from the user. However, a number of user interface routines (in Fortran 77) are available for users with special requirements. To attain a reasonable flexibility while minimizing the need for user-written code, the program has been provided with a large number of options available to the user, and has been completely restructured introducing dynamic dimensioning [109].

Most of the calculations presented in this thesis have been obtained using the MC FLUKA [109-111, 114] code. However, for some studies Geant4 [106, 107] has been used. Versions: geant4 5.9.5 [107] and FLUKA 2011.2b.4 [111] have been used during the research period.

4.2. Monte Carlo characterization of VHEEs

In the past decade several studies have revived interest in radiotherapy using very high energy electron (VHEE) beams with energies exceeding 150 MeV, which allow maximum dose deposition deep in tissue. Previous theoretical studies using the PENELOPE code [35, 37] have shown the potential of 150–250 MeV VHEE beams. But before such a beam can be implemented into clinics many provisional studies need to be undertaken to study the aspects of applying VHEE radiotherapy. One of the questions is how to define properties of VHEE beams, including percentage depth dose profile, essential for treatment planning for patients or the radiobiological effectiveness of such beams. Another aspect that needs to be considered with respect to VHE electron beams is radiation safety. There have been previous studies on VHE electron beams [115] pointing out concerns regarding neutron production due to irradiation with VHEEs. To examine this a set of MC simulations on neutron production and induced activity has been carried out. Equivalent doses are scored in order to evaluate average measure of the radiation that accounts for the potential biological damage due to irradiation using electron beams. This quantity is significant from the point of view of assessing the health risk of radiation exposure. All of these quantities, including dose depositions profiles have been benchmarked with low energy electron beams, used in conventional radiotherapy.

The methods and results presented in this section do not aim to achieve clinical accuracy for the FLUKA simulation system, as this would require a larger amount of data and a much more detailed analysis. They have been conceived as a test for the chosen physics settings, and a means of gaining understanding of how FLUKA reproduces the irradiation with very high energy electron beams.

4.2.1. Geometry modelling

FLUKA can handle even very complex geometries, using an improved version of the well-known Combinatorial Geometry (CG) package from MORSE [116], with additional bodies (e.g. infinite circular and elliptical cylinder parallel to X,Y,Z axis, generic plane, planes perpendicular to the axes, generic quadrics etc.). The FLUKA CG has been designed to correctly track charged particles (even in the presence of magnetic or electric fields). CG exhibits accurate treatment of boundary crossing with multiple scattering and magnetic or electric fields.

In this section the geometry is modelled as a $30 \times 30 \times 30\ \text{cm}^3$ water phantom surrounded by 6 mm thick poly-methyl methacrylate (PMMA) walls (Figure 25). The beam source is located 100 cm in front of the entrance to the phantom. All of the calculations in this chapter have been performed with this set-up.

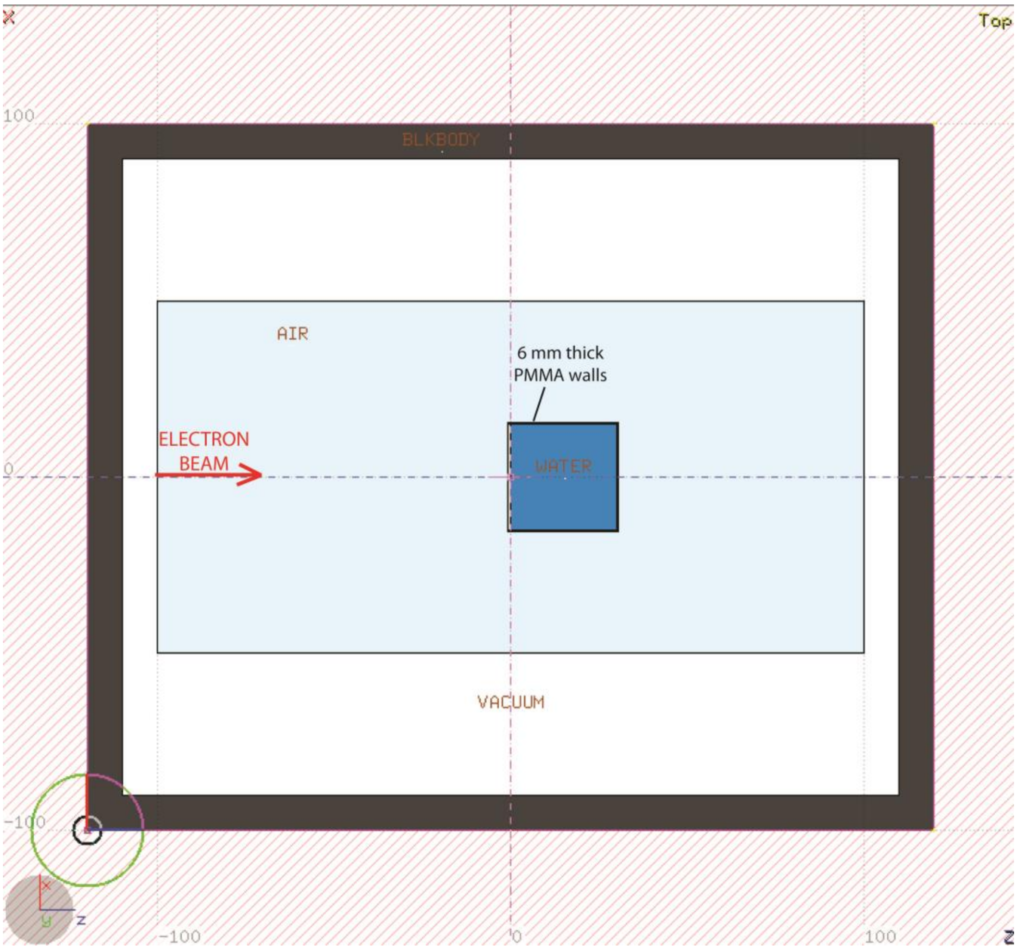

Figure 25. Modelled setup for Monte Carlo simulations (top view). The distance of the electron beam to the surface of 30 × 30 × 30 cm^3 water phantom was set to 100 cm. The thickness of PMMA phantom walls is 6 mm.

4.2.2. Interaction of radiation with matter

Physical interaction of ionising radiation with matter plays a very important role in understanding dose deposition properties of VHEEs and accessing radiation safety issues for ionising radiation. Therefore, the following section is a brief overview of mechanisms of interaction of radiation with matter.

4.2.2.1. Interaction of electrons with matter

The interaction of electrons and positrons with matter can be divided into elastic and inelastic collisions with orbital electrons and atomic nuclei.

Inelastic collisions with orbital electrons result in the excitation of the atom, or, if the energy of the incident electron (or positron) is sufficiently high, in the ionisation of the atomic nuclei. This process is known as *ionisation slowing down*.

Inelastic collisions occur with an atomic nucleus when the electron or positron enters the vicinity of the atomic nucleus; it will be deflected from its original direction by the Coulomb field of the nucleus. The electron loses energy which is emitted as photon radiation, bremsstrahlung. This interaction is called *radiation slowing down*.

Elastic scattering by atomic nuclei, without emission of photons, occurs essentially at low electron/positron energies. Rutherford scattering is of no importance in radiation protection physics, but as a result of this process more than 95% of the energy transferred to matter will produce heat.

Positrons that have been slowed down to nearly zero kinetic energy will finally annihilate. The most important process is two-photon annihilation, which results in the emission of two 511 keV photons.

The typical energy loss in tissue of therapeutic electron beams (i.e. for energies between 6 and 30 MeV), averaged over its entire range, is about 2 MeV/cm in water.

The complete description of the energy and depth of penetration of the moving electrons at any point in the medium is complicated by the fact that the electrons are very much lighter than the atomic nuclei. As a result, the electron can lose a very large fraction of its energy in a single process and, therefore, can be deflected by large angles, which depends strongly on energy. It means that even if the electrons beam is monoenergetic when first impinging on a medium, there will be a large variation among all moving electrons as to where each will stop in the medium. This is referred to as range-straggling [117, 118].

4.2.2.1.1. Macroscopic description - stopping power of electrons

In radiation physics the interaction of charged particles such as electrons or positrons is described by their *stopping power*. The stopping power is the average rate at which the charged particles lose energy at any point along their tracks. For electrons and positrons it is customary to separate the total linear stopping power into two components: the *collision stopping power*, which is the average energy loss per unit path length due to ionisation slowing down and the *radiative stopping power*, which is the average energy loss per unit path length due to radiation slowing down. The separation of the stopping power into these two components is useful because most of the energy lost via ionisation and excitation of atoms is absorbed in the medium close to the electron track, whereas most of the energy lost in the form of bremsstrahlung travels far from the track before being absorbed. Figure 26 shows the collision stopping power, radiative stopping power and total stopping power for water [119].

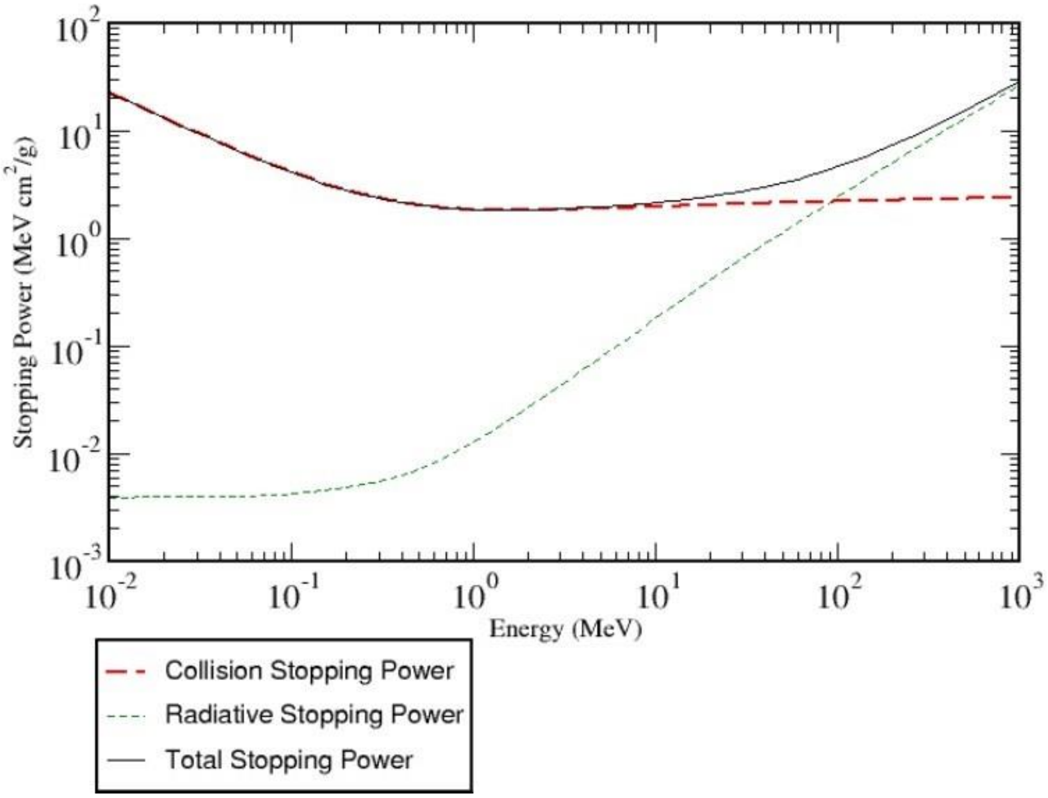

Figure 26. Stopping power as a function of electron energy in water [119].

Stopping power is defined as the average energy loss, dE, per unit path length, ds, along the track of particle. This is usually expressed as the mass collision stopping power, expressed as $(1/\rho)(dE/ds)_{col}$ or (S_{col}/ρ), given by [117]:

$$\frac{1}{\rho}\left(\frac{dE}{ds}\right)_{col} = N_A \left\langle\frac{Z}{A}\right\rangle \int_{Q_{min}}^{Q_{max}} Q \frac{d\sigma}{dQ} dQ, \tag{4.1}$$

where N_A is the Avogadro's number, Z and A are atomic and mass numbers, $\frac{d\sigma}{dQ}$ is differential in energy transfer, Q, cross-section per electron. Q_{max} is maximum energy transfer for electron with kinetic energy E_0 equal to $E_0/2$[2]. The evaluation of the minimum energy transfer Q_{min} represents a major difficulty. The integral for stopping power in equation (4.1) can alternatively be cast as an impact parameter, b, and then integrated out to $b = \infty$, yielding an infinite stopping power because of the large number of soft collisions at large distances.

The full quantum-mechanical expression for the electron mass collision stopping power given by [120, 121]:

$$\frac{1}{\rho}\left(\frac{dE}{ds}\right)_{col} = \frac{2\pi r_e^2 c^2 N_A}{\beta^2}\langle\frac{Z}{A}\rangle\left\{ln\left[\frac{\tau^2(\tau+2)}{2(I/m_e c^2)^2}\right] + F(\tau) - \delta\right\}, \tag{4.2}$$

where $F(\tau) = 1 - \beta^2 + [\frac{\tau^2}{8} - (2\tau + 1)ln2]/(\tau + 1)^2$ and $m_e c^2$ is the rest mass energy of the electron, $\tau = T/m_e c^2$ is the electron kinetic energy, T, in units of the electron rest mass, r_e is electron radius, I is mean excitation energy and δ is density effect correction (when an electron passes through matter, polarization of the atoms in the medium occurs, decreasing the electrical field experienced by the electron, causing a decrease in the stopping power).

Collision stopping power for water, shown in Figure 26, is calculated from the theory of Bethe [122] and Bloch [123] with a density-effect correction evaluated according to Sternheimer [124-126]. A detailed review of this equation, including all the relevant corrections and modifications, can be found in [127]. The stopping-power formula contains an important parameter, the mean excitation energy (I-value), which characterizes the stopping properties of a material. The mean excitation energy or potential, I, is an average of the transition energies, E_i, weighted by their oscillator strengths, f_i, according to the following expression:

$$ZlnI = \sum_i f_i lnE_i. \tag{4.3}$$

Effectively, the above equation express the geometric mean of all the ionisation and excitation potentials of the atoms in the absorbing medium. In general, I cannot be derived theoretically except in the simplest cases such as for monoatomic gases. Instead, it must be

---

[2] Two electrons after collision are indistinguishable, therefore it cannot be distinguished which was incident electron. Arbitrarily, the faster electron after the collision is taken to be the incident one, which results in $Q_{max} = T/2$

derived from measurements of stopping power or range. The most recent values of I, based largely on experimental data are given in ICRU [128]. For example, the best current estimate for water is 75.0 eV.

The radiative energy loss due to the deflection of the electron trajectory in the electric field of an elementary charge is known as *bremsstrahlung*. The scattering charge is generally a nucleus, but bremsstrahlung in the field of orbital electrons is not negligible, especially in materials with low atomic number. Three particles are involved in the collision: the electron, the emitted photon and the scattering nucleus or electron. The nucleus takes up negligible energy, due to its high mass, but its momentum may be comparable to that of the other two partners. For this reason, although one single photon is emitted per interaction, its energy and emission angle are not uniquely related.

Because the deflection is obviously stronger when the nucleus charge is large, radiation energy loss is particularly important in high-Z materials. The cross-section is approximately proportional to the square of the atomic number.

Bremsstrahlung is emitted even at low electron energies, but the cross-sections are small and about constant up to a few MeV, where they begin to increase rapidly with increasing electron energy. Because collision losses decrease with increasing electron energy, the bremsstrahlung contribution to energy loss becomes important above energies of about 10 MeV for high-Z and about 100 MeV for low-Z materials

In analogy to equation (4.1) for collision loses, one can define a *radiative stopping power* $(dE/ds)_{rad}$ or S_{rad} , which is due to the emission of bremsstrahlung –radiative losses of the electrons is the strong electric field of a nucleons in the material they traverse. The mass radiation stopping power is given by [117]:

$$\left(\frac{dE}{ds}\right)_{rad} = \frac{4r_e^2\alpha N_A}{\beta^2}\frac{Z(Z+1)}{M_A}(\tau+1)m_ec^2\ln\left(183Z^{-\frac{1}{3}}+\frac{1}{18}\right), \tag{4.4}$$

where α is the fine structure constant ($\alpha \approx 1/137$). From equation (4.4) it can be seen that the radiative stopping power increases almost linearly with kinetic energy in MeV region (Figure 26), in contrast to the weak logarithmic energy dependence of the collision stopping power. The radiative stopping powers are evaluated with a combination of theoretical bremsstrahlung cross sections described by Seltzer and Berger [129]. Analytical formulas (using a high-energy approximation) are used above 50 MeV, and accurate numerical results of Pratt *et al* [130] below 2 MeV. Cross sections in the intermediate energy region from 2 MeV to 50 MeV are obtained by interpolation, a procedure whose accuracy is confirmed by more detailed calculations for a few cases. The uncertainties of the radiative stopping powers, presented in Figure 26, are estimated to be 2 % above 50 MeV, 2 % to 5 % between 50 MeV and 2 MeV, and 5 % below 2 MeV.

At relativistic energies, there is a more gradual increase in the stopping power, which is known as the relativistic rise. This is due to Lorentz contraction at relativistic energies of the electric field of the moving primary particle. In the forward and backward direction the field is weakened by the factor γ. The field-line is changed from spherical to pancake-shape. This contraction means that the field of the moving particle acts on the bound atomic electrons for a shorter time (it means that the collision time is reduced), which leads to an increase of the impact parameter b_{max} [131]. The net result of a decrease in the collision time, a lateral broadening of the field and an increase in the maximum impact parameter is an increase in the stopping power (see Figure 26).

4.2.2.1.2. Continuous-Slowing-Down-Approximation (CSDA) Range

Given the stopping power of a charged particle in a medium, the range, r_0, of a particle with kinetic energy E_0 can be simply calculated by numerical integration [132],

$$r_0 = \int_0^{E_0} \frac{1}{S_{tot}(E)} dE, \tag{4.5}$$

where $S_{tot} = S_{col} + S_{rad}$ is the total stopping power. This procedure is called the continuous slowing down approximation (CSDA) [117]. For heavy charged projectiles it is nearly the same as the mean range R, the average traversed absorber thickness. The reason for this is that heavy ions are scattered very little and travel almost in a straight line.

Because energy loss occurs via successive ionizations, it is influenced by statistical fluctuations, which leads to the fact that two particles with exactly the same initial energy will most certainly differ slightly in their penetration depth. This effect is called *range straggling*, which causes a broadening of peak in the depth dose distribution, even for purely monoenergetic beams.

The fluctuations in energy loss follow a Gaussian distribution for a sufficiently thick absorber [26]. The variance of the range straggling σ_R^2 is related to the variance of the energy losses σ_E^2. The width of range straggling can be expressed by

$$\sigma_R = \frac{R}{\sqrt{m}} f\left(\frac{E}{mc^2}\right), \tag{4.6}$$

where m and E are the projectile's mass and energy and f is a slowly varying function that accounts for the medium dependence.

4.2.2.1.3. *Multiple Coulomb scattering*

A beam of charged particles traversing a medium has an increasing cross-section and angular divergence as it travels. This process is a consequence of *multiple scattering*, i.e., the result of a sum of discrete individual Coulomb scattering events by atomic nuclei. By basic kinematics, the ratio of masses between the incident ion and the deflecting target determines the magnitude of the scattering.

To treat a very large number of (single) scattering processes analytical theories of multiple scattering have been developed [133-135]. The simplest multiple scattering theory has a Gaussian small angle dependence [136]:

$$P(\theta)d\theta = \frac{2}{\theta^2} e^{\left(-\frac{\theta}{\theta^2}\right)d\theta}, \tag{4.7}$$

which is the probability of finding an electron with a direction between θ and $\theta + d\theta$ after transversing through an absorber. The mean square scattering angle, $\overline{\theta^2}$, is given by the product of the absorber thickness, s, and the scattering power, defined as $\overline{d\theta^2}/ds$:

$$\overline{\theta^2} = s\left(\frac{\overline{d\theta^2}}{ds}\right). \tag{4.8}$$

The scattering power is dealt with in detail in [137] and [121], which gives tables of mass scattering powers for materials and energies relevant to dosimetry.

4.2.2.2. Interaction of photons with matter

If an X-ray photon enters a thin layer of matter, it is possible that it will pass through without interaction, or it may interact (with atomic electrons, but sometimes also with atomic nuclei) via the photoelectric effect, Compton scattering or pair production. The probability that a photon will interact when it transverses through a given thickness of material is the product of the individual interaction probabilities for each of these three processes.

4.2.2.2.1. Photoelectric effect

In the photoelectric effect, the total energy of a photon is transferred to an orbital electron, usually close to nucleus and the photon disappears. The electron is than ejected from the atom with an energy equal to the energy of the incident photon minus the binding energy of the electron. The direction in which the electron is ejected depends on the energy of the incident photon and the polarisation. For low-energy photons (e.g. 50 keV) the photoelectron is ejected at a large angle with respect to the incoming photon's direction, increasing in the forward direction as the photon's energy increases. After ejection of the electron, the neutral atom becomes a positively charged ion with a vacancy in an inner shell that must be filled. The atom returns to a stable condition by filling the vacancy with a nearby, less tightly bound electron further out form the nucleus, therefore (depending on the atom) characteristic X-rays or an Auger electron is emitted [117].

The probability that a given photon will interact by means of the photoelectric process (denoted by τ/ρ) is a function of both the photon's energy and the atomic number of the target atom. For the process to occur, the incident photon must have an energy greater than the binding energy of the involved orbital electron. In general, the probability per electron that a photon will undergo a photoelectric interaction is inversely proportional to the third power of the photon's energy, $h\nu$, and directly proportional to the third power of atomic number, Z, of the target atom.

4.2.2.2.2. Compton effect

The Compton effect is the interaction of a photon with loosely bound orbital electron in which part of incident photon’s energy is transferred to the electron as kinetic energy and the remaining energy is carried away by another photon. The binding energy of the electron is insignificant compared with incident photon’s energy and therefore can be neglected. The energy of the Compton-scattered photon is equal to the difference between the energy of the incident photon and the energy transferred to the electron. If the incoming photon’s energy is low (e.g. 100 keV), very little energy is transferred to the electron. As photon’s energy increases, a greater proportion of the energy is transferred to the electron, so the scattered photon necessarily retains a smaller proportion of the incident energy. The photon may be scattered at any angle with respect to the direction of the incident photon, but the Compton electron is confined to angles between zero and 90 degrees with respect to the direction of the incident photon. If the incoming photon energy is low, the distribution of the scattered photon is isotropic. The scatter angle decreases for photons and electrons as the incident energy increases (e.g. at MeV photon energy ranges, both, photons and electrons are scattered predominantly in the forward direction).

As a result of the conservation of energy and momentum, the energy of the incident photon, $h\nu_0$, the scattered photon, $h\nu'$, and the scattered electron, E , are given by the following relations:

$$\begin{aligned} E &= h\nu_0 \frac{\alpha(1-cos\theta)}{\alpha(1-cos\theta)}, \\ h\nu' &= h\nu_0 \frac{1}{\alpha(1-cos\theta)}, \\ \cot(\phi) &= (1+\alpha)tan\frac{\theta}{2}, \end{aligned} \tag{4.9}$$

respectively. Where $\alpha = \frac{h\nu_0}{m_0c^2}$ and m_0c^2 is the rest energy of the electron (0.511 MeV).

The probability that a photon will interact with a target atom via the Compton process (σ_c/ρ) depends on the energy of incident photon, generally decreasing as the energy of the photon is increased. The probability of Compton interaction is nearly independent of the absorber and is directly proportional to the electron density [117].

4.2.2.2.3. Pair production

Pair production is possible only for photons with energies greater than 1.02 MeV. When the photon closely approaches the nucleus of the target atom, the incident photon energy may be converted directly into an electron-positron pair. Energy of the photon in excess of 1.02 MeV appears as kinetic energy, which may be distributed in any proportion between the electron and the positron. When the positron comes to rest, it combines with an electron, and both particles undergo mutual annihilation, with the appearance of two photons with an energy of 0.511 MeV travelling in opposite directions. The probability of pair production (π/ρ) occurring increases rapidly with incident photon energy above 1.02-MeV threshold and is proportional to Z^2 per atom, Z per electron and approximately Z per gram [15].

4.2.2.2.4. Relative importance of photon interaction processes

Figure 27 illustrates the relative importance of the photoelectric, Compton and pair-production processes as a function of photon energy and the atomic number of the absorber.

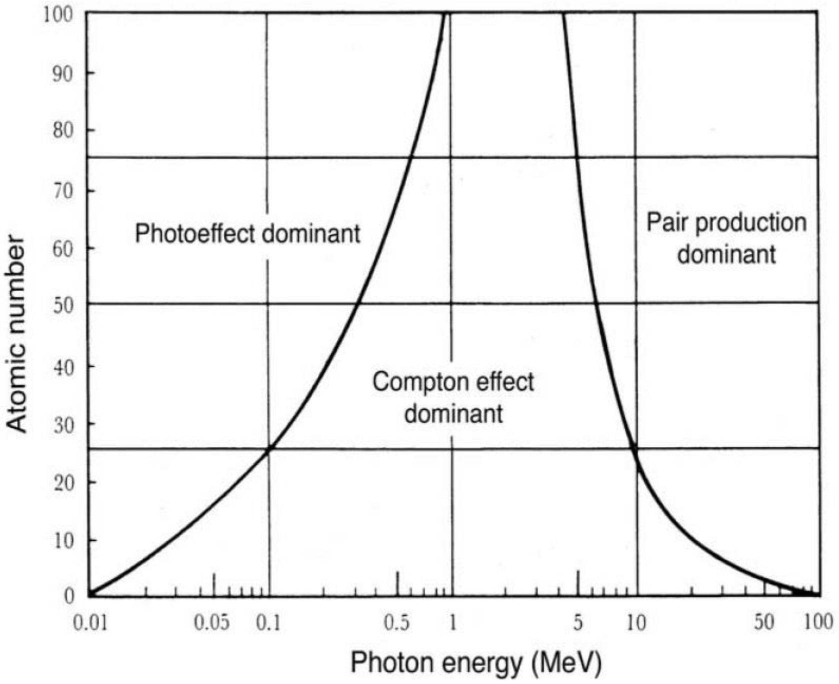

Figure 27. Regions of relative predominance of the three main forms of photon interaction with matter. The left curve represents the region where the atomic coefficients for the photoelectric effect and Compton effect are equal, the right curve is for the region where the atomic Compton coefficient equals the atomic pair production coefficient [15].

As can be seen, the photo-electric effect is the predominant effect at low energies, pair production is the predominant process at high energies, and Compton scattering is the dominant process in the intermediate energy range.

4.2.2.2.5. *Macroscopic description – attenuation coefficient*

Unlike directly ionising radiation (charged particles), when indirectly ionising radiation such as photons pass through material, they interact with atoms in a more discontinuous way, which may result in a substantial loss of energy. It is no longer useful to consider a single particle in terms of its actual energy deposition or its range. Instead one has to observe a sufficiently high number of particles and define global attenuation coefficients.

The *mass attenuation coefficient*, μ/ρ of a given material and for photons of a given energy is given by

$$\frac{\mu}{\rho} = \frac{1}{\rho N}\frac{dN}{dl}, \tag{4.10}$$

where dN/N is the fraction of photons that experience interactions while traversing a distance dl in a material of density ρ. Mass attenuation coefficients are expressed in units $\mathrm{cm}^2\cdot\mathrm{g}^{-1}$. The *linear attenuation coefficient*, μ (expressed in units cm^{-1}), and in contrast to the mass attenuation coefficient, depends on the density of the medium.

There is a direct relationship between the cross-section σ of photons and their attenuation coefficient. In accordance with the definition of the cross-section, the number of interactions produced by photons of fluence Φ per unit path length in a material containing N target centres per unit volume is $\sigma\Phi N$. The number of such interactions in an infinitesimal path length will be $\sigma\Phi N dl$. The product σN is actually the linear attenuation coefficient .

The number of target centres (atoms) N per unit volume of a material of density ρ and atomic mass A is given by

$$N = \frac{\rho}{A}N_A, \tag{4.11}$$

where N_A is Avogadro's number. Consequently the mass attenuation coefficient can be expressed as

$$\frac{\mu}{\rho} = \frac{N_A}{A}\sigma. \tag{4.12}$$

The total mass attenuation coefficient accounting for all photon interactions is given as a sum of the individual coefficients [15]:

$$\frac{\mu_{em}}{\rho} = \frac{\tau}{\rho} + \frac{\sigma_c}{\rho} + \frac{\pi}{\rho}. \tag{4.13}$$

4.2.3. Choice of physical settings for VHEE simulations

The physical settings in FLUKA have to be optimized to perform a time-efficient, yet accurate simulation for the desired application. The program includes a default set of parameters for VHEEs simulations, activated with the card[3] DEFAULTS with option PRECISIO. This set of defaults activates the maximum precision of the simulation and activates electromagnetic transport of electrons, positrons and photons. Other processes activated and defined by this set of parameters include:

- Rayleigh scattering and inelastic form factor corrections to Compton scattering and Compton profiles
- Detailed photoelectric edge treatment and fluorescence photons
- Low energy neutron transport on down to thermal energies
- Fully analogue absorption for low-energy neutrons
- Particle transport threshold set at 100 keV
- Delta ray production (with threshold 100 keV corresponding to a range of 0.14 mm in water [138])[4]

The set of parameters PRECISIO [110] is used to configure the physical model for the simulations. In these simulations electron/positron and photon production thresholds are set to 10 keV. The δ-ray[5] production threshold has been adapted to meet the requirements of the specific simulations, because simulation time grows enormously with lower δ-ray

---

[3] 'Card" is the definition of ini.file logical element from the terminology established for a given MC code

[4] More details can be found on http://www.fluka.org/fluka.php?id=man_onl&sub=20

[5] Secondary electrons with enough energy to escape a significant distance away from the primary radiation beam and produce further ionization

thresholds, as the number of electrons to be transported increases dramatically, and electron transport is a very demanding task. For the calculated quantities, described in the following section, a threshold of 10 keV is selected (instead of the default value of 100 keV) in lieu of increased accuracy and for consistency with the lowered electron transport threshold down to 10 keV.

Physics processes for electrons in FLUKA

FLUKA uses an original transport algorithm for charged particles [139], including complete multiple Coulomb scattering treatment giving the correct lateral displacement even near a boundary. The variations with energy of the discrete event cross sections and continuous energy loss in each transport step are taken into account. Differences between positrons and electrons are also included for both stopping power and bremsstrahlung [140].

Physics processes for photons in FLUKA

Physics of photon interaction with matter include: pair production with actual angular distribution of electrons and positrons, Rayleigh effect, Compton effect with Doppler broadening, photoelectric effect with actual photoelectron angular distribution. Quasideuteron interactions and giant dipole resonance are also included.

The above section is only a short overview of the capabilities of FLUKA. More detailed descriptions of the physical models, algorithms and techniques can be found in references cited and in the FLUKA reference manual [110].

4.2.4. Dose deposition

4.2.4.1. Depth-dose curve

Central axis dose distributions inside the patient or phantom are usually normalized to D_{max}=100% at the depth of dose maximum z_{max} and then referred to as the percentage depth-dose profile (PDD) distributions. The PDD is thus defined as follows:

$$PDD(z, A, SSD, E) = 100\left(\frac{D_Q}{D_P}\right), \tag{4.14}$$

where D_Q is the dose at point Q at depth z on the central axis of the phantom and D_p is the dose at point P at z_{max} on the central axis of the phantom.

The geometry for PDD is shown in Figure 28. Point Q is an arbitrary point at depth z on the beam central axis; point P represents the specific dose reference point at $z = z_{max}$ on the beam central axis. PDD depends on four parameters: depth in the phantom, z, field size, A[6], SSD and radiation beam energy E. The PDD ranges in value from 0 at $z \to \infty$ to 100 at $z = z_{max}$. The dose at point Q contains two components: primary and scattered.

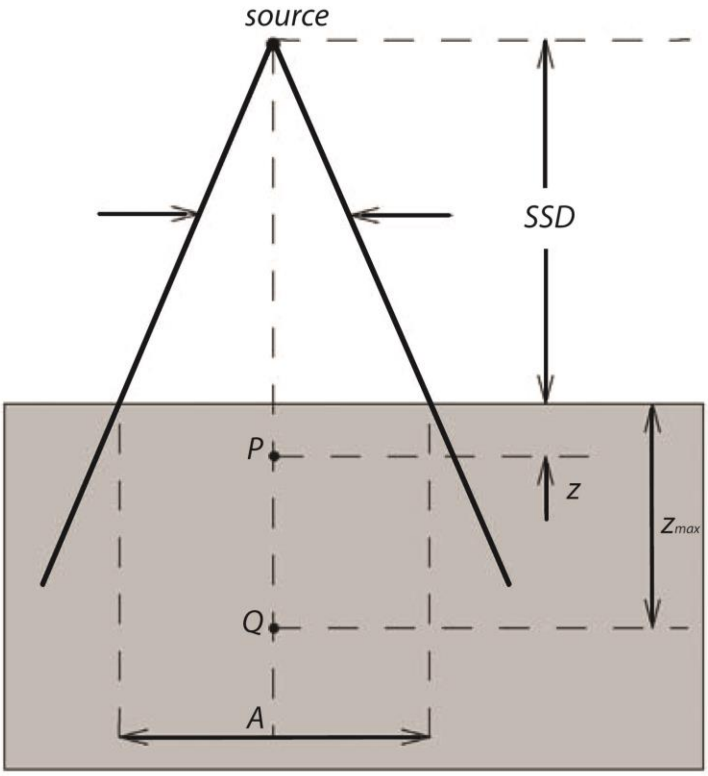

Figure 28. Geometry for *PDD* measurement. Point *Q* is an arbitrary point on the beam central axis at depth *z*, point *P* is the point at z_{max} on the beam central axis [118].

4.2.4.2. Clinical electron depth dose curve

Figure 29 illustrates the physics of electron interaction applied to electron beams used in radiotherapy (energies up to 30 MeV). The figure shows three different depth-dose curves obtained using MC simulations, corresponding to different approximations of electron

---

[6] Field size is a common term in radiotherapy physics of a beam (or radiation source) size. The field size A is defined on the surface of the phantom.

transport physics for a 30 MeV broad monoenergetic and collimated electron beam in water.

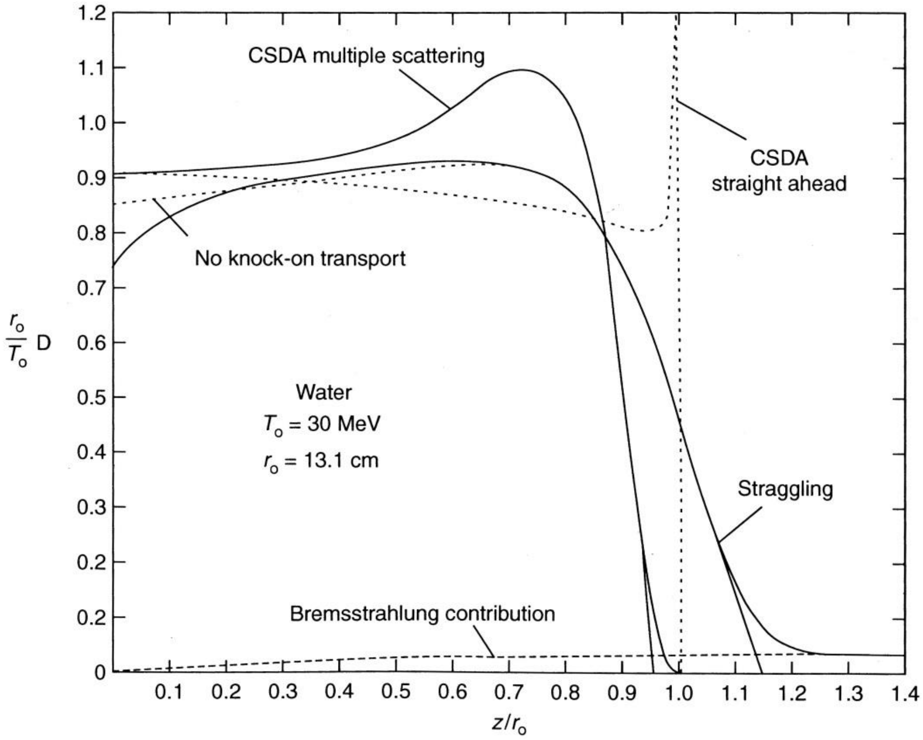

Figure 29. The effect of various approximations on the electron depth-dose curve for a broad, 30 MeV electron beam in water illustrating the physics of electron interaction [141].

The curve labelled *CSDA straight ahead* corresponds to straight tracks and shows the Bragg peak normally associated with heavy particles. This extremely simple approximation illustrates very clearly the behaviour of the total stopping power S_{tot} as the electron energy gradually decreases with depth. The decrease in dose with depth mirrors the decrease in total stopping power with falling electron energy. At an energy close to that of the electron rest mass (0.511 MeV), the collision stopping power goes through a minimum and then rises rapidly (because of the $1/\beta^2$ term in equation (4.2)).

The *CSDA multiple scattering* curve involves directional changes through multiple scattering, but does not involve any secondary particle transport or energy-loss straggling. The increase in dose away from the surface is entirely due to increasing average obliquity of electron tracks with depth and the fact that the beam is broad (i.e. there is lateral scattering equilibrium); this is known as *scatter buildup*. At around $z/r_0 = 0.7$, the planar fluence starts to decrease as electron tracks begin to reach their end. A maximum exists because of electrons reaching the end of their range.

The *no knock-on transport* curve does not include the generation and transport of knock-on electrons or delta rays, but it does include radiative loses (i.e. bremsstrahlung) and one sees the so-called bremsstrahlung tail spreading beyond the practical range. Also, now the slope of the dose falloff is much reduced. This is primarily due to the incorporation of energy-loss straggling.

Finally the unlabelled curve corresponds to the simulation including the full electron transport physics. The effect of simulation δ-ray (or *knock-on* electron) transport is clearly seen in the build-up close to the surface. This is more pronounced in the megavoltage photon beams, where ranges of Compton electrons are significantly greater than those of predominantly low-energy δ-rays [141].

4.2.4.3. Results

Percentage depth doses for small electron field sizes

When the distance between the central axis and the field edge is larger than the lateral range of scattered electrons, a lateral scatter equilibrium[7] exists and the depth dose for a specific electron energy will be almost independent of the field dimensions, as shown in Figure 30 for field sizes larger than 10 × 10 cm^2. A decreased field size that leads to decreased lateral electronic equilibrium on the central axis, which results in the depth dose being very sensitive to the field size, as shown in Figure 30.

For field sizes larger than the practical range of the electron beam, the PDD curve remains almost constant with increasing field size, because the electrons from the periphery of the field are not scattered sufficiently to contribute to the central axis depth dose. When the field is reduced below that required for lateral scatter equilibrium, the dose rate decreases, $d_{\max}$ moves closer to the surface and the PDD curve becomes steeper (see Figure 30).

The practical range, R_p, is defined as the depth at which the tangent plotted through the steepest section of the electron depth dose curve intersects the extrapolated line of the background due to bremsstrahlung, which is independent of electron beam field size and depends only on electron beam energy. Therefore, if the electron energy is increased above

---

[7] Charged particle equilibrium (also known as electronic equilibrium) is said to exist in a volume, *V*, in an irradiated medium, if each charged particle of a given type and energy leaving volume *V* is replaced by identical particle of the same energy entering *V*.

100 MeV (for a large enough field size) R_p of the electron exceeds that of a patient body (i.e. more than 40 cm).

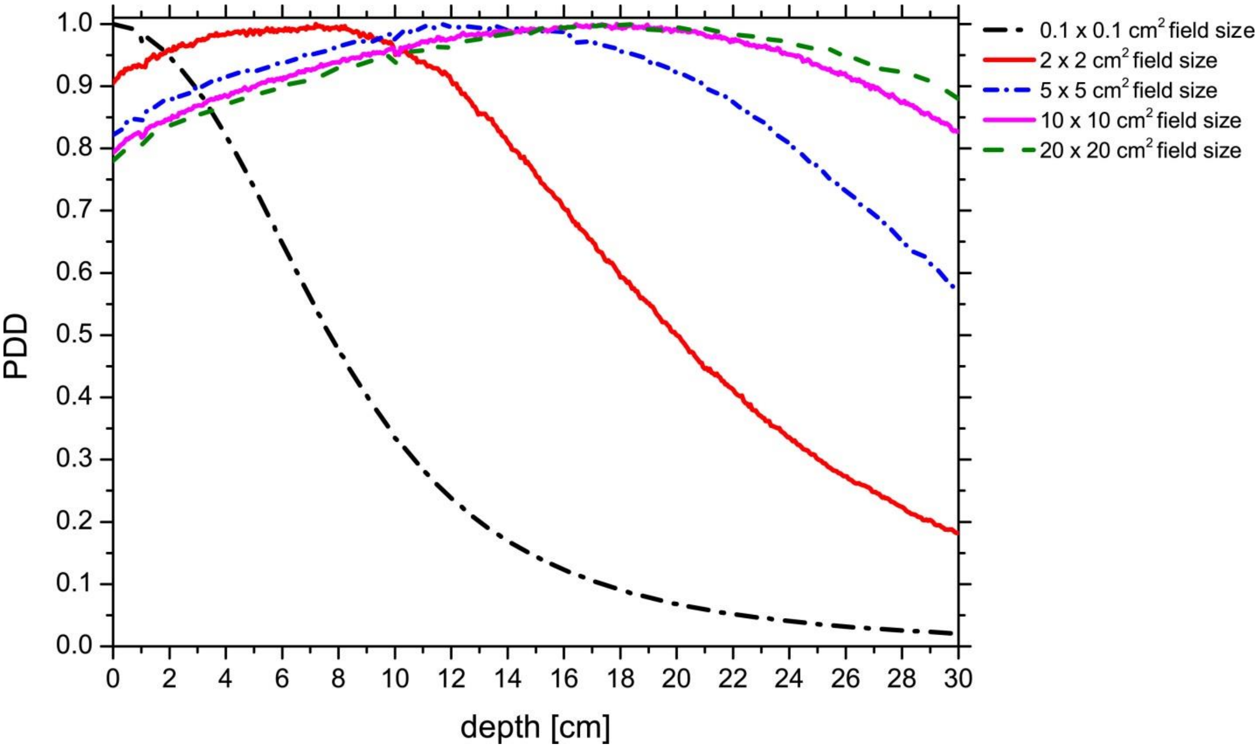

Figure 30. PDD profiles for 150 MeV electron beam far varying field size.

Model of electron beams

Spatial dose distributions in a homogenous water phantom (described in section 4.2.1) for a single 6 MeV, 10 MeV, 15 MeV, 20 MeV, 30 MeV, 40 MeV, 50 MeV, 100 MeV, 150 MeV and 200 MeV electron beams have been simulated. All particles are monoenergetic and set in motion 100 cm away from the surface of the phantom. Particles are distributed in a 5 × 5 cm^2 square beam with a spatial Gaussian distribution. Ten million particles have been used for the simulations.

Properties of the beam at the phantom surface

The scattering of monoenergetic electron beams in air for a few different initial beam energies has been investigated.

The passage of the beam through air is simulated as a 100 cm long air slab. The intensity (planar fluence) $I(z,r)$ of the beam is scored at plane $P(z)$ perpendicular to the beam axis, and situated at a distance *z* from the electron source, and at a distance *r* from the central axis of the beam. FWHM is defined on plane *P*(*z*), as separation between points where the intensity of the beam decreases from *I* = 100% to *I* = 50%, normalized to maximum value of the beam on *P*(*z*). Figure 31 shows the FWHM beam evolution, at various distances form source, for various initial beam energies.

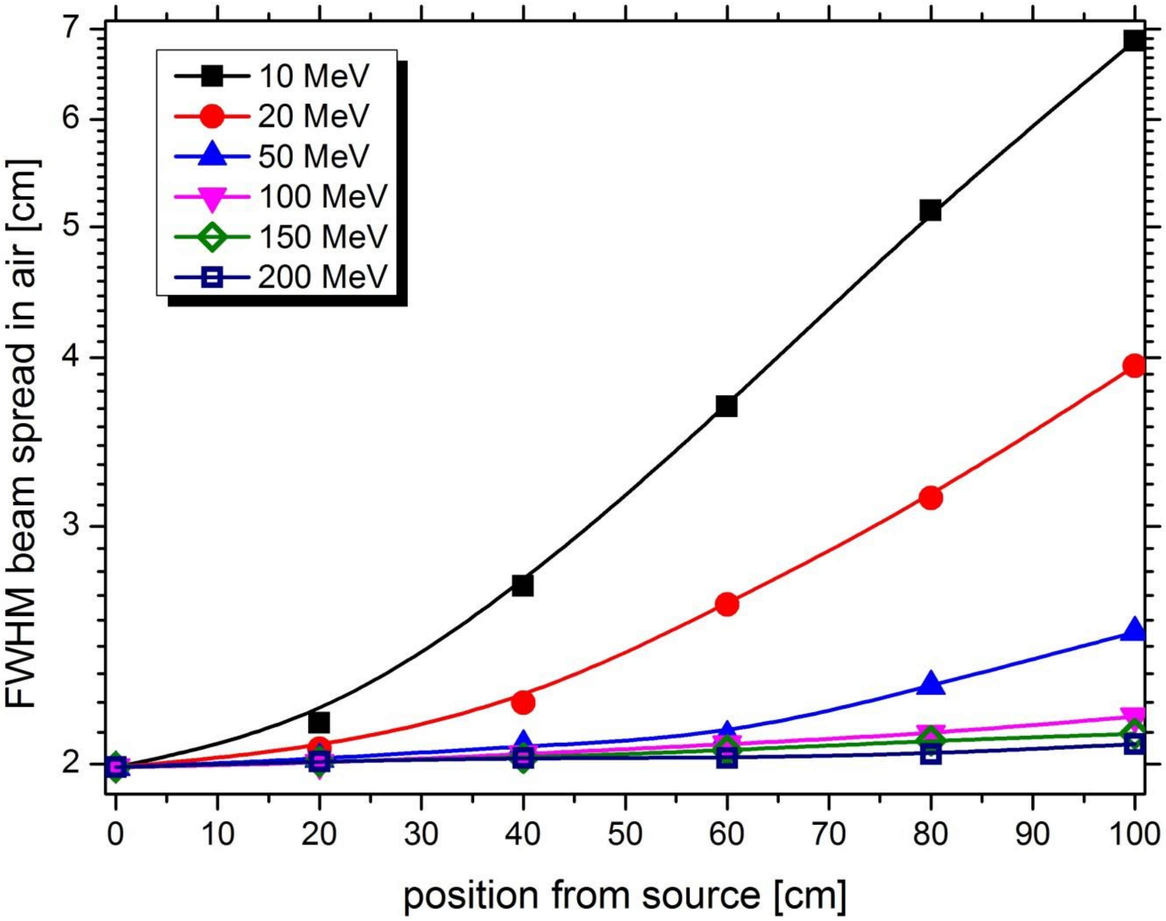

Figure 31. The FWHM beam spread in air of the Gaussian beam with intensity distribution FWHM=2 cm versus distance from the position of the source for various initial electron energies.

For these calculations the distribution of the intensity of particles in the plane at the level of the source has been assumed to be a two-dimensional, rotationally invariant Gaussian with full width (half the maximum value at $r = 0$) equal to 2 cm with no angular spread. It can be seen from this figure that the spread of the beam at conventional clinical electron energies dramatically increases with the distance from the source (to about 350% and 200% of the initial beam size for 10 and 20 MeV electron beams, respectively, at *SSD* = 100 cm) due to multiple Columb scattering in air of low energy electrons. On the other hand, for VHEEs (100 MeV and above) the monoenergetic electron beam experiences very little scattering so that at the *SSD* = 100 cm the beam size is increasing less than 8%.

This low dependence of the beam spread on the distance from the source to the surface suggests that VHEEs would be a perfect candidate for high resolution pencil beam applications.

However, it needs to be pointed out that that these investigations assumed parallel electron beam with no divergence, thus no emittance. Therefore, one may expect that a negligible angular spread of electrons in air may lead to non-negligible spatial widening of the VHE electron beam. Therefore, for beams with significant divergence in order to maintain pencil beam characteristic at the patient surface, the *SSD* distance should be kept as short as possible.

Depth-dose characteristic

A set of two-dimensional dose distributions from single electron beams, Figure 33, shows dose maps of 5 × 5 cm^2 field size beams at *SSD* = 100 cm of energies 6 MeV, 10 MeV, 15 MeV, 20 MeV, 30 MeV, 40 MeV, 50 MeV, 100 MeV, 150 MeV and 200 MeV. The centre of the coordinate system is placed at the surface of the phantom. It is seen from these figures that VHE electron beams have a relatively small spread in water up to a depth of 10 cm. Moreover, a considerable number of particles penetrate through the 30 cm thick phantom in all cases. One of the most important characteristics is the large depth of dose maximum, d_{max}, presented in Table 2.

Table 2. The relation of d_{max} and the percentage entrance dose with increasing electron beam energy. The presented values correspond to depth dose profiles shown in Figure 26.

Beam energy	d_{max}	percentage entrance dose	Beam energy	d_{max}	percentage entrance dose
6 MeV	1.3 cm	75%	40 MeV	3.9 cm	89%
10 MeV	2.3 cm	84%	50 MeV	4.2 cm	88%
15 MeV	2.5 cm	90%	100 MeV	8.1 cm	82%
20 MeV	2.7 cm	91%	150 MeV	12. 7 cm	78%
30 MeV	3.0 cm	91%	200 MeV	18.9 cm	74%

The depth dose maximum and the steepness of the PDD curve beyond $d_{max,}$ depend strongly on the size of the beam. This characteristic has already been shown in Figure 30, where the dose profile on the central axis of the beam dramatically decreases with decreasing field size. Another interesting feature for VHEEs is the decrease of the entrance dose down to about 70% for a 200 MeV electron beam and the flattening of the maximum dose deposition with increasing energy (see Table 2). We can conclude that for VHEEs the size of the buildup region[8] increases with beam energy and the surface dose decreases with beam energy.

For comparison of the dose distribution for VHEEs the analogous data for dose distributions for low energy electrons is presented. The most compelling difference between VHE and low energy electron beams is the deep penetration of high dose values for VHE electron beams. This is evident in Figure 32, which shows the percentage depth dose profiles for electron beams as a function of beam energy. Clinical electron beams (up to 30 MeV) are only used for treatment of superficial or shallow tumours. Therefore, the dose distribution characteristic for VHEEs cannot be directly compared with low energy beams, because their practical range is less than 10 cm depth for all clinically available beams. Nevertheless, it is worth pointing out that the dose distribution property of VHE electron beams can lead to an enhancement of the tumour-to-normal tissue ratio (TNR) in comparison to MeV photon beams.

Another important characteristic of VHEE beams is the very sharp penumbra. In this work penumbras are measured as the distance between the 90% and 10% intensity levels normalized to the maximum value at a given depth.

The penumbra for single beams are presented in Table 3. Penumbra of clinical range electron beams increases rapidly with increasing depth. For VHEEs (100 MeV and above) the penumbra stays very sharp up to 15 cm and more (for even higher energies), which indicates that VHEEs would be suitable for treatment of tumours located close to critical structures, such as the eye or spinal cord, sparing organs at risk (OAR).

Table 3. Penumbra (distance between 90% and 10% of dose maximum at a given depth) for a single electron beam with an energies from 20 MeV to 200 MeV.

depth [cm]	penumbra [cm]						
	20 MeV	30 MeV	40 MeV	50 MeV	100 MeV	150 MeV	200 MeV
1	3.6	2.6	2.0	1.8	1.0	0.6	0.6
5	4.2	3.2	2.6	2.1	1.1	0.8	0.8
10	--	4.4	3.6	3.3	1.6	1.2	1.0
15	--	--	--	--	2.6	1.8	1.4
20	--	--	--	--	3.4	2.6	2.0

---

[8] The dose region between the surface (depth $z = 0$) and depth $z = d_{max}$ is referred to as the dose buildup region and results from the relatively long range of energetic secondary charged particles (electrons and positrons) that first are released in a medium (here water phantom)

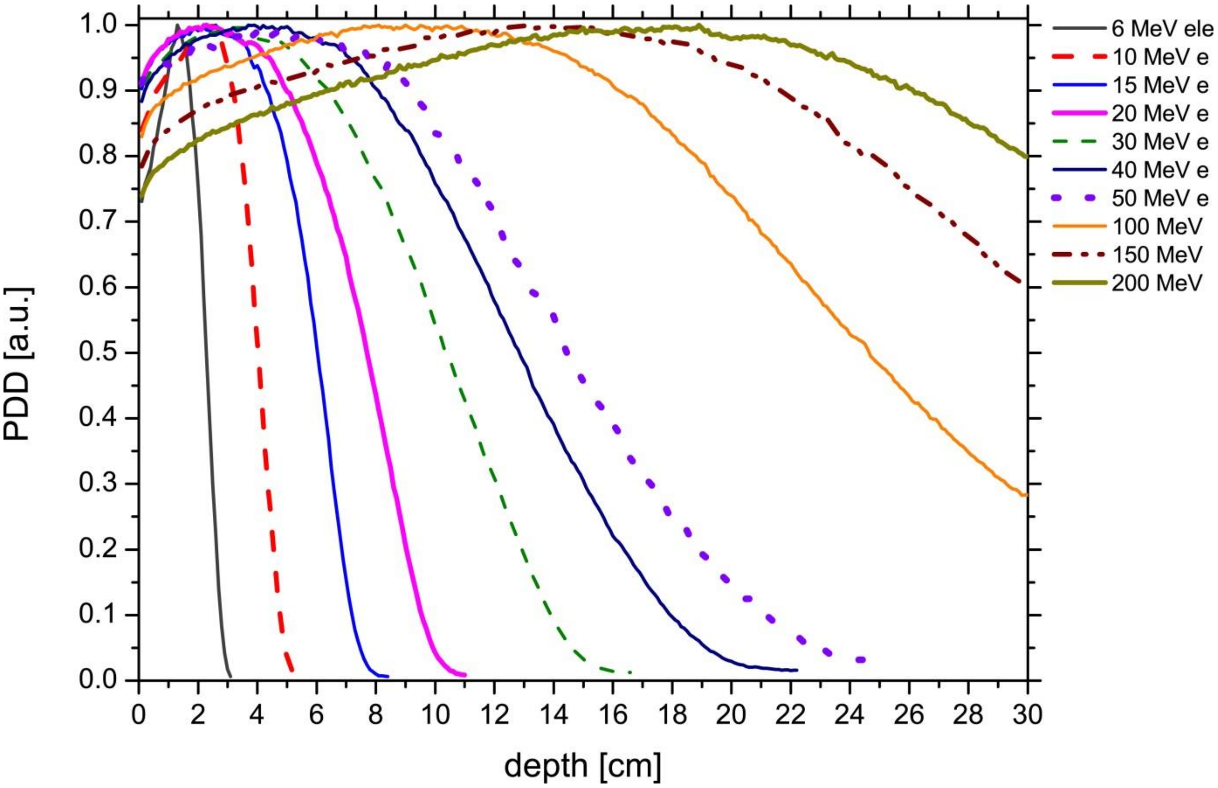

Figure 32. PDD curves for 5 by 5 cm field size for various electron energy beams with 5 × 5 cm^2 field size at SSD of 100 cm

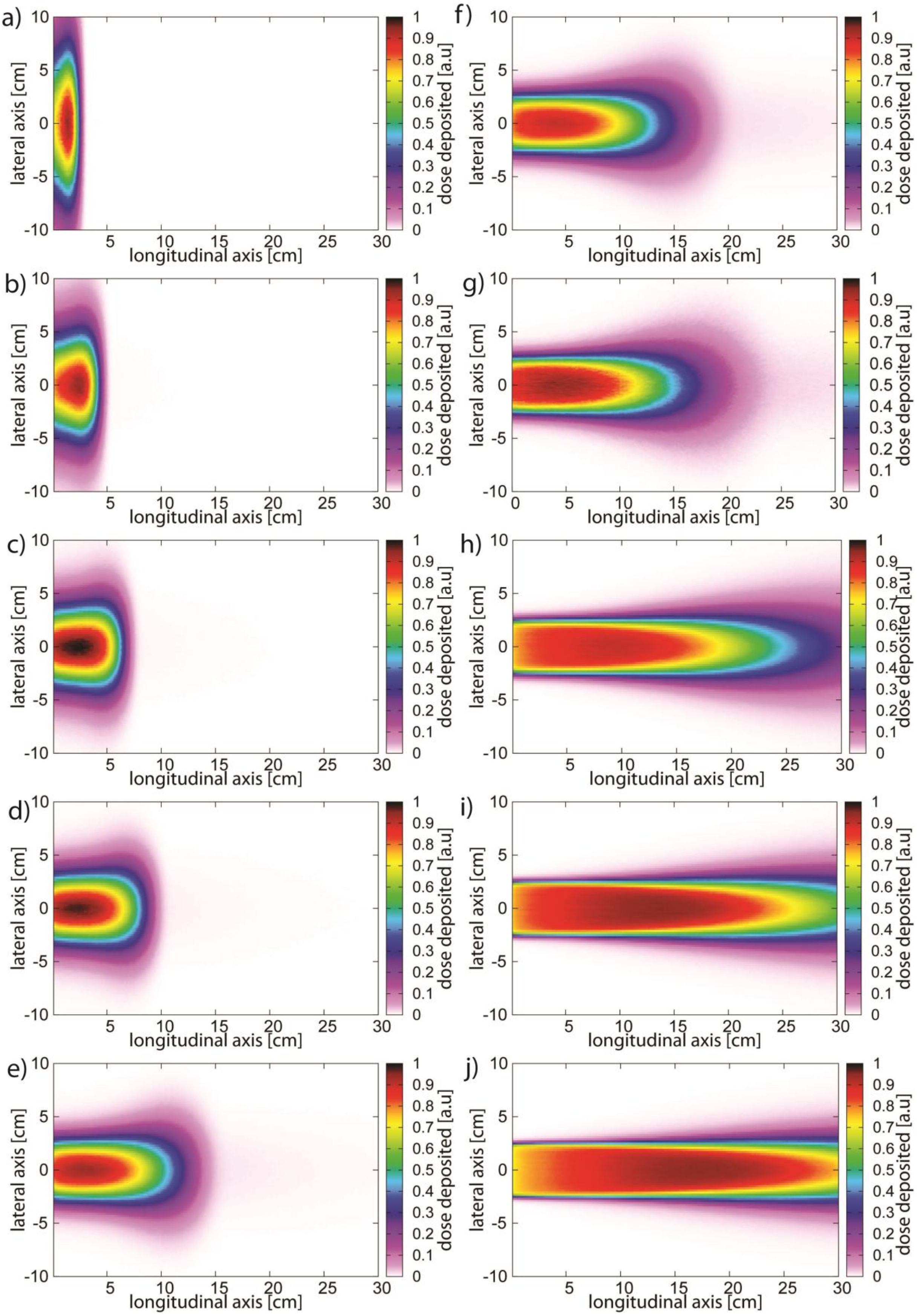

Figure 33. Two-dimensional dose maps representing relative dose distribution along beam propagation axis for (a) 6MeV, (b) 10 MeV, (c) 15 MeV. (d) 20 MeV, (e)30 MeV, (f) 40 MeV, (g)50 MeV, (h)100 MeV, (i) 150 MeV) and (j) 200 MeV electron beam with *5 × 5* cm^2 field size at SSD of 100 cm.

General conclusions

For a constant field size, the source to surface distance, and beam energy, the PDD first increases from the surface to d_{max} and then decreases with further increase in the depth. The depth of the dose maximum and the surface dose depend on the beam energy; the larger the beam energy, the larger the depth of dose maximum and the lower the surface dose. It is not well pronounced for low energy electrons (below 50 MeV) because the SSD distance has been set to 100 cm, therefore electrons in this energy range suffer significant scattering (discusses above), therefore the field size on the surface of the phantom is much larger with respect to the field size on the surface for VHEEs.

The dose distribution in charged particle therapy is due to both primary and secondary particles. The secondaries are of interest for three reasons. First, if Monte Carlo treatment planning is envisaged, the question arises whether all nuclear interaction products deliver a significant contribution to the total dose and, hence, need to be tracked. Second, there could be an enhanced relative biological effectiveness (RBE) due to secondaries. Third, neutrons originating from nuclear interactions may deliver dose outside the target volume. Therefore, these aspects are investigated in the following sections.

4.2.5. Bremsstrahlung production

The energy loss of an electron beam due to production of bremsstrahlung photons is given by the radiative stopping power discussed in section 4.2.2.1.1.

VHE electron beams, propagating through tissue-equivalent media (e.g. water), lose a large part of their initial energy to bremsstrahlung production. The data on bremsstrahlung production is important from a radiation protection standpoint and will dictate the amount of shielding required.

Bremsstrahlung radiation is always apparent when the electron beam passes through water. This component is pronounced also in the PDD profile for clinical electron beams, where the dose deposited beyond practical range does not decrease to zero. This aspect has already been discussed in 4.2.4.2, where the concept of clinical electron depth dose curve has been presented (Figure 29). Naturally VHEEs experience similar behaviour.

Calculations using FLUKA are carried out for the energy distribution of the electrons at various depths (3.5 cm, 9.5 cm and 17.5 cm) in a water tank. The spectrum of incident monoenergetic VHE electrons (for 100 MeV, 150 MeV and 200 MeV) at various depths in a water tank are calculated by scoring, using USRBDX scoring card, the energy of the particles crossing a probe detector. The probe detector is represented by a sphere of 1 cm radius, placed at a depth of 3.5 cm, 9.5 cm and 17.5 cm, respectively. The results of simulation are illustrated in Figure 34.

The evaluated electron spectra in water includes both, primary and secondary electrons. Note that for all investigated energies, at each depth there is a significant contribution to the spectrum coming from secondary low energy electrons which are produced when VHE electron beam propagates through water. The peak energy of the electron spectrum for each energy reduces with increasing depth.

Table 4. The energy shift of the incident electron beam for 100 MeV, 150 MeV and 200 MeV at various depths in the water tank.

Incident beam energy	*Spectrum maximum*		
	3.5 cm	*9.5 cm*	*17.5 cm*
100 MeV	95 MeV	82 MeV	62 MeV
150 MeV	145 MeV	131 MeV	112 MeV
200 MeV	195 MeV	182 MeV	161 MeV

Figure 34 and Table 4 show that VHEEs lose about 5 MeV from their initial energy in the first 4 cm of water. At 10 cm and 18 cm the downshift is 20 MeV and 40 MeV, respectively. This could be of a significant importance when investigating radiobiological effectiveness of VHEEs.

The bremsstrahlung spectra evaluated at the corresponding depths (i.e. 3.5 cm, 9.5 cm and 17.5 cm) for the 100 MeV, 150 MeV and 200 MeV incident electron beam are shown in Figure 35. It is seen from these figure that the number of photons increases to a maximum at the low-energy end of the spectrum. The energy spectra of radiated photons ranges from zero to the kinetic energy of the incident electron and the number of photons in a given energy interval is approximately inversely proportional to the photon energy.

Photon fluence has been evaluated in FLUKA using the USRBIN card with photon track densities as a scoring value. Figure 36 presents the photon fluence (per primary incident particle) inside the water phantom irradiated with 20 MeV and 150 MeV monoenergetic electron beams. For 20 MeV electron beam a significant lateral spread of bremsstrahlung photons is observed. As the electron energy increases up to ranges characteristic for VHE electron beams, the angular distribution of the emitted photons become increasingly forward-peaked (Figure 36 b). Therefore, the main contribution to dose distribution for the case of VHEE irradiation due to bremsstrahlung will be along the channel (cross section) of the initial electron beam. The flux of low energetic photons increases with the increasing depth while high energy bremsstrahlung decreases (see Figure 35).

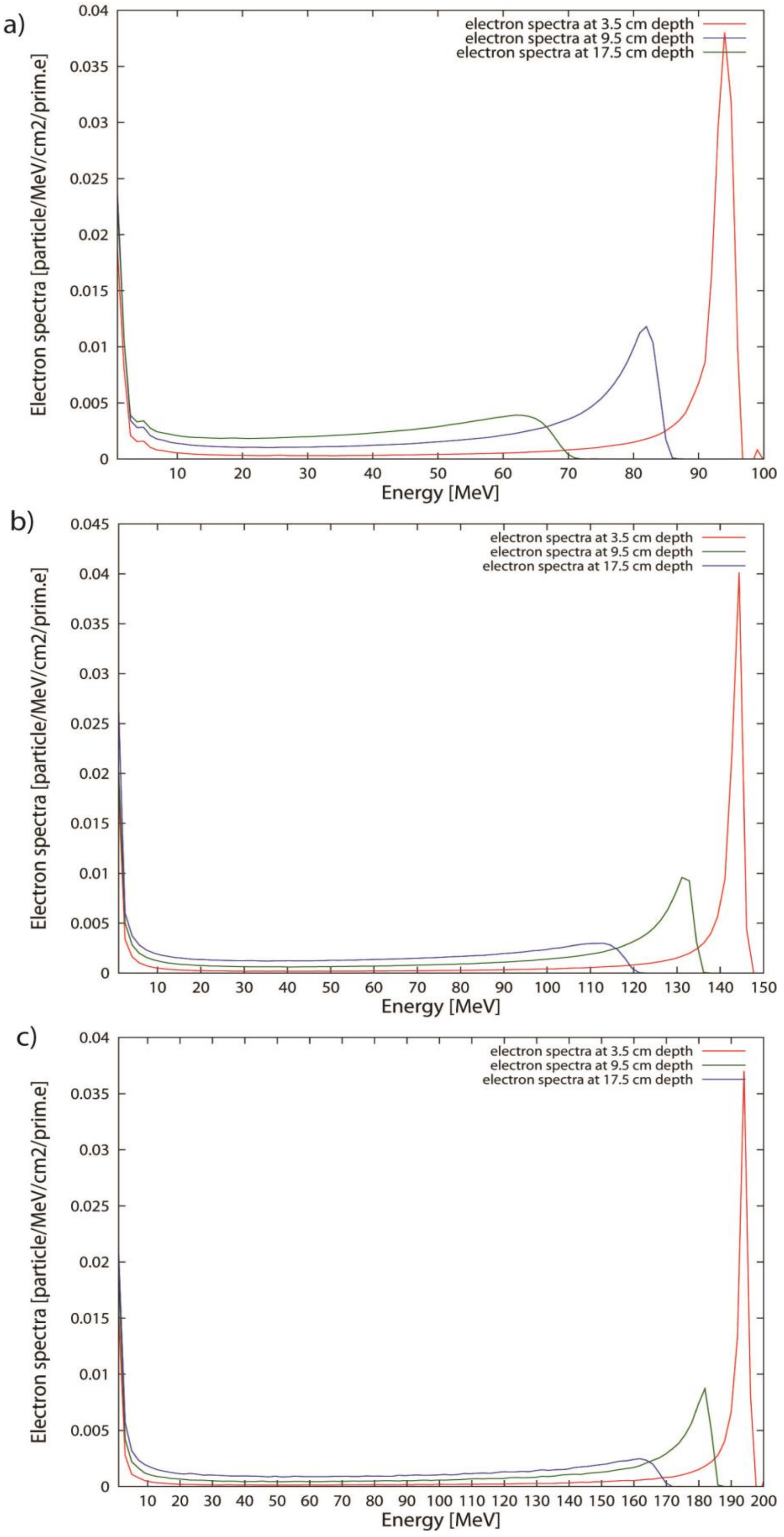

Figure 34. Electron spectra for 100 MeV (a) and 150 MeV (b) and 200 MeV (c) at various depths in a water tank.

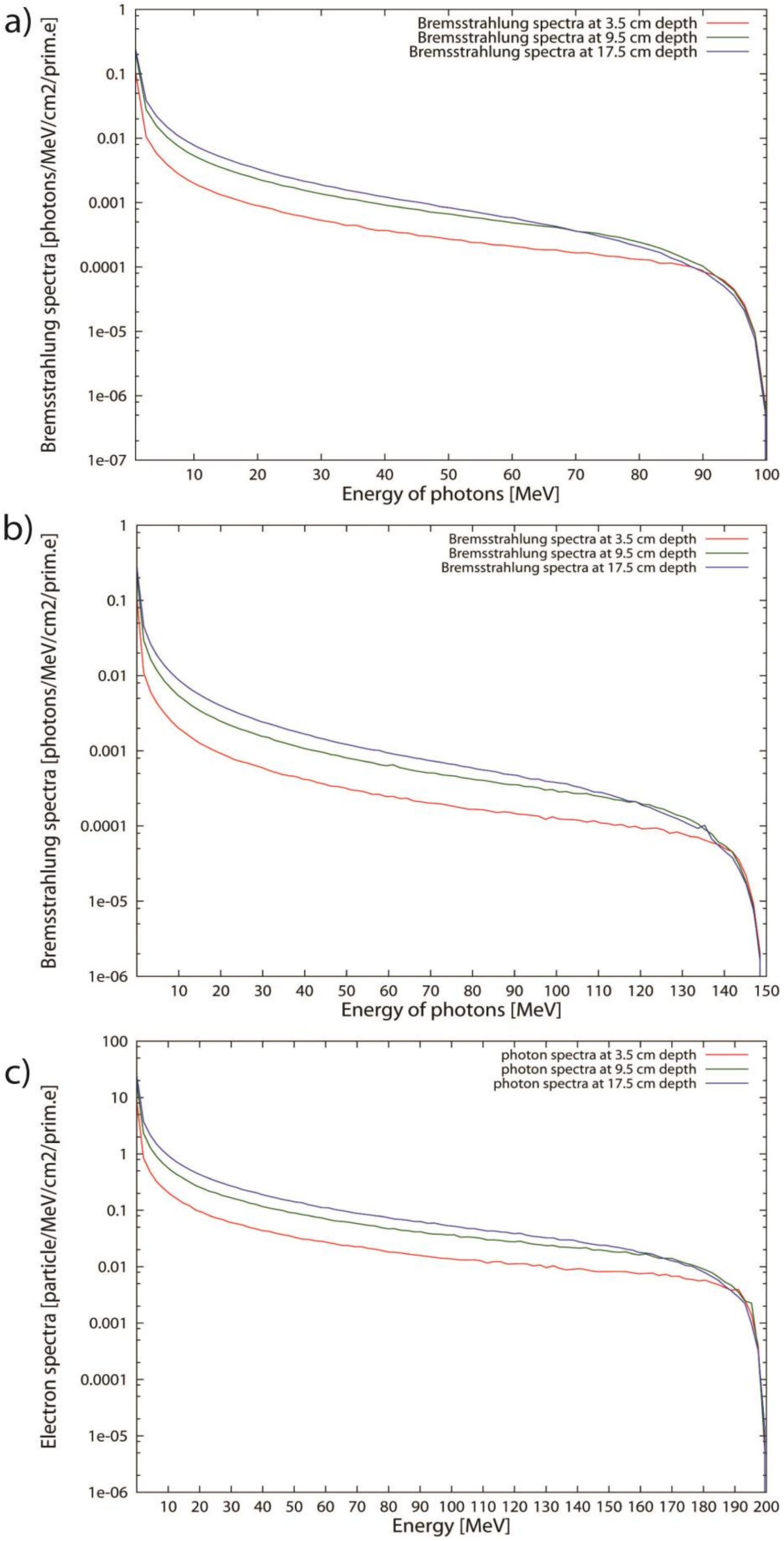

Figure 35. Bremsstrahlung spectra for 100 MeV (a) and 150 MeV (b) and 200 MeV (c) at various depths in a water tank.

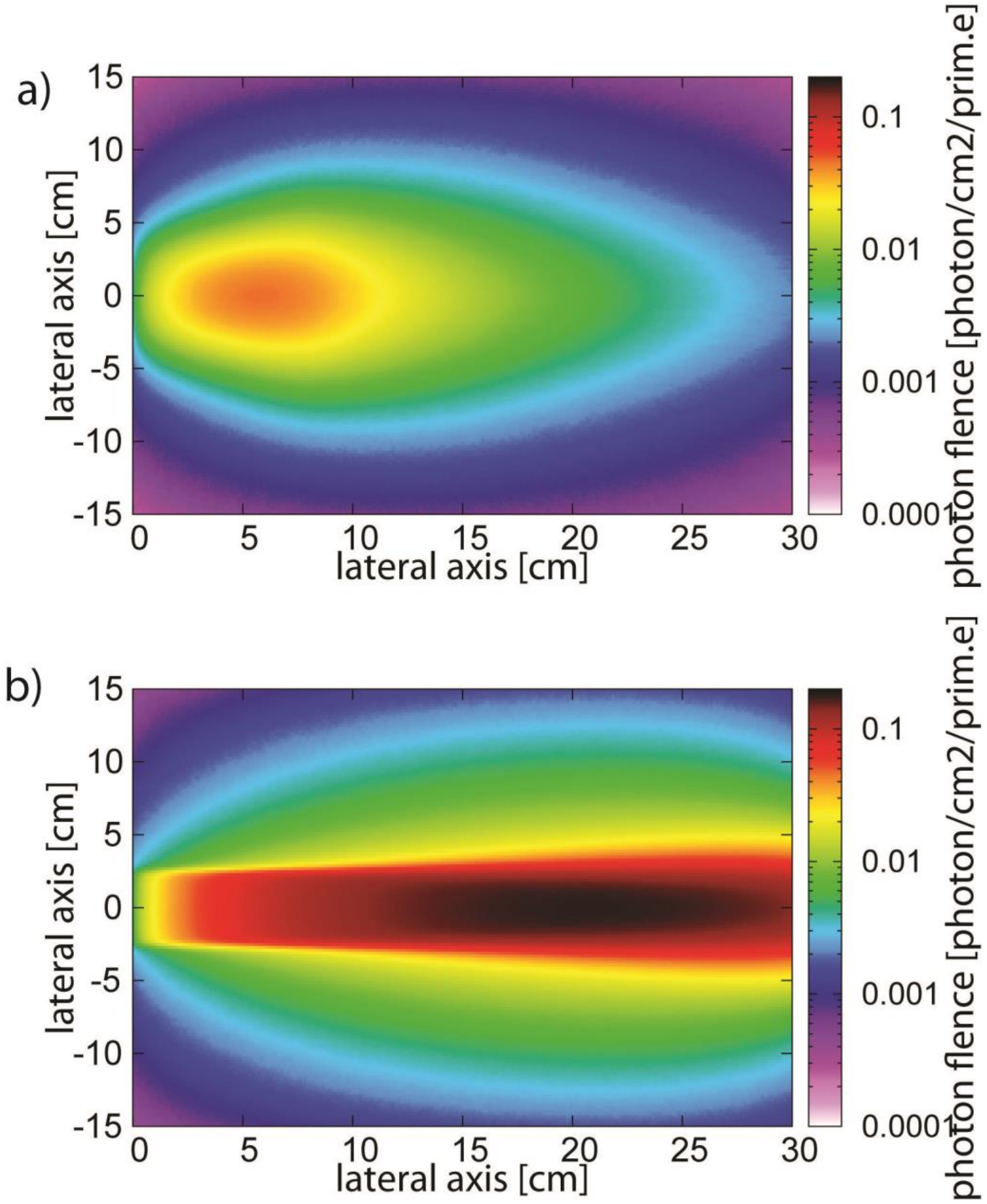

Figure 36.Photon fluence along central lateral plane of the beam in a water phantom irradiated with 20 MeV (a) and 150 MeV electron beam.

4.2.6. Neutron production

Apart from bremsstrahlung, neutrons constitute the most hazardous secondary radiation produced by electrons as they strike targets at energies above the photoneutron threshold. Almost all research electron accelerators operate at energies at which copious photoneutrons can be produced. For this reason it is important to have reliable predictions of neutron yields. Moreover, an understanding of neutron production by electrons is invaluable to those planning radiation protection for experiments with VHEEs and for evaluation of the neutron dose equivalent.

The quality factor (Q) relates the biological effectiveness of a radiation to the absorbed dose delivered in tissue, which is defined as a function of the unrestricted linear energy transfer relationship, thus taking into account the differences in the effects of different types of radiation

The interaction of high-energy neutrons in biological tissue occurs mainly through the release of low-energy protons from elastic collisions with hydrogen nuclei [142, 143]. Because the recoiling protons are heavily ionizing (high LET), their quality factor is high. At neutron energies less than about 100 eV, (n, γ) and (n, p) reactions dominate.

The effective quality factor Q^*_{eff} of the dose imparted by an external neutron beam of a given energy is a quality factor derived by an integration over the spectrum of ionizing particles released in tissue, $\phi(\varepsilon)$, by several types of contributing interactions. The Q^*_{eff} values vary considerably with neutron energy, ε,

$$Q^*_{eff} = \frac{H^*(10, \varepsilon)}{D^*}. \tag{4.15}$$

Effective quality factors for neutrons, Q^*_{eff}, and conversion factors for fluence to dose equivalent (H*) have been recommended by ICRP [144]. The reference [145] lists effective quality factors for $H^*(10, \varepsilon)$. The aspect of dose equivalent is discussed in more detail in section 4.2.8.

4.2.6.1. Neutron production mechanisms

Nuclear interactions are of importance for potential VHEE radiation therapy for three reasons. First, they contribute to the total absorbed dose. Second, they may have high-LET values causing an increase of the beam's relative biological effectiveness (RBE) and third, they produce secondary neutrons leading to dose deposition outside the target volume. However, because of their low cross-section they are very penetrating.

4.2.6.1.1. The giant dipole resonance

Above a threshold energy which varies from 10 to 19 MeV for light nuclei and from 4 to 6 MeV for heavy nuclei, neutron production occurs in any material struck by an electron or bremsstrahlung beam. Neutron production may be a radiation hazard in itself and can cause induced activity (discussed in section 4.2.7).

Between the threshold and approximately 30 MeV, neutrons are produced primarily by a process known as the *giant photonuclear resonance* [146, 147]. The physical mechanism can be described as one in which the electric field of the photon transfers its energy to the nucleus by inducing an oscillation in which the protons as a group move oppositely to the neutrons as a group, i.e. undergo dipole oscillation.

Neutron spectra from the giant resonance consist of two distinct components: the *evaporation spectrum* and the *direct-emission spectrum*. Evaporation spectra are usually adequately described by a Maxwellian distribution, which dominates the low-neutron energy region, using the following equation (normalized to the unit area):

$$\frac{dN}{dE_n} = \frac{E_n}{T^2} exp\left(-\frac{E_n}{T}\right), \tag{4.16}$$

where T is the nuclear temperature (in units of MeV) characteristic of the particular target nucleus and its excitation energy. With this distribution, the most probable neutron energy is $\hat{E}_n = T$ and the average energy is $\bar{E}_n = 2T$. Evaporation neutrons are emitted almost isotropically. The direct-emission neutrons tend to have a higher energy than evaporation neutrons and may be emitted non-isotropically [148].

4.2.6.1.2. The quasi-deuteron effect

At photon energies above the giant resonance, the dominant neutron production occur due to photon interacting initially with a neutron-proton pair within the nucleus, rather than with the nucleus as a whole [146], therefore the term *quasi-deuteron*. The cross-section for this mechanism is about an order of magnitude lower than the giant-resonance peak. The cross-section is related to the deuteron photodisintegration crosssection $\sigma_D(k)$, qualitatively as [149]:

$$\sigma_{QD}(k) \cong L\frac{NZ}{A}\sigma_D(k), \tag{4.17}$$

where N, A and Z are for the target nucleus ($N + Z = A$), σ_D is the cross-section for deuteron photodisintegration as a function of photon energy k, and the dimensionless coefficient L is in the range 3-13. L may be regarded as a measure of the probability that a neutron-proton pair is within a suitable interaction distance relative to the deuteron[9].

4.2.6.1.3. High-energy neutrons

Above 140 MeV, the cross-section for photons on nuclei rises again, owing to channels for photopion production. At high-energy accelerators, high-energy neutrons dominate the dose outside of the massive concrete shields employed, even though the reverse is true on the inside of the shields where bremsstrahlung and giant-resonance neutrons dominate completely [150].

4.2.6.1.4. Neutron yield from VHE electron beams

Clinical application of very high-energy electron beams requires careful consideration of the dose contribution to the patient from neutrons and induced radioactivity (discussed in 4.2.7). To assess the radiological significance of neutrons produced by VHE electron beams, it is necessary to combine the cross-sections for photoneutron production, which can be taken from the EXFOR data base [151], with a realistic energy spectrum of photons released within tissue equivalent material struck by the electrons. To estimate neutron yields produced inside the patient, in the first approximation, the human body can be modelled as described in section 4.2.1. To evaluate neutron yield in FLUKA customized parameters are set. Neutron fluence inside and around the target (the water phantom) is scored using the USRBIN [110] scoring card. Because of the smaller photo nuclear cross-sections for electromagnetic interactions with atoms and electrons, the interaction length for nuclear inelastic interactions of photons is reduced in water and walls of the tank made of PMMA by a factor 1000 using the LAM-BIAS [110] card.

---

[9] The value of L depends greatly on the assumptions of the analysis used. Values close to 10 take into account details of quasi-deuteron kinematics

For an accurate description of nuclear processes the evaporation model is activated at its maximum accuracy (although it should not be relevant for our application with light targets), because of its minimal computational overhead. Fragments and nuclear recoils are transported in detail, including energy loss, multiple scattering and nuclear interactions. To assure good statistical uncertainty of evaluated neutron yields 1×10^7 initial electrons trajectories are used for the calculation.

The neutron yields (inside and around a water phantom) of VHEEs are calculated and benchmarked for electron beams with energies corresponding to those from a medical LINACs, which are shown in Figure 37.

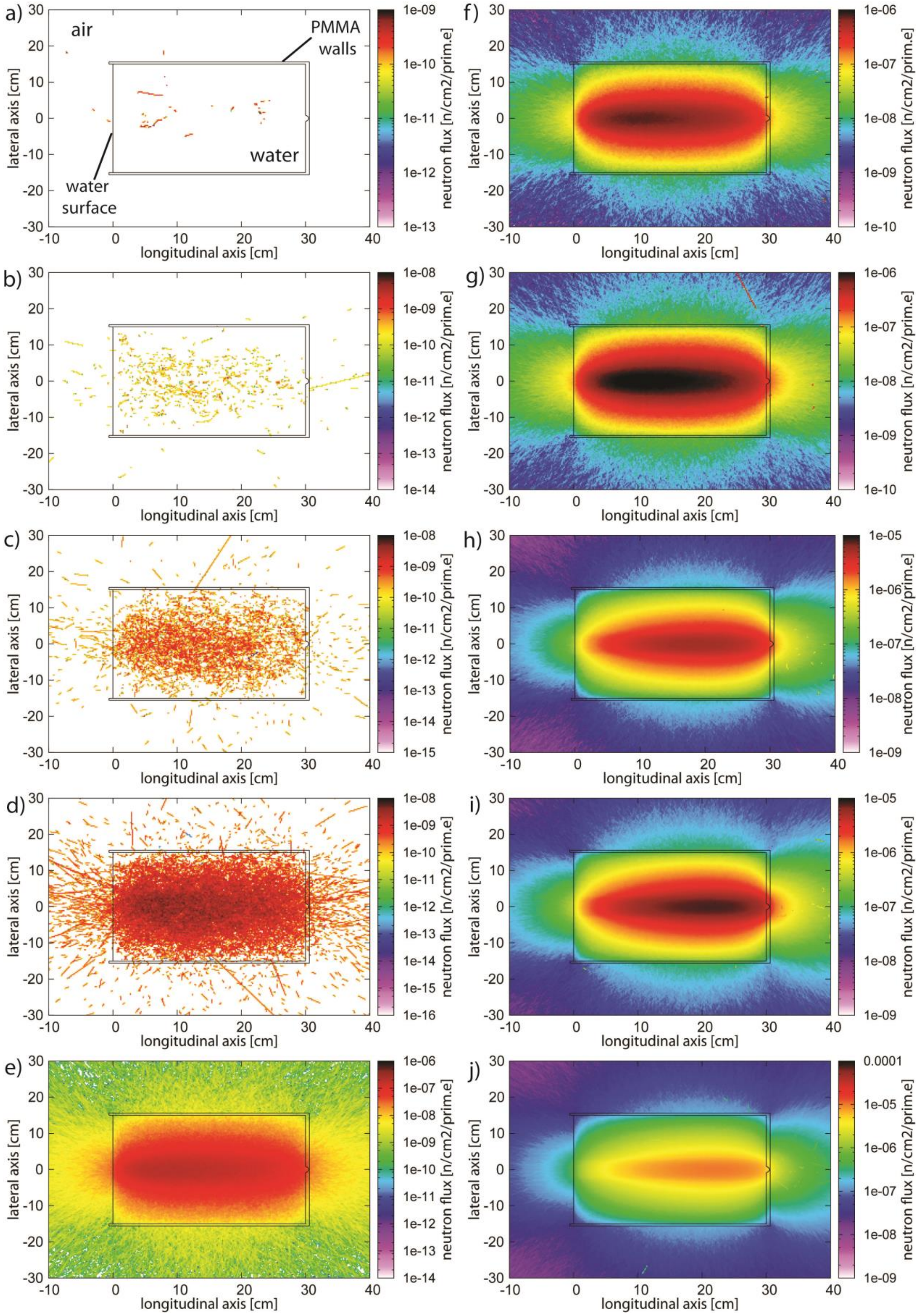

Figure 37. Neutron yield per primary particle for generated in water irradiated with (a) 6MeV, (b) 10 MeV, (c) 15 MeV. (d) 20 MeV, (e)30 MeV, (f) 40 MeV, (g)50 MeV, (h)100 MeV, (i) 150 MeV) and (j) 200 MeV electron beam with 5 × 5 cm^2 field size.

The main channels of neutron production in a target for very high electron energies are (*γ,n*), (*γ,p*), (*γ,2n*) and (*γ,pn*) reactions. Considering the bremsstrahlung spectrum of photons generated in water by VHEEs (shown in Figure 35), we can select two regions of photon energy with respect to mechanisms of neutron production. The first is the region of a giant dipole resonance phenomenon (described in 4.2.6.1.1) and second one is the region of energies above the giant resonance (described in 4.2.6.1.2 and 4.2.6.1.3).

The field of giant dipole resonance begins above the threshold of the (γ,n) reaction, which is approximately equal to the binding energy of a nucleon. A photon wavelength, with an energy less than 30 MeV exceeds the size of nucleus [147]. Above the giant resonance, the nuclei–nuclei shower is initiated in the nucleus prior to evaporation of neutrons by interactions of photons with nuclear clusters. This channel of neutron production is important for high-atomic-number materials, which is not discussed in this work. The yield of neutrons increases as the upper limit of the bremsstrahlung spectrum increases. Other photo-nuclear reactions in the energy region under consideration are (*γ,p*), (*γ,2n***)** and (*γ,pn*) [146].

The neutron yield for electron energies below 15 MeV (Figure 37 (a)-(c)), electron energies most commonly used for treatment of the superficial tumours, is less than 10^{-9} neutrons/(cm^2·primary electron), which gives a negligible additional dose. The neutron fluence distribution in and around the target for a 20 MeV and 30 MeV incident electron beam (Figure 42 (d) and (e)) clearly shows that the neutron distribution is isotropic [152]. This is due to the dominance of the giant dipole resonance, as described in section 4.2.6.1.1. Neutrons emitted as a consequence of the giant dipole resonance mechanism are similar (analogous) to an evaporation of neutrons from a compound nucleus. The deviation from this behaviour for the 100 MeV and above (Figure 37 (f)-(j)) is due to the anisotropic emission of neutrons from the other two processes (i.e. the quasi-deuteron effect and high energy neutron generation). The neutron yield for VHEEs has been evaluated as 10^{-4} neutrons/(cm^2·primary electron) inside the water phantom around the position of the maximum dose delivered and approximately 10^{-7} neutrons/(cm^2·primary electron) 10 cm downstream from the exit wall of the tank.

Even though the calculated neutron fluence due to irradiation with VHEEs has a minor effect on dose deposition, it should be noted that neutrons are also generated in accelerator components (jaws, flattening filters etc.), therefore before commissioning very high energy electron source as a radiotherapy accelerator the neutron yields needs to be evaluated for detailed construction of a machine.

4.2.7. Induced radioactivity

Radioactivity may be induced following irradiation by an electron or bremsstrahlung beam, to an extent that depends on the energy, beam flux and type of material. Some activity is probable at energies above about 10 MeV. Precise thresholds for various reactions can be found in [153]. Three types of photon-induced reactions, already described in section 4.2.6.1, produce most of the activity.

In the clinical accelerators the components to be most suspected for activation are those that absorb most of the bremsstrahlung energy, in particular: beam dumps, targets, collimators and jaws and filters. Therefore, very detailed calculations and analysis ought to be done before VHE electron beams are introduced to clinics.

In addition, significant activity may be induced by secondary neutrons if the beam power is high enough to release large neutron fluences. The subject of induced activity has been extensively treated by Barbier [154], and a shorter review of the subject has been published by Gollon [155].

The overall quantity of radioactivity induced in an accelerator depends on the primary beam loss (power), whereas the probability of producing a particular isotope depends essentially on the composition of the material struck and the cross section of the isotope.

Activation is a two-step process. The first step is a nuclear reaction that leaves the target nucleus in an excited state, and the second step is nuclear decay.

Induced activity in air and water

Activation starts to be of concern if the accelerator energy E_0 exceeds the production threshold (10.55 MeV in air, 15.67 MeV in water), therefore for VHEEs induced activity needs to be considered.

Radioactive gases are produced by the interaction of bremsstrahlung with air nuclei whenever the accelerator operates above 10.55 MeV the production threshold. Furthermore, an electron beam without bremsstrahlung will not cause significant air activation because the nuclear cross-sections of electrons are smaller by about two orders of magnitude than those of photons.

Such airborne activity is in general short-lived, and even if produced in significant amounts, dilution and radioactive decay quickly reduce the concentrations to moderate levels. Only in very unusual circumstances would exposure to radioactive air be a limiting factor for personnel access to a containment area. The limiting factor is almost always external exposure from components therefore, in this work air activation is not studied.

Radioactivity in water is formed by the interaction of bremsstrahlung with the ^{16}O component of water. The dominant radionuclides in the activation of water are identified as $^{11}_{6}C$ (22.3 minute half-life) and $^{15}_{8}O$ (122.4 s half-life). The primary channel of radioisotope production is (γ,n) reaction, which is dominant in previously described giant dipole resonance (section 4.2.6.1.1). For example, $^{15}_{8}O$ radioisotope is generated via following channel: $^{16}O(\gamma,n)^{15}O$. The energy threshold for this reaction is 15.7 MeV. In the energy range above the giant dipole resonance the (γ,p), (γ,pn) and numtineutron (γ,xn) reactions occur, which can lead to generation of $^{11}_{6}C$ radioisotope. Subsequent $^{15}O(\gamma,p)^{14}N$, $^{14}N(\gamma,np)^{13}C$, $^{13}C(\gamma,n)^{12}C$ and $^{12}C(\gamma,n)^{11}C$ reactions are responsible for creation of $^{11}_{6}C$ radioisitope.

The activation formula

The formula to calculate the activity of a target bombarded by a given particle flux. The number of target atoms per gram of target material is given by: $N_t = N_A/A_t$, where N_A is Avogadro’s number and A_t is the atomic weight of the target material.

Using the definition of cross section, the number of radioactive nuclei, n_i, of the i^{th} isotope per gram of target material produced per unit time is given by:

$$n_i = \Phi \frac{N_A}{A_t} \sigma_t^i, \tag{4.18}$$

where Φ is the incident fluence rate, defined as the number of particles incident on the target per cm^2 and per s, σ_t^i is the cross section for the production of the i^{th} isotope (cm^2).

The number of nuclei of the i^{th} isotope at any time is the result of two competing mechanisms, the production of these nuclei, given by equation (4.18) and their decay, due to their unstable nature. The decay law is given by:

$$n_i(t) = n_i(0)exp\left(-\frac{t}{\lambda_i}\right). \tag{4.19}$$

Using equations (4.18) and (4.19), the number of nuclei of the i^{th} isotope at a given time t during the irradiation time is given by:

$$n_i(t) = \Phi \frac{N_A}{A_t} \sigma_t^i \int_0^t \exp\left(-\frac{t-\tau}{\lambda_i}\right) d\tau = \Phi \frac{N_A}{A_t} \sigma_t^i \lambda_i \left(1 - e^{-\frac{t}{\lambda_i}}\right), \tag{4.20}$$

where λ_i is the decay constant of the i^{th} isotope and τ is the isotope half-life multiplied by ln(2).

At the end of an irradiation period of duration T_{irr}, after a cooling time $T_{cool,}$ the number of nuclei of the i^{th} isotope will therefore be given by

$$n_i(T_{irr}T_{cool}) = \Phi \frac{N_A}{A_t} \sigma_t^i \lambda_i \left(1 - e^{-\frac{T_{irr}}{\lambda_i}}\right) e^{-\frac{T_{cool}}{\lambda_i}}. \tag{4.21}$$

The activity a_i of the i^{th} isotope, per gram of target material, is given by:

$$a_i(T_{irr}T_{cool}) = -\frac{dn_i}{dt}(T_{irr}T_{cool}) = \frac{n_i(T_{irr}T_{cool})}{\lambda_i}. \tag{4.22}$$

Using equation on (4.21) we finally obtain:

$$a_i(T_{irr}T_{cool}) = \Phi \frac{N_A}{A_t} \sigma_t^i \left(1 - e^{-\frac{T_{irr}}{\lambda_i}}\right) e^{-\frac{T_{cool}}{\lambda_i}}. \tag{4.23}$$

4.2.7.1. Radionuclide production

To evaluate the induced activity due to radionuclide production FLUKA simulations are performed. The generation and transport of decay radiation in FLUKA (so far limited to γ, β-, and β+ emissions) producing radionuclides is carried out in one-step. A dedicated database of decay emissions is available in FLUKA, using mostly information obtained from NNDC (National Nuclear Data Centre) data [156].

To evaluate activation in the water phantom an additional model of water diffusion in time should be considered. For the calculation, the two 2 mm layers, of striated muscle defined according to ICRU Report 37 [157], with a density of 1.04 g/cm^3, are modelled at 1 and 10 depth. The rest of the set-up is assembled according to the description in section 4.2.1.

For the calculations presented in this work, the RADDECAY card is set to simulate decay of produced radioactive nuclides. FLUKA gives large flexibility in defining the irradiation profile (i.e. beam intensities and irradiation times) and score quantities with different cooling times. Therefore, the IRRPROFI is set to deliver $5{\cdot}10^{11}$ electrons in 1 s interval with 5 × 5 cm^2 field size. DCYTIMES and DCYSCORE cards are assembled to define the decay (cooling times) and associate detectors with particular cooling times (i.e. 1 min, 5 min, 10 min, 20 min, 45 min, 1 h, 2 h and 24 h).

Table 5. Activation in 2 mm thick layer of skeletal muscle positioned at 1 cm and 10 cm depth in the water irradiate with 50 MeV, 100 MeV, 150 MeV and 200 MeV electron beam calculated for various cooling times.

depth [cm]	**Beam energy** (Dose deposited)	radionuclide activity after 1 min [Bq(%)]		radionuclide activity after 5 min [Bq(%)]		radionuclide activity after 10 min [Bq(%)]		radionuclide activity after 20 min [Bq(%)]	
		$^{11}_{6}C$	$^{15}_{8}O$	$^{11}_{6}C$	$^{15}_{8}O$	$^{11}_{6}C$	$^{15}_{8}O$	$^{11}_{6}C$	$^{15}_{8}O$
1.0	**50 MeV** (5.7 Gy)	3.17 (5.5)	53.2 (91.8)	2.77 (16.0)	13.6 (79.0)	2.34 (44.6)	2.49 (47.5)	1.66 (86.7)	0.08 (4.3)
	100 MeV (6 Gy)	5.08 (6.6)	69.4 (90.8)	4.43 (19.3)	17.8 (77.4)	3.74 (50.8)	3.25 (44.1)	2.66 (91.3)	0.13 (4.5)
	150 MeV (6.2 Gy)	6.4 (7.0)	81.7 (89.0)	5.58 (20.0)	20.9 (74.9)	4.71 (50.71)	3.82 (41.2)	3.97 (77.3)	0.70 (13.6)
	200 MeV (6.3 Gy)	6.77 (7.1)	85.42 (88.8)	5.91 (20.0)	21.9 (74)	4.99 (50.7)	4.00 (40.6)	3.55 (88.1)	0.13 (3.3)
10.0	**50 MeV** (5 Gy)	7.89 (4.5)	162 (91.9)	6.89 (13.5)	41.5 (81.5)	5.81 (42.3)	7.57 (51.2)	4.14 (86.0)	0.25 (5.25)
	100 MeV (6.4 Gy)	23.8 (6.0)	360 (90.2)	20.7 (17.4)	92.2 (77.4)	17.5 (46.8)	16.8 (45.0)	12.5 (87.2)	0.56 (3.9)
	150 MeV (6.8 Gy)	32.9 (6.71)	436 (88.8)	28.7 (19.34)	112 (75.2)	24.2 (49.9)	20.4 (41.9)	17.3 (88.4)	0.68 (3.5)
	200 MeV (7.1 Gy)	35.3 (6.45)	486 (88.7)	30.8 (18.7)	125 (75.6)	26.0 (48.9)	22.7 (42.1)	18.5 (86.5)	0.76 (3.5)

depth [cm]	**Beam energy** (Dose delivered)	radionuclide activity after 45 min [Bq(%)]		radionuclide activity after 1 h [Bq(%)]		radionuclide activity after 2 h [Bq(%)]		radionuclide activity after 24 h [Bq(%)]	
		$^{11}_{6}C$	$^{15}_{8}O$	$^{11}_{6}C$	$^{15}_{8}O$	$^{11}_{6}C$	$^{15}_{8}O$	$^{11}_{6}C$	$^{7}_{4}Be$
1.0	**50 MeV** (5.7 Gy)	0.84 (95.3)	--	0.43 (97.6)	--	0.06 (99.3)	--	--	$1.8{\cdot}10^{-4}$ (85.0)
	100 MeV (6 Gy)	1.35 (97.5)	--	0.68 (98.7)	--	0.09 (99.4)	--	--	$3.6{\cdot}10^{-4}$ (81.1)
	150 MeV (6.2 Gy)	1.7 (95.7)	--	0.86 (97.7)	--	0.11 (98.2)	--	--	$5{\cdot}10^{-4}$ (81.0)
	200 MeV (6.3 Gy)	1.8 (95.4)	--	0.91 (97.3)	--	0.12 (96.5)	--	--	$6{\cdot}10^{-4}$ (85.9)
10.0	**50 MeV** (5 Gy)	2.10 (95.5)	--	1.06 (97.7)	--	0.14 (99.2)	--	--	$2.7{\cdot}10^{-4}$ (71.0)
	100 MeV (6.4 Gy)	6.31 (95.3)	--	3.20 (97.4)	--	0.42 (97.7)	--	--	$1.5{\cdot}10^{-3}$ (80.9)
	150 MeV (6.8 Gy)	8.74 (96.8)	--	4.43 (97.8)	--	0.58 (98.7)	--	--	$3{\cdot}10^{-3}$ (79.9)
	200 MeV (7.1 Gy)	9.38 (94.6)	--	4.75 (97.0)	--	0.62 (97.6)	--	--	$3{\cdot}10^{-3}$ (80.0)

The activity is scored in two layers made of skeletal muscle at a depth of 1 and 10 cm. The calculations have been carried out for 50 MeV, 100 MeV, 150 MeV and 200 MeV incident monoenergetic electron beams with irradiation parameters defined above. The activity in absolute terms (Bq) has been given for the whole volume of the skeletal muscle. The resulting radionuclide production and their evolution in time due to their decays has been calculated for two different positions in the water bath. Activity in the skeletal muscle is evaluated (in absolute and relative terms) and the results are summarized in Table 5.

For each case the electron beam has the same geometrical size and is constituted of the same number of particles, i.e. $5 \cdot 10^{11}$ electrons delivered in 1 s. The dose deposition for each of the energy ranges varies (section 4.2.4), therefore the total dose deposited in the skeletal muscle detectors varies with its position in water and beam energy. Generally, for all cases the dose delivered to the detector is around 6 and 7 Gy (the exact doses delivered are presented in Table 5), which is an average dose delivered daily to the tumour per fraction in radiotherapy for palliative therapy or in cases with bone metastases. Typically, the daily dose for a cancer patient undergoing radiation therapy is 1.5 - 3.3 Gy, depending on the cancer type and its grade [158]. For doses up to 3 Gy the activation levels considered in this studies would be considerably lower.

For both positions of the skeletal muscle detector 1 minute after the beam irradiation ceased, the activation is determined mainly by ${}^{11}_{6}C$ (22.3 minute half-life) and ${}^{15}_{8}O$ (122.4 s half-life) radionuclides. The ${}^{15}_{8}O$ radionuclide is produced most abundantly, but decays quickly and after 20 min of cooling it has negligible effect on the total activation.

It is generally agreed that ^{11}C is the dominant radionuclide 1-5 hours after irradiation [159]. We observe that the residual activity 24 hours post irradiation is mainly due to activity of ${}^{7}_{4}Be$, and is negligible.

The total activity of the skeletal muscle detector expressed in absolute terms is summarized in Table 6. The total induced activity (summed for all induced radionuclides) is larger in the detector placed deeper. The majority of the radionuclides are located at the centre of the water phantom and slightly shifted to the downstream surface for the higher energies where the majority of (γ,n) reactions occur, therefore the scored activation is higher at 10 cm than at 1 cm depth. The maximum yield of radionuclide production in the tank can be easily identified in Figure 37 (g-j), where the maximum neutron yield corresponds to the position where the highest activity will be induced.

Table 6. The total induced activity in the skeletal muscle detector for various cooling times.

Beam energy	cooling time	activity at 1 cm depth	activity at 10 cm depth
50 MeV	1 min	58.0 Bq	176.0 Bq
	5 min	17.3 Bq	50.9 Bq
	10 min	5.2 Bq	14.5 Bq
	20 min	1.9 Bq	4.8 Bq
	45 min	0.9 Bq	2.2 Bq
	1 h	0.4 Bq	1.1 Bq
	2 h	0.06 Bq	0.1 Bq
	24 h	$2\cdot10^{-4}$ Bq	$3.8\cdot10^{-4}$ Bq
100 MeV	1 min	76.5 Bq	398.7 Bq
	5 min	23.0 Bq	119.1 Bq
	10 min	7.4 Bq	37.4 Bq
	20 min	2.9 Bq	14.3 Bq
	45 min	1.4 Bq	6.6 Bq
	1 h	0.7 Bq	3.3 Bq
	2 h	0.09 Bq	0.4 Bq
	24 h	$4.5\cdot10^{-4}$ Bq	$1.9\cdot10^{-3}$ Bq
150 MeV	1 min	91.8 Bq	490.3 Bq
	5 min	28.0 Bq	148.5 Bq
	10 min	9.3 Bq	48.6 Bq
	20 min	3.8 Bq	19.5 Bq
	45 min	1.8 Bq	9.1 Bq
	1 h	0.9 Bq	4.5 Bq
	2 h	0.1 Bq	0.6 Bq
	24 h	$6.5\cdot10^{-4}$ Bq	$2.7\cdot10^{-3}$ Bq
200 MeV	1 min	98.2 Bq	547.5 Bq
	5 min	29.6 Bq	164.9 Bq
	10 min	9.8 Bq	27.2 Bq
	20 min	4.3 Bq	21.4 Bq
	45 min	1.9 Bq	9.9 Bq
	1 h	0.9 Bq	4.9 Bq
	2 h	0.1 Bq	0.6 Bq
	24 h	$7.0\cdot10^{-4}$ Bq	$3.7\cdot10^{-3}$ Bq

Summarising, irradiation with VHEE beams yields induced radioactivity. The dominant radionuclides in the activation of tissue equivalent material are identified as $^{11}_{6}C$ (22.3 minute half-life) and $^{15}_{8}O$ (122.4 s half-life). These radionuclides have a short lifetime and after 30 minutes following irradiation the residual activity is negligible. Therefore, there are no major safety issues for tissue irradiation with VHEEs. However, in clinical scenario much more complex system will be used. Beam dumps, collimators or filters (made of high-Z materials) are inherent part of the radiotherapy unit, therefore for a clinical applications a detailed analysis of activation of the accelerator's components should be performed. This aspects would require much deeper analysis which is out of scope of this work.

4.2.8. Dose equivalent

In this section the methodology of calculating the conversion coefficient, i.e. fluence-to-ambient dose equivalent, for radiological protection, using FLUKA is presented.

There are two types of quantities specifically defined for use in radiological protection. *Protection quantities*[10], defined by the International Commission on Radiological Protection (ICRP), are used to assess the exposure limits to ionising radiation. The *operational quantities*, defined by the International Commission on Radiation Units and Measurements (ICRU), are intended for monitoring of external exposure. Operational quantities are dose quantities defined for use in radiation protection measurements for external exposure (area or individual monitoring). They provide an estimate of the upper limit for exposure. Operational quantities are needed for monitoring external exposures because protection quantities are generally not measurable.

ICRP (ICRP Publication 74 [160]) and ICRU (ICRU Report 57 [161]) recommended conversion coefficients for use in radiological protection for electrons and photons of energies up to 10 MeV, and for neutrons up to 180 MeV. However, the data for conversion coefficients for higher energies and other kinds of radiation (including VHEEs) were not previously available. Therefore, in recent years these vaules have been calculated with the FLUKA MC code and currently the fluence-to-ambient dose equivalent conversion coefficients for all kind of radiation (photons, electrons, positrons, protons, neutrons, muons, charged pions and kaons) and for incident energies (up to 10 TeV) are available [162-170].

Protection quantities

---

[10] These quantities are established for the limitation of stochastic effects, i.e. secondary cancer induction and hereditary effects due to exposure to ionizing radiation. Protection quantities take account of human body properties.

The methodology of calculation of conversion coefficient in FLUKA is based on the set of protection quantities [171]. They include the tissue or organ equivalent doses (H_T) and the effective dose (E). The equivalent dose H_T in a tissue or organ T is given by:

$$H_T = \sum_R \left(w_R \cdot D_{T,R} \right), \tag{4.24}$$

where $D_{T,R}$ is the average absorbed radiation dose R, in tissue T, w_R is the radiation weighting factor for radiation R and the sum is performed over all types of radiation that constitute the radiation field being considered. Table 7 gives the values of radiation weighting factors as recommended by the ICRP.

Table 7. Values for radiation weighting factors recommended in ICRP Publication 60 [171]

RADIATION	w_R
Photons	1
Electrons and muons	1
Neutrons:	
E < 10 keV	5
10 keV < E < 100 keV	10
100 keV < E < 2 MeV	20
2 MeV < E < 20 MeV	10
E > 20 MeV	5
Protons, other than recoil protons (E > 2 MeV)	5
α particles, fission fragments, heavy nuclei	20

For radiation types and energies that are not included in Table 7 an approximation to w_R factor is calculated using the average quality factor, $\bar{Q}$, at a depth of 10 mm in ICRU sphere[11] [172]:

$$\bar{Q} = \frac{1}{D} \int_L^\infty Q(L) \cdot D(L) \cdot dL, \tag{4.25}$$

where $D(L)dL$ is the absorbed dose at 10 mm between linear energy transfer values of L and $L + dL$, and $Q(L)$ is the corresponding quality factor[12]. The relation between Q and L (originally recommended by the ICRP 60, but in 2007 superseded by ICRP 103) is shown in Table 8.

---

[11] A sphere of 30 cm diameter made of tissue equivalent material with a density of 1 g/cm^3 and a mass composition of 76.2% oxygen, 11.1% carbon, 10.1% hydrogen and 2.6% nitrogen specified by ICRU

[12] Is a radiation quantity defined by ICRP 60. Q(L) depends on unrestricted LET, therefore it takes into account the differences in effects of different types of radiation.

Table 8. Relation between L in water and the quality factor Q, as recommended by ICRP Publication 103 [173].

LET in water [keV/μm]	Q(L)*
<10	1
10-100	$0.32 \cdot (L) - 2.2$
>100	$300 \cdot (L)^{-1/2}$

Another important quantity in radiotherapy is the effective dose, E, defined as the sum of the weighted equivalent doses in all the tissues and organs of the body, which is given by:

$$E = \sum_T w_T \cdot H_T, \tag{4.26}$$

where H_T is the equivalent dose in tissue or organ T, w_T is the weighting factor for tissue T and the sum is performed on all tissue and organs involved in irradiation. Table 9 gives the values of tissue weighting factors as recommended by the ICRP.

Table 9. Tissue weighting factors recommended in the ICRP Publication 60 [171].

TISSUE or ORGAN	w_T
Gonads	0.20
Red bone marrow, Colon, Lung, Stomach	0.12
Bladder, Breast, Liver, Oesophagus, Thyroid	0.05
Bone surface, Skin	0.01
Remainder	0.05

Calculations of effective dose in FLUKA for clinical radiation sources is based on equation (4.26) using the radiation weighting factors shown in Table 7. However, for unconventional sources, such as VHEEs, the approximation given by equation (4.25) is used.

Operational quantities

The protection quantities are not directly measurable [174], but may be inferred from calculation of the radiation field if the conditions of irradiation are known. The only way to estimate H_T and E is to measure the radiation field outside the body and convert it to H_T and E using previously calculated conversion coefficients.

The mean absorbed dose $D_{T,R}$ is a quantity that cannot be evaluated experimentally, therefore operational quantities [175] (defined in terms of the quality factor Q) should be used. Operational quantities are more stable than protection quantities, because the tissue weighting factor does not appear in their definitions. The operational quantities are intended to provide a reasonable estimate of the protection quantities, the goal is that the value of the appropriate protection quantity is less than that of the corresponding operational quantity. For strongly penetrating radiation (as for VHEEs) the appropriate operational quantity for area monitoring is the ambient dose equivalent. The ambient dose equivalent $H^*(d)$ at a point in a radiation field is the dose equivalent that would be produced by the corresponding expanded and aligned field in the ICRU sphere at a depth d, on the radius opposing the direction of the aligned field. The recommended value of d for penetrating radiation is 10 mm. The dose equivalent at other depths may be considered when the dose equivalent at 10 mm provides an unacceptable underestimate of the effective dose.

The ambient dose equivalent calculated with FLUKA is given by:

$$H^* = \int f_{H*}(\varepsilon) \cdot \Phi(\varepsilon) \cdot d\varepsilon, \tag{4.27}$$

where $\Phi(\varepsilon)$ is the fluence (in cm^{-2}) of primary particle of energy ε and $f_{H*}(\varepsilon)$ are the fluence-to-ambient dose equivalent conversion coefficients that can be found in [176].

4.2.8.1. Setup to determine the equivalent dose rates using MC simulation in FLUKA

Ambient dose equivalent H*(10) from residual activity produced in the film by a very high energy electron beam has been calculated using ICRP 74 data AMB74 [176]. AMB74 model adopts ICRP 74 [176, 177] data and contains conversion coefficients for protons, neutrons, charged pions, muons, photons and electrons. For calculating the doses equivalent, equation (4.27) has been used. The IRRPROFI and DCYTIMES cards have been used in FLUKA to define irradiation profile and cooling times. Beam properties used in these calculations have been described in section 4.2.7.1.

The USRBIN card has been used to score the distribution of the dose equivalent (DOSE-EQ) quantity by multiplying the dose by a LET-dependent quality factor and AUXSCORE card to associate this scoring estimator with dose equivalent conversion factors. The calculated equivalent doses has been associated with different cooling times by the DCYTIMES card, therefore the evaluated output quantity is a dose equivalent rate determined in pSv/s. The dose equivalent rates are scored for 50 MeV, 100 MeV, 150 MeV and 200 MeV monoenergetic electron beams and the 2D evolution for different cooling times are shown in Figure 38 - Figure 41.

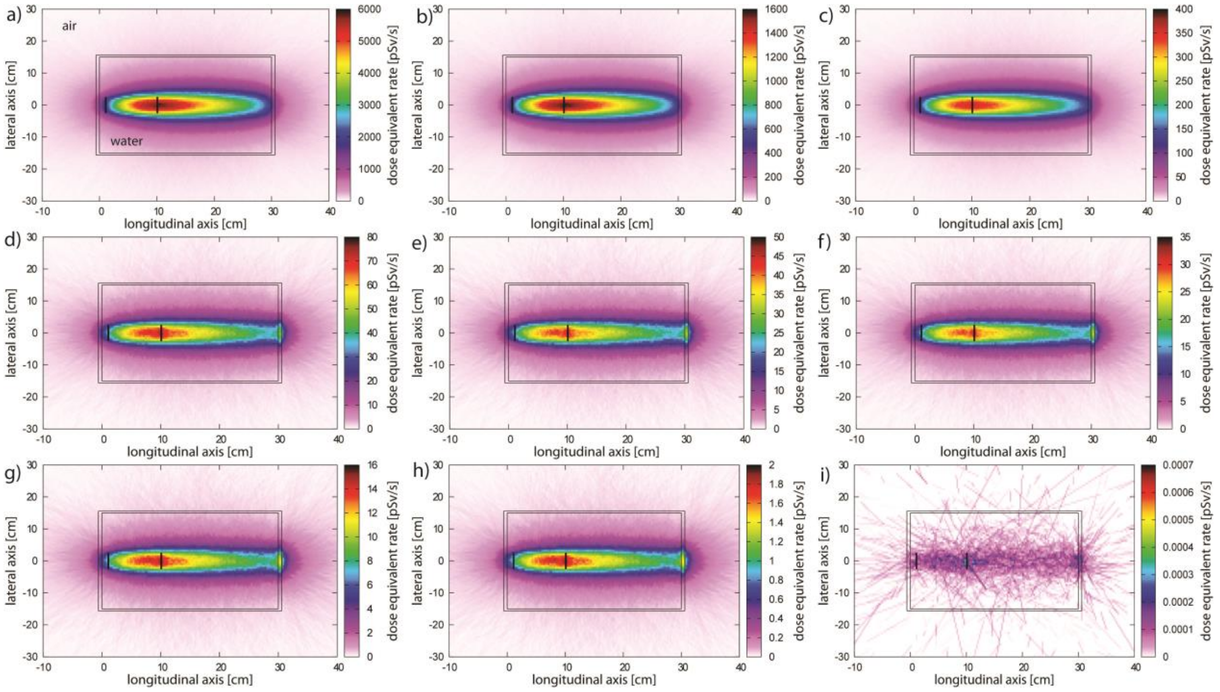

Figure 38. Ambient dose equivalent rate for irradiation with 50 MeV electron beam from induced radioactivity after (a) 1 min, (b) 5 min, (c) 10 min, (d) 20 min, (e) 30 min, (f) 45 min, (g) 1h, (h) 2h, (i) 24 h cooling time. The beam enters from the left hand side.

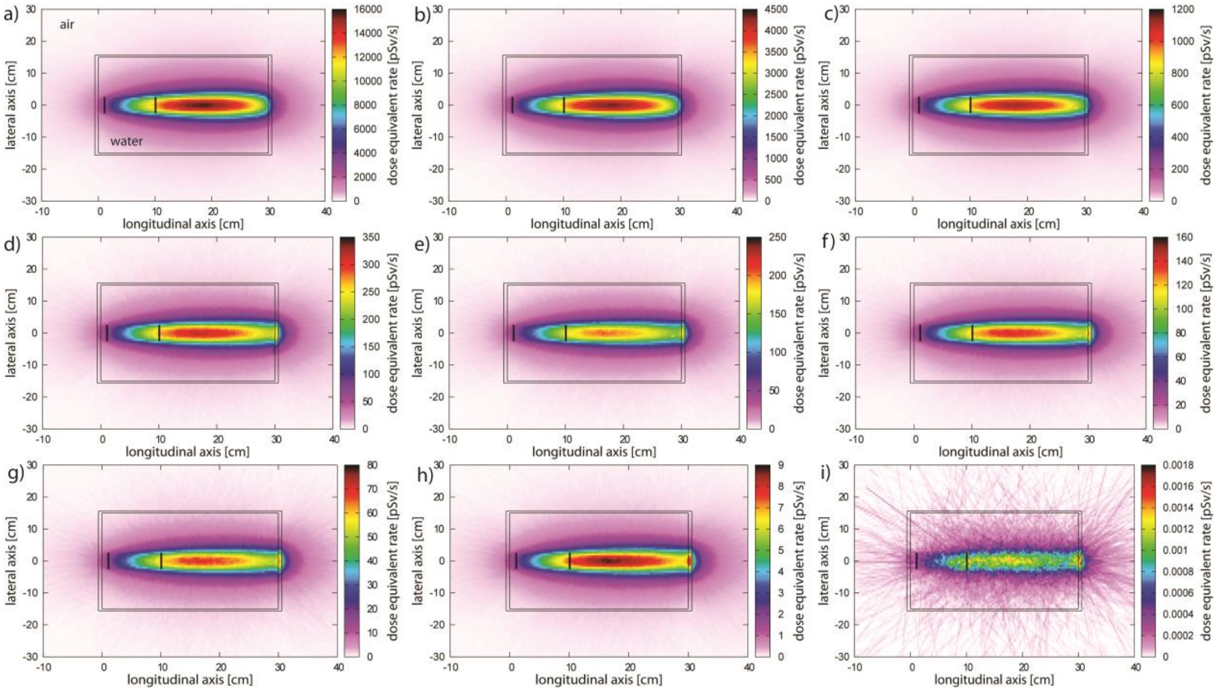

Figure 39. Ambient dose equivalent rate for irradiation with 100 MeV electron beam from induced

radioactivity after (a) 1 min, (b) 5 min, (c) 10 min, (d) 20 min, (e) 30 min, (f) 45 min, (g) 1h, (h) 2h, (i) 24 h cooling time. The beam enters from the left hand side.

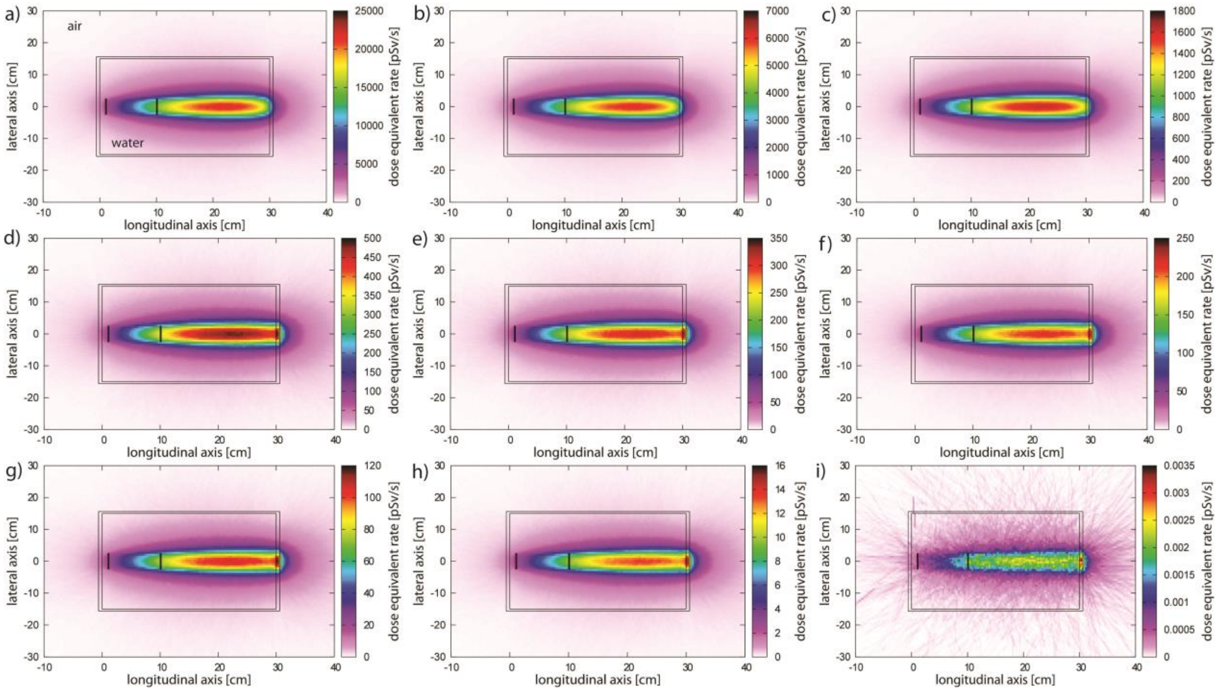

Figure 40. Ambient dose equivalent rate for irradiation with 150 MeV electron beam from induced radioactivity after (a) 1 min, (b) 5 min, (c) 10 min, (d) 20 min, (e) 30 min, (f) 45 min, (g) 1h, (h) 2h, (i) 24 h cooling time. The beam enters from the left hand side.

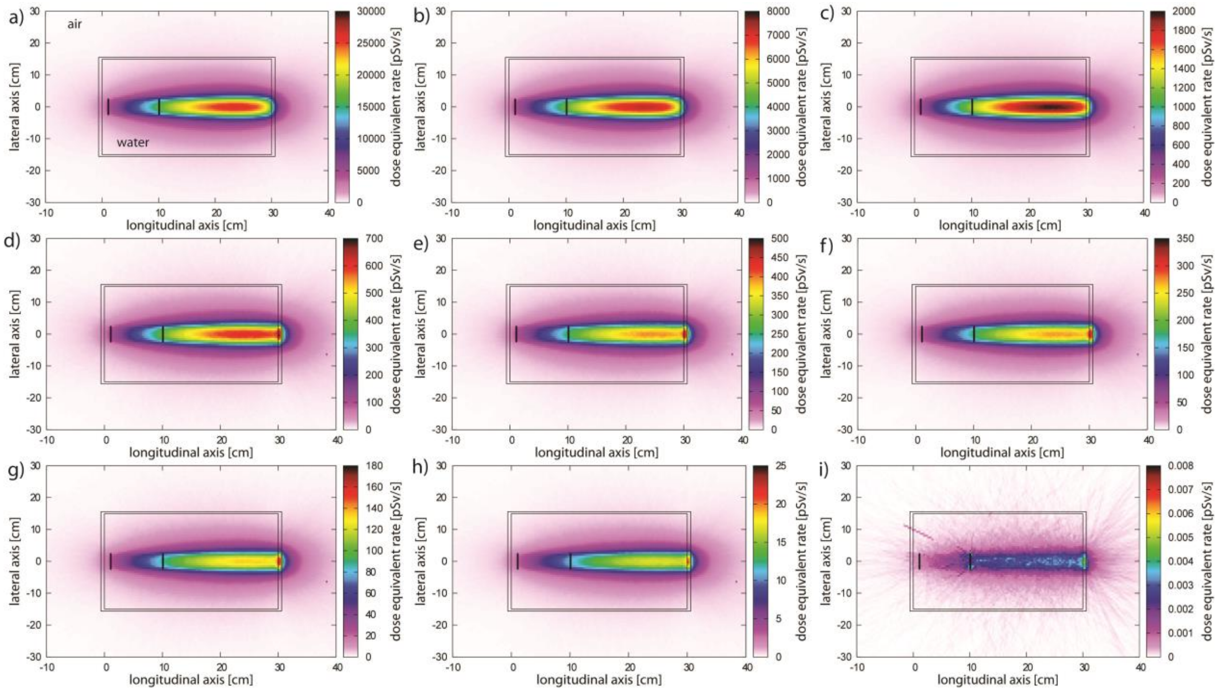

Figure 41. Ambient dose equivalent rate for irradiation with 200 MeV electron beam from induced radioactivity after (a) 1 min, (b) 5 min, (c) 10 min, (d) 20 min, (e) 30 min, (f) 45 min, (g) 1h, (h) 2h, (i) 24 h cooling time. The beam enters from the left hand side

The dose equivalents decay times are inherently connected with induced activity due to radionuclides production, as discussed in the previous section (4.2.7). We observe higher equivalent doses for higher energies, which is a consequence of higher media activation. Even for highest dose equivalent yields obtained (here, for 200 MeV) the scored quantity is small. For example, 1 minute after irradiation with 200 MeV has ceased, the dose equivalent rate at a depth of 25 cm in water is 30 nSv/s, which keeps decreasing with time. Therefore, it can be concluded that neutron production due to irradiation of VHEEs does not significantly affect the equivalent doses.

Even though the evaluated quantities for VHEEs (neutron yield, induced activity and equivalent doses) are low, in the future more detailed radiobiological analysis is required to predict if radiotherapy with VHEEs has undesirable effects the on patient’s health, such as increased probability of inducing secondary cancers. No such analysis has been carried out, but from studies on proton beams the necessity to investigate the possibility of inducing negative outcomes of VHEE therapy should become apparent. For example, even though Paganetti [178] states that secondary fragments are not important in proton therapy, Moskvin *et. al* [179] have provided the evidence of the role of secondary fragments (i.e. induced radioactivity) in the skin reaction and risks of secondary cancer. Table 10 shows the dose equivalent rates at the front and rear surfaces of the water. As mentioned in section 4.2.7, the dose delivered in that example is much larger than a patient would receive in a single radiotherapy session, therefore the values of the quantities evaluated here (activation and dose equivalents) may be higher than would appear in prescribed radiotherapy treatment. Nevertheless, it is necessary to keep in mind that a full radiotherapy treatment consists of several (20 or more) radiation fractions repeated regularly over several weeks, therefore the actual effect of irradiation with VHEEs accumulated over entire radiotherapy treatment could induce secondary cancers.

Table 10. H*(10) values at the front and the rear surface of the water phantom for various cooling times for irradiation with 50 MeV, 100 MeV, 150 MeV and 200 MeV.

cooling time		**dose eq. rate at the front surface [pSv/s]**				**dose eq. rate at the rare surface [pSv/s]**			
	energy	***50 MeV***	***100 MeV***	***150 MeV***	***200 MeV***	***50 MeV***	***100 MeV***	***150 MeV***	***200 MeV***
1 min		847.3	1393.2	1591.7	1757.6	1049.1	4254.8	6894.5	8662.9
5 min		236.1	396.0	454.2	493.6	301.5	1262.9	2076.1	2616.3
10 min		60.8	111.9	129.3	142.1	86.0	399.4	684.9	885.1
20 min		16.8	37.0	43.2	48.8	29.2	157.0	283.2	376.6
30 min		10.8	24.3	28.3	32.1	19.4	105.9	191.8	255.4
45 min		7.5	16.9	19.7	22.3	13.6	74.4	134.7	179.3
1 h		3.7	8.4	9.7	11.0	6.8	37.4	67.3	89.5
2 h		0.5	1.1	1.2	1.4	0.9	4.8	8.6	11.5
24 h		$6.4\cdot10^{-5}$	$2.5\cdot10^{-4}$	$1.9\cdot10^{-4}$	$3.0\cdot10^{-4}$	$1.1\cdot10^{-4}$	$7.2\cdot10^{-4}$	$1.9\cdot10^{-3}$	$2.4\cdot10^{-3}$

4.2.9. Linear Energy Transfer

4.2.9.1.1. LET and track structure

Ionization, one of the pathways of energy deposition by VHEEs, is the excitations of electrons, which, if given enough kinetic energy, are ejected from their atoms. If the electrons are sufficiently energetic, they will, in turn, cause further ionization. These energetic secondary electrons (delta rays) form a characteristic track structure as they are ejected from the path of the primary particle. Their kinetic energy is usually very low: the most probable energy loss in individual collisions is of the order of 20 eV, and in light elements, 80% of the collisions cause losses lower than 100 eV [180]. As part of that energy is lost overcoming the binding energy, most delta electrons have a kinetic energy of only a few eV. Note that a 10 keV electron of has a range of only a 2.5 μm in water [119]. Continuous slowing down approximation (CSDA) range of electron in water is shown in Figure 42.

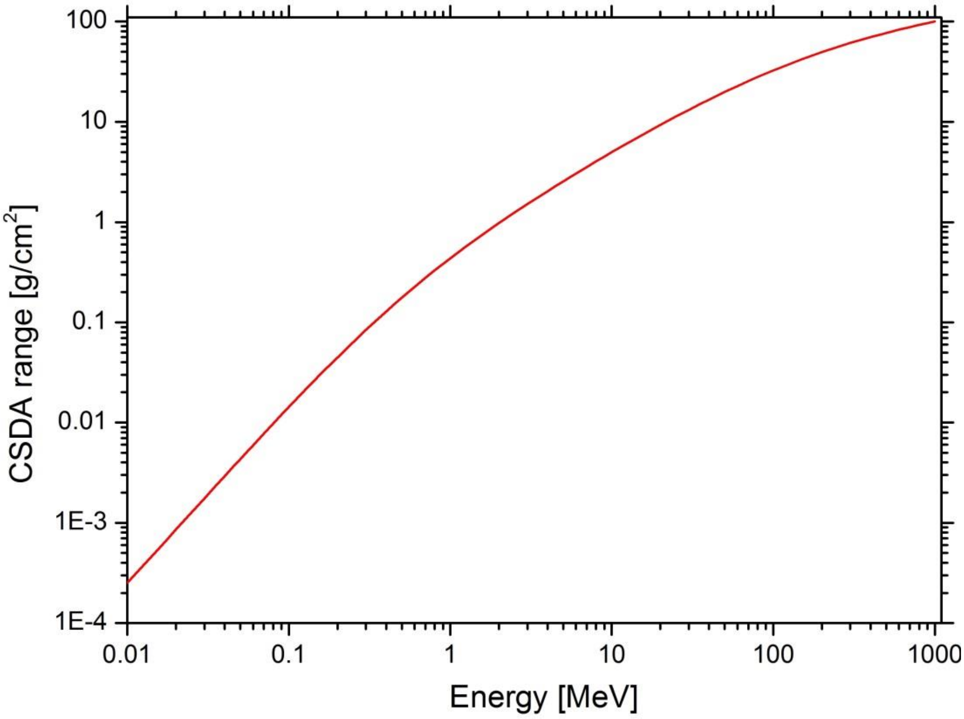

Figure 42. CSDA range of electrons in water [119].

Only a few delta electrons have sufficient kinetic energy to travel a non-negligible distance away from the track of the primary electron. The energy deposited can be difficult to account for, because it is carried away from the point of interaction. Because of this, the concept of *restricted stopping power* has been introduced, which refers to the stopping power (as described in section 4.2.2.1.1), but only including collisions where an energy lower than a certain threshold is transferred. The concept is very useful, for example, in Monte Carlo simulations, where some collisions deposit energy locally (through the restricted stopping power), and other collisions eject a delta electron, which is explicitly transported.

LET (*Linear Energy Transfer*) is the physical quantity defining the quality of an ionizing radiation beam which is useful in radiobiology and radiation protection. When discussing dose deposition, the concept of LET is preferred to the concept of stopping power. Although they denote basically the same quantity, the former focuses on the energy absorbed by the medium, while the latter refers to the slowing down of an incident projectile. LET, generally expressed in MeV/mm or keV/μm, is closely related to the biological effects caused by ionizing radiation. Stopping power and LET are nearly equal for heavy charged particles. However, for β radiation LET does not include delta-rays or bremsstrahlung.

The ICRU defines the LET as follows: LET of charged particles in a medium is the quotient $\frac{\mathrm{dE}_\Delta}{\mathrm{dl}}$, where dE_Δ is the average energy locally imparted to the medium by a charged particle of specified energy in traversing a distance *dl*,

$$L_\Delta = \frac{dE_\Delta}{dl}. \tag{4.28}$$

Most commonly, the quantity L_Δ is expressed in keV μm^{-1}. The average energy is obtained by dividing the particle track into equal energy increments and averaging the length of the track over which these energy increments are deposited.

The linear energy transfer, L_Δ, can also be given by

$$L_\Delta = S_{el} = \frac{dE_{ke,\Delta}}{dl}, \tag{4.29}$$

where S_{el} is the linear electronic stopping power, and $dE_{ke,\Delta}$ is the mean sum of the kinetic energies, greater than Δ, of all the electrons released by the charged particle in traversing a distance dl [181].

To investigate the potential advantage of VHE electron beams compared with low energy electrons, a set of simulations to evaluate LET spectra for various energy ranges has been carried out. The spectra are scored in FLUKA at 1 cm depth of the water phantom using the USRYIELD utility, and the results are shown in Figure 43.

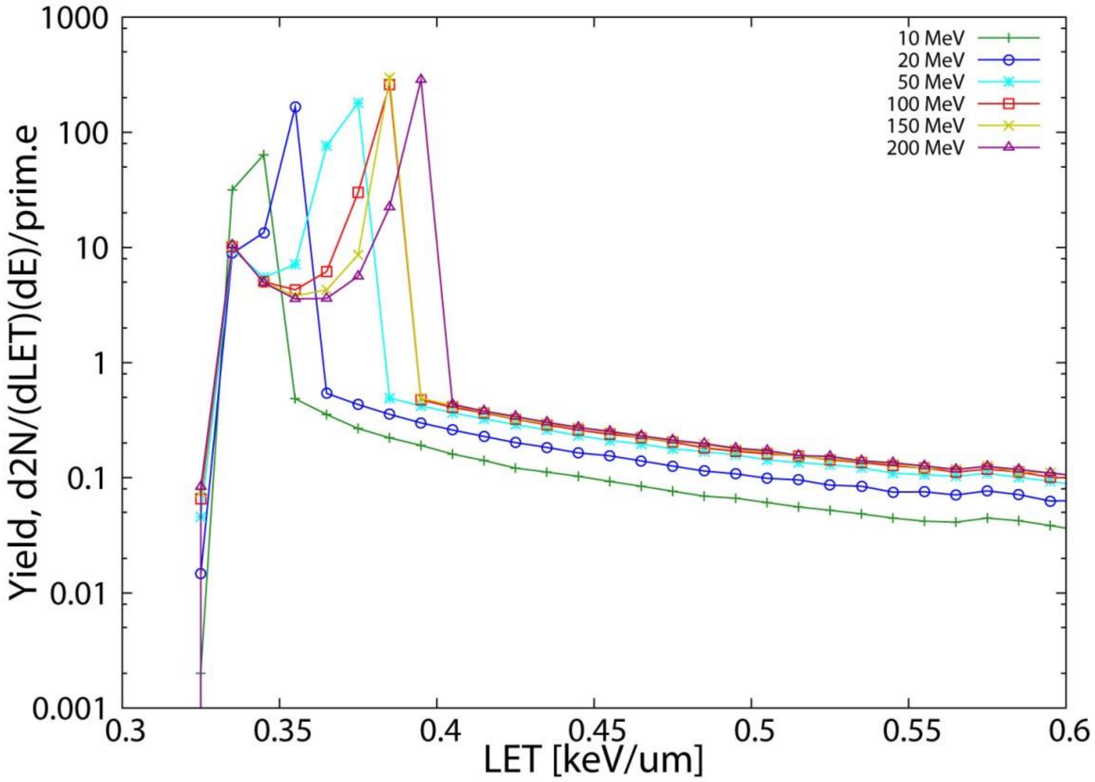

Figure 43. LET spectra for 10 MeV, 20 MeV, 50 MeV, 100 MeV, 150 MeV and 200 MeV monoenergetic incident electron beams at 1 cm from the front surface of the water phantom.

The LET spectra for all energy ranges has a well-pronounced maximum between 0.34 and 0.40 keV/μm, and a long tail decaying with increasing LET values. There is a visible LET shift of the peak with increasing electron beam energy. The peaks of LET spectra for all investigated beam energies are summarized in Table 11. We see a gradual increase of LET with rise of the beam energy, which suggests a potentially small rise in radiobiological effectiveness (RBE) of very high energy electron beams compared with clinically used electron beam energies. One can observe that for electron energies above 20

MeV the spectra have substantial lower LET contribution (at 0.34 keV/μm). This is due to the fact that the LET was scored at 1 cm depth in the water, where significant amount of lower energy electrons is generated.

Table 11. Maximum LET value for various incident beam energies at 1 cm depth in a water phantom.

Incident beam energy	LET [keV/μm]
10 MeV	0.34
20 MeV	0.36
50 MeV	0.38
100 MeV	0.39
150 MeV	0.39
200 MeV	0.40

Nevertheless, from the calculated LET spectra shown in Figure 43, it should be pointed out that the computation has been performed using a MC algorithm based on a Markovian approach, which involves a "memoryless" stochastic processes. In this approach each particle trajectory is treated independently therefore any collective effects of bunched particles (such as for relativistic LWFA VHEEs) are not taken into account.

Summarising, comparison the MC calculated LET spectra for low and VHEE beams show a shift of the LET peak for VHEEs, which could indicate a possible difference in radiobiological action for these beams.

4.2.10. Temporal duration of LWFA electron bunch

The LWFA electron bunch is ultra-short (femtosecond), which is more than 10^8 times shorter than conventional clinical LINACs, which produce microsecond duration electron bunches.

The electron bunch length has been measured experimentally in ALPHA-X beamline using transition radiation produced by the electron beam while passing through a thin foil. The ALPHA-X bunch, measured 1 m after the gas jet is just few femtoseconds (1-10 fs) [182].

It is expected that the bunch length will increase when the electron beam passes through a patient body. To estimate the bunch stretching due to the interaction MC calculations using GEANT4 have been carried out.

The bunch lengthens when the electron bunch interacts with matter. To evaluate bunch stretching of a laser-plasma accelerated electron bunch propagating through a patient the following geometry has been modelled in GEANT4. A $30 \times 30 \times 30\ cm^3$ water phantom (without any walls) is positioned 100 cm from the 150 MeV monoenergetic electron beam source. The (100 cm) distance in air corresponds to source-to-surface distance (SSD), in a clinical scenario, i.e. the radiation source to skin of the patient. The electron source is modelled as a cylinder of 50 mm radius and 0.3 μm length (along the beam propagation direction), which corresponds to a bunch length of $\approx$ 1 fs.

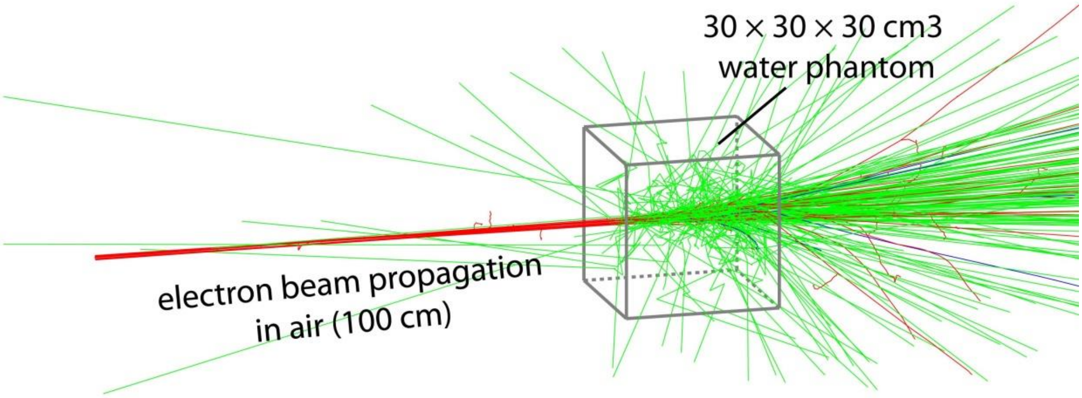

Figure 44. The setup of the GEANT4 simulation.

The geometry is presented in Figure 44. The calculations are carried out for $5{\cdot}10^5$ electrons. The electron beam passing through air and water experiences dispersion arising from the electron beam energy spread and scattering, therefore the bunch duration increases. Evaluated from the time of flight (TOF) the length of electron bunch at various positions along propagation through air and the water phantom. Table 12 shows the temporal lengthening of a 0.3 μm long electron bunch after 100 cm of propagation in air and 1 cm, 10 cm, 20 cm and 30 cm propagation in water. The bunch duration at each position is estimated from the time of flight distribution.

Table 12. Electron bunch evolution along propagation path.

Propagation distance	**Evaluated bunch length**
100 cm of air	$\sim 1.1\ fs$
100 cm of air and 1 cm of water	$\sim 5.0\ fs$
100 cm of air and 10 cm of water	$\sim 100\ fs$
100 cm of air and 20 cm of water	$\sim 0.25\ ps$
100 cm of air and 30 cm of water	$\sim 1.0\ ps$

After propagating through 100 cm slab of air the electron bunch is not sufficiently scattered and the bunch length is still close to 1 fs. The electron beam propagating through the water experiences multiple scattering events, generating bremsstrahlung while losing its initial energy. The broadening of the electron energy spectrum at different depths in water (see Figure 34 (b)) implies a temporal lengthening of the initial electron bunch. After 5 cm of propagation in water the bunch is elongated to 5 femtoseconds. At the exit of the water phantom the electron bunch temporal duration increases to 1 ps. This is still several orders of magnitudes lower than that of a clinical linear accelerator. This unique property, which is consistent with extremely high peak currents, makes laser-plasma accelerators very interesting candidate as a new modality in radiotherapy, because neither of the existing sources have similar properties.

Considering radiobiological action there is a more fundamental question: how radiobiological damage is induced in a cell and what possible effect could be conferred by very short pulses. An overview of molecular radiation effects and some previous studies of impact of spatial and temporal proximity of ion tracks are discussed in the next section.

4.2.10.1. Temporal effects in molecular radiation biology

The time scale of radiation action spans at least twenty-six orders of magnitude extending from the earliest physical events following transit of a fast particle or quantum through a small atom, to the late genetic and carcinogenic effects of radiation which may not manifest themselves until decades after irradiation. For convenience, three broad time scales are defined, namely the physical, chemical, and biological stages of radiation action (Table 13). Although the precise separation of these three time stages is somewhat arbitrary, but is conceptually very useful.

The Physical Stage

The physical stage essentially begins with the passage of a fast electron or high energy photon and the resultant transfer of energy to the atoms or molecules in the absorbing medium. Since the energy of the incident electron or photon exceeds of the normal binding energies of molecules, the most important initial event is the ejection of electrons with energies considerably greater than the binding energies. These secondary electrons lose energy by causing secondary ionizations and eventually attain thermal energies or are captured. Electronic excitation processes occur on the time scale of $10^{-16}-10^{-15}$ s. Changes in molecular configurations caused by vibrational excitation are somewhat slower because they are limited by the inertia of the atoms and the binding forces between them. Rotational excitation time is lower and can extend from about 10^{-12} s. Such processes are important in polar liquids and can be considered to mark the transition from the physical to the chemical stage. In liquid water, thermalized electrons interact with the water dipoles thus causing reorientation of the $H_2 0$ molecules. The period, the dielectric relaxation time, is a few picoseconds and is the time of formation of the hydrated electron, one of the most fundamental and important species in free radical chemistry.

Table 13. Time scales and processes occurring as a result of radiation action [183].

Time [s]	**Occurring process**
Physical stage	
10^{-18}	Fast particle traverses small atom
$10^{-17}-10^{-16}$	ionization: $H_2O \rightsquigarrow H_2O^+ + e^-$
10^{-15}	Electronic excitation: $\mathrm{H_2O} \rightsquigarrow \mathrm{H_2O^*}$
10^{-14}	Ion-molecule reactions, e.g., $H_2O + H_2O^+ \longrightarrow \bullet\, OH + H_3O^+$
10^{-14}	Molecular vibrations - dissociation of excited states: $H_2O^* \longrightarrow H \bullet + \bullet\, OH +$
10^{-12}	Rotational relation, hydration of ions: $e^- \longrightarrow e^-_{aq}$
Chemical stage	
$< 10^{-12}$	Reactions of e^- before hydration with reactive solutes at high concentration
10^{-10}	Reaction of e^-_{aq} and other radicals with reactive solute (concentration$\sim 1\, mol \cdot dm^{-3}$)
$< 10^{-7}$	Reactions in spur
10^{-7}	Homogeneous distribution of radicals
10^{-3}	Reaction of e^-_{aq} and other radicals with reactive solute (concentration $\sim 10^{-7}\, mol \cdot dm^{-3}$)
1	Free-radical reactions largely complete
$1-10^3$	Biochemical processes
Biological stage	
$hours$	Cell division affected in prokaryotic and eukaryotic cells
$days$	Damage to CNS and GI tract evident
$\sim month$	Haemopoietic death
$several\ months$	Late kidney damage, lung fibrosis
$years$	Carcinogenesis and genetic death

The hydrated electron (e^-_{aq}) is the major reducing species formed in irradiated water (80%) [the other is the hydrogen atom (20%)] and, depending upon conditions, this electron can have a lifetime extending into the micro- or even millisecond time range.

The oxidizing species produced during radiolysis of water, is the hydroxyl radical, OH, which is formed in the ion molecule reaction:

$$H_2O + H_2O^+ \longrightarrow \bullet\, OH + H_3O^+. \tag{4.30}$$

Reaction, described by equation (4.30) occurs very rapidly before solvation can provide the energy necessary to stabilize H_2O^+.

The Chemical Stage

The chemical stage of radiation action extends, in water, from about 10^{-12} s. Initially, the free-radical products of water radiolysis, e_{aq}^- , $H\bullet$, and $\bullet OH$ radicals, are not homogeneously distributed throughout the medium. They are formed along, or near to, the "tracks" of the ionizing particle and then diffuse out into the bulk of the solution. Homogeneous distribution is not achieved until approximately $10^{-8} - 10^{-7}$ s after the initial ionizing event. Rate constants for reactions between these radicals are of the order of $10^{10}\ dm^3 \cdot mol^{-1} \cdot s^{-1}$, and since the initial radical concentrations in the regions around the tracks are high, some interaction between radicals occurs during the period of diffusion into the bulk of the solution. These reactions give rise to the so-called "molecular yields" of radiation chemistry, H_2 and H_2O_2.

If the concentration of a given solute is, for example, 10^{-3} molar, the time scale for reaction of free radicals with this solute can be as short as 10^{-7} s. The chemical stage of radiation action continues with the reaction of the products of these early free radical reactions with other constituents in the medium.

The Biological Stage

In an organised tissue, some effects can appear quite early, e.g. damage to the central nervous system and gastrointestinal tract which usually appears a few days after irradiation. Damage to the haemopoietic tissue occurs after a month or so, and effects on lung and kidney function after several months. However, very long term effects, such as genetic changes or cancer-induction may not become observable until many years later.

As laser-driven accelerated electrons might be used for tumour radiation therapy in the future. The question of whether radiochemical and radiobiological yields might be influenced by the short pulse duration in a non-linear way has to be raised. Than we should ask: whether the yield of chemical species produced in the radiolysis of water and the yield of DNA damage patterns depend on the spatial and temporal separation between two particle tracks.

Liquid water is the major component of biological systems; the water content in the male human body is between 0.5 and 0.7 l/kg (ICRP 23 [184]). Thus, modelling of the processes induced by ionising radiation in liquid water is a suitable approach to obtain quantitative understanding of radiobiological effects in tissue. The interaction of ionising radiation with liquid water can be divided into the stages described above. Initial conditions are set in the physical stage within a few femtoseconds, when a track of ionised and excited atoms and molecules is left behind by the incident particle. In the subsequent prechemical stage, secondary electron thermalisation and the formation of chemical species from the initial excitation or ionisation events is completed within about 1 ps after irradiation [185], followed by the chemical stage, i.e. diffusion and reaction of the chemical species. Local concentrations of the radiolytic products reach a steady state at the end of the chemical stage about 1 μs after the initial physical energy deposition [185]. Then in the biological phase, biochemical and biophysical reactions dominate the dynamic modifications of the charged particle track structure.

Kreipl *et al.* [186] presented a systematic analysis of the impact of spatial and temporal proximity of ion (protons and He^{2+}) tracks on the yield of higher-order radiolytic species for picosecond pulses. In this studies, the biophysical Monte Carlo code PARTRAC is employed to investigate the influence of intertrack interactions[13] between ion tracks on water radiolysis and radiobiological effects [186]. The impact of intertrack effects on the radiolysis of water has been found to be more pronounced for incident ions producing higher event densities because of the increased probability for reactions of species produced by different ion tracks. If the tracks are close in space and time, the yield of the chemical species produced is influenced by intertrack effects in the same way as for higher LET values of the same ion type. In particular, the yield of $\bullet OH$ radicals is found to be reduced in the radiolysis of overlapping ion tracks. Kreipl has shown that the calculated yield of DNA damage patterns are not influenced by the short pulse duration (of the order of picoseconds), because the spatial separations are not sufficiently small. So, generally, there is no increase in the yield of DNA damage compared with ion beams for longer bunch lengths commonly used in radiotherapy.

---

[13] Interactions of pairs of ion tracks separated by small spatial and/or temporal distance

It should be noted that Kreipl's studies [186] have been carried out for proton beams with picosecond temporal duration. LWFA VHEE, have femtosecond temporal duration. However, they experience significant pulse-lengthening (refer to Table 12), and therefore, the track densities of these beams is significantly reduced while traversing tissue. Electrons have a much smaller cross section of interaction than protons, therefore based on Kreipl's studies [186], one would not expect increased yield of DNA damage due to tissue irradiation with fs electron bunches.

4.3. Conclusions

In this section Monte Carlo calculations for very high energy electrons have been presented.

It has been shown that VHEEs do not suffer from extensive multiple scattering in air, which does not lead to significant increase in field size. The reduction of field size results in a lower lateral electronic equilibrium level on axis. When the field size is reduced significantly, electrons from the periphery of the field do not scatter sufficiently to contribute to the central axis depth dose, and therefore d_{max} moves closer to the front surface of the water phantom.

Irradiation of tissue-like media with VHEE beams induces radioactivity. However, the dominant radionuclides activated are identified as ${}^{11}_{6}C$ and ${}^{15}_{8}O$. These have a short lifetime and after 30 minutes following irradiation the residual activity is negligible, therefore no major safety issues are envisaged. The calculated induced radioactivity is found to be small and would be expected to be inconsequential in terms of increased dose.

A neutron yield for VHEEs of the order of 10^{-5} neutrons/cm^2 per incident electron has been estimated, and together with induced activity due to radionuclide production is found to have a negligible effect on total dose deposition.

Even though the evaluated doses equivalents for VHEEs (neutron yield, induced activity and equivalent doses) are at a low level, a more detailed radiobiological analysis needs to be undertaken to predict if radiotherapy with VHEEs has undesirable effects on patients' health, such as increased probability of inducing secondary cancers.

The consequences of short temporal LWFA electron bunches has been discussed. However, based on previous data on proton and ion beams, an increased yield of DNA damage due to tissue irradiation with femtosecond electron bunches is not expected. On the other hand, the calculated LET spectra for VHEE beams, exhibit a shift of the LET peak with respect to low energy electron beams. It could be speculated that this may indicate a possible difference in radiobiological action for very high energy electron beams.

5. Dosimetry of electron beams

Radiotherapy relies on accurate dose delivery to the prescribed target volume. The ICRU recommends an overall accuracy in tumour dose delivery of ±5%, based on an analysis of dose response data and on an evaluation of errors in dose delivery in a clinical setting.

Before a radiation source can be used in radiotherapy, its output must be calibrated. The calibration of electron beams is carried out using radiation dosimeters and special radiation dosimetry techniques.

The dosimetry measurements presented in this work do not aim to achieve clinical accuracy (±5%), but to demonstrare that available detectors can be used for dose measurements of unconventional very high energy electron beams.

5.1. Dosimetric detectors used in radiation therapy

The main techniques of available dosimetry systems widely used in radiation treatment are discussed in this chapter.

5.1.1. Radiation dosimeters

A radiation dosimeter is a device capable of measuring the dose of ionising radiation deposited in its sensitive volume. A dosimeter that does not require calibration in a known field of radiation is referred to as an absolute dosimeter. Dosimeters requiring calibration are called relative dosimeters.

Calibration of a clinical radiation beam in water under specific reference conditions, is referred to as reference dosimetry. There are three types of reference dosimetry techniques:

- Calorimetry
- Fricke dosimetry
- Ionization chamber dosimetry

The following section (5.1.1) is based on reference [118].

5.1.1.1. Calorimeters

Calorimetry is the most fundamental of the three reference dosimetry techniques, because it relies on basic definitions of either electrical energy or temperature. In principle, calorimetric dosimetry is simple. However, in practice the need for measuring extremely small temperature differences makes the technique very complex and relegates it to sophisticated standards laboratories.

Two main types of absorbed dose calorimeter are currently used in standards laboratories:

- Graphite calorimeters;
- Sealed water calorimeters.

The standards for absorbed dose for radiotherapy photon beams are based on calorimetry measurements at primary standards laboratories [187], e.g. National Physical Laboratory (NPL) in the UK. Water calorimeters have been successfully used with proton and carbon ion beams ([188] and others), but no primary standard has been developed yet for very high energy electrons.

5.1.1.2. Fricke dosimetry

The energy of ionizing radiation absorbed in certain media produces a chemical change in the absorbing medium, and the amount of this chemical change may be used to measure absorbed dose. The best known chemical radiation dosimeter is the Fricke dosimeter, which relies on oxidation of ferrous ions into ferric ions in an irradiated ferrous sulphate solution. The amount of ferric ion produced in the solution is measured by absorption spectrometry with ultraviolet light at 304 nm, which is strongly absorbed by the ferric ion.

Fricke dosimetry (sometimes referred to as ferrous sulphate dosimetry) depends on accurate knowledge of the radiation chemical yield of ferric ions, measured in moles produced per Joule of energy absorbed in the solution. The chemical yield is related to the number of ferric molecules, G, produced in the ferrous sulphate solution by 100 eV of absorbed energy. An accurate value of the chemical yield is difficult to ascertain because it is affected to a certain degree by the energy of the beam, dose rate and temperature of the solution during irradiation and readout. The best G value for ^{60}Co γ rays is 15.6 molecules per 100 eV, corresponding to a chemical yield of 1.607×10^{-6} mol/J. The typical dynamic range for ferrous sulphate Fricke dosimeters is from a few grays to about 400 Gy, making Fricke dosimetry impractical for routine use in a clinic.

5.1.1.3. Ionization chambers

Ionisation chambers consist of a gas-filled receptacle with two electrodes between which a voltage is applied. The radiation ionises the gas, and the electric field causes the movement of charges between the electrodes (anode and cathode), creating a current that can be measured with an electrometer. More details on ionisation chamber are given in section 5.4.1.

5.1.1.4. Other dosimetry systems

Film dosimtery

The Gafchromic film dosimtery and an extensive description of its calibration and measurement is presented in section 5.2.

Gel dosimetry systems

Gel dosimetry (e.g. BANG gel [189]) systems are the only true 3-D dosimeters suitable for relative dose measurements. The dosimeter is simultaneously a phantom and a device that can measure absorbed dose distribution in a full 3-D geometry. Gels are nearly tissue equivalent and can be moulded to any desired shape or form.

In polymer gel, monomers such as acrylamide are dispersed in a gelatin or agarose matrix. Upon radiation exposure, monomers undergo a polymerization reaction, resulting in a 3-D polymer gel matrix that is a function of absorbed dose, which can be measured using NMR, X-ray computed tomography (CT), optical tomography, vibrational spectroscopy or ultrasound. A number of polymer gel formulations are available, including polyacrylamide gels, generally referred to as PAG gels (e.g. BANG gel). One needs to be very careful handling them, because these dosimeters are very sensitive to atmospheric oxygen [190].

5.2. Gafchromic film dosimetry system

5.2.1. Characterization of EBT2 Gafchromic® film

5.2.1.1. Background

Poly-diacetylyne based radiochromic films (RCF) (GAFCHROMIC®, International Specialty Products, Wayne, NJ) derives its name from the kinetic effect of electromagnetic energy (radio) induced colour change (chromic) to the film medium. Gafchromic films are a standard dosimetry tool in external beam radiotherapy and brachytherapy. They exhibit high spatial resolution, tissue equivalence and are virtually independent for various radiotherapy modalities that make them suitable for dose measurement in radiation fields with high dose gradients.

Radiochromic film research has undergone an evolution over five decades, where each decade has resulted in improvements in the radiation response in energy range and sensitivity. The first RCF film detectors were developed for dose monitors in industrial radiation processing [191, 192]. One of the first radiochromic film models, HD-810 or DM-1260 (Nuclear Associates, Model no. 37-040), has only a 6 μm thick sensitive layer, which is suitable only for clinical dosimetry research for relatively high doses exceeding 50 Gy [193]. More sensitive MD-55 (Nuclear Associates, Model no. 37-041) has a 15 μm thick sensitive layer and covered a dose range from 10 - 100 Gy [194]. Subsequently the MD-55-2 model was developed which has two MD-55 layers [195, 196], with a sensitive layer thickness of 32 μm sensitive to 1 - 250 Gy. However, reported non-uniformity by 8-15% [195] for this model limited its use in clinical applications. As a consequence, the HS model was introduced, which has only a single 40 μm sensitive layer leading to higher sensitivity and better uniformity than its precursor. Further radiochromic film developments led to the introduction of EBT (standing for External Beam Therapy) GAFCHROMIC® model designed to replace silver halide radiographic film for intensity modulated radiotherapy (IMRT) and quality assurance (QA) procedures[197], where two 17 μm thick active layers are placed symmetrically around the middle of the film. This film type allows the analysis of dose measurements using commercially available flat-bed document scanners in RGB (red-green-blue) mode. According to the manufacturer, the useful range of EBT model is up to 8 Gy. However, it is shown that using all three channels of the scanned images the dynamic range of the film can be extended to over 100 Gy [198]. The next generation, EBT2 GAFCHROMIC® film is used in the studies presented in this thesis. EBT and EBT2 films have been extensively studied as two-dimensional dosimeters, and research on these detectors has been published in over 100 peer reviewed articles.

5.2.1.2. EBT2 Gafchromic® film

EBT2 film is composed of five layers consisting of: a polyester overlaminate, an adhesive layer, a topcoat, an active layer and a polyester substrate. A schematic of these structures is shown in Figure 45 and the composition, thickness and density of the layers can be found in Table 14.

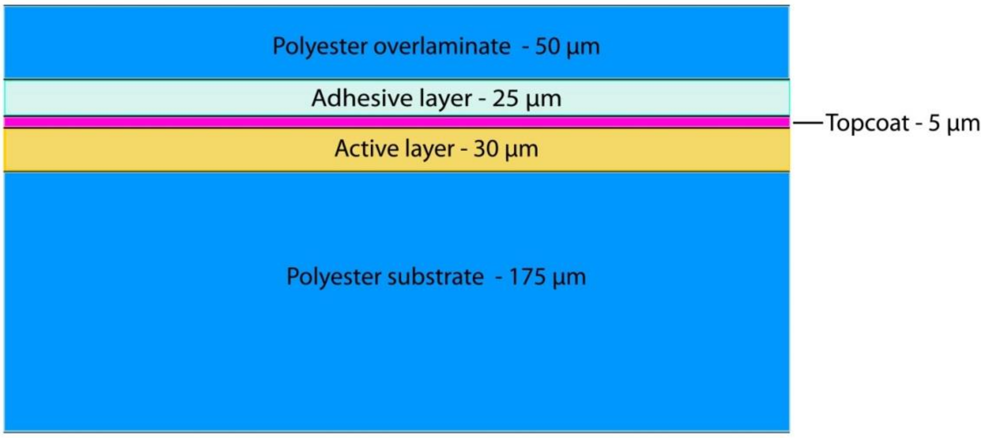

Figure 45. Configuration of GAFCHROMIC® EBT2 Dosimetry Film[199].

Table 14. Configuration and atomic composition of GAFCHROMIC® EBT2 film[199].

Layer	**Thickness [µm]**	**Density [g/cm^2]**	**COMPOSITION (ATOM%)**							
			H	Li	C	N	O	Cl	K	Br
Polyester film base	50	1.35	36.4	0.0	45.5	0.0	18.2	0.0	0.0	0.0
Adhesive	25	1.2	57.1	0.0	33.3	0.0	9.5	0.0	0.0	0.0
Surface layer	5	1.2	56.9	0.9	25.7	0.0	15.6	0.9	0.0	0.0
Active layer	30	1.2	58.3	0.8	29.6	0.1	10.7	0.3	0.1	0.1
Polyester film base	175	1.35	36.4	0.0	45.5	0.1	18.2	0.0	0.0	0.0
Overall composition			40.85	0.10	42.37	0.01	16.59	0.04	0.01	0.01

RCF, unlike its radiographic film counterpart, is a processor-less film that does not require latent-chemical or thermal processes for development [200]. Instead, RCF undergoes a topotactic solid-state polymerization reaction to the kinetic energy released per unit mass (KERMA) of the incident ionizing radiation. The sensitive component of EBT2 films is the lithium salt of pentacosa-10,12-diynoic acid (LiPCDA), a micro-crystalline diacetylene, where the hydrogen atom of the carboxyl end group is replaced by lithium [199]. Polymerization of the PCDA monomer yields two mesomeric polymer structures shown in Figure 46 [201]. Energy deposited by incident ionizing radiation randomly starts polymerization of the diacetylene monomers in the active layer [202]. Triple bond breaking generates intermediate radical states, acting as active centres for monomer attachment. Each of the initiated polymer chains grow independently from the others. As a first step, polymers with a butatrien-like structure are formed, which are finally rearranged into an acetylene-like structure. The degree of initialized active centres depends on absorbed energy and, thus, dose. The polymerization reaction occurs nearly instantaneously [203]. Film colouring is, therefore, a measure for the deposited dose. When the diacetylene polymer (active layer in the film) is exposed to radiation, it reacts to form a blue coloured polymer with an absorption maxima at about 636 nm and 585 nm. However, to the human eye, the exposed film appears green owing to the presence of a yellow marker dye in the active layer. Since the peak absorption in the exposed film occurs at about 636 nm, with a secondary peak at about 585 nm, the greatest response occurs when measurements are made with red light. Figure 47 shows the absorption spectra of GAFCHROMIC® EBT2 film before and after irradiation. Before irradiation the active component contains almost no polymer so the film has low absorbance at 636 nm. The prominent feature in the spectrum of the unexposed film is the band centred at approximately 420 nm resulting from the presence of the yellow marker dye [199].

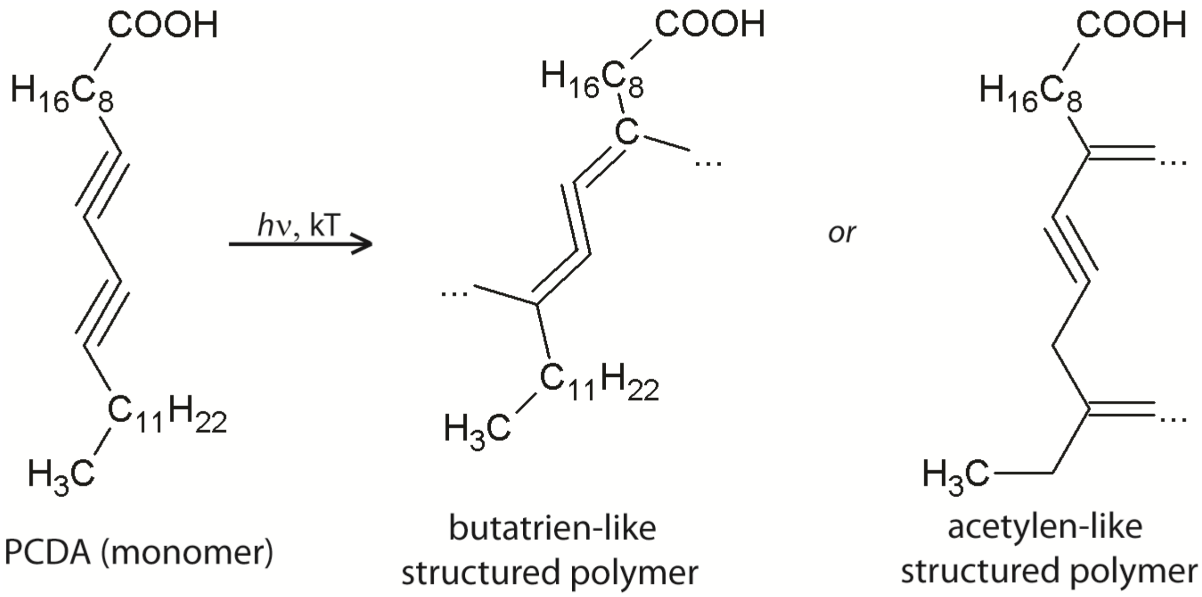

Figure 46. Structural formula of PCDA (pantacosa-10,12-diynoic acid).

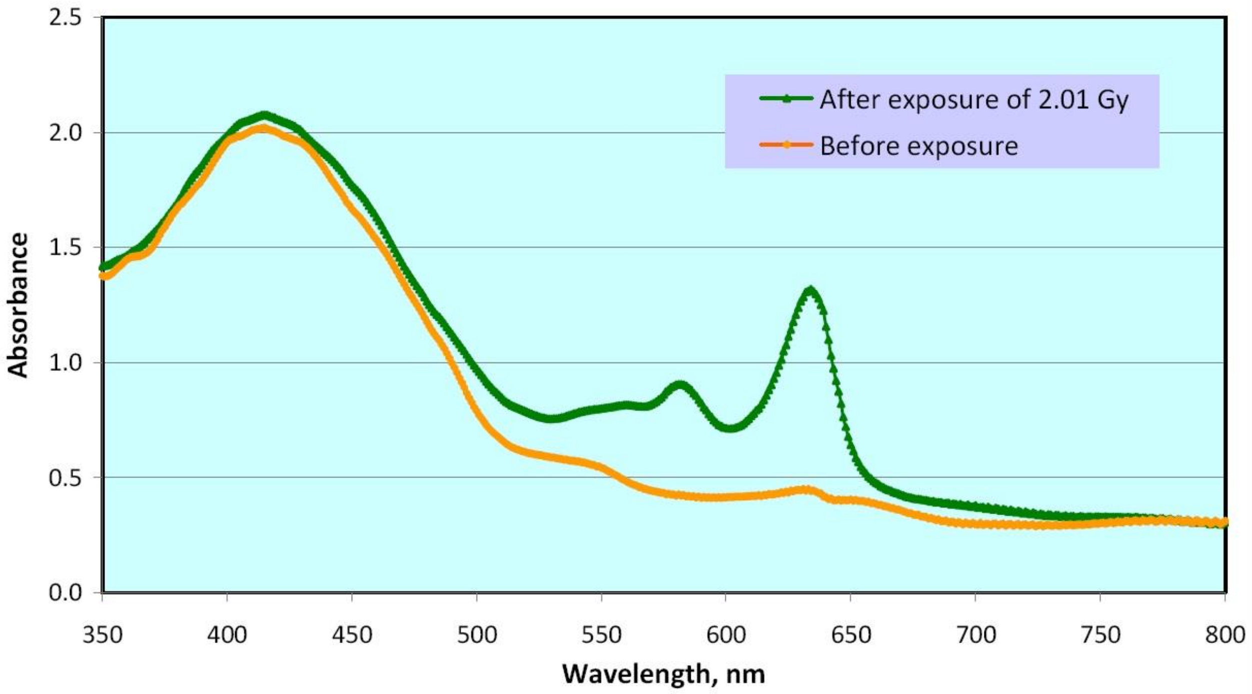

Figure 47. Absorption spectra of EBT2 before and after irradiation [199].

The EBT2 film structure, shown in Figure 45, consists of a 30 µm thick active layer with the elemental composition summarized in Table 14, with effective atomic number Z_{eff} of 5.7, and a density of 1.32 g/cm^3.

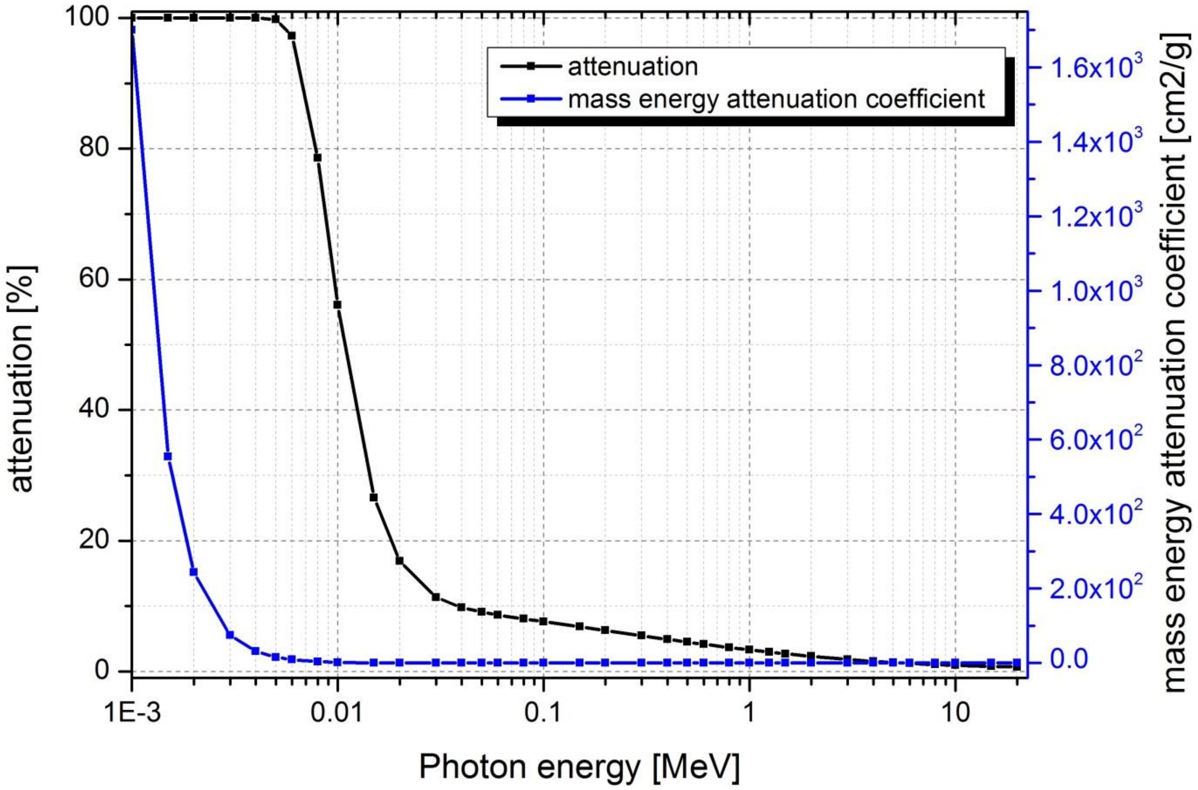

Figure 48. EBT2 mass energy attenuation coefficient plotted as a function of photon energy.

The interaction efficiency of the EBT film, Figure 48, has been determined using the National Institute for Standards and Technology (NIST) [119] calculated mass energy attenuation coefficients for the known atomic composition of the films (Table 14). The elemental mass energy attenuation coefficients are summed and plotted versus photon energy. Knowing the mass energy attenuation coefficient and the densities of the film, attenuation is calculate using Beer's law:

$$attenuation = 1 - exp\left(-\frac{\mu_{en}}{\rho} \cdot \rho \cdot T_0\right), \tag{5.1}$$

where μ_{en}/ρ is the mass energy attenuation coefficient, ρ is the density, and T_0 is the thickness of the dosimeters. The interaction efficiency is the percentage of the incident fluence absorbed in the film, which results in electrons from the interaction being absorbed in the active layer and inducing coloration in the film. The film can capture a high amount of the radiation beam fluence for very low energies. The predominate interaction at the film interface is Compton scattering. Therefore, the primary photon will scatter with the bound electrons in the valance bands within the film's polyester layer. These electrons gain energy from the incident photons consistent with the conservation of momentum and energy. The range of the scattered electrons can be calculated by considering the continuously slowing down approximation (CSDA), r_0, [204] for an electron in a medium described previously by equation (4.5), where the E_0 defined in the limits of integration is the starting energy of the electron. r_0 for a 0.001 MeV, assuming $\theta = \pi$ photon scatter interaction, is ~98 μm, and even if one adds an additional distance equal to the mean free path ($1/\mu$) of the incident photon, ~1 mm, then the incident radiation of 0.001 MeV isn't sufficient to induce a signal in the film's active layer.

The film has a detection efficiency comparable to that of an ion chamber with its increased photoelectric cross-section due to a higher Z_{eff} composition.

Exposure of EBT2 to ionising radiation results in the production of blue-colored dye-polymer. This measurable film darkening, i.e. change in optical density (OD) is given by the base 10 logarithm of the light transmission T (equation (5.2)). A well-defined relation of absorbed dose and the background corrected OD yields the so-called *netOD*.

$$netOD = -\log_{10}(T) = OD^{exp} - OD^{unexp}, \tag{5.2}$$

where OD^{exp} and OD^{unexp} are the measured optical densities of exposed and unexposed films, respectively. The detection principle of EBT films relates the observed change in optical density to the amount of dose deposited.

Post-exposure optical density growth

Nearly full colour development of all radiochromic films is very rapid. McLaughlin *et al.* [205] showed that radiation-induced reactions has an incubation period of at least 1 μs. They also showed that polymerization can continue after irradiation has ceased causing a post-exposure density growth, which manifests itself as a significant increase in the optical absorption. EBT radiochromic film produces a post-irradiation colouration effect of approximately 9%–11%, which mostly occurs within the first 6 h [206]. To reduce uncertainties related to optical density growth and improve the level of accuracy, following the recommendations of the American Association of Physicists in Medicine (AAPM) Report No. 63 [207], the common practice is to increase post-exposure waiting times to 24h when further film development is negligible. Moreover, calibration films must be read out with the same post-irradiation time to enhance the accuracy of dosimetry.

5.2.1.3. Environmental conditions

The response of radiochromic dosimeters is influenced by temperature, relative humidity and ambient light. Relative humidity variations from 20% to 80% have a large impact on optical density and can introduce dose errors of up to 15% [208]. According to the manufacturer, prolonged (more than 1 day) continuous exposure to temperatures of 50°C should not affect the performance of EBT2 films. Nevertheless, temperatures > 60°C cause instability of the polymerization reaction and should be avoided [200]. Although the active component in EBT2 films is not particularly sensitive to visible light, it is sensitive to shorter wavelengths (in particular to UV light). The interior sources, where film processing takes place, are usually illuminated by fluorescent light bulbs which produce red, green and blue light which potentially could affect dosimetric measurement, however for EBT2 type films this effect is relatively small (it would take over 22 days of constant exposure to light to cause change in OD corresponding to 1 Gy). To perform dose measurements with highest accuracy the variations in environmental conditions during calibration, exposure and storing process should be minimized. This can be achieved by protecting films from excessive ambient light (e.g. by storing films in an opaque envelope) and keeping surrounding conditions constant.

5.2.1.4. Fractionation and Dose Rate Effects

Studies of the effect of fractionating the dose delivered to both EBT and EBT2 films have shown no clear trend of dose fractionation dependence and net optical density variation lies within 1% for the both film types [209]. Other studies confirmed no significant differences for various dose-rate irradiations [210]. Therefore, EBT film is considered to be a fraction- and dose-rate independent dosimeter.

5.2.1.5. Energy dependence

The properties and sensitivity of EBT2 film have been well documented for a wide range of energies from different radiation sources used in radiotherapy [211-217]. Data provided by the manufacturer indicates that the response of EBT film may be even 10%

higher for keV X-rays compared with MeV X-rays [218]. However, Buston *et al.* [214], have shown that EBT2 has a very low energy dependence with a 6.5% ± 1% variation in optical density to absorbed dose response for X-ray beam irradiation from 50 keV to 10 MeV. Regarding the MeV energy range Fuss *et al.* [219] found no significant energy dependence between 6 MeV and 25 MeV for the EBT film. Generally, the energy dependence (apart for kV X-ray beams) has been found to be relatively small within measurement uncertainties (1σ ± 4.5%) for all radiotherapy energies and modalities commonly used [212]. There have been several investigations of radiochromic film as a dosimetric tool in proton therapy [220-222]. They show under-response of EBT films at the Bragg peak. The main cause for this is attributed to the higher LET within the Bragg peak [220-222].

5.2.1.6. Film read-out

Several studies have evaluated the performance of commercial flatbed scanners for EBT film dosimetry [223, 224]. The microscopic structure of radiochromic films strongly influences their light scattering properties. The flatbed scanners, where the film is stationary during reading, have shown better results than roller-based scanners. Film response depends strongly on the film orientation with respect to the scanning direction. The manufacturer claims that this is related to the needle-like structure of the polymers, which have a diameter of 1-2 μm and length of 15-25 μm. In addition, the structures align preferably parallel to the film coating direction, which corresponds to the short side of a whole film sheet, which results in different light scattering properties for landscape and portrait orientation [199]. Therefore, it is important to maintain the same scanning orientation in scanner-based film dosimetry. An unexposed film has an absorption spectrum, that is centred around 420 nm, which is related to the active's layer marker dye. After irradiation the polymerization produces additional absorption peaks in the red part of the spectrum (Figure 47) [199]. Therefore, the best film response is measured in the red colour channel up to doses of the around 20-30 Gy.

With most scanners, the response of EBT2 film is not completely even over the scan field, which can yield differences in the response of the order of 5% or more depending on dose and position and is largest along the lateral edges of the scan field (orthogonal to scan direction). This problem is minimized by utilizing an A3 field size digitizer (e.g. EPSON

Expression Pro 1000 XL) and positioning the exposed parts of the films at the centre of the scan window in the lateral direction.

5.2.1.6.1. *Epson Expression Pro 1000 XL Scanner- EBT2 film Digitizer*

The EPSON scanner not only has very good noise characteristics and superior repeatability, but the software has a feature that allows all the image adjustment tools to be turned off. These tools must not be used for film dosimetry because they apply non-linear, transformations to the measured colour values. For this application the data file must contain only the unaltered data acquired by the scanner.

The flatbed scanner Epson Expression 10000XL, used here, is a high-quality scanner with a reading area of 310×437 mm^2. It can digitize films in transmission or reflection mode up to a colour depth of 48 bits, a maximum resolution of 2400 dpi and a maximum optical density of 3.8. The incident light, from a xenon gas fluorescent lamp, is captured by a linear charged coupled device (CCD) array. Performance of the scanner has been widely studied in dosimetry of EBT film [225, 226]. All tests and detailed analysis show the superior accuracy and reproducibility of this digitizer. Therefore, this model is considered to be the top recommendation among flat-bed document scanners for Gafchromic film dosimetry.

5.2.2. *Calibration of EBT2 films with 20 MeV electron beams*

5.2.2.1. *Phantom and irradiation procedure with 20 MeV LINAC*

Irradiation with 20 MeV electron beams on a Varian Clinac iX [227] linear accelerator (Varian Medical Systems, Inc., Palo Alto, CA) has been carried out at the Royal Surrey County Hospital. This LINAC operates at 180 Hz pulse repetition rate and produces microsecond duration nanocoulomb electron bunches at milliampere average current in a macro-pulse.

Figure 49. Experimental setup for 20 MeV LINAC calibration of EBT2 films.

For exposure to the beam, the films are placed in a standard grade solid water phantom (Gammex, Middleton, WI) composed of 20 × 20 cm^2 slabs with 5 cm of build-up material above the film and 10 cm under the film to provide adequate backscatter (Figure 49). The individual films are positioned at a depth corresponding to 95% of the maximum dose for the 20 MeV electron beam. The source-to-surface distance (SSD) is set to 100 cm, as commonly used in radiation therapy with the MeV photon beams. Exposure of the films for dose calibration is carried out using a 10 × 10 cm^2 field size, and the film is positioned perpendicularly to the axis of the beam. Calibration films are generated for five discrete exposures for doses ranging from 100 cGy to 1000 cGy. One film is used for each dose level. Prior to irradiation, the output beam is characterized using an N3401 IBA PTW plane-parallel ion chamber (PTW, Freiburg, Germany) calibrated by the National Physical Laboratory (Teddington, UK).

5.2.2.2. Handling procedure

The film used in this study is Gafchromic® EBT2, has dimensions of 20.3x 25.4 cm^2 and is handled according to the procedures described in the (AAPM) task group 55 report [228] taking into account all the precautions for accurate film dosimetry discussed in the previous sections. After irradiation, exposed and unexposed films (for background correction) are stored together in black envelopes at room temperature to minimize exposure to light while the films are not being handled for scanning.

Digitalization and image processing

The films are digitized with an Epson Expression 10000XL Pro flat-bed colour scanner. The scanner is fitted with a transparency adapter and the images are acquired in transmission mode. RGB positive images are digitised with a depth resolution of 16 bits per colour channel and a spatial resolution of 72 dpi. Scans are acquired using the EPSON Scan Utility v3.04A software, with all filters switched off to disable colour correction options and thereby record the raw image data. Data is saved in uncompressed tagged image file format (TIFF). To account for the post-exposure changes all calibration films are scanned 24 ± 2 h after exposure, which allows errors due to time-after-exposure differences to be neglected. As already mentioned, the scan response of EBT2 radiochromic is sensitive to the orientation of the film on the scanner [224]. Therefore, the orientation of the film is marked. The scanner response of EBT2 films is sensitive to the position of the film on the scanner relative to the scan axis [229] therefore a plastic template is used to position films in a reproducible central location in the middle of the scan window, where no correction of scan field uniformity is required. Ten preview scans are taken before the start of film scanning to allow the scanner temperature to stabilize, which prevents temperature induced effects. Each film is scanned three times post-irradiation and an average of three repeat scans are used for analysis. Averaging multiple successive scans is carried out with intention of removing the noise in the image. Transmission scanner readings (PV_{unexp} and PV_{exp}) and standard deviations ($\sigma_{PV_{unexp}}$ and $\sigma_{PV_{exp}}$) are determined for every piece of film as a mean pixel value over the region of interest (ROI). The exposed area of calibration films is uniform. Therefore, calculating the mean and standard deviation of all pixels in an homogeneously exposed ROI, is applicable. A typical example of a homogeneously irradiated EBT2 dosimeter and result of the accomplished analysis is shown in Figure 50.

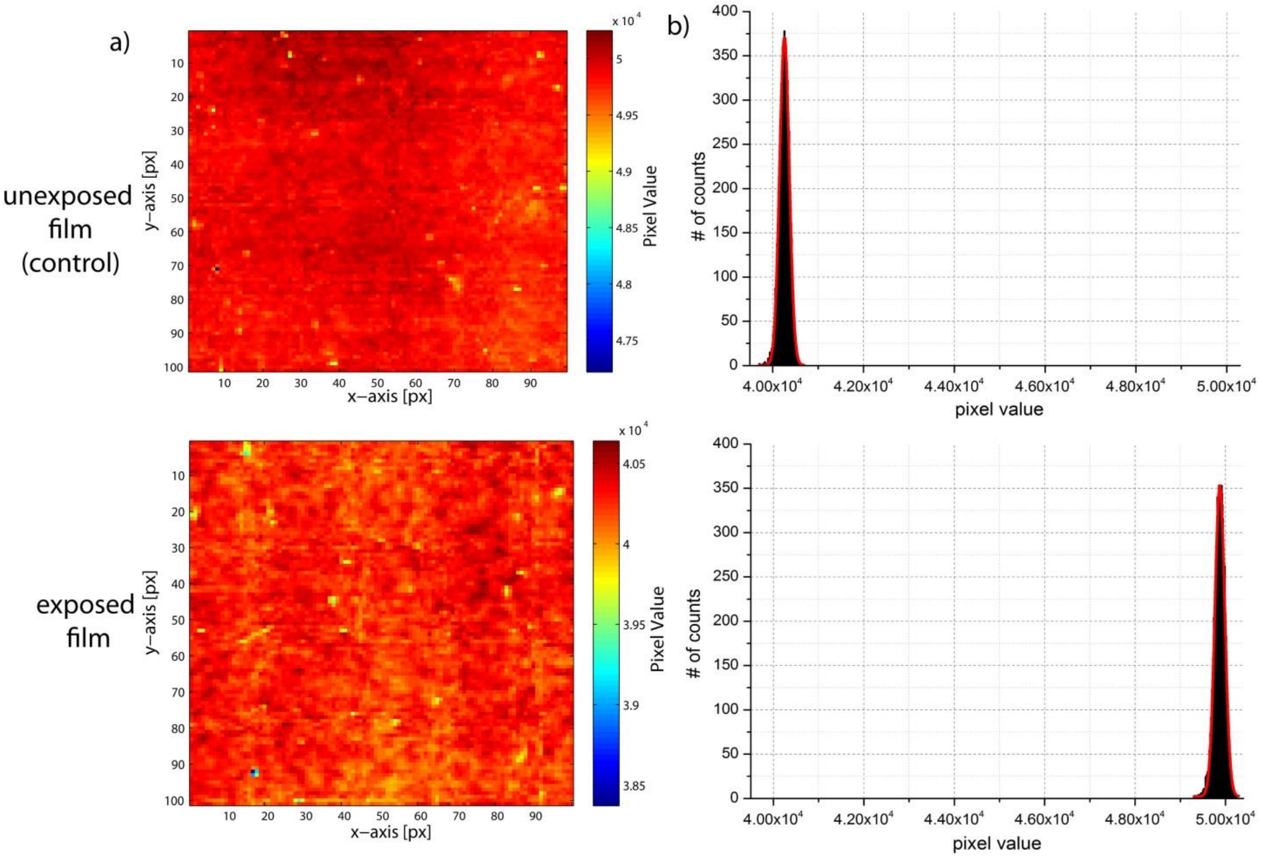

Figure 50. EBT2 film calibration. a) Typical irradiation pattern on EBT2 film, obtained in calibration measurements with a 20 MeV clinical LINAC. The whole area represents the ROI that is used for analysis. b) Distribution of the pixel value from the irradiated with 1 Gy calibration patch fitted with Gaussian representing mean pixel value (in arbitrary units) used to determine the *netOD* and its uncertainty for the dose calibration curve.

5.2.2.3. Image processing uncertainties

Following scanning of the film, the images are imported into an in-house written ImageJ (National Institutes of Health, Bethesda, MD) routine, which extracts the red component of the RGB scanned image and determines the *netOD* of the irradiated film patches.

Dose response relation and uncertainty analysis

For densitometers that do not read *OD* directly, the *netOD(D_j)* for a dose D_j can be calculated using the following relationship:

$$netOD^{i}(D_j) = OD^{i}_{exp}(D_j) - OD^{i}_{unexp}(D_j) = \log\left(\frac{I^{i}_{unexp}(D_j)}{I^{i}_{exp}(D_j)}\right), \qquad (5.3)$$

where $I^i_{unexp}(D_j)$ and $I^i_{exp}(D_j)$ are the readings of pixel value (PV) for the unexposed and exposed film piece for the i^{th} film packet, respectively.

The film dose-response curve is usually plotted as a function of the measured *netOD* and the data fitted with an appropriate function using the least-squares method. This process is subject to uncertainties arising from two basic sources: (1) experimental uncertainties and (2) non-experimental uncertainties due to fitting of the data points with a calibration function. The experimental uncertainties include the *netOD* measurement reproducibility, uncertainties in accelerator calibration, mismatch in temporal and thermal history of the film, differences in the mean response from one piece of film to another, etc. Using an error propagation expression, which ignores cross correlations (therefore assuming that the uncertainties are statistically independent), we can calculate uncertainly of $netOD^i(D_j)$ as follows:

$$\sigma^i_{netOD}(D_j) = \sqrt{\frac{\left(\sigma^i_{I_{unexp}}(D_j)\right)^2}{\left(I^i_{unexp}(D_j)\right)^2} + \frac{\left(\sigma^i_{I_{exp}}(D_j)\right)^2}{\left(I^i_{exp}(D_j)\right)^2}}. \tag{5.4}$$

To find the most suitable function for our dosimetry system the following criteria is used: (i) the fit function must be monotonically increasing, (ii) the function chosen should give the minimum relative uncertainty for fitting parameters. Based on this criteria and the manufacturer's recommendation we fitted the dose-response calibration points to a polynomial of the form:

$$D(netOD) = A_0 + A_1 \cdot netOD + A_2 \cdot (netOD)^2 + A_3 \cdot (netOD)^3. \tag{5.5}$$

The measured dose response for EBT2 film (lot#: A08301204) irradiated with the 20 MeV Varian iX Clinac is shown in Figure 53, where dose (in Gy) is plotted against net OD. Response curve is fitted with the third order polynomial given by equation (5.5). To predict the uncertainty in the measurement of an unknown dose for a calibration curve for each dosimetry system the expression for error propagation is used [230]:

$$\sigma_y^2 = \sum_i \left(\frac{\partial y}{\partial x_i}\right)^2 \cdot \sigma_{x_i}^2, \qquad (5.6)$$

where σ_y is the total estimated uncertainty (standard deviation) for a dose determined using equation (5.6), while $\sigma_{x_i} (i = 1,2,3)$ represents the standard deviations for *netOD*. From equations (5.5) and (5.6), it follows that:

$$\sigma_{D_{tot}}^2(\%) = \left[\left(\frac{\partial D_{fit}}{\partial netOD}\right) \cdot \sigma_{netOD}^2\right] + \left[\sum_{i=0}^{3} \left(\frac{\partial D_{fit}}{\partial A_i}\right) \cdot \sigma_{A_i}^2\right] = \sigma_{D_{exp}}(\%) + \sigma_{D_{fit}}(\%), \qquad (5.7)$$

where $\sigma_{D_{exp}}$is the term giving the experimental uncertainty of the measured *netOD*(σ_{netOD}) for the selected fit functional form and $\sigma_{D_{fit}}$is related to the fitting parameter uncertainties (σ_{A_0}, σ_{A_1}, σ_{A_2} and σ_{A_3}) for the selected function form. The experimental and fit related uncertainties for the third order polynomial (equation (5.5)) are given by the following expressions:

$$\sigma_{D_{exp}}(\%) = \frac{\sqrt{[A_1^2 + 4A_2^2(netOD)^2 + 9A_3^2(netOD)^4] \cdot \sigma_{netOD}^2}}{D_{fit}} \times 100, \qquad (5.8)$$

$$\sigma_{D_{fit}}(\%) = \frac{\sqrt{\sigma_{A_0}^2 + (netOD)^2 \cdot \sigma_{A_1}^2 + (2netOD)^2 \cdot \sigma_{A_2}^2 + (3netOD)^4 \cdot \sigma_{A_3}^2}}{D_{fit}} \times 100. \qquad (5.9)$$

For all calibration measurements, uncertainty in *netOD* is usually below 5%, introduced by film inhomogeneity [199] and fluctuations of experimental conditions.

Comparison of the dose response for different EBT2 lot numbers

Three different lot numbers of EBT2 films have been used for the experiments: A12171003B, A04181101 and A08301204 (Table 15). Therefore, it is important to assess the difference in dose response for these three batches.

Table 15. Lot number list of EBT2 films used in these studies.

Lot #	*Expiry Date*
A12171003B	December 2012
A04181101	April 2013
A08301204	August 2014

Films are irradiated with a calibrated 225 kV X-ray radiobiological cabinet at 50 cm filter to source distance (FSD). These three lot numbers are used to establish the dose response curves shown in Figure 51 with fit parameters provided in Table 16 for 225 kV X-rays.

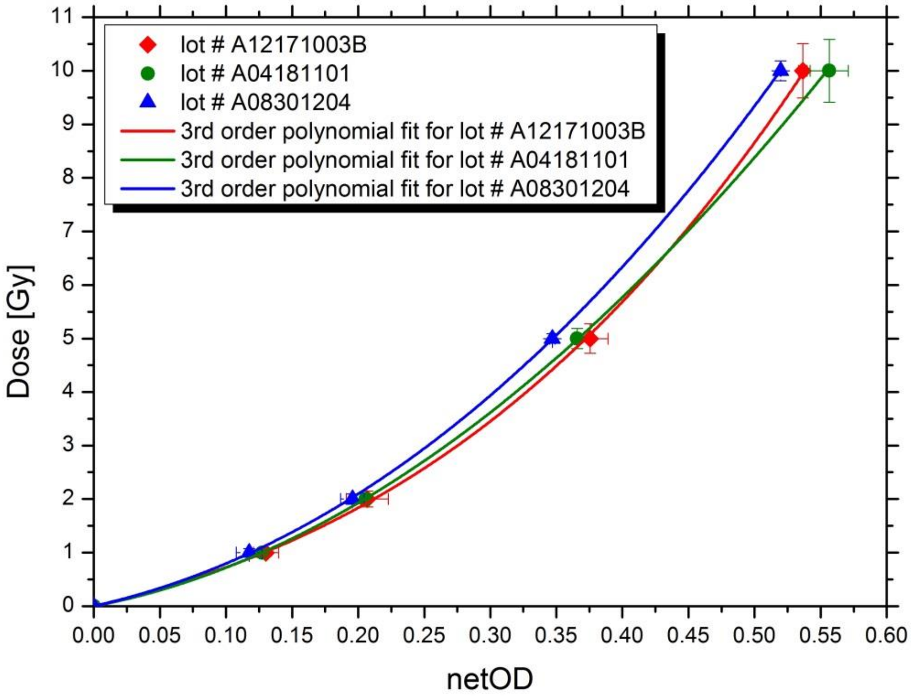

Figure 51. Dose-response curve of the EBT2 film for A12171003B, A04181101 and A08301204 lot numbers calibrated with 225 kV X-ray source.

Table 16. Fit parameters for dose response curves established for 3 different EBT2 lot numbers irradiated with 225 kV X-rays.

Lot #	*fit parameters*			
	A_0	A_1	A_2	A_3
A12171003B	-5.8E-07	5.708	13.459	19.51
A04181101	5.12E-07	4.684	25.14	-1.978
A08301204	5.35E-07	5.529	23.683	5.248

The calibration curves presented in Figure 51 cannot be used for dose measurements for VHEEs, because of the different dose response of the film for kV photons compared with high energy (MeV) radiation (for more details see radiochromic film energy dependence subsection). This difference is presented in Figure 52 for the EBT2 film, lot # A08301204 used in the experiments, which clearly shows a higher sensitivity for X-ray photons compared with an MeV electron beam. This feature of EBT films has already been described previously (section 5.2.1.5).

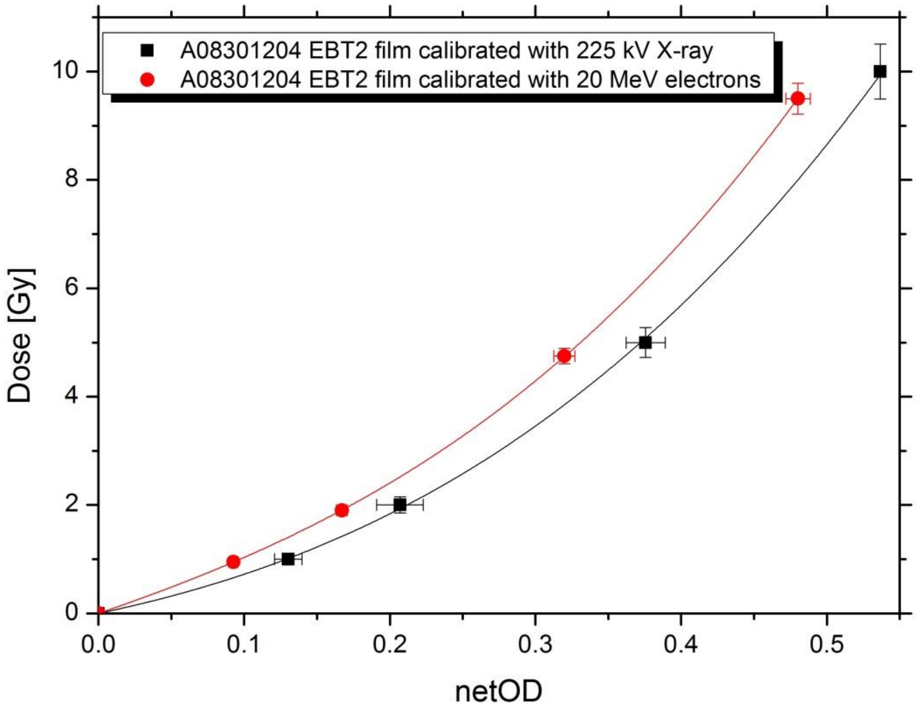

Figure 52. Calibration curves for EBT2 lot# A08301204 for 225 kV X-ray photons (black line) and 20 MeV electron (red line) beams.

As previously investigated [231] the uncertainty between different lot numbers is dose dependent becoming poorer at lower doses. Details of dose response variations between different film lots have been investigated in previous studies, which show that variations can be as small as 0.1% [232], but this is mainly due to variation in the film composition.

The calibration for the LINAC accelerated 20 MeV and 165 MeV electrons have been performed with EBT2 lot # A08301204. However, for dosimetric measurements in ALPHA-X laboratory lot # A04181101 has been used. This lot of EBT2 film has not been calibrated with the 20 MeV electron source. Therefore, based on measurements with 225 kV photon source, the relative uncertainties have been evaluated. The uncertainties, calculated for A04181101 and A12171003B lots, are dose level dependent and are shown in Table 17.

Table 17. Relative dose uncertainties for lot numbers: A04181101 and A12171003B analysed with A08301204 calibration curve.

	relative uncertainty [%]			
lot #	*1 Gy*	*2 Gy*	*5 Gy*	*10 Gy*
A04181101	6.0	5.1	4.6	10.1
A12171003B	5.8	4.2	4.0	3.4

Several investigations have described the local heterogeneity in EBT2 films [233-236]. Many of these studies reported that intra- and intersheet uniformities are not more than 5% but can be as little as 0.5%. Several years ago EBT2 film suffered from inconsistency in heterogeneity for a particular lot number. However, more recently development EBT2 film has had a very good inter- and intrasheet uniformity. The finding in Mizuno's studies [232] suggest that film homogeneity is independent of the expiration date, but only on lot number, which is also confirmed in these studies. Therefore, for very precise film dosimetry, which is required in clinical scenario, it is important to establish calibration curve for each lot number separately.

5.2.2.4. Calibration curve for VHEE experiments

Calibration curve (Figure 53) with 20 MeV LINAC has been produced according to methodology described in previous chapters.

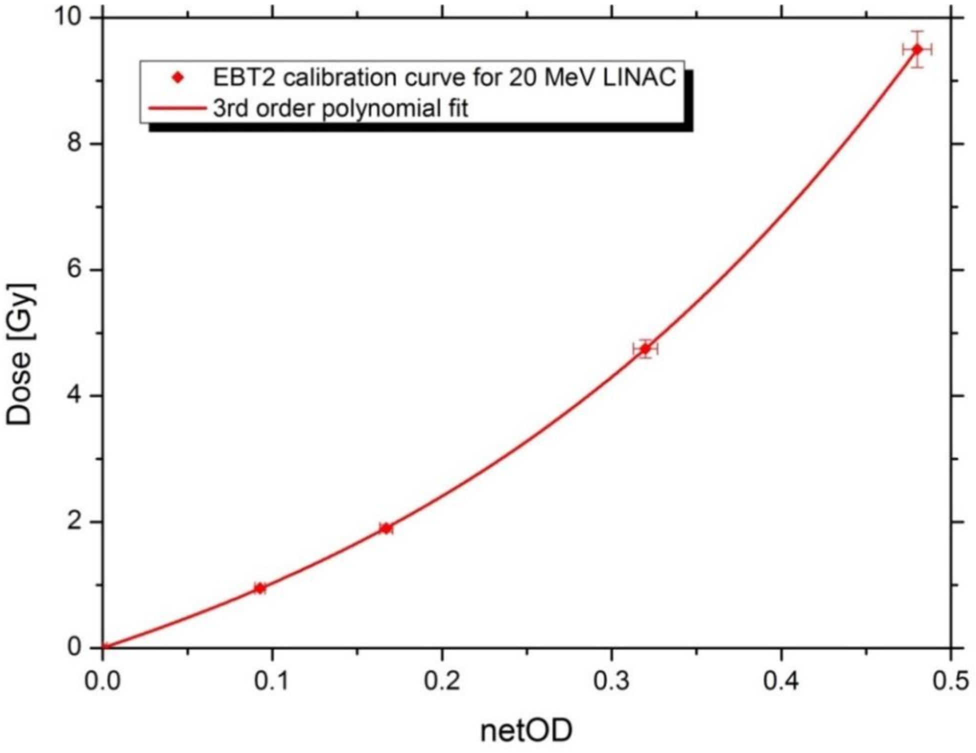

Figure 53. EBT2 film calibration curve (lot#: A08301204) used in this study.

The film response is converted to *netOD* using equation (5.3). To provide *netOD*-to-dose calibration the dataset in Figure 53 has been fitted in OriginPro 8.6 with a nonlinear function (equation (5.5)). Since there are no explicit solutions to the normal equations, an iterative strategy to estimate the parameter values is employed. This process starts with some initial values. With each iteration, a χ^2 value is computed and then the parameter values are adjusted to reduce the χ^2. When the χ^2 values computed in two successive iterations are small enough (compared with the tolerance), the fitting procedure converges. OriginPro uses the Levenberg-Marquardt (L-M) algorithm to adjust the parameter values in the iterative procedure. This algorithm, combines the Gauss-Newton method and the steepest descent method. During L-M iteration, the partial derivatives matrix F of the fitted function f is calculated, after which the variance-covariance matrix is calculated by: $C = (F'F)^{-1}s^2$, where s^2 is the mean residual variance, or the deviation of the model, and can be calculated as follows: $s^2 = RSS(n-p)^{-1}$, where n and p are the indexes of a measured and estimated values, respectively. The square root of a main diagonal value of this matrix is the standard error, which describes uncertainty of the fitted parameters given in Table 18.

Table 18. Fit parameters of the dose response curve.

Fit parameters			
A_0 [Gy]	A_1 [Gy]	A_2 [Gy]	A_3 [Gy]
0.0014±0.0080	9.0563±0.166	9.5698±0.8883	26.5996±1.2336

Dose uncertainties are *netOD*-dependent, therefore need to be calculated for each dose level. The calculated experimental and fit uncertainties are calculated according to equations (5.8) and (5.9) and together with the combined estimated uncertainty for each dose level are shown in Figure 54.

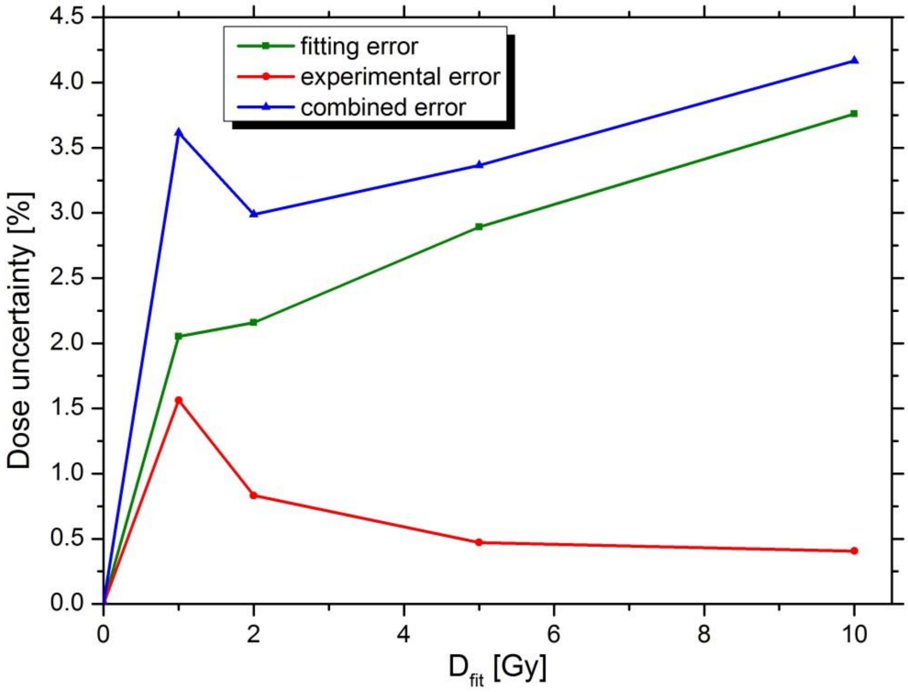

Figure 54. Total dose uncertainty associated with EBT2lot # A08301204 films used in the experiments.

The combined dose uncertainties related to fit parameters (according to equation (5.9)) increase with increasing dose level up to 3.7% for 10 Gy dose level for the calibration fit. Accounting for additional uncertainty in the measured *netOD*, the total uncertainty in dose determination is better than 4.5% for all investigated dose levels.

5.2.2.5. Radiochromic Film Scanning Protocol using a Flat Bed EPSON 10000XL Pro Scanner

In light of the results of this section, the following scanning protocol has been developed:

1. Scan films 24 hours post-irradiation.
2. Warm up scanner by initiating 5-10 consecutive scans of the empty scanner bed.
3. Make sure that all image enhancement options are off.
4. Position short axis of the film perpendicular to the motion of the light source (landscape mode).
5. Move the film to the central region of the scan field – this eliminates light non-uniformity effects.

6. Scan post-irradiated films 3 times and save acquired images in 48 bit mode with 72 dpi resolution.
7. Post process films in ImageJ.
    a. Register films.
    b. Make an average of 3 scans for each dose level.
    c. Calculate *netOD* and its uncertainty.
    d. Apply *netOD*-to-*dose* calibration function to obtain dose maps for irradiated films.

5.2.3. Calibration of EBT2 film with 165 MeV VHEE

5.2.3.1. INFN SPARC Laboratory

SPARC (Sources for Plasma Accelerators and Radiation Compton with Lasers and Beams) LINAC test bench beamline has been used to perform a reference dosimetry measurements for very high energy electron beam [237]. The concept of operation of linear accelerators used in other medical applications has been widely described in the literature [238-241].

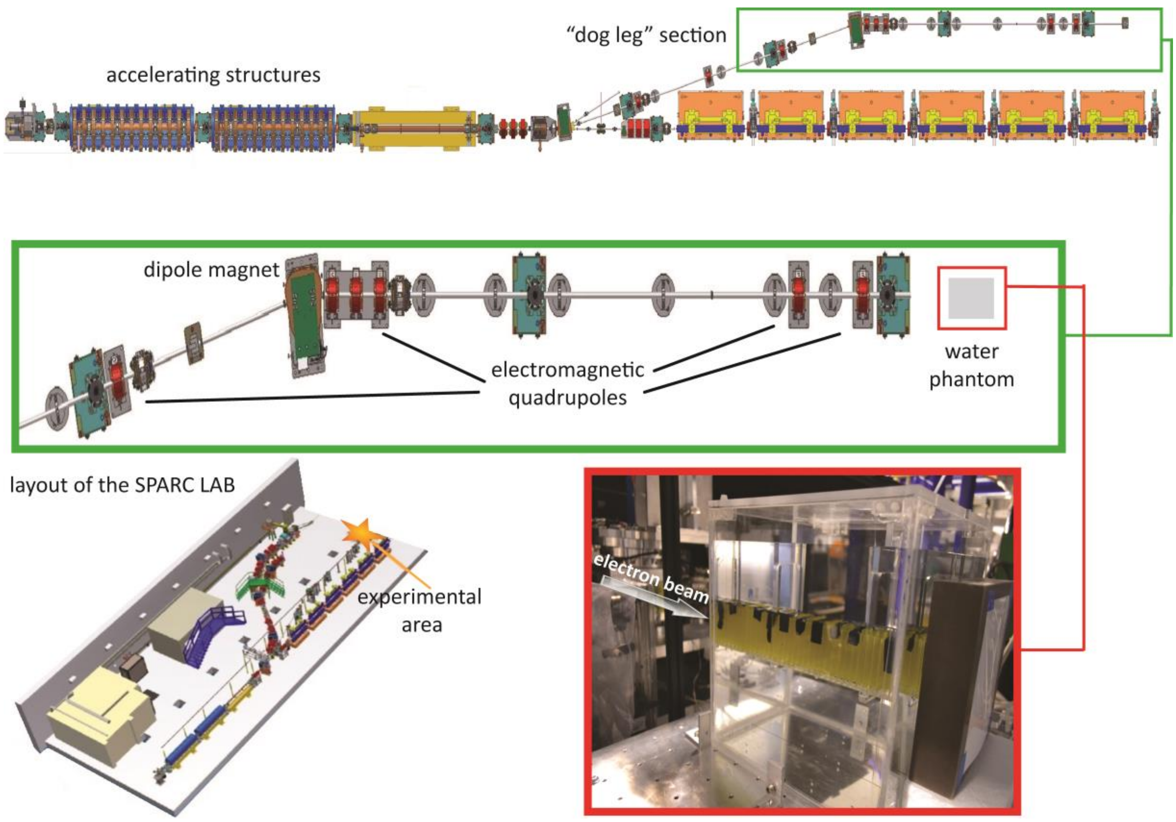

Figure 55. Layout of experiment conducted in SPARC LAB.

The SPARC photoinjector consists of a 1.6-cell RF gun of the BNL/UCLA/SLAC type [242] operating at S band (2856 MHz), with a Cu photocathode (with a high peak field of the order of 120-140 MeV/m) which generates a 5.6 MeV electron beam. Three accelerating sections follow, S-band TW, raising the energy up to about 170 MeV [243]. The transport system consisting of 8 electromagnetic quadrupoles allowed to guide the beam with to interaction area (shown in Figure 55).

5.2.3.2. Beam parameters of the SPARC accelerator

The energy measurements of the SPARC electron beam are performed using dipole electron spectrometer presented in section 3.2.5. Typical energy distribution is shown in Figure 56.

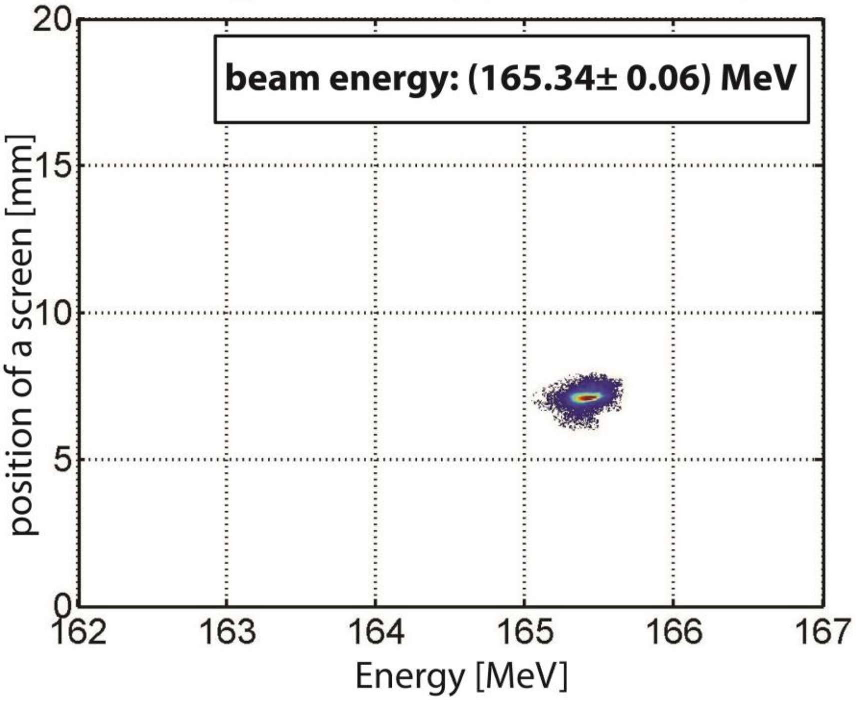

Figure 56. Typical electron beam energy distribution used during dosimetry measurements of VHEE LINAC.

The energy of the SPARC electron beam for the experiment is set to 165 MeV and the bunch length duration is 0.87 ps with an average charge, monitored with integrating current transformer (ICT), of (65 ± 3) pC/shot, giving a peak current ~0.1 kA.

5.2.3.3. Irradiation of EBT2 calibration films with 165 MeV electron beam.

The irradiation setup for the film calibration with the 165 MeV electron beam is shown in Figure 57. A 30 × 30 × 30 cm^3 water phantom surrounded by 6 mm thick poly-methyl methacrylate (PMMA) walls is positioned 41 cm from a 3 mm thick PMMA window. The shape of the SPARC VHEE beam is Gaussian with a 0.43 cm × 0.35 cm FWHM size, and 15 mrad full angle divergence.

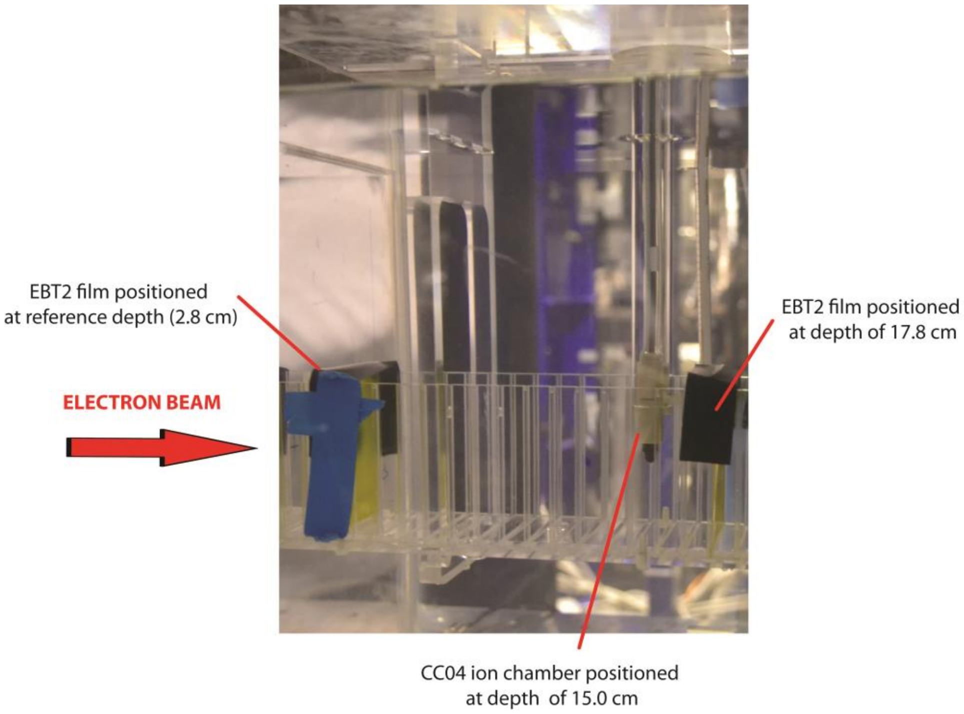

Figure 57. The irradiation setup of theEBT2 film calibration with 165 MeV electron beam. The calibration film is positioned at a reference depth (2.8 cm from the entrance wall of the tank). The ion chamber is positioned at a depth of 15 cm to monitor the beam over the irradiation time.

Prior to film calibration a PDD measurement (described in section 5.3.2.1) of the VHE SPARC beam is carried out. This measurement allows the establishment of the position of the film for calibration. For calibration the film is placed at depth of 2.8 cm from the front wall of the water phantom. The CC04 ion chamber, positioned 12 cm from the calibration film, does not contribute an extra dose to the calibrated film due to backscatter radiation from the chamber.

The EBT2 films (lot#: A08301204) are calibrated with 6 different doses. The films are handled, scanned and analysed according to the procedures described in section 5.2.2. For measurements of the absorbed dose, the 20 MeV calibration curve shown in Figure 53 has been used. To ensure that the calibration curve obtained with 20 MeV electron beam is valid for VHEEs a set of MC calculations for every irradiation dose level is carried out using FLUKA. To simulate the dose absorbed in the active layer of the EBT2 film the dosimeter is modelled as a 5×5 cm^2 sheet composed of five layers: a polyester over-laminate, an adhesive layer, a topcoat, the active layer and a polyester substrate. The film is embedded in a $30 \times 30 \times 30$ cm^3 water phantom surrounded by 6 mm thick poly-methyl methacrylate (PMMA) walls. The SPARC VHEE beam parameters (beam size, energy,

energy spread, divergence, number of shots and charge/shot) are recorded and used for the FLUKA simulations.

The results of the MC calculations and measurements are shown in Figure 58.

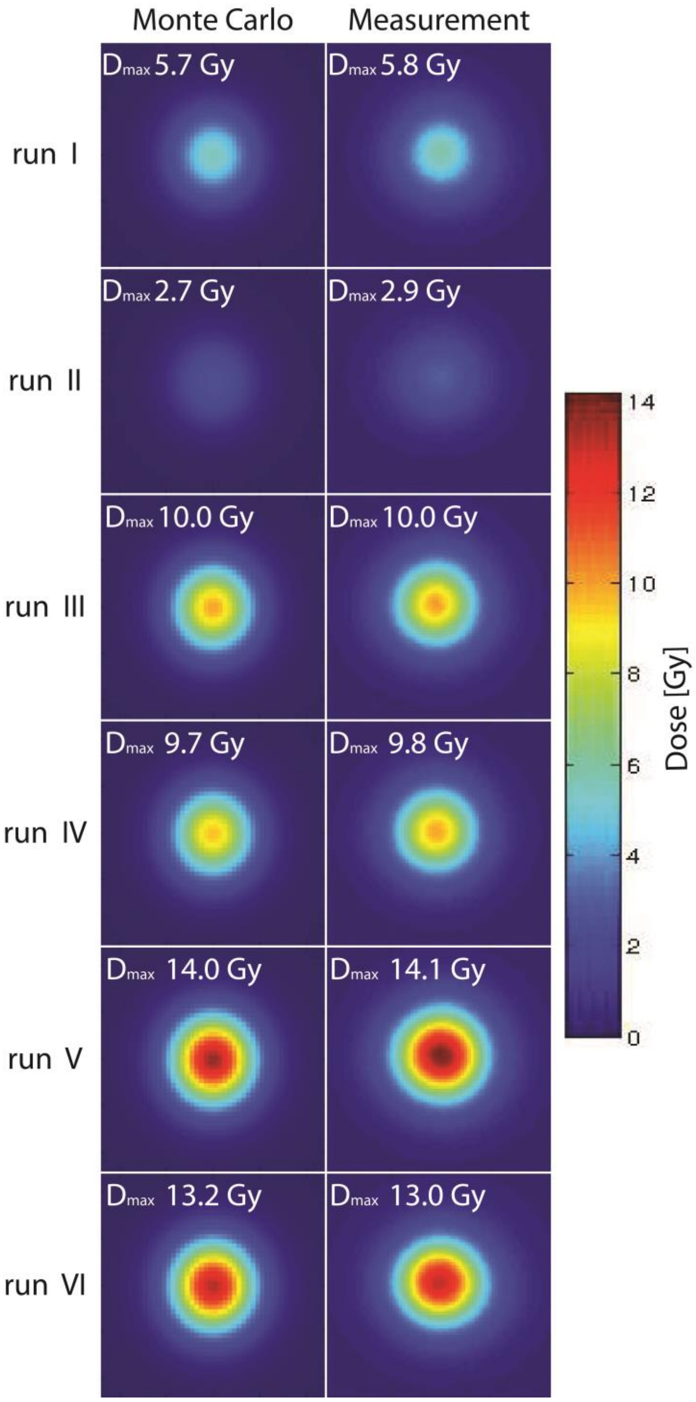

Figure 58. The MC calculated and measured doses absorbed in the EBT2 film exposed to the 165 MeV electron beam.

The calculated and measured (with 20 MeV calibration curve from Figure 53) absorbed dose maps, shown in Figure 58, are in a very good agreement. The MC calculations give statistical uncertainties on the beam axis of the order of 0.5%. The main uncertainties in calculated dose comes from the uncertainty of the average measured charge in a shot, which has been estimated (see the charge/shot standard deviation in Table 20). The measured uncertainties depend on dose level and are mainly related to the film analysis procedure. The evaluated uncertainties for the measured and calculated doses on the central axis of the beam are presented in Table 20.

Table 19. The summary of measured and calculated absorbed doses in EBT2 film.

run #	# of shots	charge/shot [pC]	charge/shot SD [pC]	MC absorbed dose [Gy]	Measured absorbed dose [Gy]
run I	20	69.1	4.5	**5.7±0.3**	**5.8±0.2**
run II	11	56.5	3.2	**2.7±0.1**	**2.9±0.1**
run III	38	64.3	4.4	**10.0±0.6**	**10.0±0.4**
run IV	41	57.7	2.4	**9.7±0.3**	**9.8±0.4**
run V	59	56.8	4.0	**14.0±0.6**	**14.1±0.7**
run VI	62	55.1	4.9	**13.2±1.1**	**13.0±0.7**

5.2.4. MC calculated LET spectra for electron beams

Several investigations of Gafchromic films as a dosimetric tool for proton beams have been presented in references [220-222]. All of these studies show an under-response of EBT films at the Bragg peak. This, so-called quenching effect has been associated with the higher LET of proton beams at their Bragg peak. To investigate if the LET of VHEEs have an effect on the EBT2 film response MC calculations have been carried out. The LET spectra is scored for 20 MeV and 165 MeV beams (Figure 59) using the FLUKA USRYIELD utility.

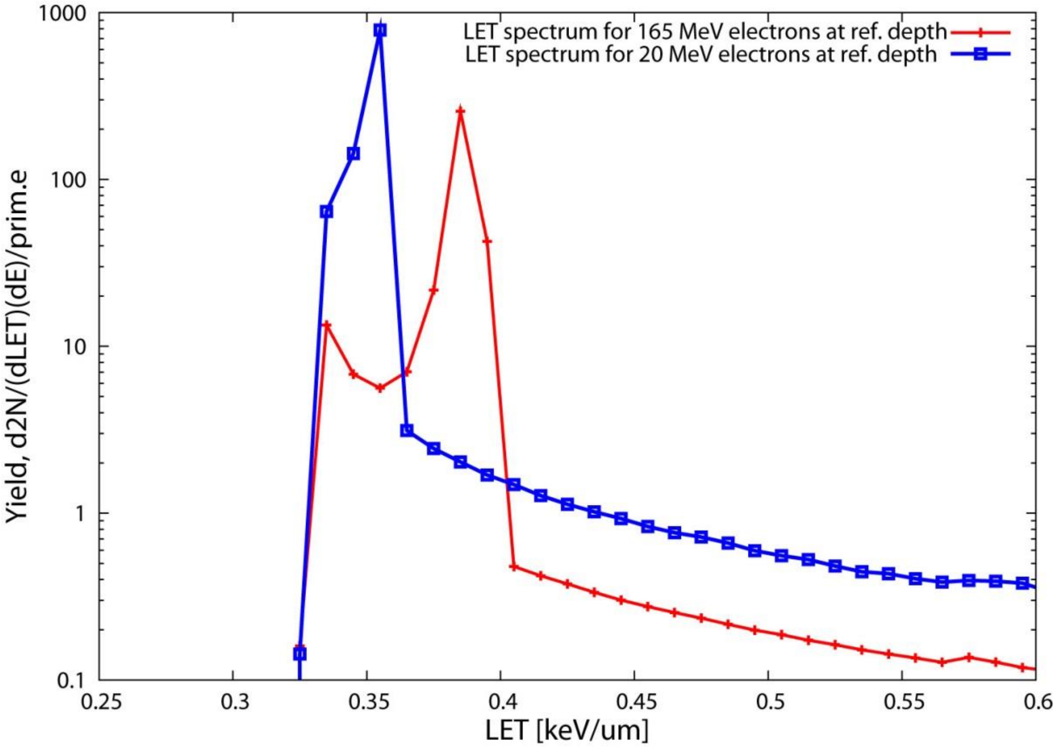

Figure 59. LET spectra for 165 MeV and 20 MeV at the reference depth in water.

The LET spectra for the 165 MeV beam have a maximum at 0.39 keV/μm, and a long tail decaying with increasing LET values. There is a visible LET peak downshift to 0.35 keV/μm for the 20 MeV electron beam. However, the LET values for both of the modalities are very similar.

5.2.5. Conclusions

In this section characterization of the dosimtery system, which consists of EBT2 Garchromic® film and the EPSON Expression 10000XL Pro flat-bed scanner has been presented. This system has been chosen for dosimetry of very high energy electrons due to its many advantages over other available detectors. EBT2 film exhibit a high spatial resolution, tissue equivalence and is suitable for dose measurement in small radiation fields with high dose gradients, which VHEEs exhibit. A flat-bed scanner, on the other hand, is chosen as a primary film digitizer because of its availability, OD range, functionality and speed. An investigation into a universal EBT2 calibration fitting function, equation (5.5) with fitting parameters listed in Table 14**,** demonstrated a superior goodness of fit over a large range of absorbed dose. The total uncertainty is less than 4.5% for all investigated dose levels. Nevertheless, care needs to be taken when using different lot numbers because the sensitivity of the film for various batches can differ.

The calibration of EBT2 film (lot#: A08301204) has been performed with two different LINAC-generated electron sources: clinical 20 MeV electron and 165 MeV VHEE beams. The dose absorbed in the EBT2 film for the irradiation with 165 MeV LINAC is modelled using the Monte Carlo code.

No difference in film response is observed for low and very high energy electron beams. The calculated LET spectra (Figure 59) for both beams, low energy electrons and VHEEs, are very similar, therefore one could expect the EBT2 film response difference to be indistinguishable for these modalities.

The results presented in this section show that EBT2 film is an energy-independent dosimeter within the investigated electron energy range and therefore can successfully be used in dosimetry of unconventional VHEE beams.

5.3. Film dosimetry of electron beams

The EBT2 and EPSON Expression 10000XL dosimetry system has been used for dose measurements with 3 different electron sources: 20 MeV medical electron LINAC, 165 MeV VHEE LINAC and 135 MeV LWFA.

5.3.1. Dosimetry with 20 MeV LINAC

5.3.1.1. PDD measurements with EBT2 film

One of the fundamental parameters used in dose calculations in a patient treatment plan is the percentage depth-dose typically measured using an ionization chamber. However, there are situations where ion chambers are difficult to use or are problematic. In such cases, radiochromic film may be an alternative. The EBT2 model GAFCHROMIC film is investigated as a potential tool for depth-dose measurement of radiotherapy beams over a broad range of energies and modalities [213].

PDD is one of the essential data sets required for commissioning treatment-planning systems, for calculating patient monitor units, or treatment-time, or dose distribution. In addition, it allows verification of beam energy stability during quality-assurance tests. PDDs are commonly measured in a water phantom using ionization chambers. However, for some beam modalities and in some physical situations (e.g. for a small field sizes), use of ionization chamber for measuring PDD can be problematic. Good spatial resolution in depth-dose measurements becomes very important in high-gradient regions of small fields, as with VHEEs. The spatial resolution (for ion chambers) is limited by the physical size of ionization cavity [244-246]. With introduction of radiochromic films, several investigators [228, 247, 248] have evaluated the film for reference dosimetry and in some instances for depth-dose measurements as an alternative to most commonly used dosimeters such as diode or ion-chamber detectors [249].

The availability of EBT2 films has provoked several research groups to study its energy dependency for reference dosimetry [216] and it has been shown [212] that the energy dependence of the EBT2 film is very weak over a broad range of beam qualities and modalities used in radiation therapy. Because EBT2 film is near-tissue equivalent, has good spatial resolution (< 0.1 mm) and is usable in water, it is an attractive candidate as a dosimeter for PDD measurements.

We performed a PDD measurement of LINAC-generated 20 MeV electron beam and compare it with ion chamber measurements. The irradiation setup is presented in Figure 60.

Film PDD measurement results for 20 MeV electron beam are presented in Figure 61. Comparison is shown against multilayer ion-chamber data. Film data are normalized to match the ion-chamber data at depth of 2.5 cm in the plateau region.

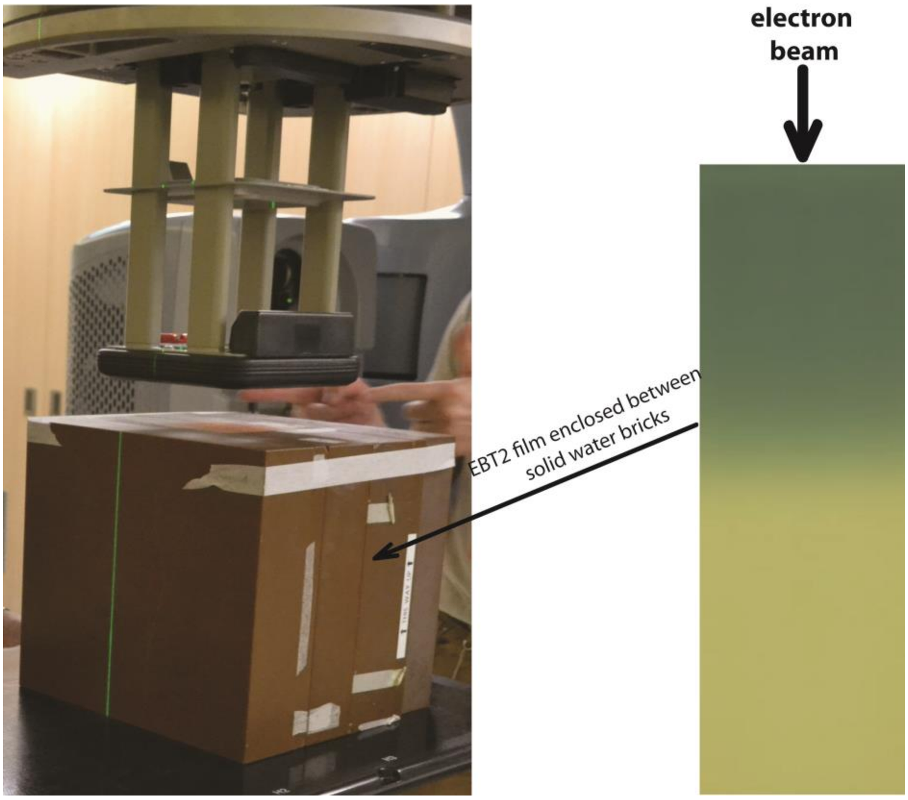

Figure 60. Irradiation setup in 20 MeV clinical LINAC to obtain PDD profile with EBT2 film.

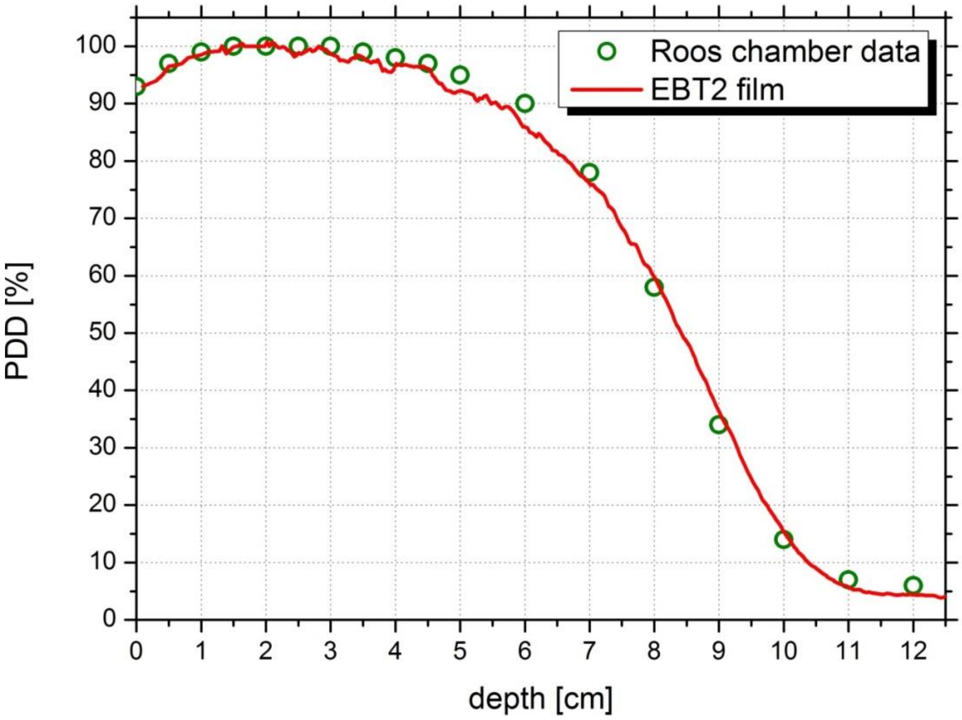

Figure 61. Comparison of percentage depth-dose data measured with EBT2 film and ion chamber (CC04) for a 20 MeV electron beam. The data are normalized to depth of maximum dose at 2.5 cm.

The agreement between PDD curves obtained with ion chamber (green solid circles) and EBT2 film (solid red line) is, in general, very good and the maximum difference between PDD values is found to be 3% at a depth of 6 cm. This is most probably due to nonuniformity of the EBT2 sheet used for that measurement. Inter-batch film nonuniformities can result in few percent *netOD* variations [213, 229], which in turn can slightly distort PDD measurements.

Generally, we conclude that film dosimetry can provide high spatial resolutions PDD measurements for small field size and cause less or no distortion in high-gradient regions such as the buildup region.

5.3.2. INFN SPARC Laboratory- dosimetry with 165 MeV electron beam

In this section a set of dose measurements for a VHE electron beam with EBT2 films (lot# A08301204) is presented. The measurements are compared with simulations using the MC FLUKA code (described in chapter 4). For radiation safety assessment, a set of MC simulations investigating neutron generation, activation and equivalent doses after irradiation with VHEEs are presented.

FLUKA [110, 250] is used to simulate the dose deposition of VHEE beams in the active layer of EBT2 film. Customization of all FLUKA utilities (cards) used to calculate neutron production, induced radioactivity and equivalent doses have been described in chapter 4. The set of parameters PRECISIO [110] is used to configure the physical model for the simulations. In these simulations electron/positron and photon production thresholds are set to 10 keV. 1×10^7 initial electrons trajectories are used for the calculation.

5.3.2.1. Depth dose measurements of LINAC VHE electron beam

The dosimetric measurements of VHEE beam have been carried out at the INFN Laboratories on the SPARC beamline. The experimental setup has been described in section 5.2.3.1 and the layout with the experimental area is shown in Figure 55.

As described in section 5.3.1.1, PDD measurements of very high energy electron beams can be performed with EBT2 films. However, for small field size beams (as for VHEEs) the alignment of the central beam axis (where the PDD measurements are performed), with a longitudinally placed film (top image in Figure 62), is necessary.

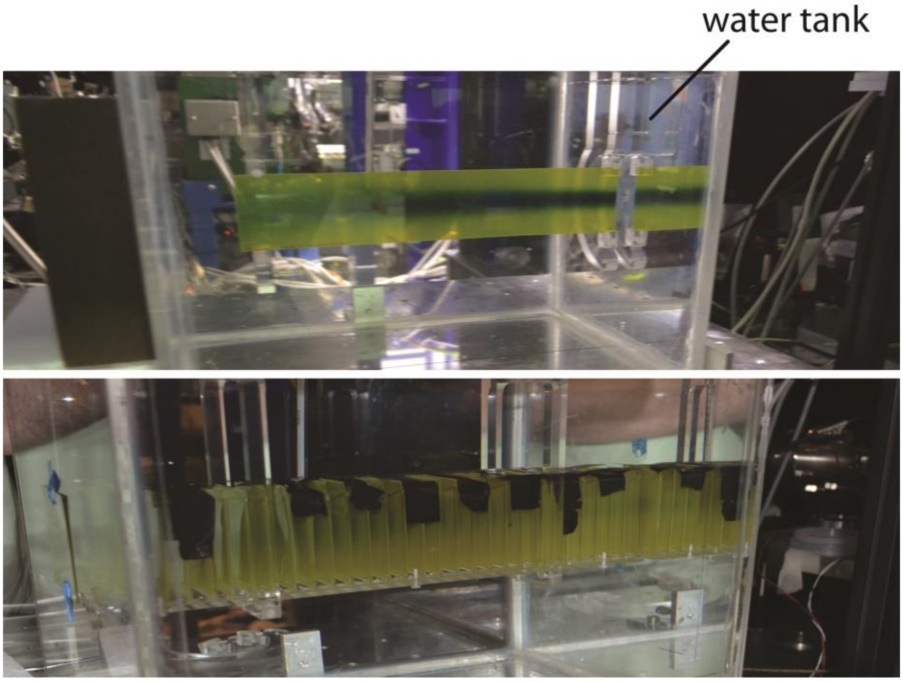

Figure 62. Film irradiation setup. Film positioned longitudinally (top) and transversely (bottom) to the electron beam propagation axis. Electrons propagate from left to right.

The measured 2D longitudinal relative dose distribution is shown in Figure 63. For the comparison the 2D dose map along beam central axis has been calculated using FLUKA. It can be seen that the simulation is not in good agreement with the experimental result. The reason for this is the slight misalignment of the central axis of the film with the central axis of the beam propagation. This is not an issue in clinical LINACs, where a laser system is used for the alignment of the irradiation setup.

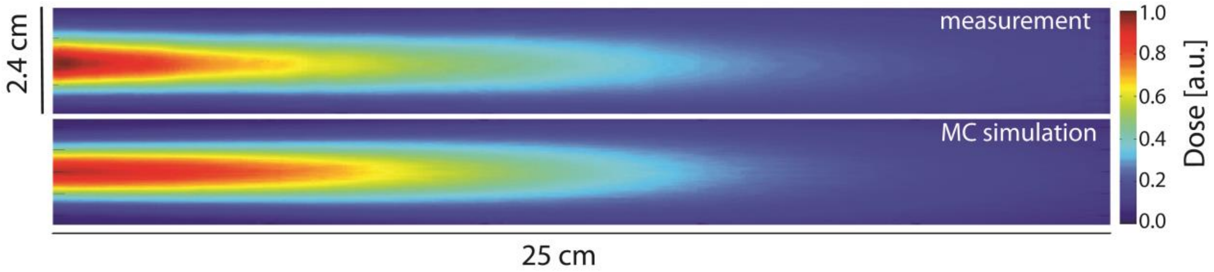

Figure 63. 2-dimensinal measured (top) and MC calculated (bottom) dose maps of 165 MeV SPARC electron beam (experimental layout shown in the top of Figure 62). For the calculation the experimental set-up was modelled using FLUKA. All dose measurements in these studies are calibrated using the calibration curve shown in Figure 53.

There is another, very robust, method of measuring depth dose profile using EBT2 films where a precise alignment to the central axis of the beam is not required. It is possible to place a set of Gafchromic films sheets at various depths in a water phantom normal to the beam propagation axis (see bottom image in Figure 62). Two-dimensional dose maps, recorded on film, allow to measure the dose on the central axis of the beam. This allows reconstruction of the depth dose profile.

The irradiation setup and the beam parameters is discussed in section 5.2.3.3. The irradiated films have been analysed according to procedure described in section 5.2.2.5. To compare with measurements MC calculations have been carried out.

To simulate the dose deposition of SPARC 165 MeV VHEE beam in the active layer of the EBT2 film the dosimeter is modelled as described in section 5.2.3.3. A set of 18 EBT2 Gafchromic film sheets are equi-spaced every 1 cm along the beam axis in the water tank.

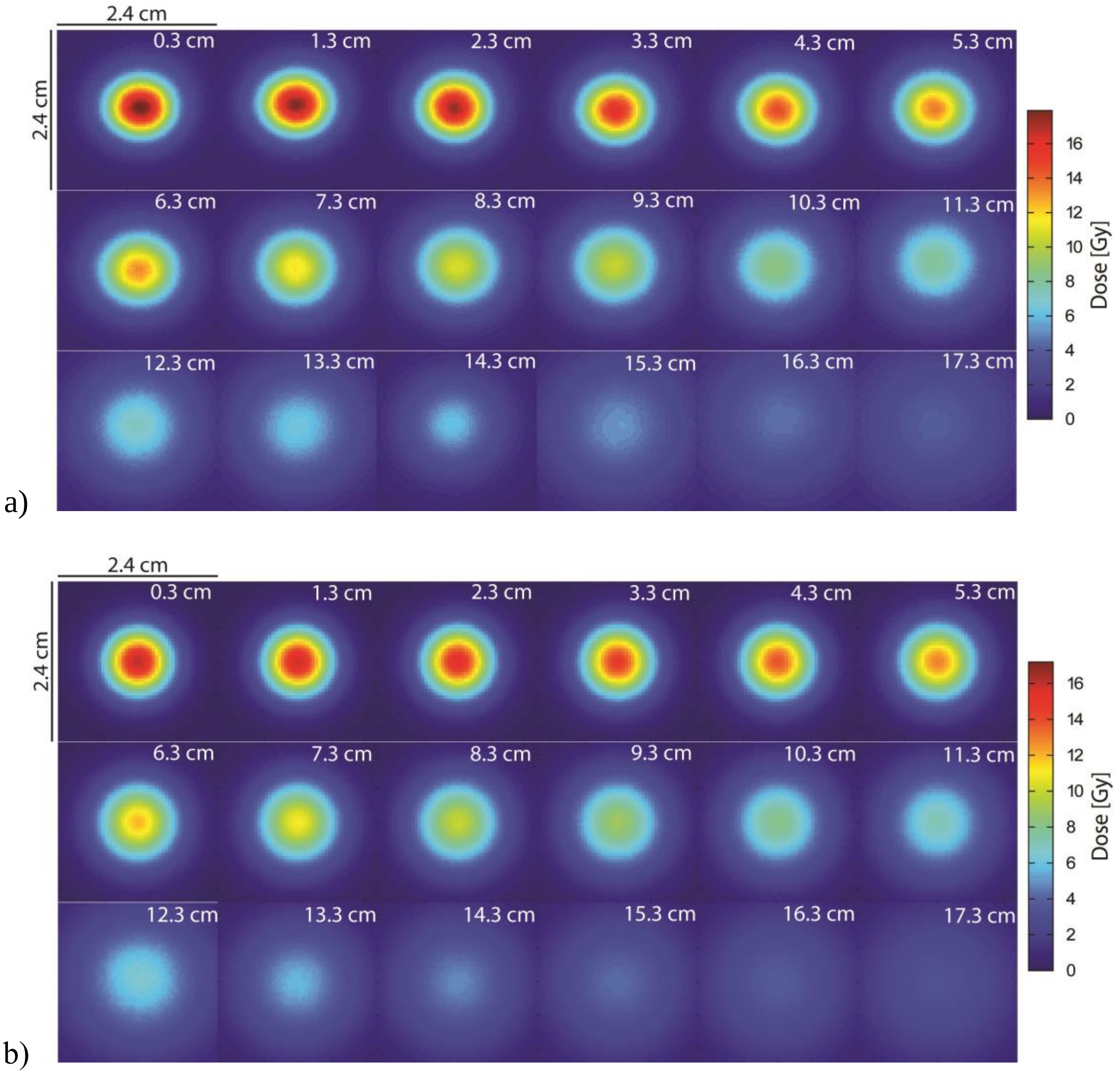

Figure 64. Measured (a) and calculated (b) two-dimensional dose maps for the 165 MeV SPARC electron beam in planes normal to beam central axis at different depths in the water phantom. The 2D dose distributions are normalized to maximum dose deposition for both the measurements and simulations.

Figure 64 shows a comparison between the measured and calculated dose maps for a 165 MeV very high energy electron beam from the SPARC accelerator. All beam parameters (beam energy, charge, field size) are measured and these values are used in FLUKA to precisely model the beam. To emphasise the evolution of the beam spatial distribution, the colour scale dose maps in Figure 64 are normalized to the maximum dose deposited in the film at 0.3 cm depth. The calculated transverse dose maps are in excellent agreement with the measurements. In such film configuration the precise alignment of the film centre to the central axis of the beam is not vital, and the percentage depth dose profile can be easily reconstructed. Measuring the maximum dose deposited at each film position along beam propagation in the phantom gives the depth-dose profile for the SPARC VHE electron beam. The results of the measurement are shown in Figure 65. The FLUKA simulated energy deposition curves represent dose deposited in absolute terms, i.e in Gy.

The measured PDD curve is in a good agreement with the simulation. There is a small discrepancy between measurement and calculation for the first three points in the curve and at a depth of 14-16 cm. These are mainly due to measurement uncertainties, which arise from the uncertainties due to the dosimetry system, which are dose dependent. The combined uncertainties for the calibration curve is presented in Figure 54. Additional uncertainty is due to film non-uniformity (inhomogenities), which has been reported to be less than 2% [199, 213, 229].

Statistical uncertainties of the Monte Carlo simulations are less than 0.5% on the beam axis within the first 10 cm of the beam propagation and gradually increase with increasing depth. The main uncertainty in the calculated dose is due to charge/shot jitter, which is estimated to be ± 4pC.

To more carefully study the measured and calculated lateral dose maps (from Figure 64), the FWHM lateral beam size has been investigated at each depth and the results are shown in Figure 66.

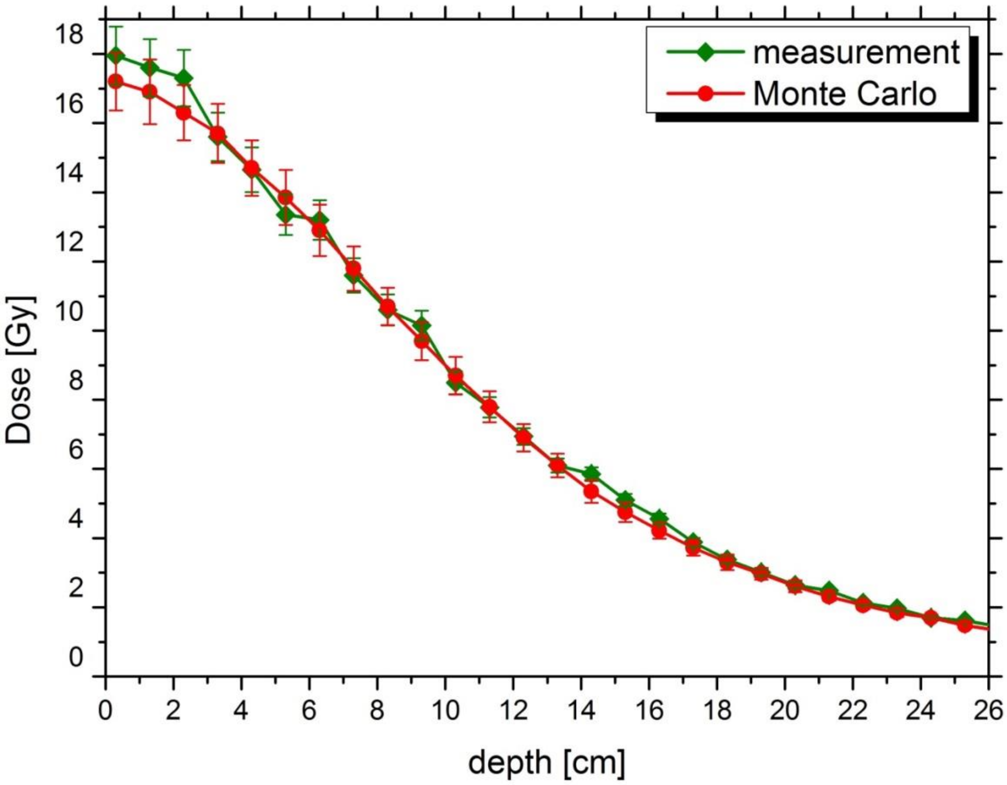

Figure 65. Measured (green curve) and calculated (red curve) depth dose profile for 165 MeV electron beam from the SPARC beamline.

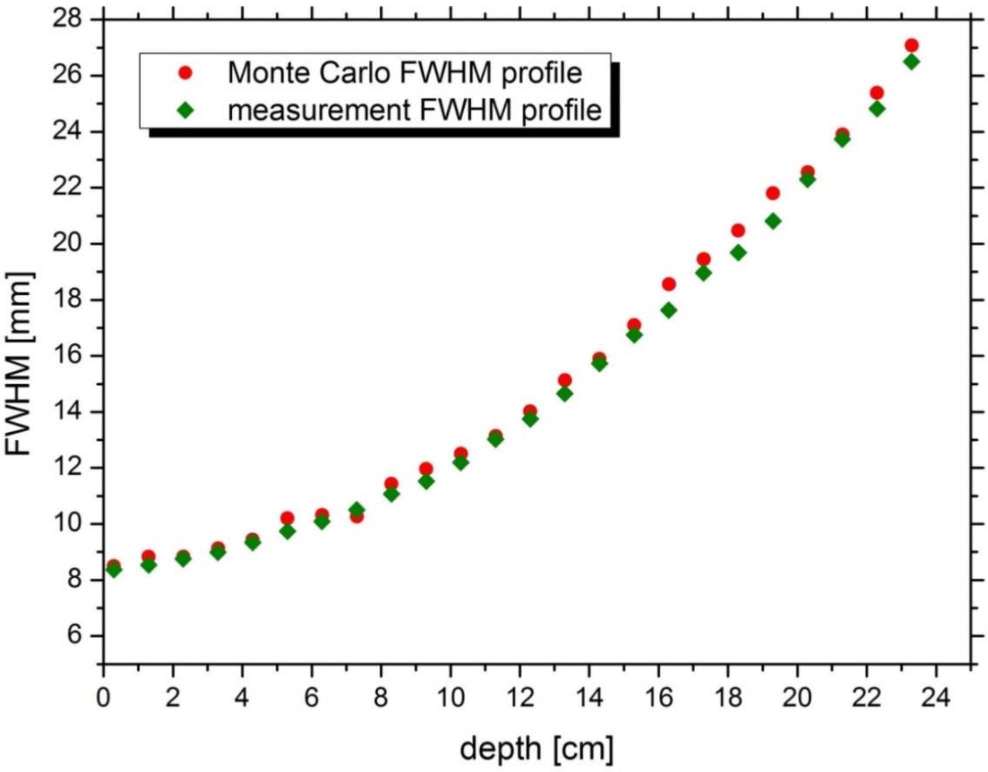

Figure 66. Evolution of the FWHM beam profile as a function of depth within the water phantom.

The evolution of FWHM width of the beam lateral profiles at various depths in the water phantom for SPARC (Figure 66) strongly depend on the initial beam divergence. The field size width, close width to the rear of the water phantom, is approximately three times that at the entrance. This is due to multiple Coulomb scattering which deflects electrons transversely.

5.3.2.2. MC calculations for the SPARC VHEE beam in relation to neutron production

The possible risks associated with working with VHEE radiation have been outlined in chapter 4. To investigate the possible effect of neutron production during conducted experiment in INFN Laboratories, Monte Carlo simulations for the SPARC irradiation setup have been performed. Neutron production in radiation therapy has already been described in section 4.2.6. The set of FLUKA parameters for the MC calculations is specified in section 4.2.6.1.4. The calculated neutron yield generated in and around water phantom irradiated with the SPARC beam is presented in Figure 67.

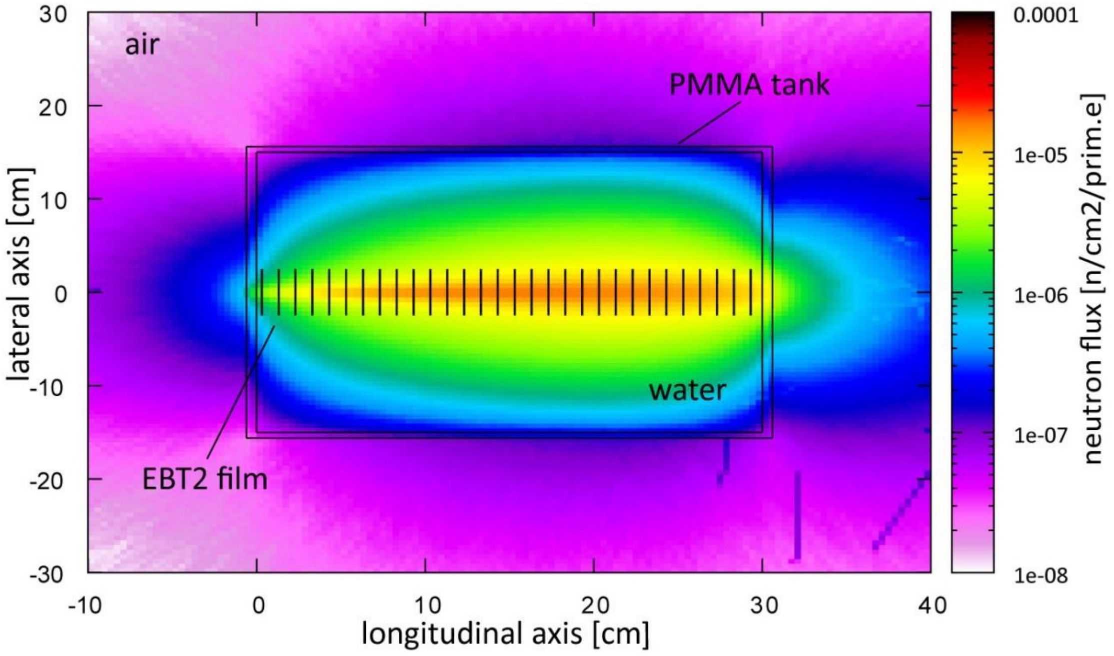

Figure 67. Neutron fluence inside and around the 30×30×30 cm^3 water phantom with transversely distributed EBT2 films for 165 MeV beams.

The statistical uncertainty evaluated at the exit wall of the phantom is less than 2.5%. The neutron fluence (neutrons/cm^2), shown in Figure 67, is of the order of 10^{-5} neutrons per incident electron in the area of maximum dose deposition and 10^{-7} at 10 cm from the back wall of the water phantom.

To evaluate the extra dose deposited on the film and the cooling time before handling, it is necessary to consider the induced activity in the film. For this case the activity is scored for the first (0.3 cm depth), middle (14.3 cm depth) and last film (29.3 cm depth) for each layer of EBT2 film separately. The customization parameters are described in section 4.2.7. The results expressed in absolute values (Bq) and percentage activity are presented in Table 20. The activation due to the generation of radionuclides is separately scored for each film layer.

Table 20. Activation in first, middle and last EBT2 film irradiated in the SPARC beamline calculated for various cooling times specified for each film layer.

		radionuclide activity after 1 min [Bq(%)]		radionuclide activity after 5 min [Bq(%)]		radionuclide activity after 10 min [Bq(%)]		radionuclide activity after 20 min [Bq(%)]	
depth [cm]	layer(*)	$^{11}_{6}C$	$^{15}_{8}O$	$^{11}_{6}C$	$^{15}_{8}O$	$^{11}_{6}C$	$^{15}_{8}O$	$^{11}_{6}C$	$^{15}_{8}O$
0.3	PO	0.96(93.18)	--	0.84(100)	--	0.7(100)	--	0.5(100)	--
	ADL	0.43(40.38)	0.58(53.83)	0.38(70.15)	0.15(27.47)	0.32(90.65)	0.03(7.68)	0.23(98.39)	--
	TC	--	--	--	--	--	--	--	--
	ACL	0.38(30.59)	0.81(65.04)	0.32(57.55)	0.21(35.94)	0.28(81.92)	0.04(11.07)	0.20(94.47)	--
	PS	0.98(95.58)	--	0.84(100)	--	0.72(100)	--	0.51(100)	--
14.3	PO	9.62(98.21)	--	8.4(100)	--	7.09(100)	--	5.04(100)	--
	ADL	4.26(37.38)	7(61.33)	3.72(67.08)	1.79(32.34)	3.14(89.97)	0.33(9.38)	2.24(99.02)	--
	TC	3.25(25.29)	8.89(69.14)	2.48(53.91)	2.28(43.29)	2.40(82.02)	0.42(14.24)	1.7(95.76)	--
	ACL	4.26(34.12)	7.6(60.90)	3.72(63.52)	1.59(33.30)	3.14(87.12)	0.36(9.88)	2.23(97.30)	--
	PS	9.58(98.19)	--	8.36(99.98)	--	7.05(100)	--	5.02(100)	--
29.3	PO	11.60(97.7)	--	10.10(100)	--	8.55(100)	--	6.09(100)	--
	ADL	5.02(39.80)	7.30(57.94)	4.38(69.42)	1.87(29.69)	3.69(90.64)	0.34(8.38)	2.63(98.83)	--
	TC	4.19(27.39)	10.2(66.54)	3.66(57.08)	2.61(40.75)	3.09(84.52)	0.48(13.05)	2.20(96.96)	--
	ACL	4.82(33.20)	9.10(62.68)	4.21(61.49)	2.33(34.35)	3.55(85.64)	0.43(10.27)	2.53(96.19)	--
	PS	11.3(97.65)	--	9.83(100)	--	8.29(100)	--	5.90(100)	--

(*) PO- polyester layer, ADL- adhesive layer, TC- topcoat, ACL – active layer, PS- polyester substrate

Activity in films at all depths for adhesive layer, topcoat and active layer, 1 minute after the beam irradiation ceased, is determined by $^{11}_{6}C$ (22.3 minute half-life) and $^{15}_{8}O$ (122.4 s half-life) radionuclides with the activity specified in Table 20. After 20 min of cooling, the activity is determined in these 3 layers of the film mostly by $^{11}_{6}C$.

In absolute terms, the total activity for the film irradiated in SPARC is 1.6 Bq, 16.5 Bq and 19.5 Bq, for the first (0.3 cm depth) middle (14.3 cm depth) and last (29.3 cm depth) film, respectively, after 20 min of cooling. The amount of the radionuclides scored in EBT2 films increases towards the exit of the water tank where the majority of (γ,n) reactions occur.

The equivalent doses (discussed in section 4.2.8) due to induced radioactivity also has been calculated.

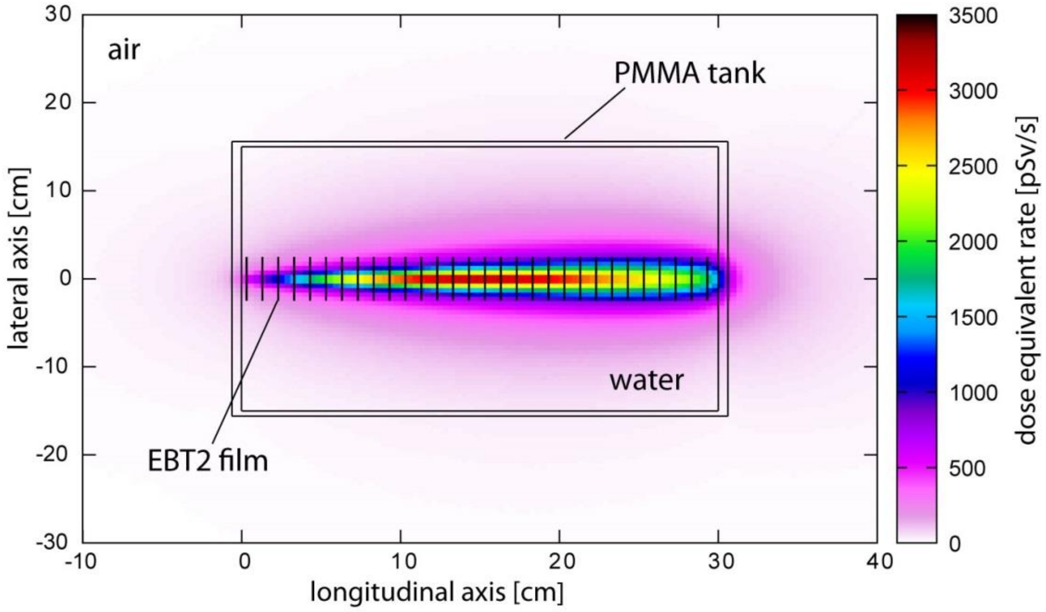

Figure 68. Ambient dose equivalent rate for irradiation in the SPARC beamline from induced radioactivity after 1 minute cooling time. The beam enters from the left hand side.

Figure 68 shows the ambient dose equivalent H*(10) rate values across the central beam axis for various positions inside and around the water phantom irradiated with a 165 MeV beam, 1 minute after beam ceased. The figure shows a two dimensional distribution of the equivalent doses. From the handling and radiation safety point of view it is important to estimate the dose equivalent around the water tank. Table 21 presents the values of H*(10) at 1 mm from the front and rear wall of the water tank surface along beam central axis for various cooling times.

Table 21. H*(10) values at 1 mm distance from the front and the rear wall of the water tank for various cooling times for the SPARC beam.

Cooling time	front surface		rear surface	
	eq. dose rate [pSv/s]	stat. error [%]	eq. dose rate [pSv/s]	stat. error [%]
1 min	125.31	0.53	571.56	0.56
5 min	36.70	0.48	175.74	0.45
10 min	11.46	0.45	61.04	0.24
15 min	6.07	0.57	35.37	0.20
20 min	4.42	0.64	26.71	0.23

The largest cooling time presented in the table (i.e. 20 minutes) corresponds to the moment of removing films from the water. At this time the dose equivalent rate at the rear of the phantom is just 26 pSv/s.

5.3.3. *ALPHA-X Laboratory*

The experimental layout and components of ALPHA-X accelerator has already been discussed in chapter 3. The setup of the dosimetry experiment with LWFA VHEE beam is shown in Figure 69.

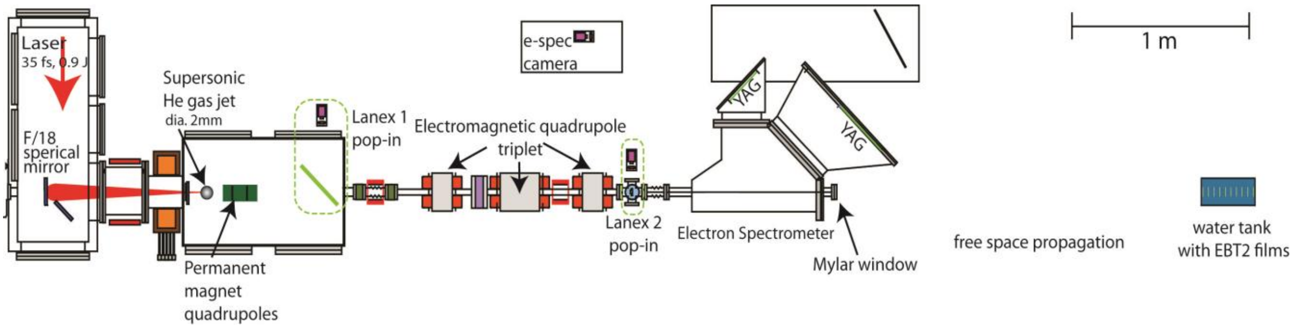

Figure 69. The schematic of the ALPHA-X laser-plasma wakefield accelerator, showing the positions of the gas jet relative to the key detection systems and dosimetry measurement setup.

A 22 cm long water phantom (15 × 30 × 22 cm) is placed 185 cm after a 50 μm thick Mylar window. A set of 10 EBT2 Gafchromic film sheets are placed equi-spaced every 2 cm along the beam axis in the water tank. Characterization of the electron energy spectra is carried out using a magnetic dipole electron spectrometer, as described in section 3.2.5. Electron spectra are observed on scintillating Ce:YAG crystals positioned in the focal plane of the spectrometer and the image is captured on a 12-bit CCD camera. The accumulated spectra of 200 shots is shown in Figure 70.

Charge recorded using Fuji BAS-SR image plates [91] is on average between 5 and 10 pC/shot. Typical r.m.s. lengths of the laser-plasma accelerated electron bunches are in the range of 1-10 fs [182]. To estimate the charge density during the experiment, a bunch length of 5 fs is assumed because of dispersion arising from the beam energy spread, which gives a peak current of the order of 1 kA at the entrance to the phantom. The accelerator pulse repetition rate is restricted to 0.33 Hz for the dosimetry measurements. Following optimal collimation and focusing of the beam using permanent and electromagnetic quadrupole magnets, the mean transverse cross-sectional diameter of the Gaussian beam at the entrance of the water tank is 1.6 cm full-width at half-maximum (FWHM).

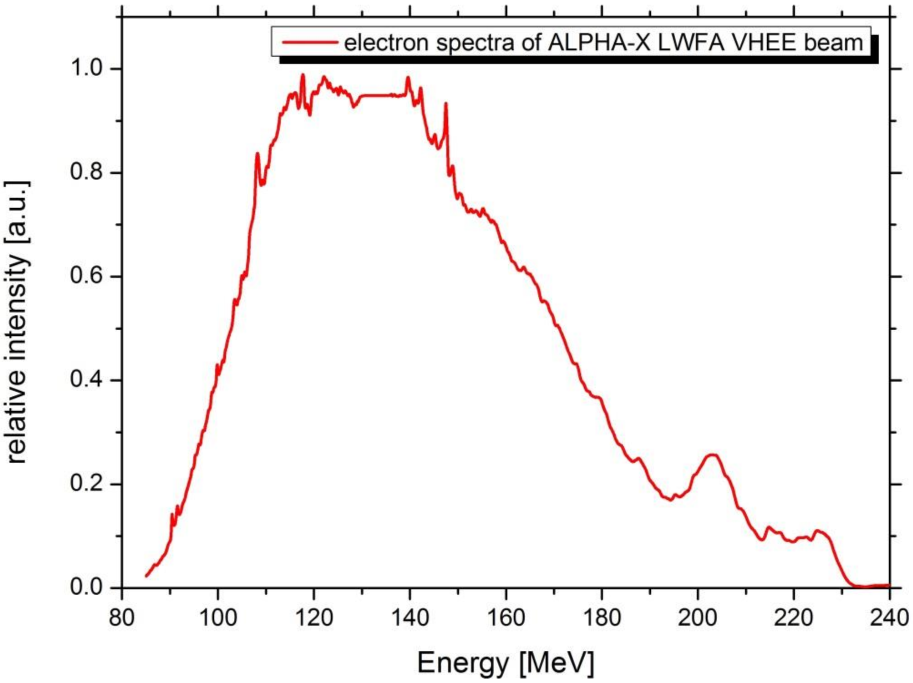

Figure 70. Electron spectra of the ALPHA-X LWFA VHEE beam during the dosimetry experiment. For the approximation of Gaussian spectra the central energy corresponds 135 MeV, with a 44 MeV r.m.s. energy spread.

5.3.3.1. Depth dose measurements of LWFA VHE electron beam

The ALPHA-X beam dose deposition measurements have been carried out using EBT2 lot# A04181101. Due to small variations in the film composition the batch has a slightly different response to lot# A08301204 used for calibration, as has already been shown in Figure 55. The dose response difference of the two batches are of the order of 6.0% and 10.1% for 10 cGy and 100 cGy dose levels, respectively (please, refer to Table 17).

As the ALPHA-X LWFA VHEE beam exhibits shot-to-shot variations in lateral beam profile and pointing stability, the field shape and size is averaged over the number of shots.

This profile is well approximated by a Gaussian with 0.75 cm by 0.7 cm FWHM field size and 8 mrad divergence. A user written FLUKA SOURCE subroutine [110] is used to sample energy from the experimental cumulative energy distribution curve over hundreds of shots (shown in Figure 70).

To simulate the dose deposition of the 135 MeV LWFA VHEE beam in the active layer of the EBT2 film the dosimeter is modelled as described in section 5.2.3.3.

Figure 71 shows the measured and calculated 2D dose maps for the ALPHA-X very high energy beam. The colour scale dose maps are normalized to the maximum dose deposited on the film at 3.8 cm depth to emphasise the evolution of the beam spatial distribution. The calculated transverse dose maps are in good agreement with the measurement.

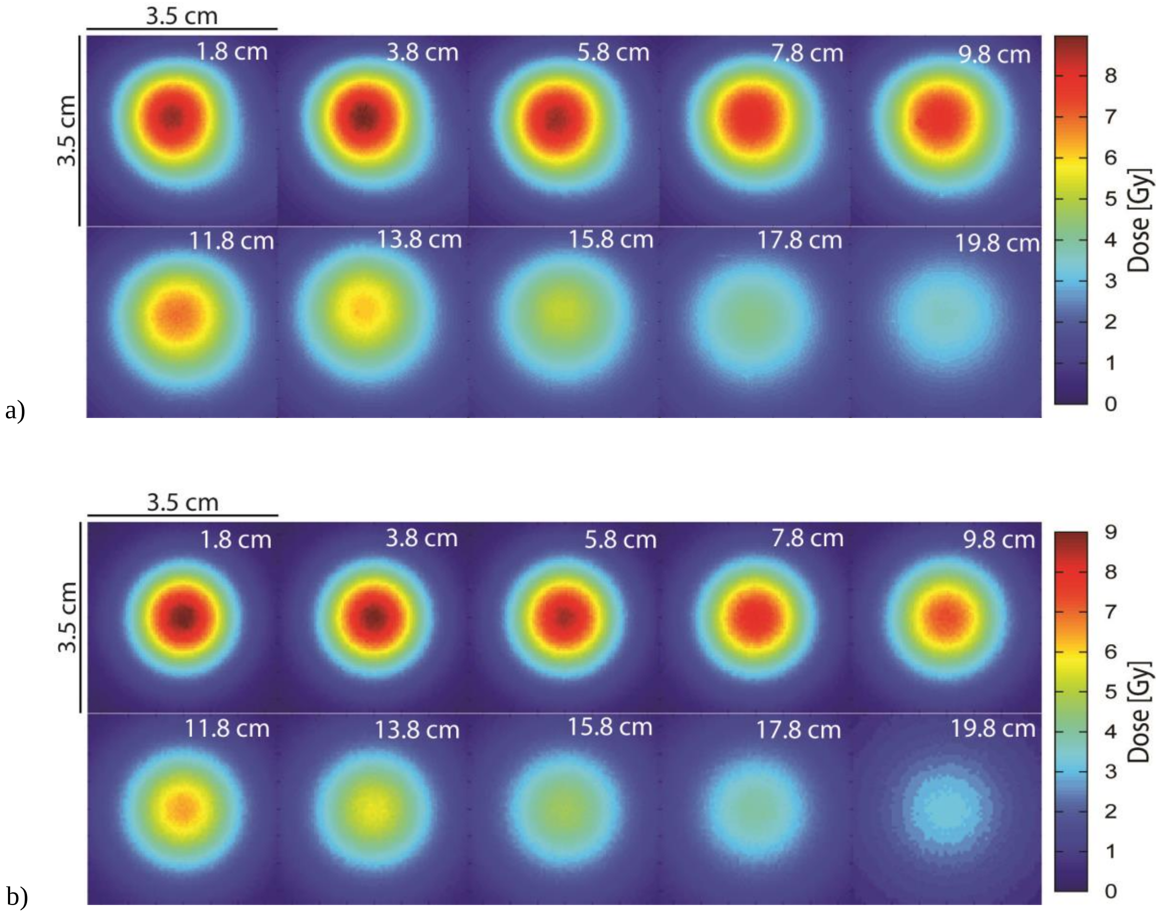

Figure 71. Measured (a) and calculated (b) two-dimensional dose maps for the ALPHA-X electron beam in planes lateral to beam central axis at different depths in the water phantom. The 2D dose distributions are normalized to maximum dose deposition for both measurements and simulations.

Based on the 2D dose maps shown in Figure 71, the maximum dose deposited at each depth has been used to reconstruct the depth-dose profile for the LWFA 135 MeV VHE electron beam. The results of the measurement and the calculated values are shown in Figure 72. Both, measured and FLUKA simulated depth dose curves are given in absolute terms, i.e. Gy.

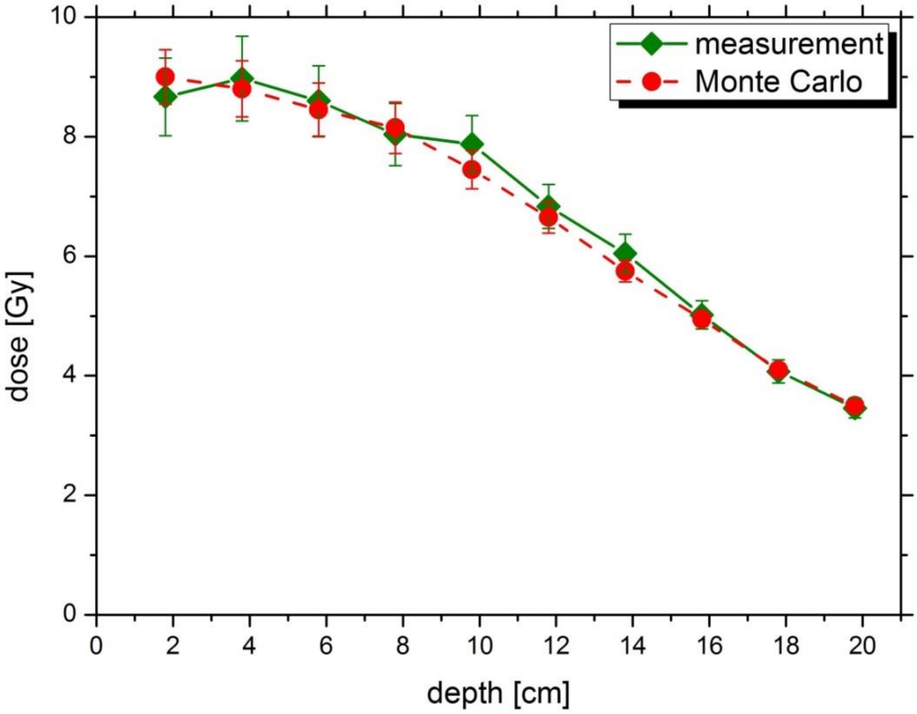

Figure 72. Measured (green curve) and calculated (red curve) depth dose profile for 135 MeV electron beam from the ALPHA-X beamline.

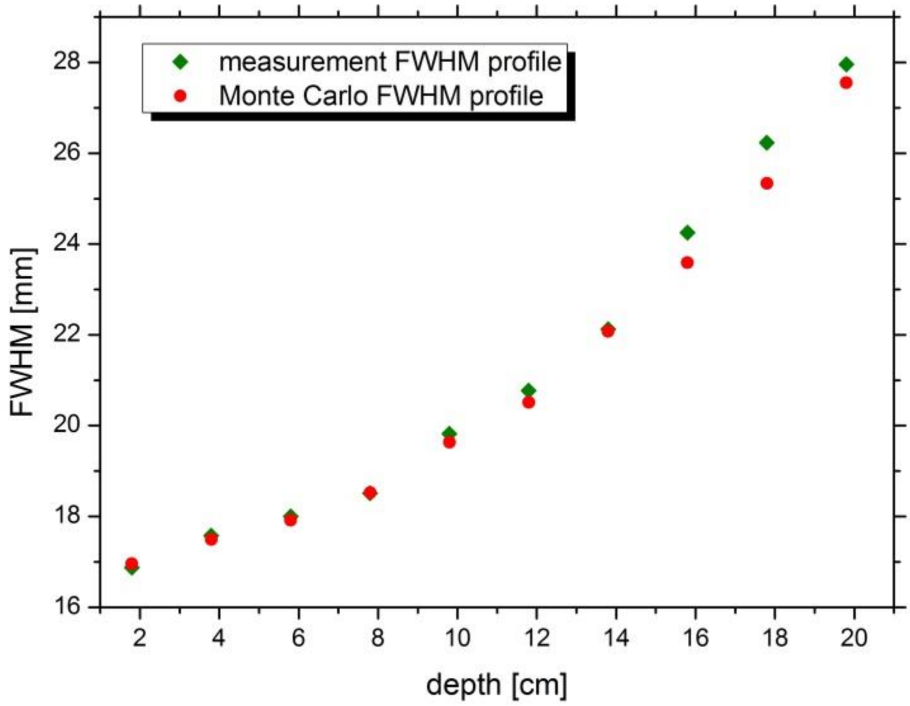

Figure 73. Evolution of the FWHM ALPHA-X beam profile as a function of depth within the water phantom.

Figure 73 shows the evolution of FWHM beam lateral profiles at various depths. The FWHM field size close to the rear of the water phantom is approximately twice that at the entrance. This is due to initial divergence of the beam in addition to multiple Coulomb scattering which deflects electrons transversely. This result, again, shows a good agreement between measurement and simulation.

5.3.3.2. *MC calculations for the ALPHA-X VHEE beam in relation to neutron production*

It was not possible to measure the charge on-line during experiments on the ALPHA-X beamline, but only just before and after every irradiation. The charge variation in LWFA can be significant (between 1 and 10 pC per shot). The dosimetric measurements using 135 MeV LWFA electron beam have been carried out with the previously calibrated (see section 5.2) EBT2 films. The average charge per shot is approximately 5 pC/shot. MC calculations are carried out using this estimation to calculate the induced radioactivity and equivalent dose rate.

The calculated neutron yield generated in and around water phantom irradiated with ALPHA-X beam during the experiment is shown in Figure 74.

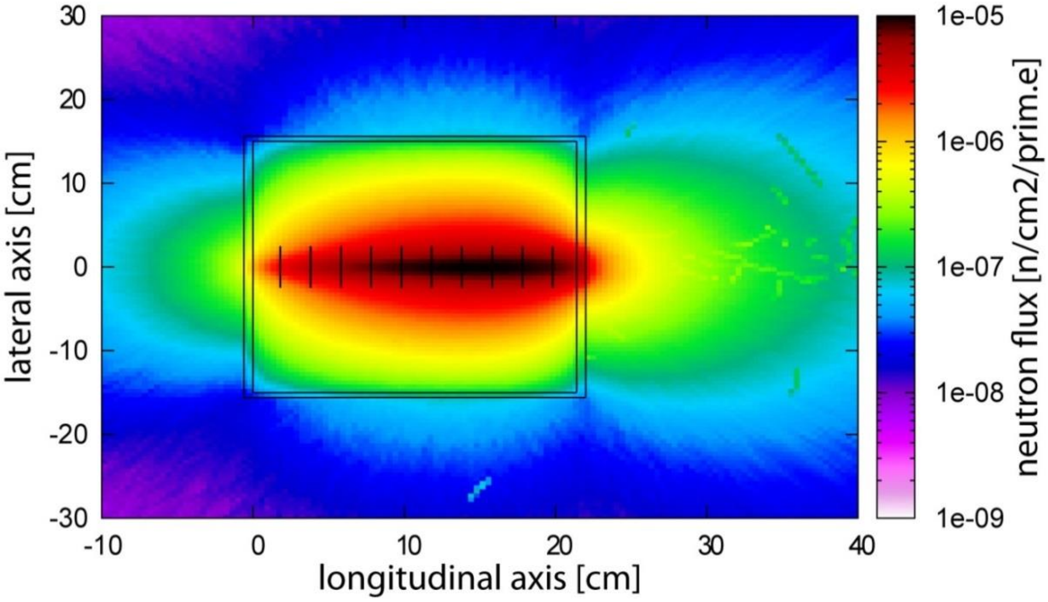

Figure 74. Neutron fluence inside and around the 15×30×22 cm^3 water phantom with transversely distributed EBT2 films for 135 MeV LWFA electron beam.

The neutron fluence for a 135 MeV LWFA beam is ≈ 10^{-5} neutrons per incident electron in the area of dose deposition within the phantom on the beam central axis and an order of magnitude lower 10 cm from the back wall of the water phantom.

To evaluate the extra dose deposited on the film and potential cooling time before handling, the induced activity in the film has been calculated (parameters have been described in section 4.2.7) . For this reason the activity is scored in the first (1.8 cm depth), middle (9.8 cm depth) and last film (19.8 cm depth) for each layer of EBT2 film separately. The results expressed in absolute values (Bq) and percentage activity are presented in Table 22. The activation due to the generation of radionuclides is scored in each film layer separately.

Table 22. Activation in first, middle and last EBT2 film irradiated in the ALPHA-X beamline calculated for various cooling times specified for each film layer.

depth [cm]	layer(*)	radionuclide activity after 1 min [Bq(%)]		radionuclide activity after 5 min [Bq(%)]		radionuclide activity after 10 min [Bq(%)]		radionuclide activity after 20 min [Bq(%)]	
		$^{11}_{6}C$	$^{15}_{8}O$	$^{11}_{6}C$	$^{15}_{8}O$	$^{11}_{6}C$	$^{15}_{8}O$	$^{11}_{6}C$	$^{15}_{8}O$
1.8	PO	3.84(99.89)	--	3.35(99.99)	--	2.83(99.98)	--	2.01(99.98)	--
	ADL	1.67(75.80)	0.52(23.72)	1.45(90.06)	0.14(8.39)	1.23(96.66)	0.03(1.95)	1.23(96.66)	--
	TC	--	--	--	--	--	--	--	--
	ACL	1.42(65.67)	0.70(32.57)	1.23(85.43)	0281(12.45)	1.04(94.87)	0.03(2.99)	0.74(97.97)	--
	PS	3.90(99.82)	--	3.40(99.99)	--	2.87(99.99)	--	2.04(99.98)	--
9.8	PO	13.27(98.8)	--	11.6(99.99)	--	9.78(99.99)	--	6.96(99.98)	--
	ADL	5.62(68.34)	2.53(30.72)	4.9(87.54)	0.65(11.56)	4.14(96.41)	0.12(2.76)	2.94(99.62)	--
	TC	5.18(51.47)	4.83(47.99)	4.52(77.83)	1.24(21.31)	3.81(93.37)	0.23(5.53)	2.72(98.42)	--
	ACL	5.35(60.57)	3.08(34.79)	4.67(81.52)	0.79(13.76)	3.94(92.42)	0.14(3.37)	2.81(96.84)	--
	PS	13.56(99.8)	--	11.8(99.99)	--	9.99(99.99)	--	7.11(99.98)	--
19.8	PO	19.48(99.8)	--	17.00(99.9)	--	14.34(99.98)	--	10.21(99.98)	--
	ADL	8.31(69.67)	3.52(29.55)	7.25(88.24)	0.90(10.99)	6.12(96.69)	0.17(2.61)	4.35(99.36)	--
	TC	8.00(54.72)	6.46(43.83)	6.98(79.51)	1.66(18.86)	5.89(93.73)	0.30(4.81)	4.19(98.50)	--
	ACL	8.54(64.54)	4.14(31.27)	7.46(61.49)	1.06(11.99)	6.29(93.83)	0.19(2.89)	4.48(97.45)	--
	PS	19.95(99.8)	--	17.41(99.9)	--	14.69(99.99)	--	10.46(99.98)	--

(*) PO- polyester layer, ADL- adhesive layer, TC- topcoat, ACL – active layer, PS- polyester substrate

20 min after irradiation the total absolute activity for the film irradiated in ALPHA-X is 6.1 Bq, 22.7 Bq and 33.9 Bq, for the first (1.8 cm depth) middle (9.8 cm depth) and last (19.8 cm depth) film, respectively.

The determination of the equivalent dose due to induced radioactivity also has been carried out.

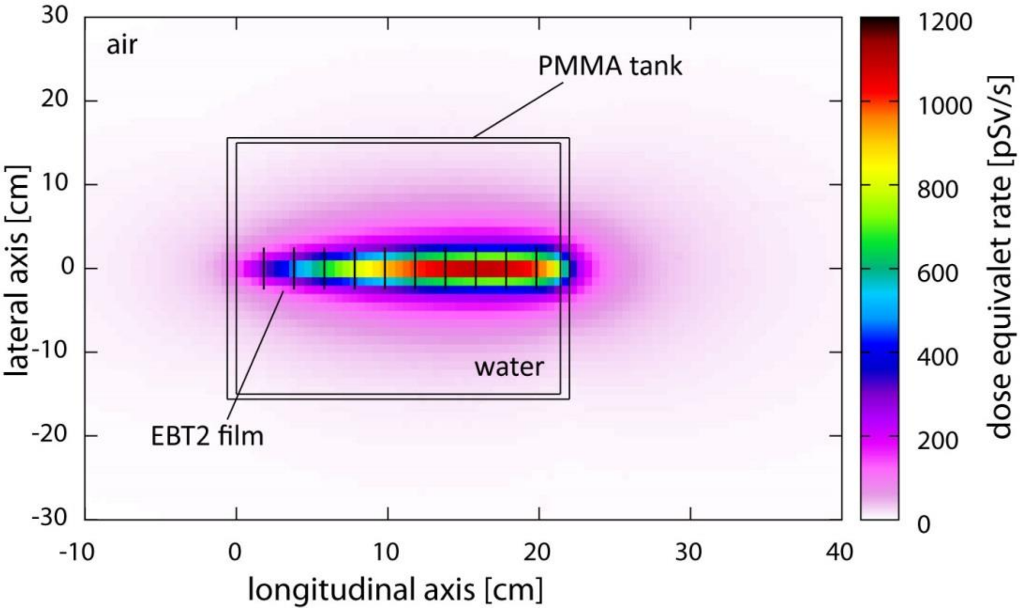

Figure 75. Ambient dose equivalent rate for irradiation in the ALPHA-X beamline from induced radioactivity after 1 minute cooling time. The beam enters from the left hand side.

Figure 75 shows the ambient dose equivalent H*(10) values for various positions inside and around the water phantom irradiated with the 135 MeV LWFA electron beam. Table 23 presents the values of H*(10) 1 mm from the front and rear wall of the water tank surface for various cooling times. The cooling time has been set to a maximum after 20 minutes, thereafter the films are removed from the water.

Table 23. H*(10) values 1 mm from the front and the rear wall of the water tank for various cooling times.

	front surface		rear surface	
Cooling time	eq. dose rate [pSv/s]	stat. error [%]	eq. dose rate [pSv/s]	stat. error [%]
1 min	69.41	0.34	345.14	0.18
5 min	25.04	0.23	144.61	0.22
10 min	11.34	0.12	78.79	0.30
15 min	1.47	0.20	56.49	0.11
20 min	0.73	2.40	47.39	0.36

It can be see that 1 minutes after radiation ceased the dose equivalent rate at the rear of the phantom is just 3.5 nSv/s, and with a longer cooling time the rate reduces to 47 pSv/s. Therefore, there are no additional handling risks associated with the activation of EBT2 films with VHEEs.

5.3.4. Conclusion

In this section the dosimetry of electron beams with different energy ranges have been presented.

The measured depth dose profiles (in Gy) along the central axis of the beam using normally orientated EBT2 films in the water phantom for the 165 MeV LINAC (Figure 65) and 135 MeV laser-plasma generated (Figure 72) beams are in excellent agreement with the Monte Carlo calculations. The difference in depth dose profiles between VHEE LINAC and LWFA electrons is due to their distinct beam parameters i.e. energy, divergence and lateral beam size. For 165 MeV electrons from the SPARC beamline, the beam emerging from the water tank has a field size of 0.8 cm FWHM with a 15 mrad divergence. In the case of ALPHA-X electrons the beam field size is twice as large: 1.6 cm FWHM and a divergence of 8 mrad. Therefore, the practical range (R_p) for the ALPHA-X beam exceeds that of the SPARC beam. It is well known that with a reduction of field size there is a lower level of lateral electronic equilibrium at the beam central axis. As a consequence, the depth dose should be highly sensitive to field shape and size [118]. This aspect has been also investigated in MC studies on VHEE beams in section 4.2.4.

We can summarize that for SPARC and ALPHA-X VHEEs, there are two ranges of photon energy for neutron production mechanisms. The first one is the giant dipole resonance (GDR) giving rise to a (γ,n) reaction that is approximately equal to the binding energy of the nucleon, and the second one is the processes above the giant resonance. The neutron yield also increases because of bremsstrahlung contribution. This is pronounced in Figure 67 and Figure 74, which show the quasi-isotropic neutron fluence for SPARC and ALPHA-X irradiation, respectively, around and inside the water phantom. As the VHEE beam propagates through water the primary electron energy decreases and the bremsstrahlung photon flux rises with increasing depth. The isotropic nature of the neutron emission is due to the dominance of the GDR mechanism [152]. The deviation from ideally isotropic behaviour for VHEEs is a consequence of anisotropic emission of neutrons due to other processes, such as quasi-deuteron effects. These studies estimate the neutron fluence in water that contribute to the dose delivered inside the phantom. The Monte Carlo calculated neutron fluence inside the phantom for both VHEE setups (SPARC and ALPHA-X) is of the order 10^{-5} neutrons/($\text{cm}^2\cdot$primary electron). This is almost three orders of magnitude lower than the results for 150 MeV electrons presented in previous studies based on a semi-empirical evaluation [35] established for a higher particle beam density approach.

The total activity of the films due to radioisotope generation in both SPARC and ALPHA-X beamlines is of the order of 10 Bq, depending on the film position inside the water tank (Table 20 and Table 22). The induced activity increases slightly with increasing depth due to the accumulation of bremsstrahlung generation radiation downstream where the majority of (γ,n) reactions occur. The dose equivalent rates due to low induced radioactivity of ${}^{11}_{6}C$ and ${}^{15}_{8}O$ play a minor role here. 20 minutes after cooling the dose equivalent rate is of the order of 20 pSv/s. Thus we conclude that neutron and proton production due to VHEE irradiation does not significantly affect the equivalent doses. In summary, the induced radioactivity from neutron fluence is found to be small and therefore it has negligible effect on total dose deposition.

5.4. Ion chamber dosimetry under reference conditions

Ion chambers are considered to be the gold standard in radiotherapy, because their operation with conventional clinical beams is well understood. The detector enables instant readout. However, precise measurements required for clinical applications involve several readout corrections. This section presents the principles of operation, calibration and measurements of ionisation chambers. Ion chamber calibration measurements with 20 MeV clinical electron beam and VHEEs have been carried out based on IPEM code of practice for electron dosimetry [251], which provides guidelines of carrying out dosimetry measurements with clinical electron beams.

5.4.1. Ionization chambers

The ionization chamber is the most practical and most widely used type of dosimeter for accurate measurement of the output in clinical LINAC. It can be used as an absolute or a relative dosimeter. Its sensitive volume is usually filled with ambient air and the dose or dose rate measured quantities are the ionization charge Q or ionization current I, respectively, produced by radiation in the chamber sensitive air mass m_{air}. Charge Q and air mass m_{air} are related to absorbed dose in air D_{air} by the following relation:

$$D_{air} = \frac{Q}{m_{air}}\left(\frac{W_{air}}{e}\right), \tag{5.10}$$

where (W_{air}/e) is the mean energy required to produce an ion pair in air per unit charge (the value for dry air is 33.97 eV/ion pair or 33.97 J/C).

It is generally assumed that a constant value of (W_{air}/e) can be used for the complete photon and electron energy range used in radiotherapy dosimetry. However, there is no direct experimental support for such an assumption, because the available data have been obtained only from measurements with ^{60}Co and ^{137}Cs γ ray beams and 2 MV X rays. The two methods for deriving the absorbed dose to graphite must yield the same dose value, and one obtains:

$$\frac{W_{air}}{e} = \frac{D_{calorimetry}}{(Q/m_{air})S_{graphite,air}}, \tag{5.11}$$

where Q is the charge collected in air mass m_{air}; and $S_{graphite,air}$ is the ratio of collision stopping powers for graphite and air calculated for the photon or electron beam energy. Following the introduction of new electron stopping power data by the ICRU in 1984 [157], the value of (W_{air}/e) has been modified to (33.97 ± 0.06) J/C for dry air.

Analysis of the available experimental data at higher energies, mainly for electron beams, suggests that an energy dependence of (W_{air}/e) cannot be ruled out. However, experimental uncertainties, and the use of different stopping power ratios over the years, has not allowed a definitive conclusion to be reached on this question.

It is known that the (W_{air}/e) value for air at 20ºC, 101.325 kPa and 50% relative humidity is 0.6% lower than that for dry air at the same temperature and pressure, giving a value of 33.77 J/C instead of 33.97 J/C. Thus, for the same amount of energy available for creating charge, 0.6% more charge will be created in air at 50% relative humidity than in dry air (at 20ºC and 101.325 kPa).

To measure the absorbed dose in a medium, it is necessary to introduce a radiation sensitive device (dosimeter) into the medium. Generally, the sensitive medium of the dosimeter is not made of the same material as the medium in which it is embedded. Cavity theory relates the absorbed dose in the dosimeter's sensitive medium (cavity) to the absorbed dose in the surrounding medium containing the cavity. The conversion of the air cavity dose D_{air} to dose in medium (usually water) D_w is based on the Bragg–Gray or Spencer–Attix cavity theories [252, 253]. These relate the absorbed dose at a point in a medium (water), D_w, to the mean absorbed dose in the air, $\overline{D}_{air}$, through the mass collision stopping power ration water/air ($S_{w,air}$) by the following relation:

$$D_w = \overline{D}_{air} S_{w,air}. \tag{5.12}$$

Electron stopping-power ratios have astrong dependence on energy and depth in water. This dependence is due to the considerable differences in energy spectra at various depths in water. The selection of appropriate stopping-power ratio at the particular depth for specific beam has been discussed in [128, 254, 255]

The key assumption of the Bragg-Gray theory is that the electron fluence present in the detector is identical to that in the (undisturbed) medium at the position of interest. Any deviations from perfect Bragg-Gray behaviour are corrected by perturbation correction factors. Further discussion on the ion chamber dosimetry theory is beyond the scope of this work. More details on the theory and the perturbations correction factors can be found in [117, 118, 252, 253].

The dose-to-water conversion factor, D_w, for a given chamber is provided by Measurement Standards Laboratories. The National Physical Laboratory provides a calibration service for a direct calibration of ionisation chambers in terms of absorbed dose to water.

5.4.2. Corrections to the ion chamber readings

The calibration factor for a chamber is the ratio of the best estimate of the stated dosimetric quantity being measured to the instrument reading under standard conditions. For measurements taken in non-standard conditions, various precautions and/or corrections may be necessary to take account of the differences, in order to ensure that the calibration factor is applied to the correct reading. During dosimetric measurements as many as possible of these factors should be controlled, e.g. ensuring that measurements are not significantly affected by warm-up effects, drift, leakage currents with or without radiation present, stem effects, cable effects, etc. However, some cannot be controlled and therefore the measurement must be corrected to the standard conditions used during chamber calibration, which was performed at measurement standards laboratory (e.g. NLP). These are dealt with in the following sections.

Temperature, pressure and humidity

The standards laboratories provide calibration factors under standard ambient conditions.

For the NPL, these are 20 °C, 1013.25 mbar (1013.25 hPa), and 50% humidity. If conditions are different from these during a measurement, the response of an unsealed chamber will change and will need to be corrected to the standard conditions. All the designated chambers are unsealed.

All unsealed ion chamber measurements have to be corrected to standard conditions by multiplying the instrument reading at temperature T (in °C) and pressure p (in hPa) by the correction factor

$$f_{T,p} = \frac{(273.15 + T)}{293.15}\frac{1013.25}{p}. \tag{5.13}$$

It is difficult to determine the humidity of the air in the chamber, particularly when in a water phantom. However the effect of water vapour on the measured ionization is a maximum of 0.1% for relative humidities between 10% and 90% can generally be neglected.

Polarity

Reversing the polarity on an ionization chamber may yield different readings. This phenomenon is known as a polarity effect.

The polarity effect should be measured and a correction applied, unless it is insignificant to measurement of absorbed dose. This should be carried out under the same conditions for absorbed dose measurements. The effect depends on the chamber, beam energy, depth and field size. Generally polarity effects for Farmer chambers used with clinical energy range beams can be up to 1%.

The polarity correction is given by following relation:

$$f_{pol} = \frac{|M^{+}| + |M^{-}|}{2M}, \tag{5.14}$$

where the superscripts + or − indicate the reading (M).

Ion recombination

The chamber response (i.e. current I or charge Q for an applied voltage V with constant dose rate or dose) is known as a saturation curve. It first rises linearly at low voltages, then saturates at high voltages and eventually breaks down at even higher voltages. A sketch of a typical saturation curve is shown in Figure 76.

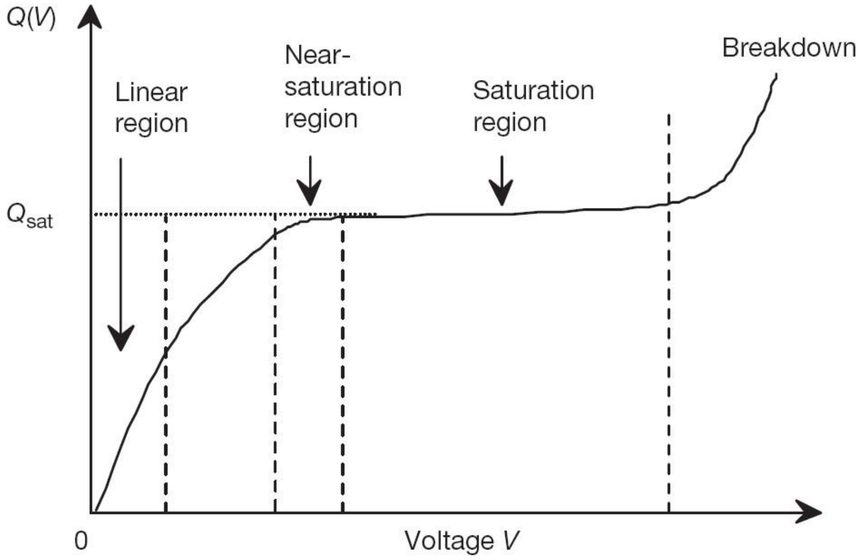

Figure 76. Typical saturation curve for an ionization chamber. The saturation charge is represented by Q_{sat} is the parameter describing the radiation signal. Ionization chambers are used in the near-saturation region and Q_{sat} is calculated by dividing the measured signal by the collection efficiency [118].

The ratio $Q(V)/Q_{sat}$ or $I(V)/I_{sat}$, where Q_{sat} and I_{sat} are the saturation values, respectively, are referred to as the collection efficiency f of the ionization chamber at the applied voltage V. In radiation dosimetry, ionization chambers are commonly used in the near-saturation region where $f > 0.98$.

At saturation, all charge produced is collected, which produce Q_{sat} and I_{sat}. When the chamber is used below saturation, some of the charge produced by radiation recombines. This results in a decrease of the dosimetric signal. Such charge loss occurs through three different mechanisms:

- General recombination: opposite charges from different tracks collide and recombine.
- Initial recombination: opposite charges from same tracks collide and recombine.
- Ionic diffusion loss: charges diffuse against the electric field.

To account for the incomplete collection of charge due to ion recombination in the chamber volume, a correction is required. The correction for ion recombination is the sum of two components: initial recombination and general recombination. Both depend on the chamber geometry and the collecting voltage. Initial recombination is independent of dose rate, but general recombination depends on the ion density in the cavity. The ion density depends on the dose rate for continuous radiation and on the dose per pulse for pulsed beams. Initial recombination in radiotherapy electron beams is typically around 0.1% for the usual cylindrical chambers and collecting voltages employed in radiotherapy. General recombination is typically a small effect for continuous radiation, however for pulsed beams it can often be significant.

Theoretical correction factors can be calculated following Boag's work on experimental corrections by determining $1/M$ against $1/V$ (known as Jaffe plots) [256-259]. However, a convenient practical procedure for determining the appropriate factor for a given measurement is to use the experimental two-voltage technique [257, 260], which is accurate over: $(4.33 \cdot 10^{-6} - 1.27 \cdot 10^{-3})\mathrm{C}/(\mathrm{m}^3 \cdot \mathrm{pulse})$ densities [257].

In the *two-voltage technique.* In this approach two ionization chamber readings are taken under the same irradiation conditions, one at the normal (recommended by the manufacturer of a chamber) collecting voltage (V_1, reading M_1) and one at a lower voltage (V_2, reading M_2). The ratio V_1/V_2 should have a value of two or three. The recombination correction factor to be applied at the normal collecting voltage, f_{ion}, can be obtained from the solutions of the particular expressions for pulsed beams [257, 261]. To simplify this, Weinhous and Meli [261] give the following quadratic fit:

$$f_{ion} = a_0 + a_1 \frac{M_1}{M_2} + a_2 \left(\frac{M_1}{M_2}\right)^2, \tag{5.15}$$

where the coefficients, a_i, are given in table A.1. in reference [251].

For small corrections (($f_{\text{ion}} - 1) < 0.05$) the theoretical expression reduces, in a first approximation, to:

$$f_{ion} - 1 = \frac{\left(\frac{M_1}{M_2} - 1\right)}{\left(\frac{V_1}{V_2} - 1\right)}. \tag{5.16}$$

5.4.3. IBA CC04 ionization chamber

The dosemeter used in this study is the CC04, which is manufactured by *IBA Dosimetry GmbH* [262] and has a high spatial resolution, small volume ionization chamber. CC04 is a Farmer-type, waterproof, vented through a waterproof sleeve, and fully guarded. The technical drawing of the detector is shown in Figure 77.

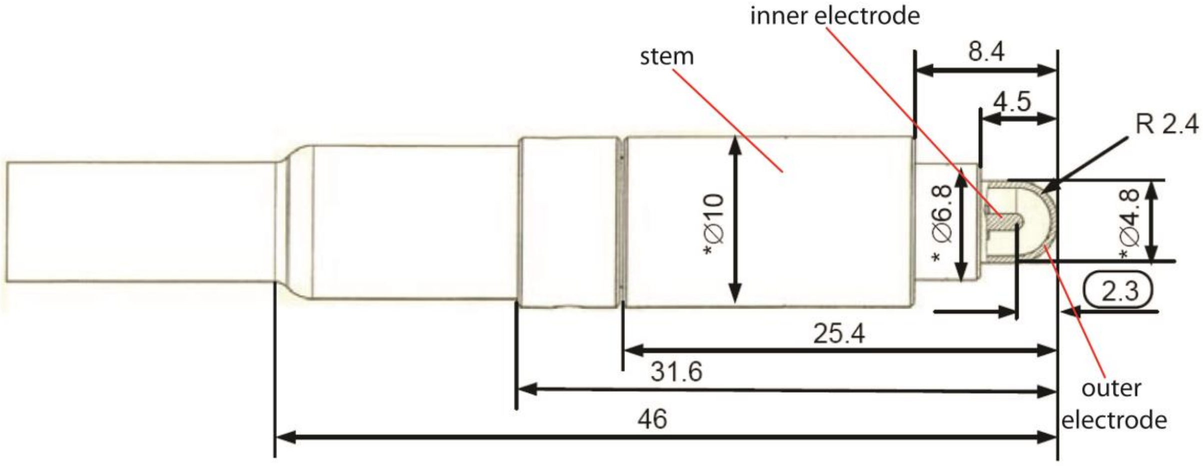

Figure 77. The geometric layout of the IBA CC04 Farmer chamber (all dimensions are given in mm)[262].

The CC04 is a small ion chamber with an active volume of 0.04 cm^3, which is suitable for measurements of small fields. Both inner and outer electrodes are made of graphite (Shonka, C-552) with a density of 1.7 g/cm^3. Such a design assures smaller scattering in dosimetric measurements due to the near-water equivalent of chamber electrodes.

The measurements with the CC04 chamber are carried out for a potential on the collecting (inner) electrode of +300 V. The calibration factor of the absorbed dose to water is provided by NPL under the reference conditions (20°C , 1013.25 hPa and 50% relative humidity). The chamber is calibrated at depth of 5 cm in a $30 \times 30 \times 30\ \text{cm}^3$ water phantom at SSD of 100 cm with 10 × 10 cm^2 ^{60}Co beam. The $N_{D,w}$ factor provided is 9.459·10^{8}Gy/C with 2.2% of measurement uncertainty. This calibration factor is applied to all dose measurements presented in this section.

DOSE-1 electrometer

Electrometers are suitable for small currents, of the order of 10^{-9} A or less, used in conjunction with an ionization chamber. A high gain, operational amplifier measures the chamber current or charge collected over a fixed time intervals [263].

A suitable electrometer of the IBA CC04 chamber is DOSE-1, which is used for all the measurements presented in this section.

5.4.4. Ion chamber measurements in 20 MeV LINAC

The set-up of the chamber irradiation is shown in Figure 78.

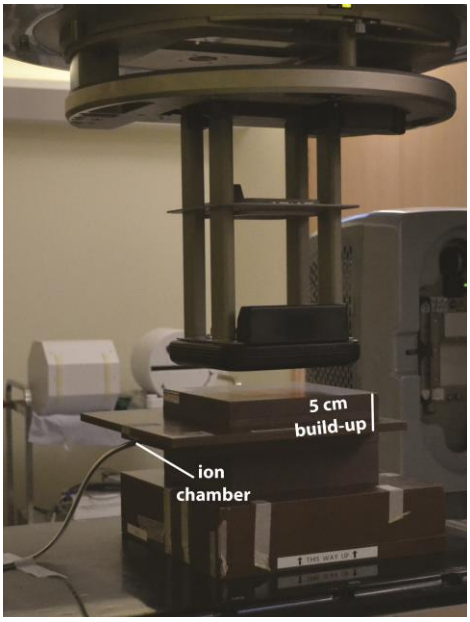

Figure 78. The set-up of the CC04 chamber calibration for 20 MeV LINAC.

The chamber is placed in a standard grade solid water phantom (Gammex, Middleton, WI) slabs with 5 cm of the build-up material above and 20 cm below to provide adequate backscattering. According to the electron dosimetry protocol [251] calibration measurements for a given accelerator the chamber should be carried out at or close to d_{max}. At this depth, for the clinical electron energy range, the flux of secondaries, and therefore the correction factor is the largest. The chamber is positioned at 5 cm (the PDD profile for the beam shown in Figure 61) and irradiated at SSD of 100 cm with a 10×10 cm^2 field size.

The measurements have been carried out in solid water, an additional correction (known as *fluence-ratio correction*) applies. The quoted standard density for Gammex solid water is 1.04 g/cm^3 [264] with the fluence-ratio correction factor of 1.00 (see Table.2 in reference [251]).

5.4.4.1. Chamber correction factors for the 20 MeV electron LINAC

The temperature and pressure correction factors have been applied directly to the electrometer data.

The incomplete collection of charge due to ion recombination in the CC04 chamber in its sensitive volume is assessed using two voltage technique, as described in section 5.4.2. The chamber readings are taken for +300 V collecting voltage (recommended by the *IBA Dosimetry*), half of this value (i.e. +150V) and a third of this value (i.e. +100V). The mean readings for five independent measurements for each voltage range are presented in Table 24.

Table 24. The averaged readings of the charge (Q for 300V, 150V and 100 V.

Bias voltage [V]	Mean Q [nC]	SD of Q [nC]	1/V [1/V]	1/Q [1/nC]
300	1.04833	0.00115	0.00333	0.9539
150	1.03750	0.00278	0.00667	0.9639
100	1.02867	0.00153	0.01000	0.9721
300	1.04800	0.00100	0.00333	0.9542

To account for ion recombination the correction factor $f_{ion}=1.0103$ has been calculated. It is a good practice to recalculate correction factors using another method extrapolating the saturation reading. The Jaffe diagrams represent the inverse reading (here reciprocal of collected charge) of an ionization chamber as a function of inverse applied voltage. The useful range for the chamber is limited to the linear part of the Jaffe diagram. If this is not the case, the ion chamber should be operated at the highest voltage of the linear range of the Jaffe diagram and the correction factor should be determined by extrapolating the linear part of the diagram to an infinite voltage (i.e. for 1/V=0). The CC04 chamber for the applied voltages operates in the linear regime. To calculate the correction factor according to Boag's work [257] we have extrapolated the saturation reading from the Jaffe diagram.

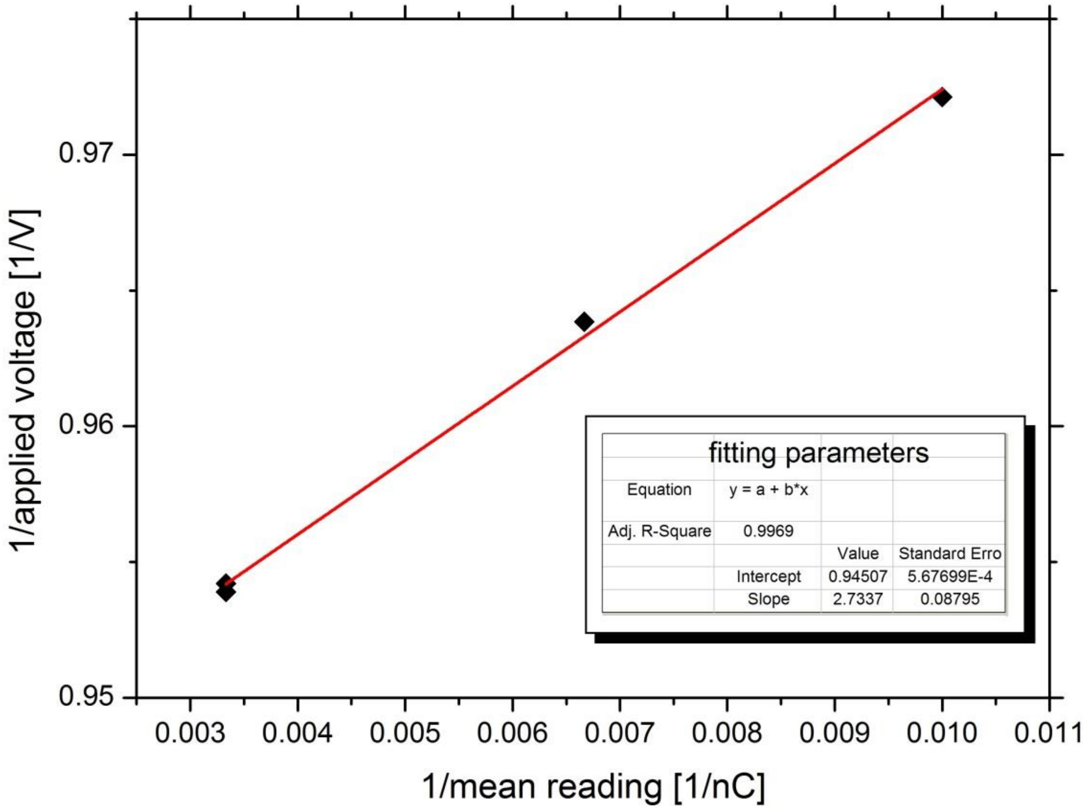

Figure 79. Jaffe diagram for the CC04 chamber irradiated with the 20 MeV Varian iX series LINAC. The least square fit to the linear part intersects the y-axis at 0.94507, which gives a saturation charge of 1.058 nC.

Based on the extrapolated saturation charge form Jaffe diagram, the correction factor due to ion recombination for the recommended bias voltage (+300V) is:

$$f_{ion}^{Jaffe} = \frac{Q_{saturation}}{Q_{+300V}}. \tag{5.17}$$

This method yields a correction factor equal to 1.01.

The polarity correction factor is calculated using equation (5.14). The measurements are acquired for 5 consecutive times, with +300V. Subsequent measurements are taken with the opposite polarity, i.e. -300 V and then again for +300 V, to take into account any drift in the accelerator output. The averaged readings are presented in Table 25.

Table 25. The averaged readings of the collected charge Q for positive and negative polarities of applied voltage.

Applied voltage [V]	Mean Q [nC]	st.deviation [nC]
+300	1.0480	0.0010
-300	1.0483	0.0006
+300	1.0480	0.0010

The calculated polarity correction factor for CC04 chamber is $f_{pol}=1.00$.

These correction factors apply only for measurements using the Varian iX series LINAC operating at 20 MeV, which have to be applied for all further measurements with the beam. The corrected chamber readings, $M_{ch,w}$, for determining the absorbed dose in water is given by:

$$M_{ch,w} = M_{raw} f_{TP} f_{ion} f_{pol} f_{elec}, \tag{5.18}$$

where M_{raw} is the raw chamber reading of the electrometer, f_{TP} , f_{ion} and f_{pol} are described above, and f_{elec} is the electrometer calibration factor.

5.4.5. Ion chamber measurements with the 165 MeV electron beam

There are no protocols for determining the absorbed dose with ionization chambers for very high energy electron beams. Very high energy electrons are unlike any other existing radiotherapy beams. The radiation pulses have very short durations (femto- or pico- second compared with microseconds for a radiotherapy LINAC). Charge recombination is a potential problem because of this. Moreover, these beams have a small area and lack the lateral electron equilibrium. Classic models of dosimetry detectors assume an electron equilibrium [117], which is why absorbed dose measurements with clinical beams are carried out using large, typically 10×10 cm^2, field size. The electron energy range above 100 MeV is considerably higher than the electron energies for which established detectors have been calibrated (4-22 MeV typically). Extrapolation to high energies is therefore a challenge.

The INFN VHEE SPARC accelerator, described in section 5.3.2, has been used to carry out absorbed dose measurements using the ionization chamber. The IPEM code of practice for electron dosimetry [251] is followed to obtain the CC04 correction factors for a 165 MeV electron beam. The estimated charge density for 65 pC, 1 ps temporal duration pulse with a 1 cm beam size is estimated as $1.3 \cdot 10^{-3} \mathrm{C/m^3}$, which is at the upper limit of the charge density range investigated by Boag [257], where the two-voltage technique still applies. The setup of the CC04 ion chamber calibration is shown in Figure 80.

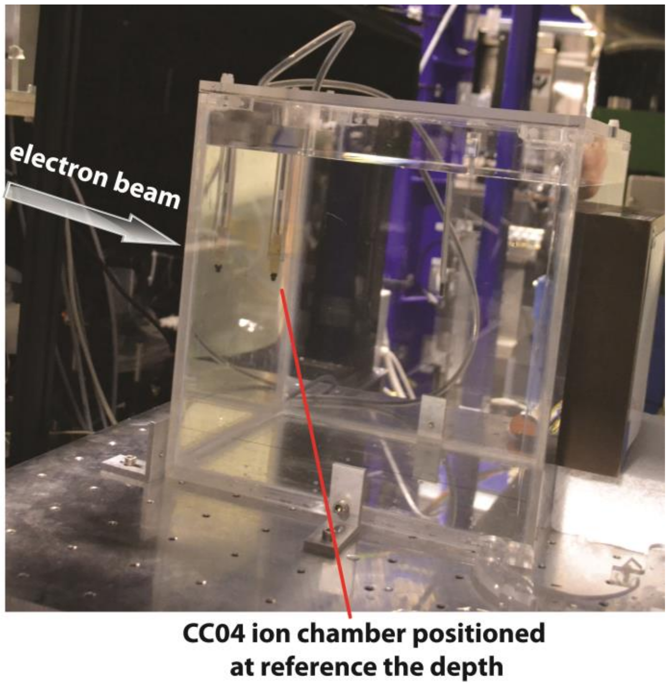

Figure 80. The experimental set-up for the CC04 chamber at the SPARC accelerator.

Based on PDD measurements (described in section 5.3.2.1) the reference position for the ionization chamber was defined. The central electrode of the CC04 is positioned 2.8 cm from the entrance wall of the phantom. All subsequent measurements to calculate the ion chamber correction factors for SPARC beam are made at this position.

The temperature and pressure corrections are applied to the DOSE-1 electrometer. The electrometer is set up in the charge integration mode to determine the accumulated charge over the whole irradiation period. Controlling the exact number of electron shots delivered by the SPARC accelerator was not possible. The number of shots and the electron charge delivered in each irradiation is recorded. To calculate the ion chamber correction factors the electrometer readings for each irradiation are normalized to the electron beam charge accumulated over the whole irradiation time for every run. This value is defined as *Q’*.

Table 26. The averaged readings of collected charge at the electrode for 300V, 150V and 100 V normalized to accumulated electron charge. The reciprocal of applied voltage and mean collected charge were used to plot Jaffe diagrams

Bias voltage [V]	Q'	1/V	1/Q'
300	0.0017	0.0033	588.6
150	0.0013	0.0067	789.4
100	0.0010	0.0100	997.2

The chamber readings are taken with collecting voltages, described in section 5.4.4.1. The recorded mean values are normalized to the accumulated electron charge in each irradiation and the results are presented in

Table ***26***. The calculated ion recombination factor for CC04 chamber is f_{ion}=*1.595*.

The Jaffe diagram (Figure 81) is plotted to calculate Q'_{sat} and obtain the f_{ion}^{Jaffe} factor, based on equation (5.17). The f_{ion}^{Jaffe} is equal to 1.536 giving 5.92% difference with respect to the calculated f_{ion}. Such a high factor suggests that there is significant ion-pair recombination within the active volume of the ion chamber.

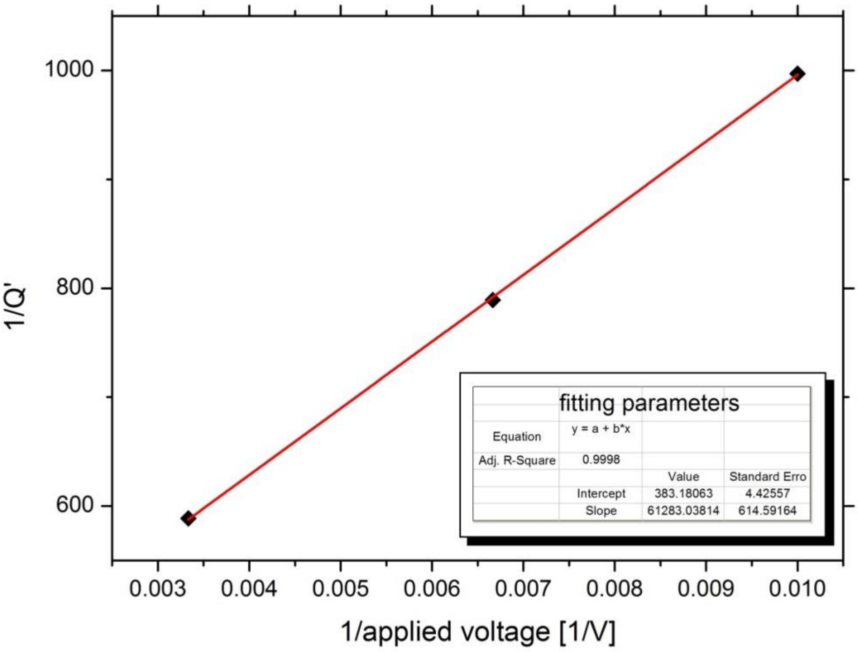

fitting parameters

Equation	y = a + b*x		
Adj. R-Square	0.9998		
		Value	Standard Erro
	Intercept	383.18063	4.42557
	Slope	61283.03814	614.59164

Figure 81. Jaffe diagram for CC04 chamber irradiated with 165 MeV SPARC VHEE beam. The least squares fit to the linear part intersects the y-axis at 383.18 giving a in saturation value Q'_{sat} of 0.0026.

Measurements of Q' have been carried out for +300V and -300 V to calculate the correction factor for the polarity effect. The averaged readings are presented in Table 27.

Table 27. The averaged Q' values for positive and negative polarities of applied voltage under 165 MeV electron exposure.

Applied voltage [V]	Mean Q'
+300	0.00170
-300	0.00167

The calculated polarity correction factor of the CC04 chamber for the 165 MeV SPARC electron beam is equal *0.992*. The polarity correction factor is close to that for the 20 MeV clinical LINAC.

The recombination factor due to polarity effect and ion recombination at 2.8 cm depth is 1.58.

5.4.5.1. Comparison between film and chamber measurements for VHEE

The absorbed dose measurement with the CC04 chamber has been carried out at a reference depth (i.e. 2.8 cm) in the SPARC beamline for a 165 MeV electron beam.

The centre of the detection system is aligned to the central axis of the beamline. However, the electron beam is displaced by few mm from the central axis. This misalignment is determined.

EBT2 films not only allow dose measurements. In some circumstances, when film is positioned close enough to an object, composed of different Z material to the surrounding media, the image of the object can be captured on the film. This allows to measure the deviation of the beam axis from the central axis of the detection system (here CC04 chamber).

Measurements with CC04 chamber positioned at 2.8 cm depth are recorded on a DOSE-1 electrometer. The response of the ion chamber to the incident electron charge is calculated. After correcting the reading with the polarity and ion recombination factors the calculated dose per pC is 1.87 mGy/pC in a shot.

A simultaneous dose measurement is carried out using EBT2 film (placed at the reference depth) and the ionisation chamber (at 15 cm depth). The setup is described in section 5.2.3.3 and is shown in Figure 57. The two detectors are positioned in the water phantom 12 cm from each other. Based on the PDD measurement (section 5.3.2.1) it is possible to compare the dose measurements using the two detectors. The relative depth dose curve of the SPARC beam is shown in Figure 82.

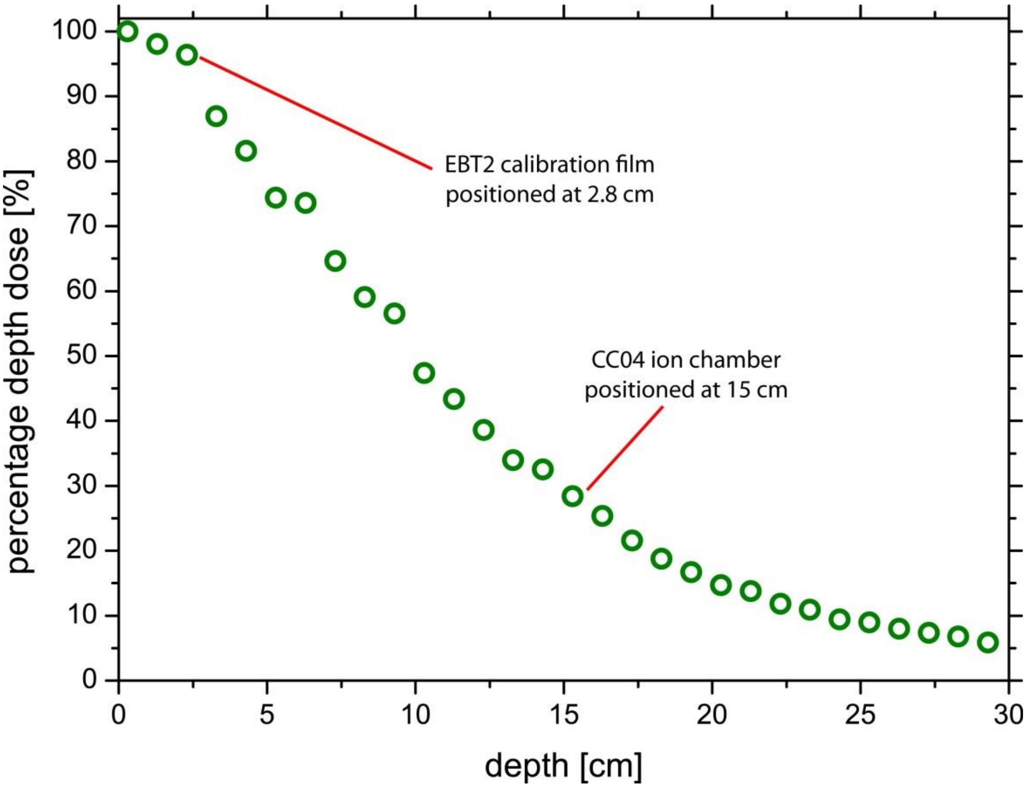

Figure 82. The position of the calibration film (at 2.8 cm depth) and the ion chamber (at 15 cm depth) during simultaneous measurement of the delivered dose.

The EBT2 calibration film is positioned at a depth corresponding to 95% of d_{max}, while the central electrode of the CC04 chamber is placed at a depth equivalent to 33% of the d_{max}. This gives a ratio of dose delivered between film and chamber of 2.9 (i.e. dose delivered at 2.8 cm is 2.85 times larger than at 15 cm).

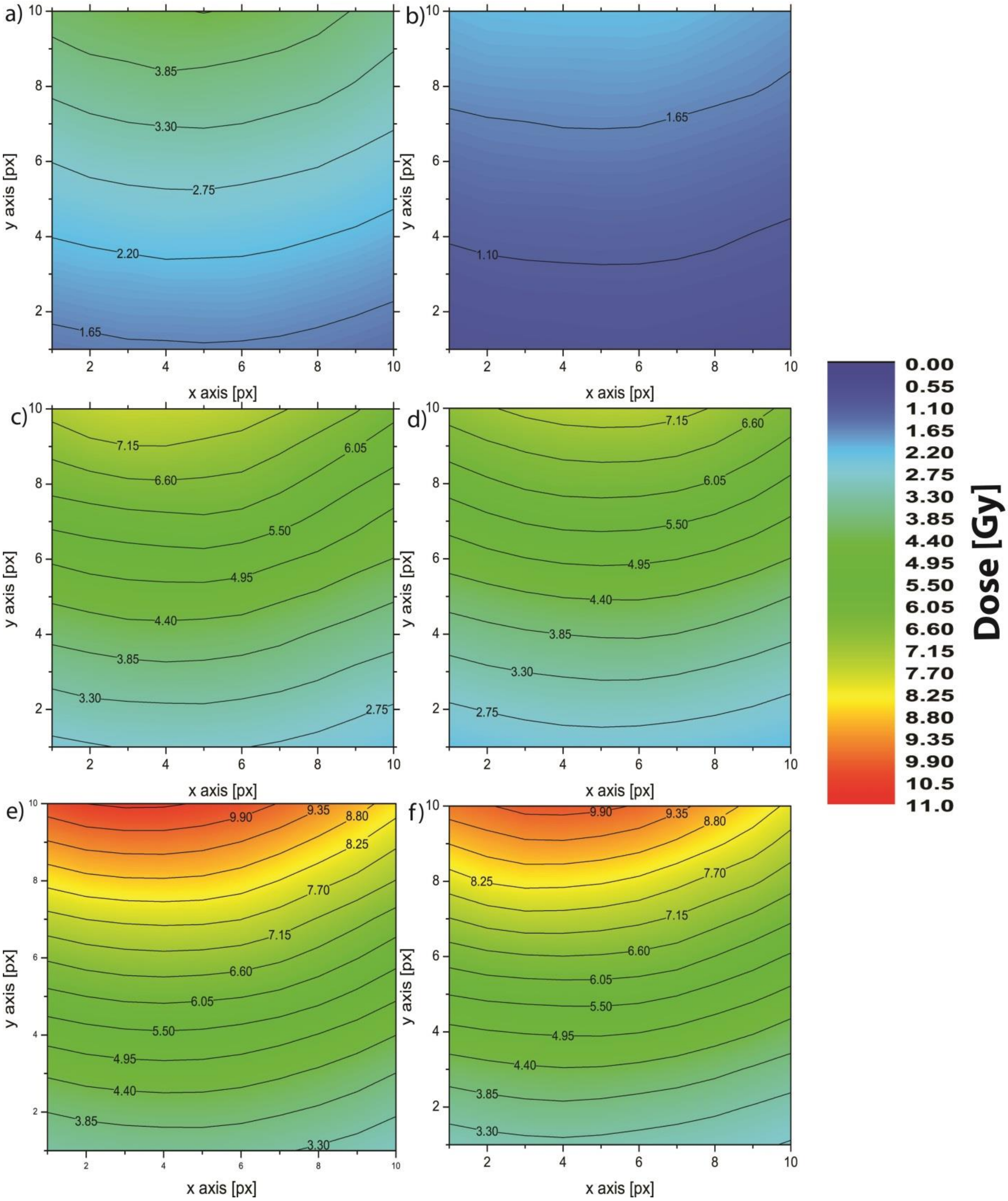

Figure 83. Absorbed dose measured on EBT2 film at 2.8 cm depth corresponding to position of CC04 chamber. The size of each dose map correspond to the size of CC04's active volume (approximately 3.5× 3.5 mm^2). The mean dose for each dose map and its standard deviation are: a) run I: (2.75±0.86) Gy, b) run II (1.40±0.43) Gy, c) run III: (4.84±1.59) Gy, d) run IV (4.63±1.56) Gy, e) run V: (6.39±2.19) Gy, f) run VI: (6.03±2.16) Gy.

Table 28. The summary of the CC04 ion chamber and EBT2 film dose measurements.

run #	# of shots	charge/shot [pC]	charge/shot SD [pC]	corresp.CC04 dose at ref. depth [Gy]*	EBT2 film dose at ref. depth [Gy]**	CC04 dose at 15 cm depth [Gy]***
run I	20	69.1	4.5	**2.59±0.17**	**2.75±0.86**	**1.00**
run II	11	56.5	3.2	**1.17±0.08**	**1.40±0.43**	**0.53**
run III	38	64.3	4.4	**4.58±0.75**	**4.84±1.59**	**1.63**
run IV	41	57.7	2.4	**4.43±0.19**	**4.63±1.56**	**1.54**
run V	59	56.8	4.0	**6.28±0.90**	**6.39±2.19**	**2.34**
run VI	62	55.1	4.9	**6.40±1.01**	**6.03±2.16**	**2.08**

* CC04 ion chamber dose at ref. depth calculated for each run based on previously evaluation of dose in a shot per incident electron charge

** The dose recorded on the film corresponding to the position of the CC04 ion chamber active volume (dose maps presented in Figure 83)

*** not corrected chamber measurements (at 15 cm depth) performed simultaneously with EBT2 film irradiation (at 2.8 cm)

Note that the absorbed dose measurements at a reference depth (2.8 cm) presented in Table 28 with CC04 chamber (column 5) and EBT2 film (column 6) are not performed simultaneously. The CC04 chamber doses listed in column 5 are calculated based on the previously estimated absorbed dose in a shot per incident electron charge equal to 1.87 mGy/pC (this value is corrected by the polarity and ion recombination factors). The dose deposited in the chamber's sensitive volume at 15 cm is presented in Table 28 (column 7). These values have not been corrected with the ion recombination and polarity factors (from section 5.4.5). Based on the PDD curve of the SPARC 165 MeV electron beam (Figure 82) we see that the dose measurements with ion chamber included in column 7 of Table 28 do not need correction with f_{ion} and f_{pol} factors established at the reference depth (2.8 cm). This suggests that the ion chamber dose correction factor at larger depths (such as 15 cm) is close to unity, therefore the ion pair recombination in the chamber's sensitive volume at this depth is much smaller than at shallow depths.

5.4.6. Discussion

The ion chamber correction factors for IBA CC04 chamber irradiated with VHEE beam are calculated according to reference [251]. The polarity correction coefficient, presented in section 5.4.4.1 is very close to unity, which is also typical for conventional clinical beams. Nevertheless, the ion recombination correction factors for the investigated chamber diverges significantly from the measurements with the 20 MeV electron beam. The calculated 165 MeV ion recombination correction factor (section 5.4.5) gives a value of

1.58. This could indicate substantial ion pair recombination. Therefore, the collected charges of the emerging ion pairs to the inner and outer electrodes are lower than the amount of ionization pairs produced due to incident radiation. As a result the CC04 chamber under-responds to the SPARC VHE electron beam.

The observed high level of ion pair recombination could be an effect of ultrashort pulse duration investigated in these studies of VHEEs and thus a high charge density per shot. The temporal duration of the SPARC electron beam is 6 orders of magnitude shorter than clinical beams. The proximity of electron tracks in a utrashort electron bunch, traversing the ion chamber sensitive volume, can yield high degree of ion pair neutralization before the charges arrive at the collecting electrodes, which results in the underresponse. More experiments to investigate this effect should be undertaken, but the preliminary results presented in this section (5.4.5.1) indicate that the dispersion of the electron bunch at higher depths is large enough for the ion recombination not to be significant.

The methodology presented in this work for chamber correction factors relies on existing data collected for conventional clinical beams. One question that arises: can we use the same protocols for VHE electron beams as for radiotherapy beams?

One more challenge of dose measurements performed in this work with VHE electron beams should be mentioned. Even though the detector used for these studies has a small sensitive volume, the investigated beam is 0.8 cm at the entrance to the water phantom resulting significant dose gradients within the area of the beam field. Moreover, the central axis of the beam is slightly misaligned from the centre of the detector. The sensitive volume of the chamber is positioned in the area of the beam where there is significant dose gradient (Figure 83). Such a configuration does not fulfil the requirements of the precise absorbed dose measurements with ion chambers where electron equilibrium across the whole volume of the detector is assumed.

The results presented in this section show that more studies of ion chambers with VHEEs are required, before the detector can be used for dose measurements. One recommendation is to use the smallest possible ion chamber, e.g. pin point chamber, which has an active volume of just 0.015 cm^3. Such a small active area would reduce the effect of dose gradients for these beams. The ion chamber correction factors should be further studied. The explanation of the measured high ion recombination could be validated performing a set of ion chamber polarity and ion recombination tests at different depths of the water phantom. If the explanation of the observed ion recombination for ultrashort duration beams is correct, then the correction factors for those beams should be calculated separately for each depth in water.

6. Radiobiology of VHEEs

6.1. Radiobiological response to radiation

The biological effects of radiation result principally from damage to the cell’s DNA. When ionising radiation is absorbed in biological material, it can interact directly with the DNA in the cells. The atoms of this target itself may be ionized or excited, initiating a chain of events that leads to a biological change. This is called *direct action* of radiation, which is the dominant process for radiation with high LET, such as neutrons or α-particles. More details on LET is discussed in section 4.2.9. For clinical photons or electrons – with low LET – the radiation interacts with atoms or molecules in the cell (particularly with water, which is the major constituent of living cells) to produce free radicals that diffuse to reach and damage DNA. This process is known as *indirect action* of radiation [265-268]. There are vast differences in the time scale involved in these events. An overview of physical, chemical and biological stage of radiation action has already been given in section 4.2.10.1. In photon therapy most of the radiation effect is through production of free radicals.

DNA damage occurs through the ionizations of DNA or the surrounding material [269]. Ionizing radiation induces single and double DNA strand breaks. The most damaging type of lesion is the DNA double strand break (DSB), which is a complete breaks of the DNA double helix.

Cells respond to radiation, and the subsequent DNA damage, by activating a complex and well-organized set of biochemical signalling and effector pathways (Figure 84), known as the DNA damage response (DDR) pathway. The DDR is a signal transduction pathway that senses DNA damage. The aim of DDR is to restore the DNA to its original configuration and maintaining the genomic stability of the cell [265]. Initially, sensor proteins detect DNA damage and/or chromatin[14] alterations that occur after damage induction. The signal is then transmitted to transducer proteins that amplify the damage signal. At the end of the chain, involved in specific pathways, are the effectors. The multiple signalling cascades implicated in DDR can result in a variety of cellular

---

[14] Complex of DNA and proteins that make up the contents of the nucleus

responses: cell cycle arrest, induction of stress response genes, DNA repair and cell death shown in Figure 84.

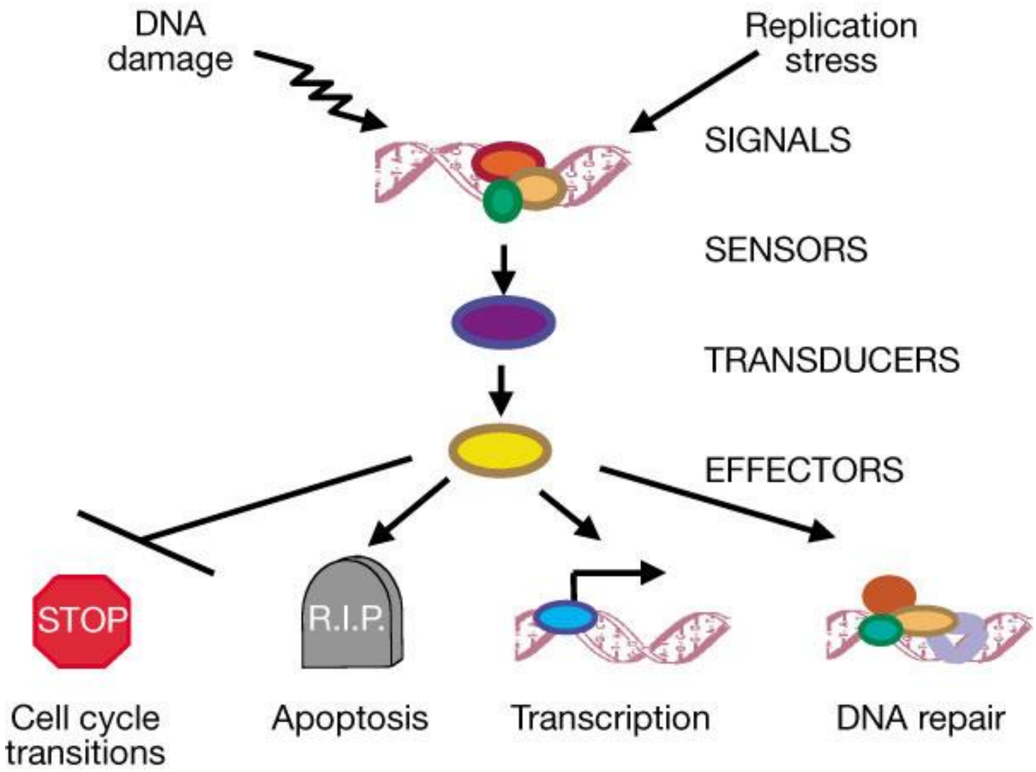

Figure 84. A contemporary view of the general outline of the DNA damage response signal transduction pathway. Arrows represent activating events and perpendicular ends represent inhibitory events. For simplicity, the network of interacting pathways are shown as a linear pathway consisting of signals, sensors, transducers and effectors [270].

The DDR is regulated by the PIKK (i.e. phosphoinositide three-kinase-related protein kinases). The PIKK primarily responsible for signalling the presence of DNA damage include ATM (Ataxia Telangiectasia Mutated), ATR (Ataxia Telangiectasia and Rad3-related protein) and DNA-PKcs (DNA Protein Kinase catalytic subunit). The signal that activates ATM and DNA-PKcs is a double-strand break (DSB), while ATR responds to single-stranded DNA gaps. All three kinases are recruited to the DNA lesion site, which promotes kinase activation. These PIKK phosphorylate[15] hundreds of proteins that maintain genome integrity through regulation of cell cycle progression, DNA repair, apoptosis, and cellular senescence [271]. Upon DSB induction by ionizing radiation, there is an extensive response in the chromatin flanking the break. Hundreds of molecules of multiple DNA damage response protein species accumulate at DSB sites forming large nuclear aggregates that appear as irradiation-induced nuclear foci (IRIF) [272] (Figure 85).

---

[15] addition of a phosphate (PO_4^{3-}) group to a protein

A key regulator of IRIF formation in mammalian cells is the histone subtype H2A isoform X (H2AX), a component of the nucleosome core structure that comprises 10%–15% of total cellular H2A [273].

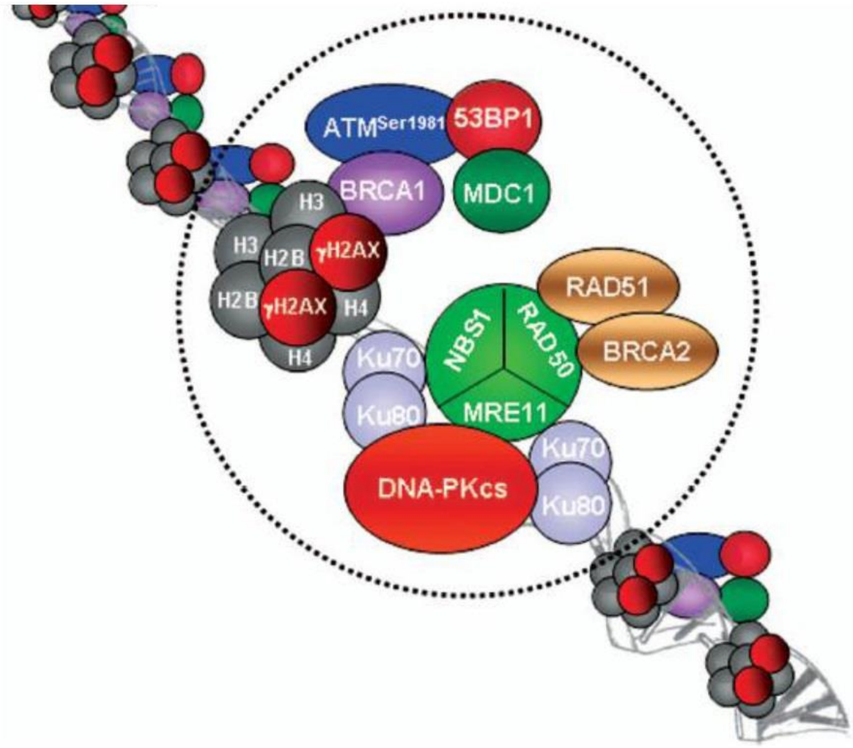

Figure 85. Recruitment of DNA sensing and repair proteins as irradiation-induced foci (IRIF) at a DSB. The DNA DSB is expanded to illustrate a histone octamer containing irradiation-induced phosphoforms of H2AX (e.g., γ-H2AX) which can involve megabase domains surrounding the DSB. At the DSB itself, are DNA-PK (DNA-PKcs kinase and Ku autoantigen subunits form Ku70-Ku80 heterodimers which act to initiate non-homologous end joining, NHEJ), RAD51-BRCA2 (if S or G2 phase to initiate homologous recombination ,HR) and the MRE11 sensing complex. Following DSB induction, MRN binds to DNA ends and facilitates recruitment and activation of ATM, the kinase responsible for the phosphorylation of H2AX. γ-H2AX mediates the recruitment of numerous DSB recognition and repair factors including MDC1, BRCA1, 53BP1 and ATM [274].

Some DDR factors have intrinsic affinity for free DNA ends. The MRN complex[16] (Mre11/Rad50/NBS1) can detect DSB and bind to the DNA ends [275]. Given its structure, the MRN complex is thought to form a microenvironment that holds the two DNA ends together [276]. ATM[17] is then indirectly recruited to DSB and activated by the MRN complex via an interaction between the C-terminus[18] of NBS1[19] and ATM [275]. One of the first substrates of ATM to be phosphorylated is histone H2AX. This modified H2AX called *γ-H2AX* forms within seconds, and reaches its maximum level at about 30

---

[16] Complex of proteins responsible for the detection of double strand brakes

[17] Enzyme responsible for phosphorylation

[18] End of amino acid chain terminated by a free carboxyl group (-COOH)

[19] A member of the DSB repair complex involved in DNA repair and DNA damage-induced checkpoint activation

min after irradiation [277]. The ratio of DNA DSBs to visible γ-H2AX foci is close to 1:1 [278], which forms the basis of a sensitive quantitative method for detection of DNA DSBs in mammalian cells [279, 280].

Although radiotherapy is an established practice currently used to treat nearly half of all cancer patients in the western world, basic radiobiological research continues to provide evidences for further improvement and optimization of cancer therapy [281]. It is well documented that increasing dose specifically to tumour tissue without increasing the dose to normal healthy tissues leads to improvement in the probability cure. The limiting factor for radiotherapy is normal tissue toxicity. One of the most common and powerful techniques introduced to modern radiotherapy is based on the radiobiological response of tumour and healthy tissue to radiation is the fractionation of the total dose to which patients are exposed to (fractionated radiotherapy). Here a number of smaller doses are delivered separated by a recovery period of several hours (between 12 and 24 hours). The time between fractions allows normal tissues to repair sublethal damage, but since most tumours have faulty repair mechanisms, they usually cannot repair DNA damage. The time between fractions also allows normal cells to repopulate thus further reducing normal tissue toxicity. Fractionation also leads to increased tumour kill efficiency due to cell cycle reassortment [20] of tumour cells and potential reoxygenation which increases the radiosensitivity of cancer cells to subsequent radiation exposures [282].

More recently intensity-modulated radiation therapy (IMRT) that allows the delivery of highly precise and conformal radiation therapy has been developed. During treatment, the beam is constantly modelled to the specific size and shape of the tumour which delivers maximum dose to the tumour while leaving adjacent healthy tissues with minimal exposure. Because the surrounding normal tissue receives less radiation, patients are likely to suffer fewer side effects and have a higher quality of life after treatment.

6.1.1. Linear Energy Transfer and Relative Biologic Effectiveness

Since experiments on cultured mammalian cells were first reported in the early 1960s [283], the pattern of biological response to different radiation types has been found to be

---

[20] Progression of cells through the cell cycle during the interval between the split doses

similar for many cell lines [284]. To assess the biological effectiveness of a test irradiation (VHEE) it is common in radiobiological studies to determine the relative biological effectiveness (RBE). RBE is defined as the ratio of the doses required by the two types of radiation to cause the same level of effect (E) [285] and is defined by:

$$RBE = \left.\frac{Dose_{reference\ radiation}}{Dose_{test\ radiation}}\right|_{E_{ref.rad}=E_{test\ rad}}. \tag{6.1}$$

Thus, the RBE depends on the dose and the biological endpoint, which defines a specific biological event during the course of an experiment. The *reference radiation*, most often used to determine the RBE of a test radiation, are X-ray photons from ^{60}Co-sources (1.17 and 1.33 MeV) or ∼200 kV X-ray tubes.

It is well established that the RBE of photons increases with decreasing photon energy [286, 287], i.e. that 200 kV X-rays are more effective than MeV X-rays [288]. Marthinsen *et al*. [288] determined the RBE based on clonogenic survival data using breast cancer cell lines following irradiation with 50 keV, 380 keV and 6 MeV X-rays. RBE values for 50 keV irradiation, with 6 MeV, as the reference radiation, was found to vary from 1.4 (at lower doses) to 3.1 (at higher doses of radiation); whilst 380 keV X-ray irradiation produced RBE values ranging from 1.3 to 2.3. Similar experiments using glioma cell lines compared the biological effect of 8 keV X rays against ^{60}Co gamma rays (1.17 and 1.33 MeV). The RBE at 50% and 10% survival using the ^{60}Co, as the reference radiation, was 2.6 and 1.9, respectively [289]. These data shows that keV X- rays produce 1.3 to 3 times the biological effectiveness of megavoltage photons.

There are several important differences in the way low-energy X-rays and high-energy photons interact with tissue. First, low energy X-rays ionize by the photoelectric effect, whilst high-energy photons produce ionization via the Compton process or pair production. Second, energy deposition by low-energy X-rays depends upon atomic number of the absorber whereas high-energy particles are independent of atomic number [290].

Furthermore, we can consider this process from the point of view of LET and stopping power: as the energy of the photons decreases, the energy of the secondary electrons emitted in the photon interactions decreases, with a corresponding increase in stopping power (linear energy transfer). For example, the LET of a 15 keV secondary photoelectron is around 2 keV/μm , which is about an order of magnitude greater than the LET of a 500 keV electrons. A review of relative biological effectiveness dependence on linear energy transfer for low-LET radiation can be found in the literature [291].

The radiation types are characterized by LET, which is defined as the average energy locally imparted over an incremental distance traversed by the incident particle [292] (see section 4.2.9). In terms of the relationship between RBE and LET, it has been shown that the RBE(LET) curve increases to a maximum for LET for ~100 keV/µm, then decreases with increasing LET (see Figure 86). It is interesting to ask why radiation with an LET of about 100 keV/µm is optimal in terms of producing a biologic effect. At this density of ionization, the average separation between ionizing events almost coincides with the diameter of the DNA double helix (2 nm). Radiation with this density of ionization has the highest probability of causing a double-strand break by the passage of a single charged particle.

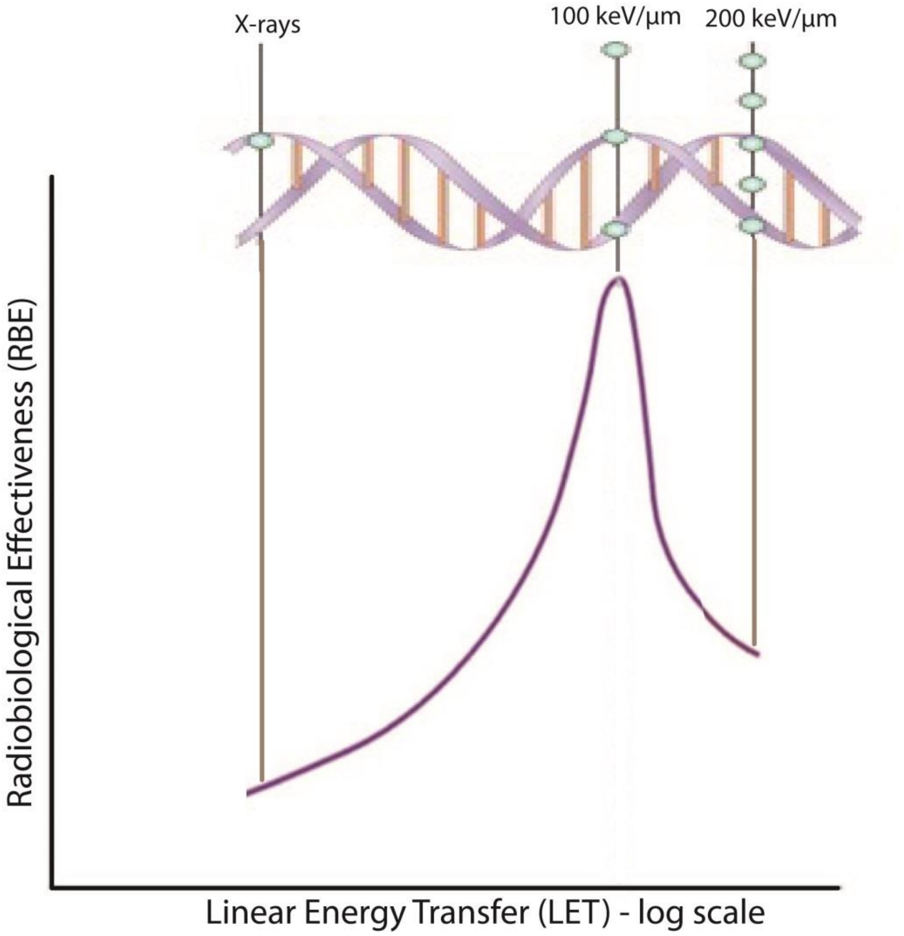

Figure 86. The relationship between radiobiological effectiveness (RBE) and linear energy transfer (LET) [293].

RBE values for various high LET radiation types have been determined for many different cell types, both *in vitro* and *in vivo*. It has been demonstrated in *in vitro* studies that RBE is highly dependent on cell type and the studied endpoint [294], but also on particle species, due to the different dose deposition profiles on a microscopic scale [295]. RBE depends also on the dose level and the number of dose fractions (or, alternatively, the dose per fraction) because, in general, the shape of the dose-response relationship is different for radiation that differ substantially in their LET. Hence LET is not sufficient as a predictor of RBE. This is one of the motivations for the development of radiobiological models that explicitly include the detailed particle energy spectrum of the applied radiation field. Several models exist which aim to predict the biological response of cells irradiated with high-LET radiation. The most prominent models in radiotherapy context are based on the amorphous track formalism established by Butts and Katz [296]. These models explicitly point out that the response of a biological system cannot be characterized with LET as a single valued parameter.

The aim of this work is to interrogate the biological effects of VHEE produced by a laser-plasma wakefield-accelerated accelerator in *in vitro* cancer cell models with the overall aim of providing the biological evidence to encourage future translation of this form of radiotherapy into clinical applications.

The efficacy of VHEEs on tumour cells *in vitro* is assessed by clonogenic assays (section 6.2.1.4) and the γ-H2AX assay (section 6.2.1.6), employing the immunofluorescence detection of signalling molecules deployed to indicate DNA double-strand breaks and their repair. The radiobiological analysis has been carried out in the Strathclyde Institute of Pharmacy and Biomedical Sciences and the data on cells irradiated with VHEEs has been provided by courtesy of Dr. Annette Sorrensen.

6.2. Radiobiological experiments with LWFA VHEE beams

The radiobiological experiments using a laser-plasma accelerator were undertaken in the ALPHA-X laboratory at the University of Strathclyde. The brief overview of the principles

Following the dosimetric characterization of the laser-wakefield accelerated very high energy electron beam, presented in chapter 5, the VHEEs are examined in terms of their radiobiological properties, i.e. their relative biological effectiveness. The cell types used in the present work are of human lung cancer cells (see section 6.2.1.3) chosen because of superior dose deposition properties in air-filled cavities (such as lungs) for VHEEs propagating through heterogeneous media with varying densities. This aspect has been discussed in section 1.2.

6.2.1. *Methodology*

6.2.1.1. *Experimental set-up and dosimetry for radiobiological experiment in ALPHA-X laboratory*

The term dosimetry conveys the determination of the absolute dose delivered to the cell sample placed inside a cell culture vessel during irradiation with VHEE from the ALPHA-X beamline.

In this work two types of dosimeters have been used to evaluate the absolute dose delivered in Gy to the cells. A standard ionization chamber (IC) (section 5.4) is used as it allows online dose monitoring during the irradiation. However, as discussed in chapter 5.4 the IC exhibits significant ion recombination in its sensitive volume due to exposure to high density radiation. Therefore, application of an additional correction factors for precise dose measurements of VHEEs with ICs is essential. Moreover, as the IC provides the integrated dose over a sensitive volume that excees the volume of a cell sample, the IC is used to determine direct beam exposures only. As an absolute dosimeter radiochromic EBT2 films (see chapter 5.3) are used. As discussed in chapter 5.3, radiochromic film can be used to measure the 2D spatial dose distribution of variable beam spot sizes and high dose gradients characterising the LWFA electron beams.

The cell samples are initially placed immediately after the Mylar window as shown in Figure 87. However, the spatial inhomogeneity of the dose distribution within the beam spot made experiments with cell samples a challenge. To increase the radiation field and improve the dose uniformity within this radiation field the beam is transmitted a further distance in air (185 cm). Under these conditions the electron beam size, due to multiple Coulomb scattering with air molecules increases (as shown in Figure 87). Monte Carlo calculations (presented in chapter 4.2) show that the electron beam after several centimeters of propagation in air still maintains its distinct properties (i.e. dose deposition characteristic, very high electron energy spectrum and short temporal duration). LWFA electrons had a quasi-Gaussian diameter of ~1.5 cm (FWHM).

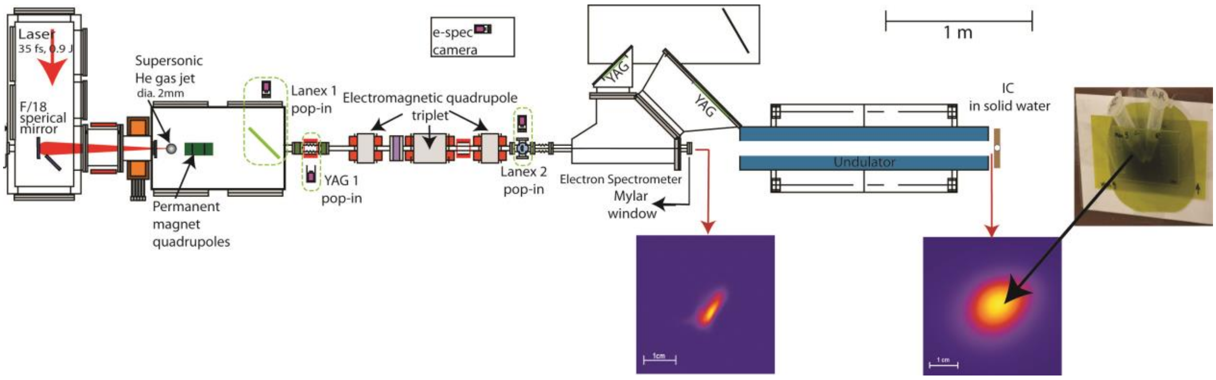

Figure 87. Cell irradiation set-up in ALPXA-X beamline. The false-colour insets before and after undulator depict the beam profiles at the vacuum window and 185 cm further.

To further ensure that the cells are irradiated within a uniform radiation field of the VHEE beam the cells are irradiated in cell pellets. As shown in Figure 87, the two pellets are positioned symmetrically within the field of the beam. Two pieces of EBT2 film were attached, one in front and the other at the rear of the sample, which allows measurement of the absolute dose deposited before and after the pellet. The dose delivered to the cell sample is calculated as the average measured dose deposited in the front and the rear film.

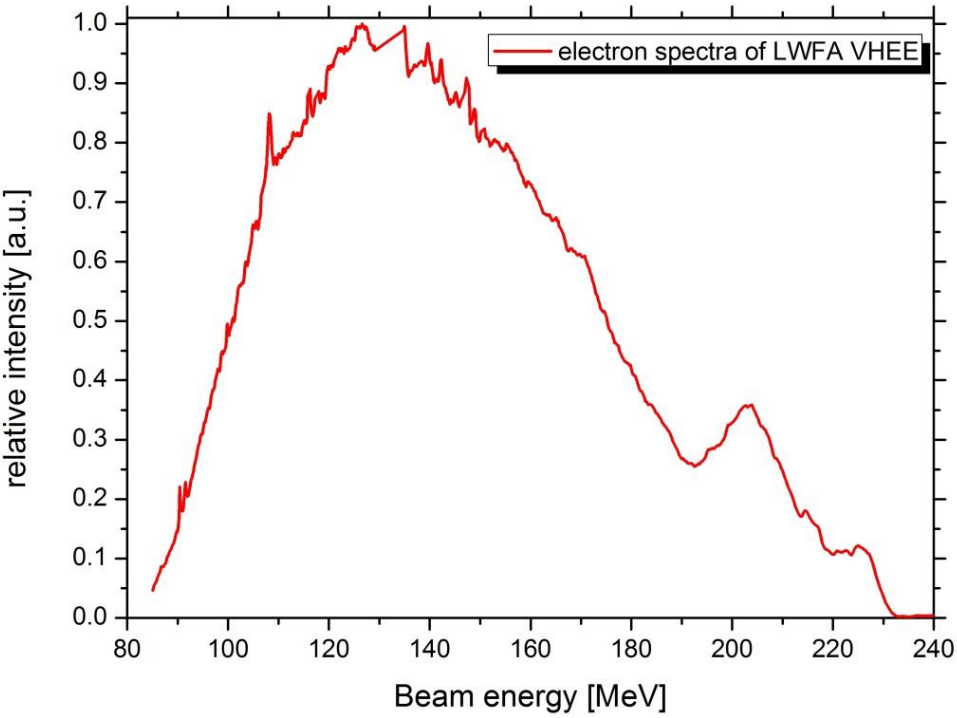

Figure 88. Typical electron spectra of the ALPHA-X LWFA VHEE beam during the radiobiology experiment. Assuming a Gaussian spectrum, the central energy corresponds 138 MeV with 50 MeV r.m.s. energy spread.

The measured electron spectra for these experiments, as described in section 3.2.5, 137 MeV with 45 MeV r.m.s. energy spread. A typical electron spectra, averaged of 200 consecutive shots, is shown in Figure 88.

6.2.1.2. 225 kV X-ray irradiation system

Faxitron's MultiRad225 X-ray irradiation system (*RPS Services*, Surrey, UK) has been used as a reference radiation for radiobiological comparative studies. The X-ray 225 irradiator generates bremsstrahlung irradiation with an energy spectra as illustrated in Figure 89. An 0.8 mm, thick beryllium filter attenuates the low energetic photons. The samples are positioned 50 cm from a 8 mm thick aluminium filter where the reference calibration is performed. The machine routinely operates at 225 nominal tube voltage (13 mA applied current) delivering at 50 cm FSD (filter-to-surface-distance) 2.2 Gy/min.

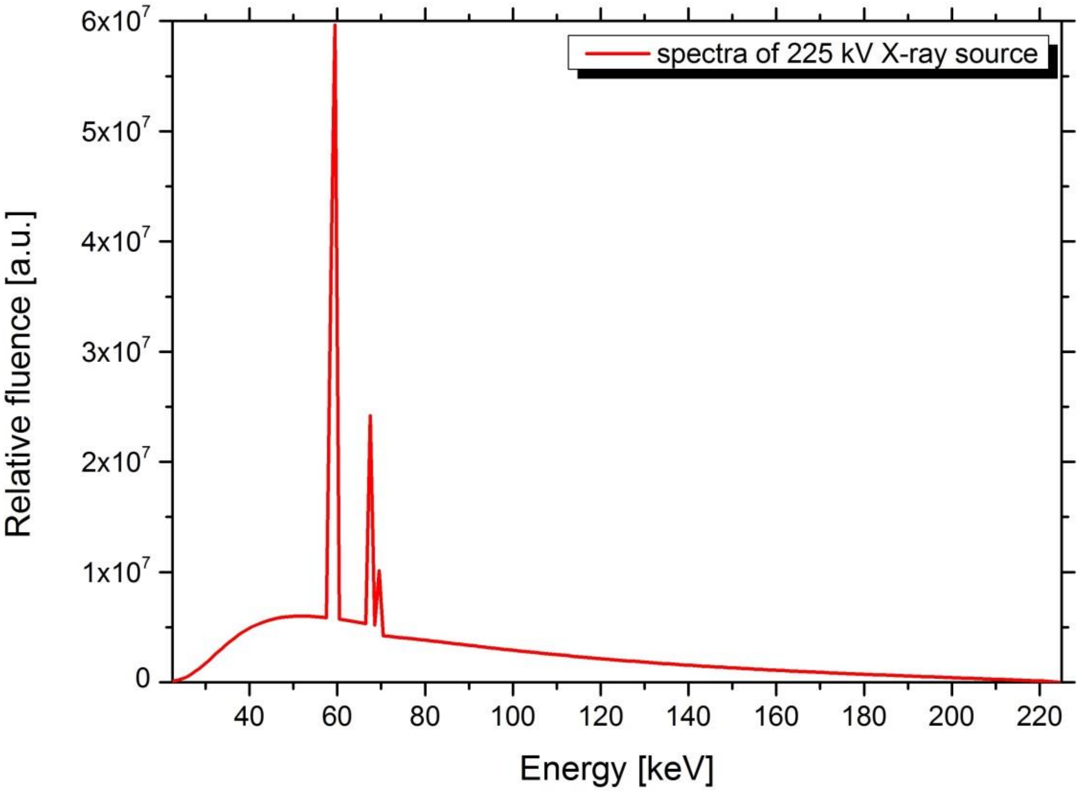

Figure 89. Bremsstrahlung spectra of the 225 kV X-ray irradiator used as a reference radiation source in the studies.

6.2.1.3. *Cell samples*

The lung cancer cell lines, A549 adenocarcinoma and H460 large-cell carcinoma purchased from *American Tissue Culture Centre* (*ATCC*, Teddington, UK) have been used in this study. Cells were cultured in growth media – RPMI 1640 (*Life Technologies, Inc*., Paisley, UK) supplemented with 1% of L-glutamine (2 mmol/L), 10% (v/v) heat-inactivated fetal calf serum (FCS) (*Biosera*, Nuaille, France), 1% of Penicillin Streptomycin (100 U/mL) (Pen Strep) (*Life Technologies*, *Inc*., Cergy Pontoise, France) and 1% of Fungiezone® Antimycotic (2 µg/mL) (*Life Technologies, Inc*., Paisley, UK), and are maintained at 37°C in a humidified atmosphere at 5% carbon dioxide.

Preparation of cells for cell irradiation

For LWFA VHEE experiment, cells are irradiated in pellets due to the small irradiation field (Figure 87). Cells are plated into a 25 cm^3 tissue culture flask ($3{\cdot}10^5$) 3 days prior irradiation. On the day of irradiation, when cells have reached a confluence of 60-70%, they are removed from the flask by the addition of 0.05% (w/v) solution of trypsin and counted using a hemocytometer. $5{\cdot}10^5$ cells are then added to a 0.5 ml eppendorf tube in a volume of 150 µl of growth media. Cells are then irradiated. Approximately 30 minutes after irradiation the cells are re-suspended in growth media and seeded for a clonogenic assay. For every irradiation a control (non-irradiated) sample, experiencing the same environmental conditions as the irradiated cells, is analysed.

For irradiation of cells with X-rays, cells are irradiated in a cell monolayer rather than in cell pellets. $1.5{\cdot}10^5$ cells are plated 2 days prior to irradiation into 35 mm diameter Petri dishes. Immediately before irradiation the media is removed and replaced with fresh growth media post-irradiation the samples are incubated at 37°C in a humidified atmosphere at 5% carbon dioxide for 24h before plating out for a clonogenic assay.

6.2.1.4. *Clonogenic assay*

In 1955 Puck and Marcus developed the clonogenic assays, which has become a basic tool for studying the effect of cell toxicity [297, 298]. A colony is defined as a cell that has the capacity to divide and proliferate indefinitely, which gives rise to a colony of cells.

Cells are seeded for a clonogenic assay as described by Boyd *et al.* [299]. Cell cultures are washed with PBS (phosphate buffered saline), harvested by incubation with trypsin (0.05% w/v) and diluted in growth media. To obtain a single cell suspension, cells are gently syringed through a 19G needle. Cells are then counted under a microscope using a hemocytometer and 250 cells are seeded into a 60 mm Petri dish filled with 5 ml of pre-warmed growth media. For each sample three replicate dishes are prepared. Samples are incubated at 37°C in humidified incubator supplied with 5% CO_2 for 7 days when discreet colonies form. Before stained with crystal violet the media is aspirated from the cells, washed with PBS and fixed with methanol for 20 minutes. The colonies are then stained with a 10% solution of crystal violet for 10 minutes. The staining solution is discarded, the plates are washed in tap water and dried in air.

Colonies counting

Colonies are counted with the naked eye to obtain the plating efficiency (PE) for each Petri dish. The term PE is defined as the percentage of colonies formed of the total number of cells seeded (equation (6.2)), which gives information both on cell cytotoxicity of the external insult and on the viability of cells.

$$PE(\%) = \frac{Number\ of\ colonies\ formed}{Number\ of\ cells\ seeded} \cdot 100. \tag{6.2}$$

A cluster of blue-stained cells is considered a colony if it comprised of at least 50 cells, the threshold at which colonies are visible to the naked eye. Following determination of PE, the fraction of cells surviving (SF) a given treatment is calculated by normalizing PE to that of the control unirradiated plates after a given dose:

$$SF(\%) = \frac{PE\ of\ treated\ sample}{PE\ of\ control} \cdot 100. \tag{6.3}$$

The survival curves are evaluated for the A549 and H460 cell lines irradiated with VHEEs and X-rays for a range of doses from 0 to 5 - 6 Gy. For visual presentation of survival after radiation, the survival fraction is plotted on a logarithmic scale (y axis), against dose on a linear scale (x axis).

Statistical evaluation of clonogenic survival curves

The clonogenic data are presented as mean values and standard error of the mean (±SEM). According to the work published by Buffa *et al*. [300], the distribution of the SF can have a Gaussian and log-Gaussian distribution curve fitted using the least square analysis. Experiments with X-ray source are repeated 4-6 times and 4 times for VHEEs for both cell lines. The X-ray source is a stable and reliable source with a dose variation of less that 3%. In contrast, the laser-wakefield accelerated electron beam exhibits fluctuations that are manifested in variations in the charge of the electrons between shots (i.e. the dose rate). The rate at which a given dose is delivered varies between different sets of experiments. The statistical evaluation of the clonogenic survival curves is carried out for cell pellets that received a dose delivered with the same dose rate.

The uncertainty of dose measurements with EBT2 Gafchromic films has been discussed in section 5.2.2.3. There is an uncertainty related to the calibration procedure, however it is relatively low (less than 4%). The largest uncertainty in the experiments with LWFA arises from the different batch number of the Gafchromic film used to produce the calibration curve, and that used during the cell irradiation experiments. These uncertainties are dose-level dependent and have been carefully considered during the analysis. Another dose uncertainty originates from the spatial distribution of the transverse profile. Because the lateral profile of these beams has a quasi-Gaussian distribution, the cells within the radiation field could receive slightly varying doses. Careful analysis of the irradiated films shows that this variation is always less than 8%. To assess the dose uncertainties in the VHEE experiments, an error propagation method, which accounts for the independent uncertainties, has been used.

6.2.1.5. Linear quadratic model

The *linear quadratic model (*LQ) model was originally developed from biophysical considerations, rather than empirical clinical observations, and it is closely associated with parameters more likely to influence biological response. The mechanistic basis for the LQ model has been extensively reviewed in the literature [301, 302]

The shape of the cell survival curves depends on factors such as the type of radiation and cell line. The linear quadratic cell survival curves for sparsely ionising radiation (X-rays) and densely ionising radiation (heavy ions) are shown in Figure 90. At lower doses, the slope of the cell survival curve following X-irradiation, is characterised as an exponential function of dose, followed by a shoulder. For densely ionising radiation the cell survival is characterised by a linear survival curve [290].

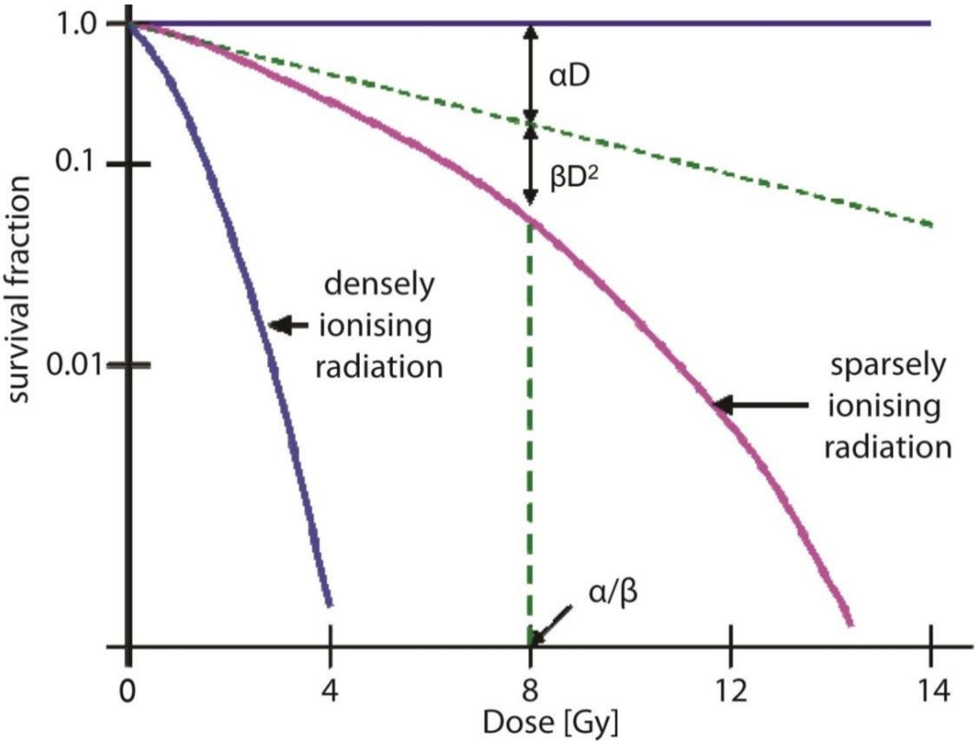

Figure 90. Typical shape of cell survival curve for mammalian cells with the fraction of cells surviving as plotted on a logarithmic scale against dose on linear scale. The linear quadratic model is described by the linear component (αD), which is proportional to the dose and quadratic component (βD^2), which is proportional to the square of dose. The α/β ratio is the value where the linear and quadratic components are equal.

Most common underlying biological rationale of the LQ model is that radiation produces a double strand DNA break using a single radiation track. The LQ model assumes that there are two components which represent the severity of cell death by radiation: one is proportional to the dose and the other one is proportional to the square of the dose. This model is described by the following equation(6.4):

$$SF = \exp(-\alpha D - \beta D^2), \tag{6.4}$$

where SF is the fraction of cells surviving a dose D, and α and β are constants. The component $e^{-\alpha D}$ is the tangent at the origin of the curve and takes into account the irradiation events which are directly lethal, i.e. those events that individually lead to the death of the cells (as for densely ionising radiation). On the other hand, the component $e^{-\beta D^2}$ describes the *shoulder* of the survival curve and expresses the fact that a constant increase of the dose causes a higher and higher mortality rate. This means that cell death results from the accumulation of events that are individually incapable of killing the cell, but which become lethal when added together (as for sparsely ionising radiation).

The ratio α/β (which is measured in Gy) gives the dose at which the linear and quadratic components of cell killing are equal. Beyond this point, the surviving fraction drops rapidly as the quadratic cell kill takes over. In clinical use:

- Early responding tissues[21] have a high *α/β* ratio, leading to a linear increase in cell kill at therapeutic doses. The average *α/β* of early responding tissues is 10.
- Late responding tissues[22] have a low *α/β* ratio, leading to less cell kill at lower doses and greater cell kill at higher doses. The average *α/β* of late responding tissues is 3.
- Most tumours have a high *α/β* ratio (above 10) [303].

6.2.1.6. Immunofluorescence detection of DNA double-strand breaks (γ-H2AX assay)

To determine γ-H2AX induction and loss kinetics, i.e. DNA damage and repair, cells were fixed at different time points: at 1h, 2h and 5 hour post-irradiation. 30 minutes after irradiation $2 \cdot 10^4$ cells are seeded onto cover slips. 1, 2 or 5 hour after irradiation the cells are fixed in 4% Paraformaldehyde for 15 minutes at room temperature washed in PBS and permeabilized with 0.5% TritonX-100:PBS for 10 minutes. To reduce non-specific antibody binding, cells are then incubated in a blocking solution containing 0.5% BSA (bovine serum albumin), 0.15% triton X-100 in PBS. Following a 1h incubation cells are washed in PBS and incubated overnight at 4°C in a humidified chamber with anti-γ-H2AX antibody (*Millipore*) diluted 1:250 in a blocking buffer. After subsequent washing in PBS anti-mouse IgG-Alexa488 (*Millipore*) diluted 1:600 in blocking buffer is applied and left for 1h at 4°C. After washing, the coverslips are mounted with VECTASHIELD® mounting medium (*Vector Laboratories*) and imaged using fluorescence microscopy.

---

[21] Self-renewing tissues characterized by a rapidly proliferating stem cell that leads to differentiation and production of the mature functioning cells

[22] Less able to tolerate retreatment tissues because they cannot recover from the initial damage; they do not have a rapidly proliferating stem cells

Microscopy

Images are captured using a Leica TCS SP5 confocal laser microscopy system. All images are processed using the same brightness and contrast parameters with a 63× objective lens (1.2 W correction, filter HC PL Apo CS). 10 z-stack images with 1 μm resolution are taken from of each image cell.

Foci quantification

The number of γ-H2AX foci are quantified in control and in irradiated A549 and H460 cells at 1h, 2h and 5h after irradiation and doses of 0 - 9 Gy for A549 and 0 – 6 Gy for H460. γ-H2AX foci are scored manually by the same operator throughout. The average number of foci per cell is calculated.

Statistical evaluation of γ-H2AX assay

All experiments with VHEEs are repeated 4 times for both cell lines. However, due to charge (per shot) variation (i.e. the dose rate), the delivered dose to the samples varied. Statistical evaluation is conducted for pellet samples that received the same dose (delivered at the same rate) with less than 10% variation.

6.2.2. Results

Following irradiation with LWFA VHEE and X-rays the clonogenicity has been determined for both cell lines. γ-H2AX foci assays have been conducted for samples exposed to VHEE.

6.2.2.1. Clonogenicity

The clonogenic capacity is determined to compare the radiosensitivity of the A549 and H460 cells lines following irradiation with two radiation sources, i.e. laser-plasma wakefield VHEEs and 225 kV X-ray photons. However, the cell irradiation setup were different for the two irradiation sources used. For X-irradiation, cells are irradiated in monolayers, whilst cell pellets are irradiated with VHEE. To assess if the response in the clonogenicity of the cells to X-rays differ depending on whether the cells were irradiated in a monolayer or in a cell pellet a pilot experiment has been conducted to compare the response in these two different setups. The clonogenicity following exposure to different doses of radiation did not differ significantly for cells irradiated in a pellet compared with cells irradiated in monolayers. Thus, the X-irradiating data can be compared with VHEE irradiation data.

Plating efficiencies in counted control samples for both X-ray and VHEE studies are summarized in Table 29. The PE was 92% ± 4% for A549 cells which are 13%± 2% higher than for H460 (PE of 79% ± 5%). Furthermore, no significant difference is found in PE between cells in monolayer compared with cells in pellets.

Table 29. Measured plating efficiency (PE) for control samples for A549 and H460 cell lines irradiated with 225 kV and LWFA VHE electron beam.

cell configuration	*Monolayer*				*Pellet*			
	A549 -1	*A549 -2*	*H460 -1*	*H460 -2*	*A549 -1*	*A549 -2*	*H460 -1*	*H460 -2*
PE [%]	0.87	0.95	0.82	0.84	0.95	0.93	0.77	0.85
	0.93	0.92	0.71	--	0.96	0.92	0.74	0.8
	0.94	0.89	0.76	--	0.83	--	0.78	0.83
Mean ± SEM	0.91±0.04	0.92±0.03	0.76±0.06	0.84	0.91±0.07	0.93	0.76±0.02	0.82±0.03
	A549		H460		A549		H460	
Mean ± SEM	**0.92±0.03**		**0.78±0.06**		**0.92±0.05**		**0.80±0.04**	

The lung cancer cell lines, A549 and H460, used in these studies had different sensitivities to ionising radiation. The survival curve following X-irradiation of the two cell lines are shown in Figure 91. The dose required to reduce cell survival to 25%, 50 % and 75 % are shown in Table 30.

Table 30. Dose required to reduce cell survival to 25%, 50% and 75% for A549 and H460 cell lines.

A549		H460	
survival fraction	Dose [Gy]	survival fraction	Dose [Gy]
SF25	4.14	SF25	2.57
SF50	2.53	SF50	1.33
SF75	1.29	SF75	0.53

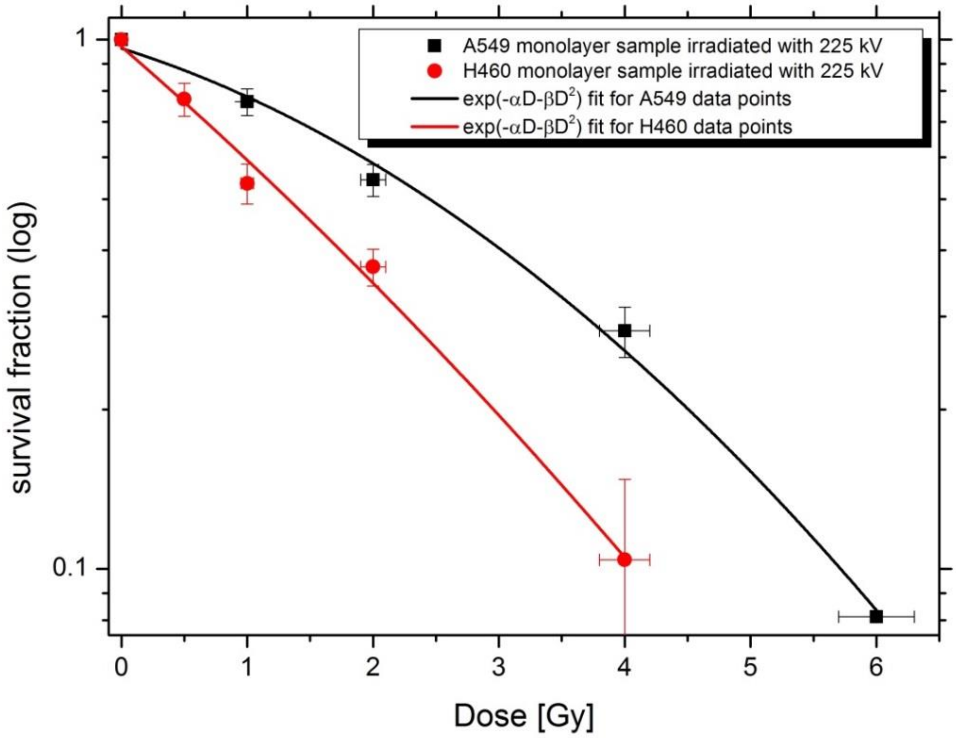

Figure 91. Shape of survival curves for A549 and H460 cell lines exposed to the 225 kV X-ray source. The experimental data are fitted to a linear-quadratic function. Note, that SF uncertainties are expressed as mean percentage of survival ± SEM (where $n \geq 4$).

The fraction of cells surviving at 2 Gy of radiation is 37% ± 6% for H460 and 54% ± 6% for A549. As shown in Table 30 and Figure 91 the dose required to kill 25%, 50% and 75% of the cells is higher for H460 cells than for A549cells. The dose required to kill 75% of the cells is 4.1 Gy and 2.6 Gy for A549 and H460 cell lines, respectively. Both, Figure 91 and Table 30 show that A549 is more radioresistant than the H460 lung cancer cell line.

In Figure 91, the cell survival curves are fitted to the LQ model for both cell lines following X-irradiation. The subsequent calculated α and β values are shown in Table 31.

Table 31. α and β coefficients from linear-quadratic model fit shown in Figure 91.

A549		H460	
α	β	α	β
0.28±0.07	0.009±0.001	0.47±0.09	0.021±0.07

Based on these data the *α/β* ratio for A549 is 31.1 which is higher than the 22.4 for H460 cells, indicating a higher sensitivity of H460 cells to radiation.

Figure 92 shows all of the individual survival fraction data points (for every single experiment separately) for the A549 and H460 cell lines exposed to LWFA VHEEs. The dose rate at which the total dose of radiation is delivered varies from 0.10 to 0.35 Gy/min between samples irradiated with LWFA VHEE. Therefore, the samples have been divided into three groups according to the dose rate.

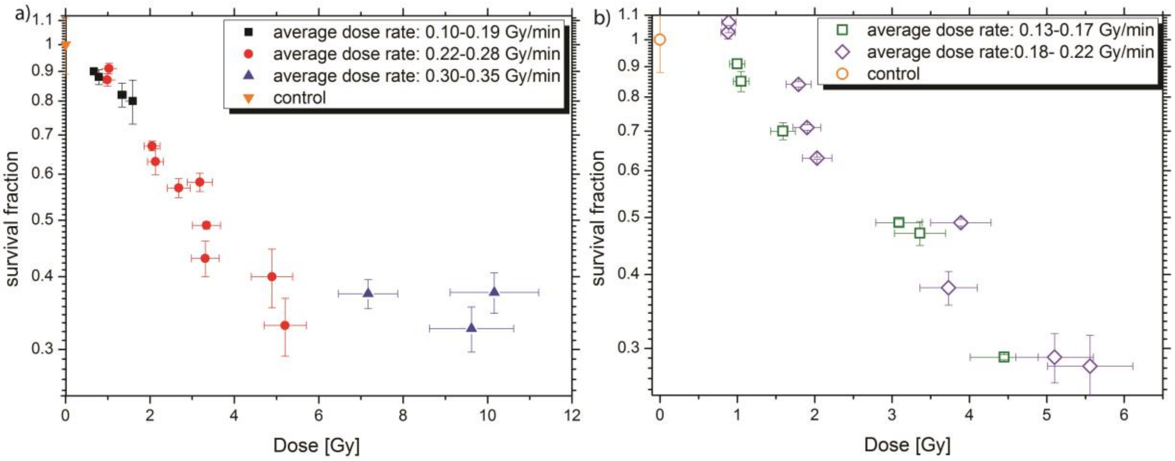

Figure 92. The clonogenic survival data points for (a) A549 and (b) H460 cells lines irradiated with LWFA VHEEs.

In both cell lines there is evident decrease in the SF with increasing dose of radiation. However, in the A549 cells at the higher doses delivered (i.e. ~10 Gy) radioresistance is observed (Figure 92 (a)). At these high doses, the dose rate is the highest (above 0.3 Gy/min).

For further analysis of the A549 cell line the SF data are averaged within the dose rate range from 0.22 to 0.28 Gy/min. The survival fraction curve is shown in Figure 93 and the SF data for both X-ray and VHHE studies are given in Table 32.

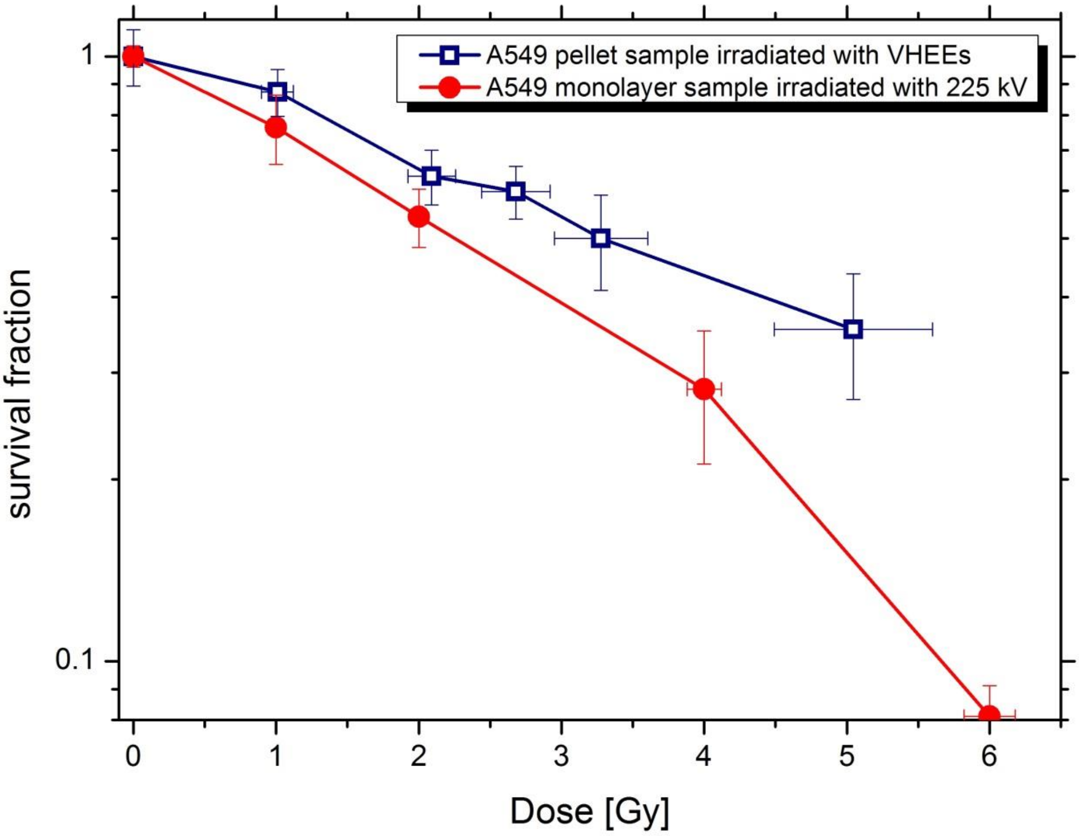

Figure 93. Clonogenic survival curve for the A549 lung cancer cell line irradiated with LWFA VHE electron beam (blue squares) and 225 kV X-ray source (red solid circles). The error bars of the SF represent standard deviation for particular dose level.

Table 32. Comparison of clonogenic data for VHEE and X-ray irradiation for the A459 cell line.

VHEEs (0.22-0.28 Gy/min)			X-ray (2.2 Gy/min)		
n	Dose [Gy]	SF	n	Dose [Gy]	SF
5	0	1.00±0.11	6	0	1.00±0.04
2	1.01±0.11	0.87±0.08	5	1.00±0.03	0.76±0.10
2	2.09±0.17	0.63±0.07	5	2.00±0.06	0.54±0.06
1	2.68±0.24	0.60±0.06	5	4.00±0.12	0.28±0.07
3	3.28±0.33	0.50±0.09	4	6.00±0.18	0.08±0.01
2	5.05±0.55	0.35±0.08			

Following 2 Gy irradiation, the survival fraction for VHEEs irradiated A549 cells is 63% ± 7%, whilst for X-irradiation the SF is 54% ± 6%.

The survival fraction for H460 samples irradiated with dose rates ranging from 0.18-0.22 Gy/min with LWFA VHEE has been evaluated. The survival curves for both LWFA VHEE and X-irradiation are shown in Figure 94. The survival fraction data are given in Table 33.

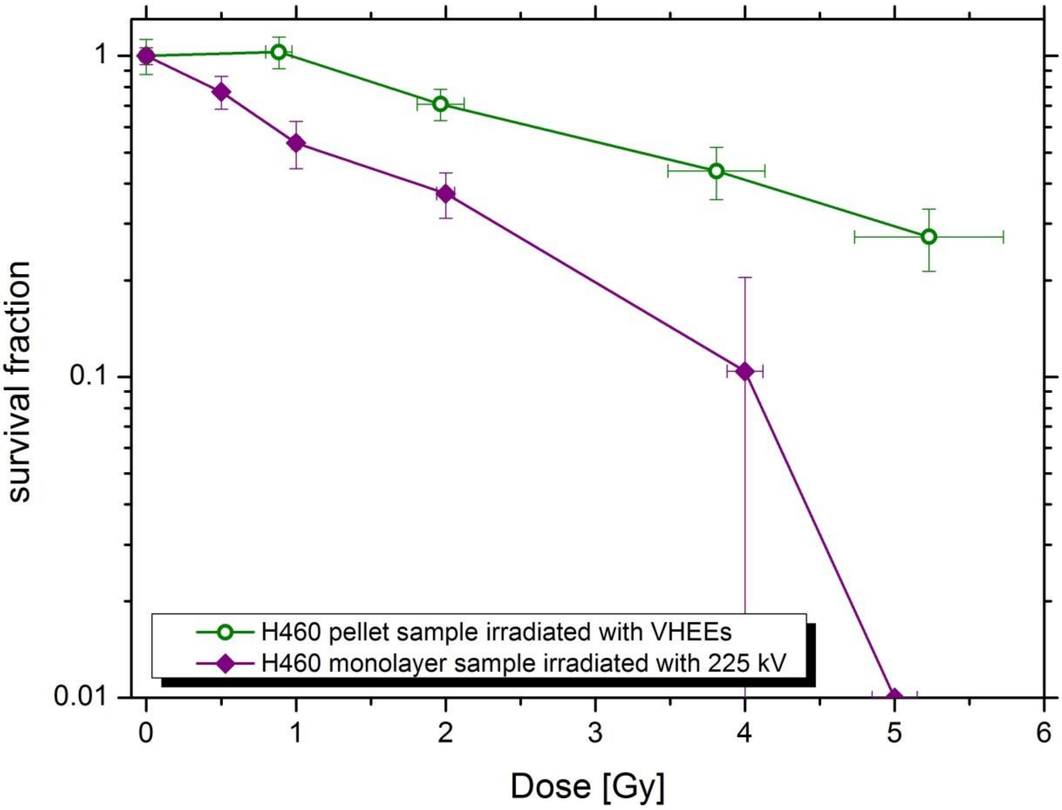

Figure 94. Clonogenic survival curve for the H460 lung cancer cell line irradiated with LWFA VHE electron beam (green circles) and 225 kV X-ray source (purple solid diamonds). The error bars of the SF represent standard deviation for the particular dose level.

Table 33. Comparison of clonogenic data for VHEE and X-ray irradiation for the H460 cell line.

VHEEs (0.20-0.25 Gy/min)			X-ray (2.2 Gy/min)		
n	Dose [Gy]	SF	n	Dose [Gy]	SF
5	0	1.00±0.12	6	0	1.00±0.06
2	0.89±0.09	1.03±0.12	5	0.5±0.02	0.54±0.09
2	1.97±0.16	0.71±0.08	5	1.00±0.03	0.53±0.09
2	3.81±0.32	0.44±0.08	4	2.00±0.06	0.37±0.06
2	5.23±0.49	0.27±0.06	5	4.00±0.12	0.10±0.10
			4	4.00±0.15	0.01±0.00

Following X- ray irradiation (delivered at a dose rate of 2.2 Gy/min) survivability of H460 cells is close to zero at 5 Gy. However, following LWFA VHEE irradiation at 5.6 ± 0.6 Gy this effect is not observed. VHEEs irradiation is less toxic than X-ray irradiation. At a total dose of 2 Gy, the survival fraction following VHEEs is 71% ± 8%, which is 34% higher than for X-irradiation (37% ± 6%). At low doses of irradiation with LWFA VHEE (~1 Gy) the H640 cells irradiated with VHEEs repaired the IR induced damage.

The survival data for very high energy electrons (Figure 93 and Figure 94) show that this type of ionising radiation is toxic and both, A549 and H460, cell lines irradiated with LWFA source. The X-ray curves, plotted for comparison, show higher toxicity than for VHEEs. However, it is crucial to emphasise that the dose rate of X-ray source used in these studies is 10 times higher (2.2 Gy/min) than of LWFA VHEEs (~0.2-0.25 Gy/min).

6.2.2.2. γ-H2AX foci quantification

To evaluate DNA double strand damage and repair in A549 and H460 cells following irradiation with LWFA VHEE cell samples are quantified for gamma H2AX foci.

Table 34 and Table 35 show the average number of γ-H2AX foci per cell from several independent experiments. Again, as for the SF data, data points are averaged according to total dose delivered and dose rate. For each of the irradiated samples, presented in the tables, the mean number of γ-H2AX foci in control samples is subtracted from the number of counted foci per cell for irradiated cells.

The kinetics of γ-H2AX focal loss in the two cell lines are shown in Figure 95 and Figure 96. The maximum number of γ-H2AX foci induced in A549 cells is evident 1h after irradiation with a dose of 9.6 Gy, where an average of 30 foci/cell’s nucleus are observed. For H460, 26 foci/cell are found after irradiation with 5.6 Gy. With decreasing dose the number of γ-H2AX foci/cell decreased. Compared to unexposed control cells the number of foci per cell nucleus remained elevated 2h after irradiation. However, in the A549 cell line the number of foci per cell nucleus have decreased compared with the earlier time point, whilst in the H460 cell line the number of foci per cell nucleus remained at the same level as for 1h post irradiation. This indicates that the rate of DNA repair is higher in A549 compared to H460 cells.

Below 1 Gy of irradiation the number of foci per cell nucleus is similar to control levels, suggesting that all DSB have been repaired. However, above 1 Gy of radiation, the number of γ-H2AX foci 5 hours post irradiation is still higher than the control values in both cell lines (see Table 34 and Table 35), suggesting that all DSB lesions are not repaired.

Figures 97 and 98 represent γ-H2AX dose response relationship for different time points in A549 and H460 cell lines, respectively, irradiated with LWFA VHEEs.

Table 34. Evaluation of γ-H2AX foci in A549 lung cancer cell line. The mean number of γ H2AX foci in control has been subtracted from irradiated cells for each time point.

	average number of foci per cell			
DOSE [Gy]	time	1 h	2 h	5 h
control		1.17±0.17 (n=2)	1.30±0.11 (n=2)	1.19±0.31 (n=2)
0.8		4.17±0.53 (n=3)	3.43±0.90 (n=1)	1.90±0.53 (n=3)
1.0		7.93 (n=1)	8.08 (n=1)	4.77 (n=1)
1.5		9.06±0.65 (n=2)	6.93±1.19 (n=2)	3.27±0.07 (n=2)
2.1		13.66±0.74 (n=2)	9.24±2.00 (n=2)	5.32±0.10 (n=2)
2.7		17.40 (n=1)	14.92 (n=1)	5.40 (n=1)
3.3		16.91±1.53 (n=3)	13.15±0.87 (n=3)	5.12±0.70 (n=3)
5.0		25.18±1.20 (n=2)	16.85±0.55 (n=2)	6.40±1.62 (n=2)
7.2		24.40 (n=1)	19.60 (n=1)	6.50 (n=1)
9.6		30.20 (n=1)	22.50 (n=1)	6.75 (n=1)

Table 35. Evaluation of *γ*-H2AX foci in H460 lung cancer cell line. The mean number of *γ*H2AX foci in control has been subtracted from irradiated cells for each time point.

	average number of foci per cell			
DOSE [Gy]	time	1 h	2 h	5 h
control		1.66±0.06 (n=2)	1.31±0.31 (n=2)	1.37±0.06 (n=2)
1.0		1.90±0.35 (n=2)	1.80±0.15 (n=2)	0.69±0.10 (n=2)
1.7		7.77±0.40 (n=2)	9.45±1.25 (n=2)	5.30±0.10 (n=2)
2.0		5.08±0.50 (n=2)	4.78±0.50 (n=2)	4.22±0.25 (n=2)
3.2		15.08±1.08 (n=2)	13.65±0.58 (n=2)	8.11±0.41 (n=2)
3.8		16.18±0.40 (n=2)	16.78±1.10 (n=2)	8.17±0.70 (n=2)
4.5		23.00 (n=1)	22.60 (n=1)	13.41 (n=1)
5.1		24.04 (n=1)	24.09 (n=1)	13.40 (n=1)
5.6		26.00 (n=1)	25.30 (n=1)	13.50 (n=1)

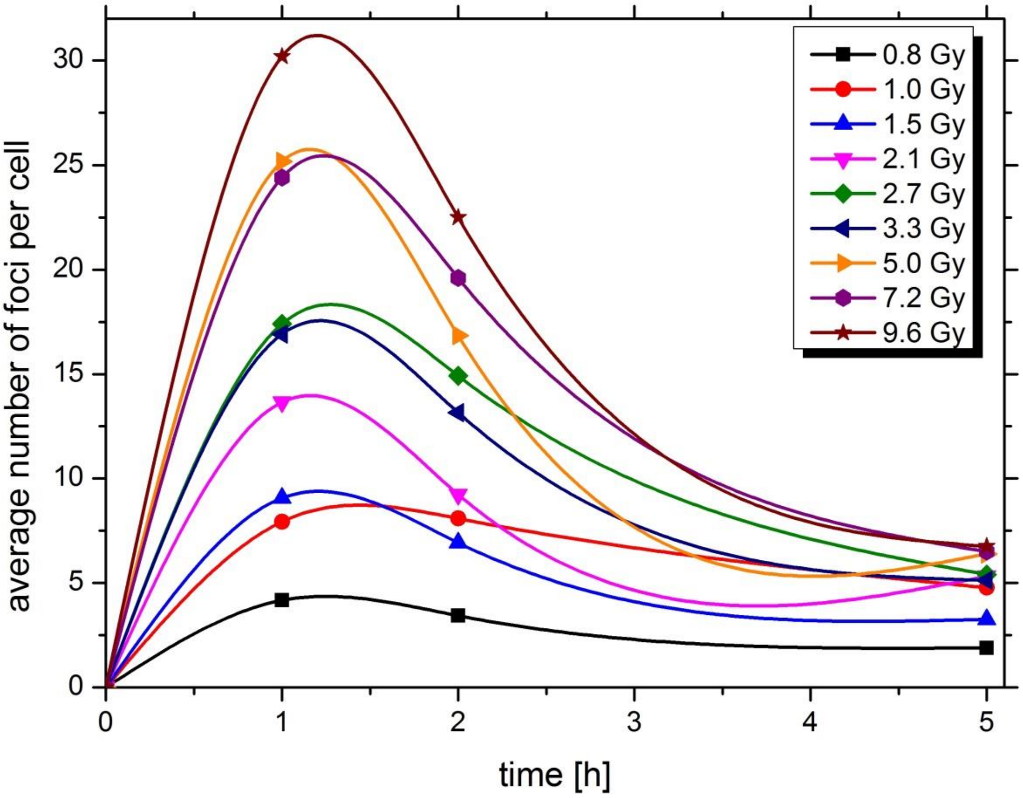

Figure 95. Kinetics of γ-H2AX focal loss in A459 cell line irradiated with LWFA VHEEs for various dose levels.

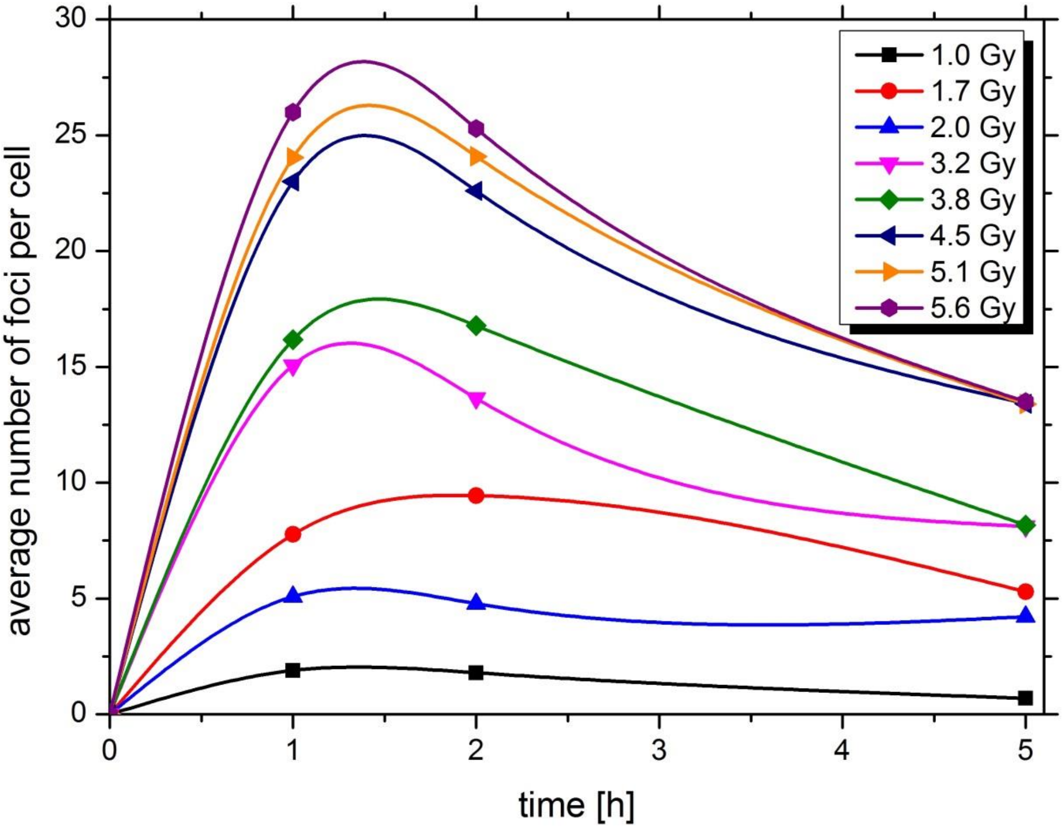

Figure 96. Kinetics of γ-H2AX focal loss in H460 cell line irradiated with LWFA VHEEs for various dose levels.

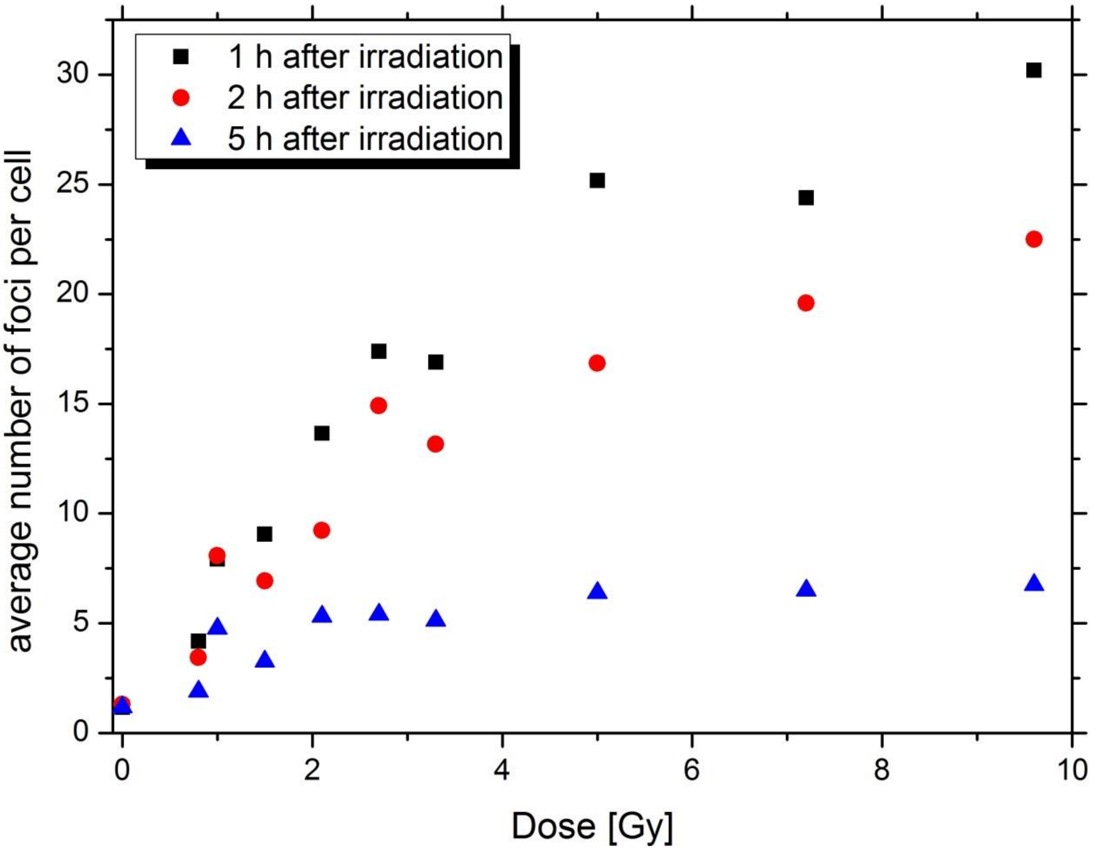

Figure 97. Dose response relationship for γ-H2AX in A549 cell line irradiated with LWFA VHEEs.

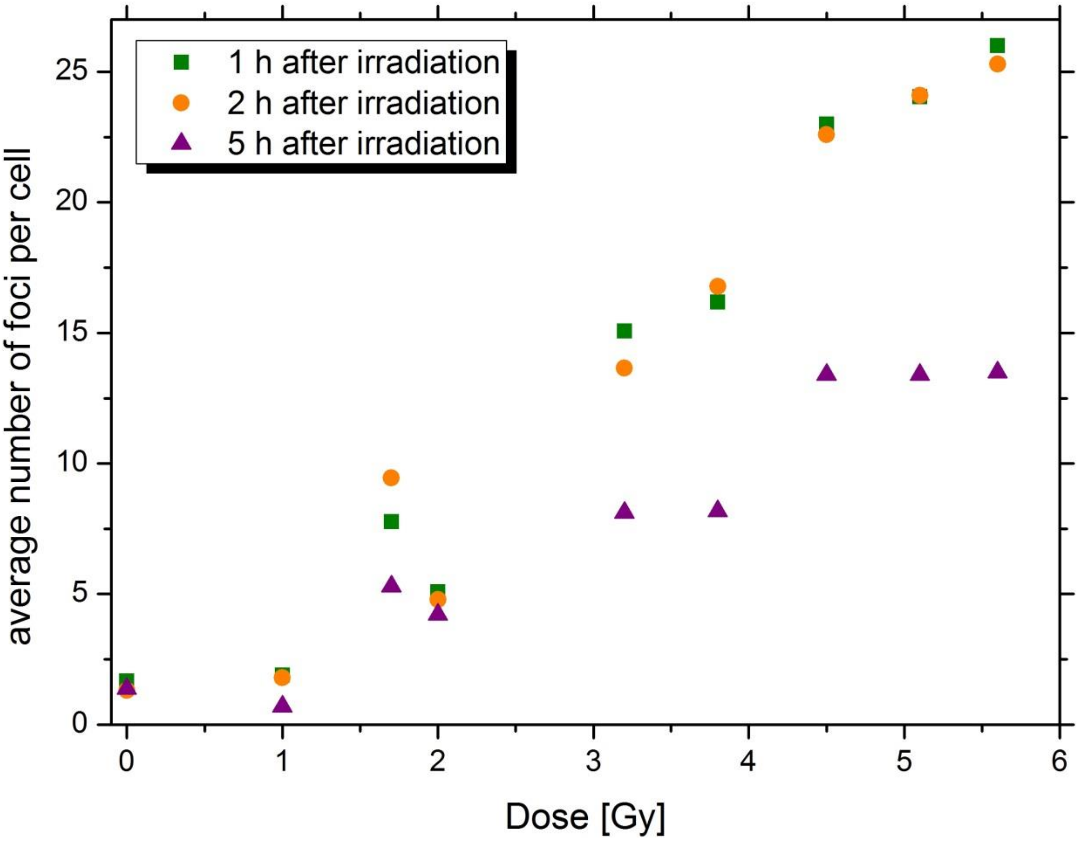

Figure 98. Dose response relationship for γ-H2AX in H460 cell line irradiated with LWFA VHEEs.

6.2.3. Discussion

The survival data for A549 and H460 cell line irradiated with the X-ray source have been fitted with LQ functions according to equation (6.4). The radiobiological parameters (shown in Table 31) derived from the linear quadratic relationship between cell viability and the delivered dose from the cell survival curves show that the α/β ratio for the experiment with X-ray source is larger for A549 than for the H460 cell line. The calculated α/β ratio are 31.1 and 22.4 for A549 and H460, respectively. These values are found to be in a good agreement with literature [304]. According to a linear-quadratic model, the lower the α/β ratio, the higher the sensitivity of the tumour to dose per fraction. Therefore, H460 is more radiosensitive lung cancer cell line than A549, as demonstrated in previous studies [305, 306].

It has been reported in the literature that the biological damage increases with increasing dose rates [307-309]. This phenomenon, called the dose-rate effect, have important implications in radiotherapeutic outcome. Therefore, the interpretation of clonogenic survival data for cell samples irradiated with different dose rates needs to be considered carefully. Survival fraction data, shown in Figure 92 for A459 and H460 exposed to LWFA VHEEs, have been divided into dose-rate dependent groups. For the highest dose levels, corresponding to ~10 ± 1 Gy of irradiated A549 cell line, an increased radioresistance has been observed (Figure 92 (a)). The cell monolayers irradiated with the 225 X-rays source (at 2.2 Gy/min) at such a high dose level exhibits complete sterilization. There are few possible reasons explain these results. The cells should not be kept in the form of pellets for an extensive period of time, because the cells located in the middle of such aggregate have limited access to oxygen (which is a well-known radiosensitizer [310]). However, no such effect is observed in pellet experiment with the X-ray source. Nevertheless, similar effect, i.e. significant cellular radioresistance has been reported in the literature for ultrashort pulses with high dose rates at dose levels of 5-10 Gy [311-313]. Possible causes for such increase in radioresistance has been explained as the local depletion of oxygen and/or a decrease in toxic radicals by neutralization. Several studies [314-320] have shown that ultra-high dose-rates cause local oxygen depletion, which results in significant cellular radioresistance. The literature data on ultra-high dose rate cell survival effects is presented in Table 36.

Moreover, for ultrashort high intensity pulses, considering the impact of special and temporal proximity of electron tracks on yield of hydroxyl radicals we could expect it to be reduced when two electron tracks overlap closely in time and space causing the decrease of radicals by neutralization. Even though, for the radiobiological studies on ALPHA-X VHEEs, the total dose of 1 Gy is delivered on average in about 5 minutes, the dose rate per electron shot in a pulse for this beam is as high as 10^{12}-10^{13} Gy/s due to ultrashort duration of LWFA VHE electron pulses. Therefore, the radioresistance of the cells at 10 Gy dose level could have been due to oxygen depletion and/or decrease of toxic reactive radicals by neutralization.

Table 36. Literature review of ultra-high dose-experiments in tumour systems.

Authors	Experimental system	Oxygen depletion dose	Radiation type	Dose rate	Pulse duration
Town et al., (1967)	HeLa S-3 cells	>9Gy exposure; effect lost for second pulse	15 MeV electrons	$3.5\cdot10^{7}$ Gy/s	1.3 μs
Prempree *et al.* *(1969)*	Human lymphocyte chromosomal aberrations	Reduction in yield	X-rays	$4.8\cdot10^{8}$ Gy/s	n/a
Nias *et al.* (1969)	HeLa	7 Gy	8-14 MeV electrons	<$1.8\cdot10^{7}$ Gy/s	1 μs
Berry *el al.* (1969)	HeLa S-3oxi and CGL-F	5-10 Gy for short pulses	2MV X-rays, 3.7 MV X-rays	10^{9}-10^{10} Gy/s	7-50 ns
Berry *et al.* (1972)	2HeLa lines and murine leukaemia	5-10 Gy; partly hypoxic cells develop radiological hypoxia above 5Gy	400 keV electrons	10^{9} Gy/s	3 ns
Purrot *et al.* (1977)	Chromosomal aberrations in human lymphocytes	No increase in yield	15 MeV electrons	$5\cdot10^{6}$ Gy/s	1 μs
Ling *et al.* (1978)	CHO cells	12 Gy depletion dose; oxygen diffusion to single cells significant after $3\cdot10^{-3}$s	Electrons	10^{9} Gy/s	3 ns
Watts *et al.* (1978)	V-79 cells	Oxygen diffusion to single cells significant after 1-$2\cdot10^{-3}$s	400 keV electrons	10^{9} Gy/s	n/a

Comparing the averaged results of irradiation with VHEEs for A549 and H460 cell lines to 225 keV X-ray test radiation (Figure 93 and Figure 94) we observe reduction of killing efficiently for the investigated high energy electron beam. The dose delivery rates for the two radiation sources are significantly different. The dose rate factor for the VHEE beam is 10 times lower than for the X-ray source. It is, therefore, expected that for a lower dose rate delivery the survival curve for X-ray will be shifted upwards [309] and possibly could exhibit the same response as VHEEs.

Another important point to make is that the relative biological effectiveness of photons has been shown to increase with decreasing photon energy [291]. Several experimental cell studies *in vitro* have shown (see data presented in section 6.1.1) that relatively high-energy low-LET radiation (e.g. high-energy X-ray radiation in MeV energy range) is several times less effective per unit dose than relatively low-energy low-LET radiation (e.g. low-energy X-radiation in keV energy range). A similar effect could have been observed in clonogenicity studies showing that RBE factor of VHEEs could potentially be higher than for MeV photon sources used in conventional radiation treatment.

The number of residual γ-H2AX foci is analysed in A549 and H460 cells 1, 2 and 5 hours after irradiation with VHEEs at dose levels of 1-9 Gy and in non-irradiated controls. Typically, the values of foci per cell observed with 225 kV source, working with ~2 Gy/min rate, are in a range of 20-30 foci/Gy/cell. Figures 97 and 98 show the dose response relationship, as a function of average foci per cell versus dose delivered, for different time points. Typically, this relationship is linear with decreasing slope of the line for longer time points after irradiation. Basal γ-H2AX foci numbers did not differ between A549 and H460 cells (1.22 ± 0.07 foci per cell for A549 and 1.45 ± 0.19 for H460, n = 2), see Tables 34 and 35. The number of foci per cell counted 1 hour after irradiation with VHEEs for all dose levels are very similar. 1 and 2 hours post-irradiation the same elevation of foci/nucleus is observed for H460 cell line. However, for A549, 2 hours after irradiation, some of the DNA DSBs are already repaired as compared with 1 hour post irradiation. This suggests that the kinetics of DNA DSBs repair is faster for A549 than H460 cell line. However, already 5 h after irradiation the excess of foci per cell in both A549 and H460 cell lines decreases considerably. We observe that the number of foci/cell is smaller for all dose levels in H460, compared with A546 (see Table 34 and Table 35). This observed trend of higher foci counts, 5 hours post-irradiation in H460 cells, confirms that H460 lung cancer cell line is more radiosensitive. These results are also in agreement with clonogenic survival data showing that A549 cell line is more radioresistant. Comparing clonogenic data (Figure 92 (a)) with γ-H2AX foci data for A549 irradiated with highest doses (7.2 and 9.6 Gy), 1 hour post irradiation, an elevated number of foci/cell's nucleus with respect to lower doses delivered is recognized. However, already 5 hours post irradiation the level of foci/cell equates to the doses corresponding to 5 Gy. This confirms the observed in clonogenic data radioresistance for A549 cell line irradiated with LWFA VHEEs. The experimental results consist of only two independent data points, therefore the hypothesis of local depletion of oxygen and/or a decrease in toxic radicals by neutralization due to irradiation with ultra-short LWFA pulses may be proved or disproved by conducting more sets of experiments for higher dose levels and investigating oxygen depletion kinetics. Increased radioresistance, at higher dose levels, is not necessarily a disadvantage. In clinical radiotherapy, the doses delivered in a single fraction to the tumour (apart palliative treatments or in hyperfractionation treatments) are never on such a high level, therefore the observed phenomena most certainly would not be a major problem in applying laser-plasma beams to radiation therapy.

It should also be emphasised that for the application of the LWFA the generated bremsstrahlung radiation, influencing induction of photo nuclear particles, e.g. due to (γ,n), (γ,p) reactions created by high-energetic bremsstrahlung (generated from VHEEs) traversing human body and hitting parts of the beam line or the concrete wall of the bunker has to be considered. In section 4.2.6.1.4 we have shown that the neutron yield arising from irradiation with VHEEs inside a water phantom is at the level of 10^{-5} neutrons per emerging particle, therefore the additional dose due to neutron and proton generation in a human body is negligible. Investigations of 50 MV bremsstrahlung compared with ^{60}Co radiation for several cell lines (V79-379A, GSH+/+ and U-1690) using clonogenic assay showed an RBE in the range of 0.988 to 1.009 [321]. Thus, an influence of photo nuclear reactions is only marginal.

Since the overall aim of this work is to provide the evidence to encourage future translation of laser-plasma accelerators into clinical application, it is important to mention the superior (with respect to clinical MeV photon beams) dosimetric properties of VHEEs. These relativistic beam can deliver much higher dose at several centimeters in depth. In addition they exhibit a very sharp penumbra (discussed in chapters 1.2 and 4.2), therefore VHEEs could provide better sparing of organs at risk, bringing a significant advantage over MeV photons.

It is also important to assess the radiobiological effect on tissue positioned at various depths of the human body exposed to VHEE incident beam. The preliminary experiments investigating this effect will be utilized in a water phantom with cell samples positioned at different depths. These experiments will investigate the effect of deep penetration of VHE electron beams in water and will examine the radiobiological response of cells exposed to different radiation components. The effect of the penetration of very high energy electron beams in water have already been discussed in Monte Carlo studies (section 4.2.5) for monoenergetic beams and it is shown that electron and bremsstrahlung spectra change significantly with increasing water depth. Similar to studies of low- and high-energy photon spectra [291], the composition of various radiation sources for VHE incident electron beam, at different depths of water, for the same dose level may confer a different radiobiological effect.

7. Discussions and Future Work

7.1. Discussion and Conclusions

The aim of this dissertation is to investigate the potential application of laser-plasma wakefield accelerated very high energy electrons as a new modality in radiotherapy. For this purpose a set of Monte Carlo calculations evaluating various important aspect in radiation therapy have been presented. The dose distributions for various field size have been characterized and the PDD profiles compared with low energy electron beams. The penumbra for VHEEs, defined in this work as the distance between the 90% and 10% intensity levels normalized to the maximum value at a given depth, is shown to be very sharp, up to 15 cm depth, which could have a significant benefit compared with MeV photon beams in the treatment of deep seated tumours located close to critical structures, such as the eye or spinal cord.

The bremsstrahlung production is important from a radiation protection standpoint and dictates the amount of shielding required. In this work, however, only the radiative losses due to propagation of VHEEs in a water phantom have been considered to evaluate neutron neutrons. For this reason the neutron yield is calculated in a water phantom to evaluate potential additional dose delivered to the patient due to neutron production. The neutron yield is estimated to be 10^{-5} neutrons/primary particle, therefore has a negligible effect on dose delivered. The irradiation of tissues with VHEE beams yields induced radioactivity, therefore this aspect is also considered in MC evaluations. It is calculated that the dominant radionuclides in the activation of tissue equivalent structures are identified as ${}^{11}_{6}C$ and ${}^{15}_{8}O$. These radionuclides have a short lifetime and after 20 minutes post irradiation the residual activity is negligible. The calculated equivalent doses due to induced radioactivity have been found to be small and are expected to be inconsequential in terms of increased dose. Therefore, the direct irradiation of a patient with VHEEs does not requiring any particular safety precautions for this type of radiation.

The potential effect of the ultra-short temporal duration of LWFA electron bunches is discussed. It is shown that femtosecond very high energy bunches maintain their ultra-short bunch duration even after 30 cm of propagation in water. However, based on previous MC studies carried out by Kreipl *et al*. [186] for picosecond proton and ion beams, the increased yield of DNA damage due to tissue irradiation with fs electron bunches is not expected. On the other hand, the MC calculated LET spectra for VHEE beams, exhibit an shift of the peak in LET spectrum with respect to low energy electron beams. This difference is very small. However, it could be speculated that slightly higher LET for VHEEs may indicate a possible difference in radiobiological action for very high energy electron beams compared with the low energy electron beams.

Another important objective of this work is to perform dose measurements in absolute terms (i.e. in Gy) of very high energy electrons. VHEEs have characteristics unlike any other radiotherapy beam. The radiation pulses are very short duration (femto- or picosecond duration), beams with small cross sections (~mm) and energies that are one order of magnitude higher than conventional electron sources. Therefore, dosimetric characterisation of these beams and the choice of the most appropriate detector has to be carefully considered. EBT2 Gafchromic film is chosen as a primary detector to measure dose deposited by VHEEs. The first aim is the development of a radiochromic film dosimetry system accomplished by characterizing the film and developing a method to calibrate film response for absolute dose measurements. The film response for the range of energies used in this work until now has been unknown. Therefore, the calibration of the film detector with a 165 MeV electron beam is performed. The results obtained are compared with detector calibrations using a 20 MeV clinical LINAC. This work shows that EBT2 film is an energy-independent dosemeter within the investigated electron energy range and therefore can successfully be used in dosimetry of unconventional VHE electron beams. Moreover, Monte Carlo calculations confirm the accurate dose measurements. The use of the MC FLUKA code is confirmed as a useful tool for interpreting experimental data from very high energy electron beams. The applicability of EBT2 film for PDD measurements with VHEEs is demonstrated. Conventionally these measurements are carried out with ionisation chambers. However, it is found that IC have a significant lower response when exposed to ultra-short radiation pulses.

Moreover, the preliminary studies on efficacy of VHEEs on tumour cells *in vitro* are assessed by clonogenic assays. γ-H2AX immunofluorescence assay is deployed to study DNA double-strand breaks and repair after irradiation with LWFA electron beam. It is found (from both clonogenic and γ-H2AX data) that VHEEs have a toxic effect on cancer cell. However, some radioresistance at high dose levels (of the order of 10 Gy) has been observed. This could be a result of oxygen depletion and/or a decrease of toxic reactive radicals by neutralization for ultrashort LWFA VHE electrons, for which the dose per pulse is of the order of 10^{12}-10^{13} Gy/s.

7.2. Outlook and future work

This work demonstrates the potential applicability of very high energy electron beams to radiation therapy. Detector for dose measurements have been calibrated and validated for dosimetry of VHE electron beams. The preliminary radiobiological data demonstrated the toxic effect of the irradiation of cancer cells.

There is still a long way to go for the laser-plasma particle accelerators before they can be translated to radiation therapy. Current, state-of-the IMRT allows delivery of highly conformal dose. The application of conformal dose delivery with LP VHEEs still needs to be studied. It is obvious that the intensity-modulation techniques for photon beams, i.e. multi leaf collimators (MLCs) will not be suitable for VHEE therapy, because of generation of copious secondaries, i.e. bremsstrahlung and neutrons. However, appropriately designed scanning system for VHE electron beams could utilize possibility of generating intensity-modulated highly conformal doses for VHEE beams. For instance, lateral electromagnetic scanning may have certain clinical advantages that are not possible using photon beams. In principle, both the energy and the number of electrons applied at each lateral position could be controlled and dynamically adjusted. This can be an advantage for image guided energy and intensity-modulated radiation therapy [322]. For example, in a dual characteristic electron beam, very high-energy electrons would be used at the beam edge, resulting in very sharp lateral edges while low-energy electrons in the middle part of the beam would create a distal edge beyond the tumour with considerable sparing of downstream organs. A similar scheme, using mixed photon and electron beams has been proposed by Korevaar *et al.* [323]. When treating deep-seated tumours with scanned electron beams, the beams at the skin entrance would not need to overlap. This is a very interesting situation of grid therapy[23] [324]. It is known from photon grid therapy that the radiation tolerance of skin (and some other organs) for spatially fractionated radiation is much higher than for uniform radiation. Spot-scanned high-energy electron pencil beams would allow grid therapy at the entrance through the skin combined with uniform

---

[23] Radiotherapy method using a grid-like pattern of small beams. This method enables delivery of higher tumour doses while minimizing radiation-induced skin damage.

irradiation of the tumour or grid therapy at both sites depending on the spatial separation and scattering of the electron beams. The broadening of the electron beam due to scattering could help sparing sensitive organs that are situated in the beam path, behind the tumour. But scattering also represents a disadvantage for radiotherapy of deep-seated tumours. Lateral scattering could be somewhat improved by bringing the source as close as possible to the patient. Another solution is to magnetically focus the beam at a point inside the patient [325]. High-energy electron beams can be focused by two or three magnetic quadrupole lenses. Conventional electromagnetic quadrupoles, however, are relatively large and do not match the compactness of the laser-plasma accelerator. Therefore, compact quadrupoles, which are based on permanent magnets and may be as small as a coin, have been developed [47, 326]. For some treatments, a beam that stays collimated all the way through the patient, might be desired. Such true pencil beams can be created by using even higher electron energies. Laser-plasma accelerators scale favourably in this respect and electrons with even higher energies could be envisaged for radiotherapy. At higher energies, the electron beam scatters only marginally when passing through the patient and may allow for very precise and laterally localized radiation fields.

The clinical use of these energetic electrons for radiotherapy and radiation safety aspects remains to be studied. As demonstrated in this work, direct irradiation of a human tissue will not give rise to any particular safety requirements. However, striking high Z-materials by VHEEs will definitely have an impact on additional bremsstrahlung, and therefore neutron generation. Thus, this challenges needs to be assessed and potential solutions for radiation protection has to be introduced. Even though as evaluated in this work equivalent doses for VHEEs are at a low level, in the future more detailed radiobiological analysis needs to be undertaken in order to predict if radiotherapy with VHEEs could have some undesirable effects on patient’s health, like increased probability of inducing secondary cancers.

Despite several challenges of laser-plasma particle accelerators, there are a number of benefits of having these accelerators in clinics. Laser-plasma accelerators can provide several modalities for radiation therapy (low, medium and very high energy electron beams, bremsstrahlung photons, protons and heavy ions). Several groups are working on applicability of laser-plasma accelerated protons and ions to radiotherapy. Many radiobiological experiments on tumour cells irradiated with laser-plasma accelerated photons, low energy electrons, protons and light ions have been undertaken [311, 312, 327-329] and all of them have shown no significant difference in RBE between conventionally used and LWFA beams. Moreover, the estimated cost of a laser-plasma accelerator is approximately £2 million [41], which is considerably lower than for both proton radiotherapy (over £100 million) and current state of the art IMRT (£3-4 million). Such a tunable source opens prospects for advanced treatment plans that not only vary the intensity but also the penetration depth of the irradiation field. The prospects of using laser-plasma accelerators for therapeutic treatments are intertwined with the developments of laser technology. Currently, the rapid evolution of Ti:sapphire multiterawatt laser technology is leading to continuously improved reliability and stability while the cost and physical footprint of the complete system reduces. A laser beam is easily transported using mirrors and does not require radioprotection. One laser system could therefore serve several treatment rooms. Since the particle beam direction follows the laser propagation axis, a point scanning treatment can be achieved by including the final focusing optics and the plasma source in a gantry. A laser-plasma accelerator is potentially very compact because the acceleration length is only a few millimeters. Laser-plasma accelerators can already produce high quality particle beams. The worldwide expansion of the number of research groups and laser facilities providing up to and beyond petawatt peak powers testifies the competition in this field and the desire to improve the particle source properties. It is expected that many engineering issues must be resolved before laser-plasma accelerated particles can be used for cancer therapy, but they definitely represent an exciting field for future research.

References

1. *CANCER INCIDENCE AND MORTALITY WORLDWIDE*. 2012, INTERNATIONAL AGENCY FOR RESEARCH ON CANCER (IARC). GLOBOCAN 2008: LYON, FRANCE.
2. JEMAL, A., ET AL., *GLOBAL CANCER STATISTICS.* CA-A CANCER JOURNAL FOR CLINICIANS, 2011. **61**(2): P. 69-90.
3. FERLAY, J., ET AL., *ESTIMATES OF WORLDWIDE BURDEN OF CANCER IN 2008: GLOBOCAN 2008.* INTERNATIONAL JOURNAL OF CANCER, 2010. **127**(12): P. 2893-2917.
4. CHAFFER, C.L. AND R.A. WEINBERG, *A PERSPECTIVE ON CANCER CELL METASTASIS.* SCIENCE, 2011. **331**(6024): P. 1559-1564.
5. HAINAUT, P. AND A. PLYMOTH, *TARGETING THE HALLMARKS OF CANCER: TOWARDS A RATIONAL APPROACH TO NEXT-GENERATION CANCER THERAPY.* CURRENT OPINION IN ONCOLOGY, 2013. **25**(1): P. 50-51.
6. HANAHAN, D. AND R.A. WEINBERG, *HALLMARKS OF CANCER: THE NEXT GENERATION.* CELL, 2011. **144**(5): P. 646-674.
7. POLLACK, L.A., ET AL., *INTRODUCTION: CHARTING THE LANDSCAPE OF CANCER SURVIVORS' HEALTH-RELATED OUTCOMES AND CARE.* CANCER, 2009. **115**(18): P. 4265-4269.
8. GLASSER, O., ET AL., *PHYSICAL FOUNDATIONS OF RADIOLOGY*. PHYSICAL FOUNDATIONS OF RADIOLOGY. 1952. 2D ED. 581P.-2D ED. 581P.
9. BERNIER, J., E.J. HALL, AND A. GIACCIA, *TIMELINE - RADIATION ONCOLOGY: A CENTURY OF ACHIEVEMENTS.* NATURE REVIEWS CANCER, 2004. **4**(9): P. 737-U15.
10. RINGBORG, U., ET AL., *THE SWEDISH COUNCIL ON TECHNOLOGY ASSESSMENT IN HEALTH CARE (SBU) SYSTEMATIC OVERVIEW OF RADIOTHERAPY FOR CANCER INCLUDING A PROSPECTIVE SURVEY OF RADIOTHERAPY PRACTICE IN SWEDEN 2001 - SUMMARY AND CONCLUSIONS.* ACTA ONCOLOGICA, 2003. **42**(5-6): P. 357-365.
11. BEGG, A.C., F.A. STEWART, AND C. VENS, *GENOMIC INSTABILITY IN CANCER STRATEGIES TO IMPROVE RADIOTHERAPY WITH TARGETED DRUGS.* NATURE REVIEWS CANCER, 2011. **11**(4): P. 239-253.
12. DELANEY, G., ET AL., *THE ROLE OF RADIOTHERAPY IN CANCER TREATMENT - ESTIMATING OPTIMAL UTILIZATION FROM A REVIEW OF EVIDENCE-BASED CLINICAL GUIDELINES.* CANCER, 2005. **104**(6): P. 1129-1137.
13. BARNETT, G.C., ET AL., *NORMAL TISSUE REACTIONS TO RADIOTHERAPY: TOWARDS TAILORING TREATMENT DOSE BY GENOTYPE.* NATURE REVIEWS CANCER, 2009. **9**(2): P. 134-142.
14. JACKSON, S.P. AND J. BARTEK, *THE DNA-DAMAGE RESPONSE IN HUMAN BIOLOGY AND DISEASE.* NATURE, 2009. **461**(7267): P. 1071-1078.
15. EDWARD C. HALPERIN, C.A.P., LUTHER W. BRADY, *PRINCIPLES AND PRACTICE OF RADIATION ONCOLOGY* 2008: LIPPINCOTT WILLIAMS & WILKINS.
16. *ADVANCING NUCLEAR MEDICINE THROUGH INNOVATION*. 2007: THE NATIONAL ACADEMIES PRESS.
17. WWW.DKFZ.DE/EN/MEDPHYS/APPL_MED_RAD_PHYSICS/BIOLOGICAL_MODELS.HTML#INHALT2.
18. WILSON, R.R., *RADIOLOGICAL USE OF FAST PROTONS.* RADIOLOGY, 1946. **47**(5): P. 487-491.
19. WORTHY, S., *HIGH-RESOLUTION COMPUTED-TOMOGRAPHY OF THE LUNGS.* BRITISH MEDICAL JOURNAL, 1995. **310**(6980): P. 615-616.

20. LOMAX, A.J., ET AL., *A TREATMENT PLANNING INTER-COMPARISON OF PROTON AND INTENSITY MODULATED PHOTON RADIOTHERAPY.* RADIOTHERAPY AND ONCOLOGY, 1999. **51**(3): P. 257-271.
21. BAUMERT, B.G., ET AL., *A COMPARISON OF DOSE DISTRIBUTIONS OF PROTON AND PHOTON BEAMS IN STEREOTACTIC CONFORMAL RADIOTHERAPY OF BRAIN LESIONS.* INTERNATIONAL JOURNAL OF RADIATION ONCOLOGY BIOLOGY PHYSICS, 2001. **49**(5): P. 1439-1449.
22. SCHNEIDER, U., ET AL., *THE IMPACT OF IMRT AND PROTON RADIOTHERAPY ON SECONDARY CANCER INCIDENCE.* STRAHLENTHERAPIE UND ONKOLOGIE, 2006. **182**(11): P. 647-652.
23. LARAMORE, G.E., *ROLE OF PARTICLE RADIOTHERAPY IN THE MANAGEMENT OF HEAD AND NECK CANCER.* CURRENT OPINION IN ONCOLOGY, 2009. **21**(3): P. 224-231.
24. *HTTP://WWW.SHI.CO.JP/QUANTUM/ENG/PRODUCT/PROTON/PROTON.HTML*.
25. SCHARDT, D., ET AL., *NUCLEAR FRAGMENTATION OF HIGH-ENERGY HEAVY-ION BEAMS IN WATER.* ADVANCES IN SPACE RESEARCH : THE OFFICIAL JOURNAL OF THE COMMITTEE ON SPACE RESEARCH (COSPAR), 1996. **17**(2): P. 87-94.
26. SCHARDT, D., T. ELSAESSER, AND D. SCHULZ-ERTNER, *HEAVY-ION TUMOR THERAPY: PHYSICAL AND RADIOBIOLOGICAL BENEFITS.* REVIEWS OF MODERN PHYSICS, 2010. **82**(1): P. 383-425.
27. DURANTE, M. AND J.S. LOEFFLER, *CHARGED PARTICLES IN RADIATION ONCOLOGY.* NATURE REVIEWS CLINICAL ONCOLOGY, 2010. **7**(1): P. 37-43.
28. KARGER, C.P., ET AL., *DOSIMETRY FOR ION BEAM RADIOTHERAPY.* PHYSICS IN MEDICINE AND BIOLOGY, 2010. **55**(21): P. R193-R234.
29. SUIT, H., ET AL., *PROTON VS CARBON ION BEAMS IN THE DEFINITIVE RADIATION TREATMENT OF CANCER PATIENTS.* RADIOTHERAPY AND ONCOLOGY, 2010. **95**(1): P. 3-22.
30. DE RUYSSCHER, D., ET AL., *CHARGED PARTICLES IN RADIOTHERAPY: A 5-YEAR UPDATE OF A SYSTEMATIC REVIEW.* RADIOTHERAPY AND ONCOLOGY, 2012. **103**(1): P. 5-7.
31. SCHULZ-ERTNER, D. AND H. TSUJII, *PARTICLE RADIATION THERAPY USING PROTON AND HEAVIER ION BEAMS.* JOURNAL OF CLINICAL ONCOLOGY, 2007. **25**(8): P. 953-964.
32. MA, C.M.C., R.L. MAUGHAN, AND C.G. ORTON, *WITHIN THE NEXT DECADE CONVENTIONAL CYCLOTRONS FOR PROTON RADIOTHERAPY WILL BECOME OBSOLETE AND REPLACED BY FAR LESS EXPENSIVE MACHINES USING COMPACT LASER SYSTEMS FOR THE ACCELERATION OF THE PROTONS.* MEDICAL PHYSICS, 2006. **33**(3): P. 571-573.
33. PEETERS, A., ET AL., *HOW COSTLY IS PARTICLE THERAPY? COST ANALYSIS OF EXTERNAL BEAM RADIOTHERAPY WITH CARBON-IONS, PROTONS AND PHOTONS.* RADIOTHERAPY AND ONCOLOGY, 2010. **95**(1): P. 45-53.
34. *HTTP://WWW.SCOTLAND.GOV.UK/PUBLICATIONS/2006/01/24131719/2*.
35. DESROSIERS, C., ET AL., *150-250 MEV ELECTRON BEAMS IN RADIATION THERAPY.* PHYSICS IN MEDICINE AND BIOLOGY, 2000. **45**(7): P. 1781-1805.
36. *HTTPS://WWW.OECD-NEA.ORG/TOOLS/ABSTRACT/DETAIL/NEA-1525*.
37. MOSKVIN, V., ET AL. *PENELOPE MONTE CARLO ENGINE FOR TREATMENT PLANNING IN RADIATION THERAPY WITH VERY HIGH ENERGY ELECTRONS (VHEE) OF 150–250 MEV*. IN *NUCLEAR SCIENCE SYMPOSIUM CONFERENCE RECORD (NSS/MIC), 2010 IEEE*. 2010.
38. FUCHS, T., ET AL., *TREATMENT PLANNING FOR LASER-ACCELERATED VERY-HIGH ENERGY ELECTRONS.* PHYSICS IN MEDICINE AND BIOLOGY, 2009. **54**(11): P. 3315-3328.
39. YEBOAH, C. AND G.A. SANDISON, *OPTIMIZED TREATMENT PLANNING FOR PROSTATE CANCER COMPARING IMPT, VHEET AND 15 MV IMXT.* PHYSICS IN MEDICINE AND BIOLOGY, 2002. **47**(13): P. 2247-2261.
40. DESROSIERS, C., ET AL., *LUNG TUMOR TREATMENT WITH VERY HIGH ENERGY ELECTRON BEAMS OF 150-250 MEV AS COMPARED TO CONVENTIONAL MEGAVOLTAGE PHOTON*

BEAMS. INTERNATIONAL JOURNAL OF RADIATION ONCOLOGY BIOLOGY PHYSICS, 2008. **72**(1): P. S612-S612.

41. DESROSIERS, C., ET AL. *LASER-PLASMA GENERATED VERY HIGH ENERGY ELECTRONS IN RADIATION THERAPY OF THE PROSTATE*. IN *PROCEEDINGS OF SPIE*. 2008.
42. YEBOAH, C., G.A. SANDISON, AND V. MOSKVIN, *OPTIMIZATION OF INTENSITY-MODULATED VERY HIGH ENERGY (50-250 MEV) ELECTRON THERAPY.* PHYSICS IN MEDICINE AND BIOLOGY, 2002. **47**(8): P. 1285-1301.
43. FAURE, J., ET AL., *A LASER-PLASMA ACCELERATOR PRODUCING MONOENERGETIC ELECTRON BEAMS.* NATURE, 2004. **431**(7008): P. 541-544.
44. GEDDES, C.G.R., ET AL., *HIGH-QUALITY ELECTRON BEAMS FROM A LASER WAKEFIELD ACCELERATOR USING PLASMA-CHANNEL GUIDING.* NATURE, 2004. **431**(7008): P. 538-541.
45. MANGLES, S.P.D., ET AL., *MONOENERGETIC BEAMS OF RELATIVISTIC ELECTRONS FROM INTENSE LASER-PLASMA INTERACTIONS.* NATURE, 2004. **431**(7008): P. 535-538.
46. LUNDH, O., ET AL., *FEW FEMTOSECOND, FEW KILOAMPERE ELECTRON BUNCH PRODUCED BY A LASER-PLASMA ACCELERATOR.* NATURE PHYSICS, 2011. **7**(3): P. 219-222.
47. WIGGINS, S.M., ET AL., *HIGH QUALITY ELECTRON BEAMS FROM A LASER WAKEFIELD ACCELERATOR.* PLASMA PHYSICS AND CONTROLLED FUSION, 2010. **52**(12).
48. BRUNETTI, E., ET AL., *LOW EMITTANCE, HIGH BRILLIANCE RELATIVISTIC ELECTRON BEAMS FROM A LASER-PLASMA ACCELERATOR.* PHYSICAL REVIEW LETTERS, 2010. **105**(21): P. 4.
49. BRAHME, A., *DOSIMETRIC PRECISION REQUIREMENTS IN RADIATION-THERAPY.* ACTA RADIOLOGICA ONCOLOGY, 1984. **23**(5): P. 379-391.
50. PAPANIKOLAOU, N., BATTISTA, J., BOYER, A., KAPPAS, C., KLEIN, E.,MACKIE, T., SHARPE,M., AND VAN DYK, J, *TISSUE INHOMOGENEITY CORRECTIONS FOR MEGAVOLTAGE PHOTON BEAMS*. 2004, AAPM TASK GROUP.
51. CHAPPELL, R. AND J.F. FOWLER, *STEEPNESS OF DOSE-RESPONSE CURVE FOR LARYNX CANCER.* RADIOTHERAPY AND ONCOLOGY, 1994. **30**(1): P. 90-90.
52. KARGER, C.P., ET AL., *DOSIMETRY FOR ION BEAM RADIOTHERAPY.* PHYSICS IN MEDICINE AND BIOLOGY, 2010. **55**(21): P. R193-234.
53. TAJIMA, T. AND J.M. DAWSON, *LASER ELECTRON-ACCELERATOR.* PHYSICAL REVIEW LETTERS, 1979. **43**(4): P. 267-270.
54. DAWSON, J.M., *PARTICLE SIMULATION OF PLASMAS.* REVIEWS OF MODERN PHYSICS, 1983. **55**(2): P. 403-447.
55. STRICKLAND, D. AND G. MOUROU, *COMPRESSION OF AMPLIFIED CHIRPED OPTICAL PULSES.* OPTICS COMMUNICATIONS, 1985. **56**(3): P. 219-221.
56. MAXWELL, J.C., *A TREATISE ON ELECTRICITY AND MAGNETISM*. 1873: OXFORD : CLARENDON PRESS.
57. BUTCHER, P.N. AND D. COTTER., *THE ELEMENTS OF NONLINEAR OPTICS*. 1990: CAMBRIDGE UNIVERSITY PRESS.
58. ESAREY, E., C.B. SCHROEDER, AND W.P. LEEMANS, *PHYSICS OF LASER-DRIVEN PLASMA-BASED ELECTRON ACCELERATORS.* REVIEWS OF MODERN PHYSICS, 2009. **81**(3): P. 1229-1285.
59. JUNG, R., *LASER-PLASMA INTERACTION WITH ULTRA-SHORT LASER PULSES*, IN *MATHEMATISCH-NATURWISSENSCHAFTLICHEN FAKULTAET*. 2007, HEINRICH-HEINE-UNIVERSITAET: DUESSELDORF.
60. BAUER, D., P. MULSER, AND W.H. STEEB, *RELATIVISTIC PONDEROMOTIVE FORCE, UPHILL ACCELERATION, AND TRANSITION TO CHAOS.* PHYSICAL REVIEW LETTERS, 1995. **75**(25): P. 4622-4625.
61. QUESNEL, B. AND P. MORA, *THEORY AND SIMULATION OF THE INTERACTION OF ULTRAINTENSE LASER PULSES WITH ELECTRONS IN VACUUM.* PHYSICAL REVIEW E, 1998. **58**(3): P. 3719-3732.
62. SUN, G.Z., ET AL., *SELF-FOCUSING OF SHORT INTENSE PULSES IN PLASMAS.* PHYSICS OF FLUIDS, 1987. **30**(2): P. 526-532.

63. DAWSON, J.M., *NONLINEAR ELECTRON OSCILLATIONS IN A COLD PLASMA.* PHYSICAL REVIEW, 1959. **113**(2): P. 383-387.
64. AKHIEZER, A.I. AND R.V. POLOVIN, *THEORY OF WAVE MOTION OF AN ELECTRON PLASMA.* SOVIET PHYSICS JETP-USSR, 1956. **3**(5): P. 696-705.
65. ESAREY, E. AND M. PILLOFF, *TRAPPING AND ACCELERATION IN NONLINEAR PLASMA-WAVES.* PHYSICS OF PLASMAS, 1995. **2**(5): P. 1432-1436.
66. JOSHI, C., ET AL., *FORWARD RAMAN INSTABILITY AND ELECTRON ACCELERATION.* PHYSICAL REVIEW LETTERS, 1981. **47**(18): P. 1285-1288.
67. ESAREY, E., J. KRALL, AND P. SPRANGLE, *ENVELOPE ANALYSIS OF INTENSE LASER-PULSE SELF-MODULATION IN PLASMAS.* PHYSICAL REVIEW LETTERS, 1994. **72**(18): P. 2887-2890.
68. BEREZHIANI, V.I. AND I.G. MURUSIDZE, *INTERACTION OF HIGHLY RELATIVISTIC SHORT LASER-PULSES WITH PLASMAS AND NONLINEAR WAKE-FIELD GENERATION.* PHYSICA SCRIPTA, 1992. **45**(2): P. 87-90.
69. UMSTADTER, D., E. ESAREY, AND J. KIM, *NONLINEAR PLASMA-WAVES RESONANTLY DRIVEN BY OPTIMIZED LASER-PULSE TRAINS.* PHYSICAL REVIEW LETTERS, 1994. **72**(8): P. 1224-1227.
70. PUKHOV, A. AND J. MEYER-TER-VEHN, *LASER WAKE FIELD ACCELERATION: THE HIGHLY NON-LINEAR BROKEN-WAVE REGIME.* APPLIED PHYSICS B-LASERS AND OPTICS, 2002. **74**(4-5): P. 355-361.
71. FONSECA, R.A., ET AL., *OSIRIS: A THREE-DIMENSIONAL, FULLY RELATIVISTIC PARTICLE IN CELL CODE FOR MODELING PLASMA BASED ACCELERATORS*, IN *COMPUTATIONAL SCIENCE-ICCS 2002, PT III, PROCEEDINGS*, P. SLOOT, ET AL., EDITORS. 2002. P. 342-351.
72. CIPICCIA, S., *COMPACT GAMMA-RAY SOURCES BASED ON LASER-PLASMA WAKEFIELD ACCELERATOR*. 2012, UNIVERSITY OF STRATHCLYDE: GLASGOW.
73. LU, W., ET AL., *GENERATING MULTI-GEV ELECTRON BUNCHES USING SINGLE STAGE LASER WAKEFIELD ACCELERATION IN A 3D NONLINEAR REGIME.* PHYSICAL REVIEW SPECIAL TOPICS-ACCELERATORS AND BEAMS, 2007. **10**(6).
74. KOSTYUKOV, I., A. PUKHOV, AND S. KISELEV, *PHENOMENOLOGICAL THEORY OF LASER-PLASMA INTERACTION IN "BUBBLE" REGIME.* PHYSICS OF PLASMAS, 2004. **11**(11): P. 5256-5264.
75. MORA, P. AND T.M. ANTONSEN, *ELECTRON CAVITATION AND ACCELERATION IN THE WAKE OF AN ULTRAINTENSE, SELF-FOCUSED LASER PULSE.* PHYSICAL REVIEW E, 1996. **53**(3): P. R2068-R2071.
76. PUKHOV, A. AND S. GORDIENKO, *BUBBLE REGIME OF WAKE FIELD ACCELERATION: SIMILARITY THEORY AND OPTIMAL SCALINGS.* PHILOSOPHICAL TRANSACTIONS OF THE ROYAL SOCIETY A-MATHEMATICAL PHYSICAL AND ENGINEERING SCIENCES, 2006. **364**(1840): P. 623-633.
77. JAROSZYNSKI, D.A., ET AL., *THE STRATHCLYDE TERAHERTZ TO OPTICAL PULSE SOURCE (TOPS).* NUCLEAR INSTRUMENTS & METHODS IN PHYSICS RESEARCH SECTION A-ACCELERATORS SPECTROMETERS DETECTORS AND ASSOCIATED EQUIPMENT, 2000. **445**(1-3): P. 317-319.
78. ANICULAESEI, C., *EXPERIMENTAL STUDIES OF LASER PLASMA WAKEFIELD ACCELERATION*, IN *PHYSICS*. 2014, UNIVERSITY OF STRATHCLYDE: GLASGOW.
79. LI, Y.M. AND R. FEDOSEJEVS, *DENSITY-MEASUREMENTS OF A HIGH-DENSITY PULSED GAS-JET FOR LASER-PLASMA INTERACTION STUDIES.* MEASUREMENT SCIENCE & TECHNOLOGY, 1994. **5**(10): P. 1197-1201.
80. LORENZ, L.V., *SUR LA LUMIÈRE RÉFLÉCHIE ET RÉFRACTÉE PAR UNE SPHÈRE TRANSPARENTE*. 1869, COPENHAGEN, DENMARK: JOHNSON REPRINT CORP.
81. LORENTZ, H.A., *LA THÉORIE ELECTROMAGNÉTIQUE DE MAXWELL ET SON APPLICATION AUX CORPS MOUVANTS.* ARCHIVES NÉERLANDAISES DES SCIENCES EXACTES ET NATURELLES, 1892. **25**: P. 363–552.
82. WEBER, M.J., *HANDBOOK OF OPTICAL MATERIALS*. 2002: CRC PRESS.

83. EULER, L., *DE INTEGRATIONE AEQUATIONUM DIFFERENTIALIUM ALTIORUM GRADUUM.* MISCELLANEA BEROLINENSIA, 1743. **7**: P. 193-242.
84. EULER, L., *EINLEITUNG IN DIE ANALYSIS DES UNENDLICHEN*. 1983, BERLIN: SPRINGER.
85. WOLTERINK, T.A.W., *HIGH-GRADIENT GAS-JET TARGETS FOR LASER WAKEFIELD ACCELERATION*, IN *FACULTY OF SCIENCE AND TECHNOLOGY*. 2011, UNIVERSITY OF TWENTE. P. 80.
86. ABEL, N.H., *RESOLUTION D'UN PROBLEM DE MECHANIQUE.* JOURNAL FÜR DIE REINE UND ANGEWANDTE MATHEMATIK, 1826. **1**: P. 153–157.
87. TOMASSINI, P., ET AL., *ANALYZING LASER PLASMA INTERFEROGRAMS WITH A CONTINUOUS WAVELET TRANSFORM RIDGE EXTRACTION TECHNIQUE: THE METHOD.* APPLIED OPTICS, 2001. **40**(35): P. 6561-6568.
88. ESPOSITO, M., ET AL., *DYNAMITE: A WAFER SCALE SENSOR FOR BIOMEDICAL APPLICATIONS.* JOURNAL OF INSTRUMENTATION, 2011. **6**.
89. HYUN-YONG YU, Y.N., LI-WEN CHANG, JIN-HONG PARK,JAE HYUNG LEE, J. JASON LIN,EDWARD MYERS, *CMOS-LOCOS, CMOS PROCESS FOR EE410, INSTRUCTION MANUAL*, E.E.D.C.F.I.S.C.A.T.S.N.F. (SNF), EDITOR. 2009, STANFORD UNIVERSITY.
90. MEADOWCROFT, A.L., C.D. BENTLEY, AND E.N. STOTT, *EVALUATION OF THE SENSITIVITY AND FADING CHARACTERISTICS OF AN IMAGE PLATE SYSTEM FOR X-RAY DIAGNOSTICS.* REVIEW OF SCIENTIFIC INSTRUMENTS, 2008. **79**(11).
91. PATERSON, I.J., ET AL., *IMAGE PLATE RESPONSE FOR CONDITIONS RELEVANT TO LASER-PLASMA INTERACTION EXPERIMENTS.* MEASUREMENT SCIENCE & TECHNOLOGY, 2008. **19**(9).
92. MIYAHARA, J., ET AL., *A NEW TYPE OF X-RAY AREA DETECTOR UTILIZING LASER STIMULATED LUMINESCENCE.* NUCLEAR INSTRUMENTS & METHODS IN PHYSICS RESEARCH SECTION A-ACCELERATORS SPECTROMETERS DETECTORS AND ASSOCIATED EQUIPMENT, 1986. **246**(1-3): P. 572-578.
93. TANAKA, K.A., ET AL., *CALIBRATION OF IMAGING PLATE FOR HIGH ENERGY ELECTRON SPECTROMETER.* REVIEW OF SCIENTIFIC INSTRUMENTS, 2005. **76**(1).
94. NAKANII, N., ET AL., *ABSOLUTE CALIBRATION OF IMAGING PLATE FOR ELECTRON SPECTROMETER MEASURING GEV-CLASS ELECTRONS*, IN *5TH INTERNATIONAL CONFERENCE ON INERTIAL FUSION SCIENCES AND APPLICATIONS*, H. AZECHI, B. HAMMEL, AND J.C. GAUTHIER, EDITORS. 2008.
95. CHIHIRO SUZUKI, T.A., TAKESHI IIMOTO, TOSHISO KOSAKO, *ENERGY RESPONSE OF AN IMAGING PLATE TO LOW-ENERGY PHOTONS FOR USE IN DOSIMETRY.* JPN. J. HEALTH PHYS., 2011. **46**(2): P. 158-162.
96. HTTP://PBPL.PHYSICS.UCLA.EDU/RESEARCH/TECHNOLOGIES/MAGNETS/ELECTROMAGNETS/.
97. BROWNE, C.P. AND W.W. BUECHNER, *BROAD-RANGE MAGNETIC SPECTROGRAPH.* REVIEW OF SCIENTIFIC INSTRUMENTS, 1956. **27**(11): P. 899-907.
98. LUDZIEJEWSKI, T., ET AL., *INVESTIGATION OF SOME SCINTILLATION PROPERTIES OF YAG:CE CRYSTALS.* NUCLEAR INSTRUMENTS & METHODS IN PHYSICS RESEARCH SECTION A-ACCELERATORS SPECTROMETERS DETECTORS AND ASSOCIATED EQUIPMENT, 1997. **398**(2-3): P. 287-294.
99. METROPOLIS, N. AND S. ULAM, *THE MONTE CARLO METHOD.* JOURNAL OF THE AMERICAN STATISTICAL ASSOCIATION, 1949. **44**(247): P. 335-341.
100. GEORGES LOUIS LECLERC, C.D.B., *SUR LE JEU DE FRANC-CARREAU.* IMPRIMERIE ROYALE, 1778: P. 139-153.
101. HALL, A., *ON AN EXPERIMENTAL DETERMINATION OF PI.* MESSENG. MATH., 1873. **2**: P. 113-114.
102. STUDENT, *THE PROBABLE ERROR OF A CORRELATION COEFFICIENT.* BIOMETRIKA, 1908. **6**: P. 302-310.

103. RICHARD G. HEWLETT, O.E.A., *THE NEW WORLD, 1939/1946*. 1962, THE PENNSYLVANIA STATE UNIVERSITY PRESS: PENNSYLVANIA.
104. ULAM, S., *A COLLECTION OF MATHEMATICAL PROBLEMS*. 1960, NEW YORK: INTERSCIENCE PUBLISHERS.
105. *LETTER CORRENCPONDENCE BETWEEN ULM AND VON NEUMAN.* 1947.
106. GEANT4. *HTTP://GEANT4.WEB.CERN.CH/GEANT4/*.
107. *GEANT4 USER'S GUIDE FOR APPLICATION DEVELOPERS.* GEANT4 COLLABORATION, 2012. **VERSION: GEANT4 9.5.5**.
108. *HTTP://GEANT4.WEB.CERN.CH/GEANT4/COLLABORATION/*.
109. BATTISTONI, G., ET AL., *THE FLUKA CODE: DESCRIPTION AND BENCHMARKING*, IN *HADRONIC SHOWER SIMULATION WORKSHOP*, M. ALBROW AND R. RAJA, EDITORS. 2007. P. 31-49.
110. FERRARI, A., ET AL., *FLUKA: A MULTI-PARTICLE TRANSPORT CODE.* CERN 2005-10, INFN/TC_05/11, SLAC-R-773, 2005.
111. FLUKA. *HTTP://WWW.FLUKA.ORG/FLUKA.PHP*.
112. P.A. AARNIO, J.L., J. RANFT, A. FASS`O, G.R. STEVENSON, *ENHANCEMENTS TO THE FLUKA86 PROGRAM (FLUKA87).* CERN DIVISIONAL REPORT TIS-RP/190, 1887.
113. BALLARINI, F., ET AL., *THE PHYSICS OF THE FLUKA CODE: RECENT DEVELOPMENTS.* ADVANCES IN SPACE RESEARCH, 2007. **40**(9): P. 1339-1349.
114. A. FASSO, A.F., J. RANFT, P.R. SALA, *FLUKA: A MULTI-PARTICLE TRANSPORT CODE.* CERN-2005-10 (2005), INFN/TC_05/11, SLAC-R-773, 2005.
115. PAPIEZ, L., T. BORTFELD, AND W.R. HENDEE, *VERY HIGH ENERGY ELECTROMAGNETICALLY-SCANNED ELECTRON BEAMS ARE AN ATTRACTIVE ALTERNATIVE TO PHOTON IMRT.* MEDICAL PHYSICS, 2004. **31**(7): P. 1945-1948.
116. EMMETT, M.B., *THE MORSE MONTE CARLO RADIATION TRANSPORT CODE SYSTEM*, IN *OAK RIDGE NATIONAL LABORATORY REPORT RNL-4972/R2*. 9884.
117. P. MAYLES, A.N., J.C. ROSENWALD, *HANDBOOK OF RADIOTHERAPY PHYSICS: THEORY AND PRACTICE* 2007: TAYLOR & FRANCIS LTD.
118. PODGORSAK, E.B., *RADIATION ONCOLOGY PHYSICS*. 2005, VIENNA: INTERNATIONAL ATOMIC ENERGY AGENCY.
119. NATIONAL INSTITUTE OF STANDARDS AND TECHNOLOGY, G., MD, *TABLES OF X-RAY MASS ATTENUATION COEFFICIENTS AND MASS ENERGY-ABSORPTIOIN COEFFICIENTS, NIST STANDARD REFERENCE DATABASE 126*. 2004.
120. MARTIN J. BERGER, S.M.S., *ADDITIONAL STOPPING POWER AND RANGE TABLES FOR PROTONS, MESONS AND ELECTRONS*. 1964: WASHINGTON, DC.
121. *ICRU REPORT 37, STOPPING POWERS FOR ELECTRONS AND POSITRONS*, IN *ICRU REPORT 37*, I.C.O.R.U.A. MEASUREMENTS, EDITOR. 1984.
122. BETHE, H., *ZUR THEORIE DES DURCHGANGS SCHNELLER KORPUSKULARSTRAHLEN DURCH MATERIE.* ANNALEN DER PHYSIK, 1930. **397**(3): P. 325-400.
123. BLOCH , F., *ZUR BREMSUNG RASCH BEWEGTER TEILCHEN BEIM DURCHGANG DURCH MATERIE.* ANNALEN DER PHYSIK, 1933. **408**(3): P. 285-320.
124. STERNHEIMER, R.M., *THE DENSITY EFFECT FOR THE IONIZATION LOSS IN VARIOUS MATERIALS.* PHYSICAL REVIEW, 1952. **88**(4): P. 851-859.
125. STERNHEIMER, R.M., *DENSITY EFFECT FOR THE IONIZATION LOSS IN VARIOUS MATERIALS.* PHYSICAL REVIEW, 1956. **103**(3): P. 511-515.
126. STERNHEIMER, R.M., S.M. SELTZER, AND M.J. BERGER, *DENSITY EFFECT FOR THE IONIZATION LOSS OF CHARGED-PARTICLES IN VARIOUS SUBSTANCES.* PHYSICAL REVIEW B, 1982. **26**(11): P. 6067-6076.
127. ZIEGLER, J.F., *STOPPING OF ENERGETIC LIGHT IONS IN ELEMENTAL MATTER.* JOURNAL OF APPLIED PHYSICS, 1999. **85**(3): P. 1249-1272.
128. *ICRU REPORT 35, RADIATION DOSIMETRY, ELECTRON BEAMS WITH ENERGIES BETWEEN 1 AND 50 MEV*, IN *ICRU REPORT 35*, B. ICRU, MD, EDITOR. 1984.

129. SELTZER, S.M. AND M.J. BERGER, *BREMSSTRAHLUNG SPECTRA FROM ELECTRON INTERACTIONS WITH SCREENED ATOMIC-NUCLEI AND ORBITAL ELECTRONS.* NUCLEAR INSTRUMENTS & METHODS IN PHYSICS RESEARCH SECTION B-BEAM INTERACTIONS WITH MATERIALS AND ATOMS, 1985. **12**(1): P. 95-134.
130. PRATT, R.H., TSENG, H. K., LEE, C. M., KISSEL, L., MACCALLUM, C., AND RILEY, M, *BREMSSTRAHLUNG ENERGY SPECTRA FROM ELECTRONS OF KINETIC ENERGY 1 KEV < T1 < 2000 KEV INCIDENT ON NEUTRAL ATOMS 2 < Z < 92.* ATOMIC DATA NUCL. DATA TABLES, 1977. **20**(175).
131. EVANS, R.D., *THE ATOMIC NUCLEUS*. 1955, BOMBAY, NEW DELHI: TATA MCGRAW-HILL PUBLISHINC CO. LTD.
132. J.F., J., *ENERGY LOSS, RANGE, PATH LENGTH, TIME-OF-FLIGHT, STRAGGLING, MULTIPLE SCATTERING, AND NUCLEAR INTERACTION PROBABILITY: IN TWO PARTS. PART 1. FOR 63 COMPOUNDS PART 2. FOR ELEMENTS 1 < Z < 92.* ATOMIC DATA AND NUCLEAR DATA TABLES, 1982. **27**(2-3): P. 147–339.
133. G, M., *THEORIE DER STREUUNG SCHNELLER GELADENER TEILCHEN.I. EINZELSTREUUNG AM ABGESCHIRMTEN COULOMB-FELD. II.* MEHRFACH UND VIELFACHSTREUUNG. Z.NATURFORSCH.A, 1947. **2**: P. 133-145.
134. G, M., *THEORIE DER STREUUNG SCHNELLER GELADENEN TEILCHEN II.* MEHRFACHUND VIELFACHSTREUUNG. Z.NATURFORSCH.A, 1948. **3**: P. 78-97.
135. GOTTSCHALK, B., ET AL., *MULTIPLE COULOMB SCATTERING OF 160 MEV PROTONS.* NUCLEAR INSTRUMENTS & METHODS IN PHYSICS RESEARCH SECTION B-BEAM INTERACTIONS WITH MATERIALS AND ATOMS, 1993. **74**(4): P. 467-490.
136. ROSSI, B., *HIGH-ENERGY PARTICLES*, ED. N.Y. PRENTICE-HALL. 1952.
137. KASE, K.R. AND W.R. NELSON, *CONCEPTS OF RADIATION DOSIMETRY*. 1978: PERGAMON PRESS.
138. M.J. BERGER, J.S.C., M.A. ZUCKER AND J. CHANG, *ESTAR, PSTAR, AND ASTAR: COMPUTER PROGRAMS FOR CALCULATING STOPPING-POWER AND RANGE TABLES FOR ELECTRONS, PROTONS, AND HELIUM IONS.* NIST, PHYSICAL MEASUREMENT LABORATORY, 2005. **HTTP://WWW.NIST.GOV/PML/DATA/STAR/INDEX.CFM**.
139. A. FERRARI, P.R.S., R. GUARALDI, F. PADOANI, *AN IMPROVED MULTIPLE SCATTERING MODEL FOR CHARGED PARTICLE TRANSPORT.* NUCL. INSTR. METH. IN PHYS. RES., 1992. **B71**: P. 412-426.
140. L. KIM, R.H.P., S.M. SELTZER, M.J. BERGER, *RATIO OF POSITRON TO ELECTRON BREMSSTRAHLUNG ENERGY LOSS: AN APPROXIMATE SCALING LAW.* PHYS. REV. A, 1986. **33**: P. 3002-3009.
141. SELTZER S.M., H.J.H., BERGER M.J., *NATIONAL AND INTERNATIONAL STANDARDIZATION OF RADIATION DOSIMETRY* IAEA, EDITOR. 1978: VIENNA.
142. *ICRU REPOET 13, NEUTRON FLUENCE, NEUTRON SPECTRA, AND KERMA*, IN *ICRU REPOET 13*, I.C.O.R.U.A. MEASUREMENT, EDITOR. 1969: WASHINGTON, DC.
143. NO.38, N.R., *PROTECTION AGAINST NEUTRON RADIATION*, IN *WASHINGTIN, DC*, N.C.O.R.P.A. MEASUREMENTS, EDITOR. 1971.
144. NO.21, I.P., *DATA FOR PROTECTION AGAINST IONIZING RADIATION FROM EXTERNAL SOURCES: SUPPLEMENT TO ICRP PUBLICATION 15*, IN *PERGAMON PRESS*, I.C.O.R. PROTECTION, EDITOR. 1973: OXFORD.
145. SCHUHMACHER, H. AND B.R.L. SIEBERT, *QUALITY FACTORS AND AMBIENT DOSE EQUIVALENT FOR NEUTRONS BASED ON THE NEW ICRP RECOMMENDATIONS.* RADIATION PROTECTION DOSIMETRY, 1992. **40**(2): P. 85-89.
146. LEVINGER, J.S., *NUCLEAR PHOTODISINTEGRATION,*. OXFORD UNIVERSITY PRESS. 1960.
147. BERMAN, B.L., FULTZ, S.C.,, *GIANT-RESONANCE MEASUREMENTS WITH MONOENERGETICBPHOTONS.* REV. MOD. PHYS., 1975. **47**(713).
148. HEATON, H.T., ET AL., *PROCEEDINGS OF A CONFERENCE ON NEUTRONS FROM ELECTRON MEDICAL ACCELERATORS: PROCEEDINGS OF A CONFERENCE HELD AT THE NATIONAL*

BUREAU OF STANDARDS, GAITHERSBURG, MARYLAND, APRIL 9-10, 1979. 1979: U.S. DEPT. OF COMMERCE, NATIONAL BUREAU OF STANDARDS : FOR SALE BY THE SUPT. OF DOCS., U.S. GOVT. PRINT. OFF.

149. LEVINGER, J.S., *THE HIGH ENERGY NUCLEAR PHOTOEFFECT.* PHYSICAL REVIEW, 1951. **84**(1): P. 43-51.
150. NELSON, W.R. AND T.M. JENKINS, *SIMILARITIES AMONG RADIATION-FIELDS AT DIFFERENT TYPES OF HIGH-ENERGY ACCELERATORS.* IEEE TRANSACTIONS ON NUCLEAR SCIENCE, 1976. **23**(4): P. 1351-1354.
151. HTTPS://WWW-NDS.IAEA.ORG/EXFOR/EXFOR.HTM.
152. MAO, X., K.R. KASE, AND W.R. NELSON, *GIANT DIOPLE RESONANCE NEUTRON YIELDS PRODUCED BY ELECTRONS AS A FUNCTION OF TARGET MATERIAL AND THICKNESS.* SLAC PUB-6628, 1996.
153. HOWERTON, R.J., BRAFF, D., CAHILL, W.J., CHAZAN, N, *THRESHOLDS OF PHOTON INDUCED REACTIONS*, IN *REP. UCRL-14006*. 1964, LAWRENCE LIVERMORE LABORATORY.
154. BARBIER, M.M., *INDUCED RADIOACTIVITY*. 1969: NORTH-HOLLAND PUB. CO.
155. GOLLON, P.J., *PRODUCTION OF RADIOACTIVITY BY PARTICLE ACCELERATORS.* IEEE TRANSACTIONS ON NUCLEAR SCIENCE, 1976. **23**(4): P. 1395-1400.
156. *NATIONAL NUCLEAR DATA CENTRE, HTTP://WWW.NNDC.BNL.GOV/.*
157. *ICRU REPORT 37, STOPPING POWERS FOR ELECTRONS AND POSITIONS*, IN *ICRU REPORT 37*, M.I.P. BETHESDA, EDITOR. 1984.
158. *RADIOTHERAPY DOSE-FRACTIONATION*. 2006, THE ROYAL COLLEGE OF RADIOLOGISTS (BOARD OF FACULTY OF CLINICAL ONCOLOGY).
159. IAEA, *RADIOBIOLOGICAL SAFETY ASPECTS OF THE OPARATION OF ELECTRON LINEAR ACCELERATORS*. 1979, INTERNATIONAL ATOMIC ENERGY AGENCY: VIENNA.
160. *ICRP PUBLICATION 74, CONVERSION COEFFICIENTS FOR USE IN RADIOLOGICAL PROTECTION AGAINST EXTERNAL RADIATION*, ANNALS OF ICRP, EDITOR. 1996.
161. *ICRU REPORT 57, CONVERSION COEFFICIENTS FOR USE IN RADIOLOGICAL PROTECTION AGAINST EXTERNAL RADIATION*, M.I.P. BETHESDA, EDITOR. 1998.
162. FERRARI, A. AND M. PELLICCIONI, *ON THE CONVERSION COEFFICIENTS FROM FLUENCE TO AMBIENT DOSE-EQUIVALENT.* RADIATION PROTECTION DOSIMETRY, 1994. **51**(4): P. 251-255.
163. FERRARI, A. AND M. PELLICCIONI, *DOSE EQUIVALENTS FOR MONOENERGETIC ELECTRONS INCIDENT ON THE ICRU SPHERE.* RADIATION PROTECTION DOSIMETRY, 1994. **55**(3): P. 207-210.
164. FERRARI, A. AND M. PELLICCIONI, *DOSE EQUIVALENTS FOR MONOENERGETIC POSITRONS INCIDENT ON THE ICRU SPHERE.* RADIATION PROTECTION DOSIMETRY, 1994. **55**(4): P. 309-312.
165. FERRARI, A., M. PELLICCIONI, AND M. PILLON, *FLUENCE TO EFFECTIVE DOSE AND EFFECTIVE DOSE EQUIVALENT CONVERSION COEFFICIENTS FOR ELECTRONS FROM 5 MEV TO 10 GEV.* RADIATION PROTECTION DOSIMETRY, 1997. **69**(2): P. 97-104.
166. FERRARI, A., M. PELLICCIONI, AND M. PILLON, *FLUENCE TO EFFECTIVE DOSE CONVERSION COEFFICIENTS FOR PROTONS FROM 5 MEV TO 10 TEV.* RADIATION PROTECTION DOSIMETRY, 1997. **71**(2): P. 85-91.
167. FERRARI, A., M. PELLICCIONI, AND M. PILLON, *FLUENCE-TO-EFFECTIVE DOSE CONVERSION COEFFICIENTS FOR MUONS.* RADIATION PROTECTION DOSIMETRY, 1997. **74**(4): P. 227-233.
168. FERRARI, A., M. PELLICCIONI, AND M. PILLON, *FLUENCE TO EFFECTIVE DOSE CONVERSION COEFFICIENTS FOR NEGATIVELY AND POSITIVELY CHARGED PIONS.* RADIATION PROTECTION DOSIMETRY, 1998. **80**(4): P. 361-370.
169. FERRARI, A. AND M. PELLICCIONI, *FLUENCE TO DOSE EQUIVALENT CONVERSION DATA AND EFFECTIVE QUALITY FACTORS FOR HIGH ENERGY NEUTRONS.* RADIATION PROTECTION DOSIMETRY, 1998. **76**(4): P. 215-224.

170. PELLICCIONI, M., *FLUENCE TO DOSE EQUIVALENT CONVERSION DATA AND RADIATION WEIGHTING FACTORS FOR HIGH ENERGY RADIATION.* RADIATION PROTECTION DOSIMETRY, 1998. **77**(3): P. 159-170.
171. ICRP, *RECOMMENDATIONS OF THE INTERNATIONAL COMMISSION ON RADIOLOGICAL PROTECTION.* ICRP PUBLICATION 60, ANNALS OF THE ICRP 21(1-3), 1991. **(OXFORD: PERGAMON)**.
172. *ICRU REPORT 33, RADIATION QUANTITIES AND UNITS*, IN *ICRU REPORT 33*, M.I.P. BETHESDA, EDITOR. 1980.
173. *ICRP PUBLICATION 103, THE 2007 RECOMMENDATIONS OF THE INTERNATIONAL COMMISSION ON RADIOLOGICAL PROTECTION*. 2007.
174. *ICRU REPORT 51, QUANTITIES AND UNITS IN RADIATION PROTECTION DOSIMETRY*, IN *BETHESDA, MD: ICRU PUBLICATIONS*. 1993.
175. *ICRU REPORT 39, DETERMINATION OF DOSE EQUIVALENTS RESULTING FROM EXTERNAL RADIATION SOURCE*, IN *BETHESDA, MD: ICRU PUBLICATIONS*. 1985.
176. PELLICCIONI, M., *OVERVIEW OF FLUENCE-TO-EFFECTIVE DOSE AND FLUENCE-TO AMBIENT DOSE EQUIVALENT CONVERSION COEFFICIENTS FOR HIGH ENERGY RADIATION CALCULATED USING THE FLUKA CODE.* RADIATION PROTECTION DOSIMETRY, 2000. **88**(4): P. 279-297.
177. ICRP, *CONVERSION COEFFICIENTS FOR USE IN RADIOLOGICAL PROTECTION AGAINST EXTERNAL RADIATION.* ICRP PUBLICATION 74, 1996. **(OXFORD: PERGAMON)**.
178. PAGANETTI, H., *NUCLEAR INTERACTIONS IN PROTON THERAPY: DOSE AND RELATIVE BIOLOGICAL EFFECT DISTRIBUTIONS ORIGINATING FROM PRIMARY AND SECONDARY PARTICLES.* PHYSICS IN MEDICINE AND BIOLOGY, 2002. **47**(5): P. 747-764.
179. MOSKVIN, V., ET AL., *ACUTE SKIN TOXICITY ASSOCIATED WITH PROTON BEAM THERAPY IN SPINE AND BRAIN PATIENTS.* JOURNAL OF RADIATION ONCOLOGY, 2013: P. 1-9.
180. *ICRU REPORT 49, STOPPING POWERS AND RANGES FOR PROTONS AND ALPHA PARTICLES.* MED. PHYS., 1994. **21**(5): P. 709-710.
181. *ICRU REPORT 85*, IN *JOURNAL OF THE ICRU*. 2011. P. NP.
182. SHANKS, R.P., *COMPREHENSIVE CHARACTERISATION OF LASER PLASMA WAKEFIELD ACCELERATED ELECTRONS*, IN *DEPARTMENT OF PHYSICS*. 2012, UNIVERSITY OF STRATHCLYDE. P. 177.
183. ADAMS, G.E. AND D.G. JAMESON, *TIME EFFECTS IN MOLECULAR RADIATION BIOLOGY.* RADIATION AND ENVIRONMENTAL BIOPHYSICS, 1980. **17**(2): P. 95-113.
184. *ICRP PUBLICATION 23, REPORT ON THE TASK GROUP ON REFERENCE MAN*, IN *ICRP PUBLICATION 23*, M.I.P. BETHESDA, EDITOR. 1975.
185. BALLARINI, F., ET AL., *STOCHASTIC ASPECTS AND UNCERTAINTIES IN THE PRECHEMICAL AND CHEMICAL STAGES OF ELECTRON TRACKS IN LIQUID WATER: A QUANTITATIVE ANALYSIS BASED ON MONTE CARLO SIMULATIONS.* RADIATION AND ENVIRONMENTAL BIOPHYSICS, 2000. **39**(3): P. 179-188.
186. KREIPL, M., W. FRIEDLAND, AND H. PARETZKE, *INTERACTION OF ION TRACKS IN SPATIAL AND TEMPORAL PROXIMITY.* RADIATION AND ENVIRONMENTAL BIOPHYSICS, 2009. **48**(4): P. 349-359.
187. *IAEA 2000, ABSORBED DOSE DETERMINATION IN EXTERNAL BEAM RADIOTHERAPY: AN INTERNATIONAL CODE OF PRACTICE FOR DOSIMETRY BASED ON STANDARDS OF ABSORBED DOSE TO WATER*. 2000: VIENNA.
188. BREDE, H.J., ET AL., *ABSORBED DOSE TO WATER DETERMINATION WITH IONIZATION CHAMBER DOSIMETRY AND CALORIMETRY IN RESTRICTED NEUTRON, PHOTON, PROTON AND HEAVY-ION RADIATION FIELDS.* PHYSICS IN MEDICINE AND BIOLOGY, 2006. **51**(15): P. 3667-3682.
189. HTTP://WWW.MGSRESEARCH.COM/CUSTOM.ASP?ID=63396&PAGE=4.

190. OLDHAM, M., ET AL., *AN INVESTIGATION INTO THE DOSIMETRY OF A NINE-FIELD TOMOTHERAPY IRRADIATION USING BANG-GEL DOSIMETRY.* PHYSICS IN MEDICINE AND BIOLOGY, 1998. **43**(5): P. 1113-1132.
191. MCLAUGHLIN, W.L., ET AL., *RADIOCHROMIC DOSIMETRY FOR VALIDATION AND COMMISSIONING OF INDUSTRIAL RADIATION PROCESSES.* RADIAT PHYS CHEM, 1988. **31**: P. 505–14.
192. SAYLOR, M.C., ET AL., *A THIN FILM RECORDING MEDIUM FOR USE IN FOOD IRRADIATION.* RADIAT PHYS CHEM, 1988. **31**: P. 529–536.
193. MUENCH, P.J., ET AL., *PHOTON ENERGY DEPENDENCE OF THE SENSITIVITY OF RADIOCHROMIC FILM COMPARED TO SILVER HALIDE FILM AND LITHIUM FLUORIDE TLDS.* MED PHYS, 1991. **18**: P. 769–775.
194. BUTSON, M.J., J.N. MATHUR, AND P.E. METCALFE, *RADIOCHROMIC FILM AS A RADIOTHERAPY SURFACE-DOE DETECTOR.* PHYS MED BIOL, 1996. **41**: P. 1073–1087.
195. MEIGOONI, A.S., ET AL., *DOSIMETRIC CHARACTERISTICS OF AN IMPROVED RADIOCHROMIC FILM.* MED PHYS, 1996. **23**: P. 1883–1888.
196. KLASSEN, N., L. ZWAN, AND J. CYGLER, *GAFCHROMIC MD-55: INVESTIGATED AS A PRECISION DOSIMETER.* MED PHYS, 1997. **24**: P. 1924–1934.
197. SANKAR, A., ET AL., *COMPARISON OF KODAK EDR2 AND GAFCHROMIC EBT FILM FOR INTENSITY-MODULATED RADIATION THERAPY DOSE DISTRIBUTION VERIFICATION.* MED DOSIM, 2006. **31**: P. 273–282.
198. DEVIC, S., ET AL., *OPTIMIZING THE DYNAMIC RANGE EXTENSION OF A RADIOCHROMIC FILM DOSIMETRY SYSTEM.* MED PHYS, 2009. **36**: P. 429–437.
199. IPS, *GAFCHROMIC® EBT SELF-DEVELOPING LM FOR RADIOTHERAPY DOSIMETRY*. 2013, INTERNATIONAL SPECIALTY PRODUCTS.
200. NIROOMAND-RAD, A. AND E. AL., *RADIOCHROMIC FILM DOSIMETRY: RECOMMENDATIONS OF AAPM RADIATION THERAPY COMMITTEE TASK GROUP 55. AMERICAN ASSOCIATION OF PHYSICISTS IN MEDICINE.* MED PHYS, 1998. **25**: P. 2093-2115.
201. TSIBOUKLIS, J., ET AL., *PENTACOSA-10,12-DIYNOIC ACID/HENICOSA-2,4-DIYNYLAMINE ALTERNATELAYER LANGMUIR–BLODGETT FILMS: SYNTHESIS, POLYMERISATION AND ELECTRICAL PROPERTIES.* J. MATER. CHEM 3(1), 1993: P. 97-104.
202. BÄSSLER, H., V. ENKELMANN, AND H. SIXL, *PHOTOPOLYMERIZATION OF DIACETYLENES.* ADV. POLYM. SCI., 1984. **63**(1).
203. RINK, A., I.A. VITKIN, AND D.A. JAFFRAY, *SUITABILITY OF RADIOCHROMIC MEDIUM FOR REAL-TIME OPTICAL MEASUREMENTS OF IONIZING RADIATION DOSE.* MED PHYS, 2005. **32**: P. 1140-1155.
204. ATTIX, F.H., *INTRODUCTION TO RADIOLOGICAL PHYSICS AND RADIATION DOSIMETRY*. 1986: JOHN WILEY & SONS.
205. MCLAUGHLIN, W.L., ET AL. *RADIOCHROMIC SOLID-STATE POLYMERIZATION REACTION*. IN *ACS SYMPOSIUM SERIES*. 1996. WASHINGTON, DC.
206. CHEUNG, T., M.J. BUTSON, AND P.K. YU, *POST-IRRADIATION COLOURATION OF GAFCHROMIC EBT RADIOCHROMIC FILM.* PHYS. MED. BIOL., 2005. **25**: P. N281-N285.
207. NIROOMAND-RAD, A., ET AL., *RADIOCHROMIC FILM DOSIMETRY*. 1998.
208. GIRARD, F., H. BOUCHARD, AND F. LACROIX, *REFERENCE DOSIMETRY USING RADIOCHROMIC FILMS.* JOURNAL OF APPLIED CLINICAL MEDICAL PHYSICS, 2012. **13**(6): P. 3994.
209. MAYERS , S., *CHARACTERISATION OF GAFCHROMIC EBT2 FILM FOR USE IN RADIATION THERAPY DOSIMETRY*. 2011: WOLLONGONG.
210. CASANOVA BORCA, V., ET AL., *GAFCHROMIC EBT3 FILM FOR IMRT DOSE VERIFICATION.* JOURNAL OF APPLIED CLINICAL MEDICAL PHYSICS, 2013. **14**(2): P. 158-171.
211. ANDRES, C., ET AL., *A COMPREHENSIVE STUDY OF THE GAFCHROMIC EBT2 RADIOCHROMIC FILM. A COMPARISON WITH EBT.* MEDICAL PHYSICS, 2010. **37**(12): P. 6271-6278.

212. ARJOMANDY, B., ET AL., *ENERGY DEPENDENCE AND DOSE RESPONSE OF GAFCHROMIC EBT2 FILM OVER A WIDE RANGE OF PHOTON, ELECTRON, AND PROTON BEAM ENERGIES.* MEDICAL PHYSICS, 2010. **37**(5): P. 1942-1947.

213. ARJOMANDY, B., ET AL., *EBT2 FILM AS A DEPTH-DOSE MEASUREMENT TOOL FOR RADIOTHERAPY BEAMS OVER A WIDE RANGE OF ENERGIES AND MODALITIES.* MEDICAL PHYSICS, 2012. **39**(2): P. 912-921.

214. BUTSON, M.J., ET AL., *ENERGY RESPONSE OF THE NEW EBT2 RADIOCHROMIC FILM TO X-RAY RADIATION.* RADIATION MEASUREMENTS, 2010. **45**(7): P. 836-839.

215. ISP. *HTTP://WWW.GAFCHROMIC.COM*. 2013.

216. LINDSAY, P., ET AL., *INVESTIGATION OF ENERGY DEPENDENCE OF EBT AND EBT-2 GAFCHROMIC FILM.* MEDICAL PHYSICS, 2010. **37**(2): P. 571-576.

217. REINHARDT, S., ET AL., *COMPARISON OF GAFCHROMIC EBT2 AND EBT3 FILMS FOR CLINICAL PHOTON AND PROTON BEAMS.* MEDICAL PHYSICS, 2012. **39**(8): P. 5257-5262.

218. ISP INTERNATIONAL SPECIALTY PRODUCTS, *HTTP://WWW.FILMQAPRO.COM/DOCUMENTS/GAFCHROMIC_EBT-2_20101007.PDF*. 2013.

219. FUSS, M., ET AL., *DOSIMETRIC CHARACTERIZATION OF GAFCHROMIC EBT FILM AND ITS IMPLICATION ON FILM DOSIMETRY QUALITY ASSURANCE.* PHYSICS IN MEDICINE AND BIOLOGY, 2007. **52**(14): P. 4211-4225.

220. ZHAO, L. AND I.I. DAS, *GAFCHROMIC EBT FILM DOSIMETRY IN PROTON BEAMS.* PHYSICS IN MEDICINE AND BIOLOGY 55, 2010.

221. KIRBY, D., ET AL., *LET DEPENDENCE OF GAFCHROIMIC FILMS AND AN ION CHAMBER IN LOW-ENERGY PROTON DOSIMETRY.* PHYSICS IN MEDICINE AND BIOLOGY 55, 2010.

222. ANGELLIER, G., M. GAUTIER, AND J. HERAULT, *RADIOCHROMIC EBT2 FILM DOSIMETRY FOR LOW-ENERGY PROTONTHERAPY.* MEDICAL PHYSICS 38 (11), 2011.

223. WILCOX, E., G. DASKALOV, AND L. NEDIALKOVA, *COMPARISON OF THE EPSON EXPRESSION 1680 FLATBED AND THE VIDAR VXR-16 DOSIMETRY PRO™ FILM SCANNERS FOR USE IN IMRT DOSIMETRY USING GAFCHROMIC AND RADIOGRAPHIC FILM.* MED. PHYS., 2007. **34**: P. 41-8.

224. PAELINCK, L., W. DE NEVE, AND C. DE WAGTER, *PRECAUTIONS AND STRATEGIES IN USING A COMMERCIAL FLATBED SCANNER FOR RADIOCHROMIC FILM DOSIMETRY.* PHYS. MED. BIOL, 2007. **52**: P. 231-242.

225. ALNAWAF, H., P.K.N. YU, AND M. BUTSON, *COMPARISON OF EPSON SCANNER QUALITY FOR RADIOCHROMIC FILM EVALUATION* JOURNAL OF APPLIED CLINICAL MEDICAL PHYSICS, 2012. **13**(5): P. 314-321.

226. L. XU, M.M., *ON THE COMPARISON OF EPSON V700 AND 10000XL SCANNERS FOR GAFCHROMIC EBT FILM DOSIMETRY.* MEDICAL PHYSICS, 2009. **36**(6): P. 2589.

227. VARIAN. *HTTP://WWW.VARIAN.COM/US/ONCOLOGY/RADIATION_ONCOLOGY/CLINAC/CLINAC_IX.HTML*.

228. NIROOMAND-RAD, A., ET AL., *RADIOCHROMIC FILM DOSIMETRY: RECOMMENDATIONS OF AAPM RADIATION THERAPY COMMITTEE TASK GROUP 55.* MEDICAL PHYSICS, 1998. **25**(11): P. 2093-2115.

229. CHUNG, H.T., B. LYNCH, AND S. SAMANT, *HIGH-PRECISION GAFCHROMIC EBT FILM-BASED ABSOLUTE CLINICAL DOSIMETRY USING A STANDARD FLATBED SCANNER WITHOUT THE USE OF A SCANNER NON-UNIFORMITY CORRECTION.* JOURNAL OF APPLIED CLINICAL MEDICAL PHYSICS, 2010. **11**(2): P. 101-115.

230. TAYLOR, J.R., *AN INTRODUCTION TO ERROR ANALYSIS : THE STUDY OF UNCERTAINTIES IN PHYSICAL MEASUREMENTS*, ED. N. EDITION. 1997: SAUSALITO, CALIF. : UNIVERSITY SCIENCE BOOKS, C1997.

231. DEVIC, S., ET AL., *PRECISE RADIOCHROMIC FILM DOSIMETRY USING A FLAT-BED DOCUMENT SCANNER.* MEDICAL PHYSICS, 2005. **32**(7): P. 2245-2253.

232. MIZUNO, H., ET AL., *HOMOGENEITY OF GAFCHROMIC EBT2 FILM AMONG DIFFERENT LOT NUMBERS.* JOURNAL OF APPLIED CLINICAL MEDICAL PHYSICS, 2012. **13**(4): P. 198-205.
233. KAIRN, T., ET AL., *TECHNICAL NOTE: MODELING A COMPLEX MICRO-MULTILEAF COLLIMATOR USING THE STANDARD BEAMNRC DISTRIBUTION.* MEDICAL PHYSICS, 2010. **37**(4): P. 1761-1767.
234. RICHLEY L, J.A., COOMBER H, FLETCHER S, *EVALUATION AND OPTIMIZATION OF THE NEW EBT2 RADIOCHROMIC FILM DOSIMETRY SYSTEM FOR PATIENT DOSE VERIFICATION IN RADIOTHERAPY.* PHYS MED BIOL, 2010. **55**(9): P. 2601-17.
235. HARTMANN B, M.M., JÄKEL O., *HOMOGENEITY OF GAFCHROMIC EBT2 FILM.* MEDICAL PHYSICS, 2010. **37**(4): P. 1753-6.
236. ALAND T, K.T., KENNY J., *EVALUATION OF A GAFCHROMIC EBT2 FILM DOSIMETRY SYSTEM FOR RADIOTHERAPY QUALITY ASSURANCE.* AUSTRALAS PHYS ENG SCI MED., 2011. **34**(2): P. 251-60.
237. SPARC. HTTP://WWW.LNF.INFN.IT/ACCELERATORI/SPARC/.
238. LAPOSTOLLE, P.M. AND A.L. SEPTIER, *LINEAR ACCELERATORS*. 1970: NORTH HOLLAND PUBLISHING COMPANY.
239. HANNA, S., *RF LINEAR ACCELERATORS FOR MEDICAL AND INDUSTRIAL APPLICATIONS*. 2012: ARTECH HOUSE.
240. WANGLER, T.P., *RF LINEAR ACCELERATORS*. 2008: WILEY.
241. CHAO, A.W. AND W. CHOU, *REVIEWS OF ACCELERATOR SCIENCE AND TECHNOLOGY - VOLUME 2: MEDICAL APPLICATIONS OF ACCELERATORS*. 2010: WORLD SCIENTIFIC.
242. PALMER, D.T., *THE NEXT GENERATION PHOTOINJECTOR, PH.D. THESIS, STANFORD UNIVERSITY.* 1998.
243. ALESINI, D., ET AL., *THE SPARC PROJECT: A HIGH-BRIGHTNESS ELECTRON BEAM SOURCE AT LNF TO DRIVE A SASE-FEL EXPERIMENT.* NUCLEAR INSTRUMENTS & METHODS IN PHYSICS RESEARCH SECTION A-ACCELERATORS SPECTROMETERS DETECTORS AND ASSOCIATED EQUIPMENT, 2003. **507**(1-2): P. 345-349.
244. WU, A., ET AL., *COMMENTS ON DOSE MEASUREMENTS FOR A NARROW BEAM IN RADIOSURGERY.* MEDICAL PHYSICS, 1993. **20**(3): P. 777-779.
245. BJARNGARD, B.E., J.S. TSAI, AND R.K. RICE, *DOSES ON THE CENTRAL AXES OF NARROW 6-MV X-RAY-BEAMS.* MEDICAL PHYSICS, 1990. **17**(5): P. 794-799.
246. SIBATA, C.H., ET AL., *INFLUENCE OF DETECTOR SIZE IN PHOTON-BEAM PROFILE MEASUREMENTS.* PHYSICS IN MEDICINE AND BIOLOGY, 1991. **36**(5): P. 621-631.
247. SCHUMER, W., ET AL., *VERIFICATION OF BRACHYTHERAPY DOSIMETRY WITH RADIOCHROMIC FILM.* MEDICAL DOSIMETRY : OFFICIAL JOURNAL OF THE AMERICAN ASSOCIATION OF MEDICAL DOSIMETRISTS, 1999. **24**(3): P. 197-203.
248. WILCOX, E.E. AND G.M. DASKALOV, *EVALUATION OF GAFCHROMIC (R) EBT FILM FOR CYBERKNIFE (R) DOSIMETRY.* MEDICAL PHYSICS, 2007. **34**(6): P. 1967-1974.
249. FLETCHER, C.L. AND J.A. MILLS, *AN ASSESSMENT OF GAFCHROMIC FILM FOR MEASURING 50 KV AND 100 KV PERCENTAGE DEPTH DOSE CURVES.* PHYSICS IN MEDICINE AND BIOLOGY, 2008. **53**(11): P. N209-N218.
250. BATTISTONI, G., ET AL., *THE FLUKA CODE: DESCRIPTION AND BENCHMARKING. M. ALBROW, R. RAJA EDITORS.* PROCEEDINGS OF THE HADRONIC SHOWER SIMULATION WORKSHOP 2006, FERMILAB 6--8 SEPTEMBER 2006, AIP CONFERENCE PROCEEDINGS, 2007. **896**: P. 31-49.
251. THWAITES, D.I., ET AL., *THE IPEM CODE OF PRACTICE FOR ELECTRON DOSIMETRY FOR RADIOTHERAPY BEAMS OF INITIAL ENERGY FROM 4 TO 25 MEV BASED ON AN ABSORBED DOSE TO WATER CALIBRATION.* PHYSICS IN MEDICINE AND BIOLOGY, 2003. **48**(18): P. 2929-2970.
252. SPENCER, L.V. AND F.H. ATTIX, *A THEORY OF CAVITY IONIZATION.* RADIATION RESEARCH, 1955. **3**(3): P. 239-254.

253. GRAY, L.H., *AN IONIZATION METHOD FOR THE ABSOLUTE MEASUREMENT OF GAMMA-RAY ENERGY.* HEALTH PHYSICS, 1980. **38**(6): P. 907-918.

254. *IAEA, ABSORBED DOSE DETERMINATION IN PHOTON AND ELECTRON BEAMS: AN INTERNATIONAL CODE OF PRACTICE*, IN *TECH. REP. SER. NO. 277*, IAEA, EDITOR. 1987: VIENNA, AUSTRIA.

255. *IAEA, THE USE OF PLANE PARALLEL IONIZATION CHAMBERS IN HIGH ENERGY ELECTRON AND PHOTON BEAMS: AN INTERNATIONAL CODE OF PRACTICE FOR DOSIMETRY* IN *TECHNICAL REPORTS SERIES NO. 381*, IAEA, EDITOR. 1997: VIENNA, AUSTRIA.

256. BOAG, J.W., *IONIZATION MEASUREMENTS AT VERY HIGH INTENSITIES .1. PULSED RADIATION BEAMS.* BRITISH JOURNAL OF RADIOLOGY, 1950. **23**(274): P. 601-611.

257. BOAG, J.W. AND J. CURRANT, *CURRENT COLLECTION AND IONIC RECOMBINATION IN SMALL CYLINDRICAL IONIZATION CHAMBERS EXPOSED TO PULSED RADIATION.* BRITISH JOURNAL OF RADIOLOGY, 1980. **53**(629): P. 471-478.

258. BOAG, J.W., *THE RECOMBINATION CORRECTION FOR AN IONIZATION-CHAMBER EXPOSED TO PULSED RADIATION IN A SWEPT BEAM TECHNIQUE .1. THEORY.* PHYSICS IN MEDICINE AND BIOLOGY, 1982. **27**(2): P. 201-211.

259. *ICRU REPORT 34, THE DOSIMETRY OF PULSED RADIATION*, IN *ICRU REPORT 34*, M.I.P. BETHESDA, EDITOR. 1982.

260. CONERE, T.J. AND J.W. BOAG, *THE COLLECTION EFFICIENCY OF AN IONIZATION-CHAMBER IN A PULSED AND MAGNETICALLY SWEPT ELECTRON-BEAM - LIMITS OF VALIDITY OF THE 2-VOLTAGE TECHNIQUE.* MEDICAL PHYSICS, 1984. **11**(4): P. 465-468.

261. WEINHOUS, M.S. AND J.A. MELI, *DETERMINING PION, THE CORRECTION FACTOR FOR RECOMBINATION LOSSES IN AN IONIZATION-CHAMBER.* MEDICAL PHYSICS, 1984. **11**(6): P. 846-849.

262. *IBA, HTTP://WWW.IBA-DOSIMETRY.COM/.*

263. ATTIX, F.H., *INTRODUCTION TO RADIOLOGICAL PHYSICS AND RADIATION DOSIMETRY*. 2007, WILEY-VCH VERLAG GMBH. P. 525-598.

264. *GAMMEX, HTTP://WWW.CNMCCO.COM/DOSIMETRY/PDFDOCS/SLABPHANTOMS/CNMC_SOLIDWATER.PDF.*

265. KAVANAGH, J.N., ET AL., *DNA DOUBLE STRAND BREAK REPAIR: A RADIATION PERSPECTIVE.* ANTIOXIDANTS & REDOX SIGNALING, 2013. **18**(18): P. 2458-2472.

266. ALLONI, D., ET AL., *TRACK STRUCTURE, RADIATION QUALITY AND INITIAL RADIOBIOLOGICAL EVENTS: CONSIDERATIONS BASED ON THE PARTRAC CODE EXPERIENCE.* INTERNATIONAL JOURNAL OF RADIATION BIOLOGY, 2012. **88**(1-2): P. 77-86.

267. ALLONI, D., ET AL., *INTEGRATION OF MONTE CARLO SIMULATIONS WITH PFGE EXPERIMENTAL DATA YIELDS CONSTANT RBE OF 2.3 FOR DNA DOUBLE-STRAND BREAK INDUCTION BY NITROGEN IONS BETWEEN 125 AND 225 KEV/MUM LET.* RADIATION RESEARCH, 2013. **179**(6): P. 690-7.

268. ALLONI, D., ET AL., *MONTE CARLO EVALUATION OF DNA FRAGMENTATION SPECTRA INDUCED BY DIFFERENT RADIATION QUALITIES.* RADIATION PROTECTION DOSIMETRY, 2011. **143**(2-4): P. 226-231.

269. GOODHEAD, D.T., *MECHANISMS FOR THE BIOLOGICAL EFFECTIVENESS OF HIGH-LET RADIATIONS.* JOURNAL OF RADIATION RESEARCH, 1999. **40**: P. 1-13.

270. ZHOU, B.B.S. AND S.J. ELLEDGE, *THE DNA DAMAGE RESPONSE: PUTTING CHECKPOINTS IN PERSPECTIVE.* NATURE, 2000. **408**(6811): P. 433-439.

271. LOVEJOY, C.A. AND D. CORTEZ, *COMMON MECHANISMS OF PIKK REGULATION.* DNA REPAIR, 2009. **8**(9): P. 1004-1008.

272. NAKAMURA, A.J., ET AL., *THE COMPLEXITY OF PHOSPHORYLATED H2AX FOCI FORMATION AND DNA REPAIR ASSEMBLY AT DNA DOUBLE-STRAND BREAKS.* CELL CYCLE, 2010. **9**(2): P. 389-397.

273. STUCKI, M., ET AL., *MDC1 DIRECTLY BINDS PHOSPHORYLATED HISTONE H2AX TO REGULATE CELLULAR RESPONSES TO DNA DOUBLE-STRAND BREAKS.* CELL, 2005. **123**(7): P. 1213-1226.

274. BHOGAL, N., F. JALALI, AND R.G. BRISTOW, *MICROSCOPIC IMAGING OF DNA REPAIR FOCI IN IRRADIATED NORMAL TISSUES.* INTERNATIONAL JOURNAL OF RADIATION BIOLOGY, 2009. **85**(9): P. 732-746.

275. LAVIN, M.F., *ATM AND THE MRE11 COMPLEX COMBINE TO RECOGNIZE AND SIGNAL DNA DOUBLE-STRAND BREAKS.* ONCOGENE, 2007. **26**(56): P. 7749-7758.

276. VAN GENT, D.C. AND M. VAN DER BURG, *NON-HOMOLOGOUS END-JOINING, A STICKY AFFAIR.* ONCOGENE, 2007. **26**(56): P. 7731-7740.

277. ROGAKOU, E.P., ET AL., *DNA DOUBLE-STRANDED BREAKS INDUCE HISTONE H2AX PHOSPHORYLATION ON SERINE 139.* JOURNAL OF BIOLOGICAL CHEMISTRY, 1998. **273**(10): P. 5858-5868.

278. ROGAKOU, E.P., ET AL., *MEGABASE CHROMATIN DOMAINS INVOLVED IN DNA DOUBLE-STRAND BREAKS IN VIVO.* JOURNAL OF CELL BIOLOGY, 1999. **146**(5): P. 905-915.

279. SEDELNIKOVA, O.A., ET AL., *QUANTITATIVE DETECTION OF (125) IDU-INDUCED DNA DOUBLE-STRAND BREAKS WITH GAMMA-H2AX ANTIBODY.* RADIATION RESEARCH, 2002. **158**(4): P. 486-492.

280. ROTHKAMM, K. AND M. LOBRICH, *EVIDENCE FOR A LACK OF DNA DOUBLE-STRAND BREAK REPAIR IN HUMAN CELLS EXPOSED TO VERY LOW X-RAY DOSES.* PROCEEDINGS OF THE NATIONAL ACADEMY OF SCIENCES OF THE UNITED STATES OF AMERICA, 2003. **100**(9): P. 5057-5062.

281. DELANEY, G., ET AL., *THE ROLE OF RADIOTHERAPY IN CANCER TREATMENT: ESTIMATING OPTIMAL UTILIZATION FROM A REVIEW OF EVIDENCE-BASED CLINICAL GUIDELINES (VOL 104, PG 1129, 2005).* CANCER, 2006. **107**(3): P. 660-660.

282. PAJONK, F., E. VLASHI, AND W.H. MCBRIDE, *RADIATION RESISTANCE OF CANCER STEM CELLS: THE 4 R'S OF RADIOBIOLOGY REVISITED.* STEM CELLS, 2010. **28**(4): P. 639-648.

283. BARENDSEN, G.W., ET AL., *EFFECTS OF DIFFERENT IONIZING RADIATIONS ON HUMAN CELLS IN TISSUE CULTURE .3. EXPERIMENTS WITH CYCLOTRON-ACCELERATED ALPHA-PARTICLES AND DEUTERONS.* RADIATION RESEARCH, 1963. **18**(1): P. 106-&.

284. SUZUKI, M., ET AL., *LET DEPENDENCE OF CELL DEATH AND CHROMATIN-BREAK INDUCTION IN NORMAL HUMAN CELLS IRRADIATED BY NEON-ION BEAMS.* INTERNATIONAL JOURNAL OF RADIATION BIOLOGY, 1997. **72**(5): P. 497-503.

285. TASK GROUP ON RADIATION QUALITY EFFECTS IN RADIOLOGICAL, P., I.C.O. COMMITTEE 1 ON RADIATION EFFECTS, AND P. RADIOLOGICAL, *RELATIVE BIOLOGICAL EFFECTIVENESS (RBE), QUALITY FACTOR (Q), AND RADIATION WEIGHTING FACTOR (W(R)). A REPORT OF THE INTERNATIONAL COMMISSION ON RADIOLOGICAL PROTECTION.* ANNALS OF THE ICRP, 2003. **33**(4): P. 1-117.

286. BRENNER, D.J. AND H.I. AMOLS, *ENHANCED RISK FROM LOW-ENERGY SCREEN FILM MAMMOGRAPHY X-RAYS.* BRITISH JOURNAL OF RADIOLOGY, 1989. **62**(742): P. 910-914.

287. *ICRU REPORT 40, THE QUALITY FACTOR IN RADIATION PROTECTION* IN *BETHESDA, MD: ICRU PUBLICATIONS*. 1986.

288. MARTHINSEN, A.B.L., ET AL., *RELATIVE BIOLOGICAL EFFECTIVENESS OF PHOTON ENERGIES USED IN BRACHYTHERAPY AND INTRAOPERATIVE RADIOTHERAPY TECHNIQUES FOR TWO BREAST CANCER CELL LINES.* ACTA ONCOLOGICA, 2010. **49**(8): P. 1261-1268.

289. SHRIDHAR, R., ET AL., *CHARACTERISTIC 8 KEV X RAYS POSSESS RADIOBIOLOGICAL PROPERTIES OF HIGHER-LET RADIATION.* RADIATION RESEARCH, 2010. **173**(3): P. 290-297.

290. HALL, E.J. AND A.J. GIACCIA, *RADIOBIOLOGY FOR THE RADIOLOGIST*. 2006: LIPPINCOTT WILLIAMS & WILKINS.

291. HUNTER, N. AND C.R. MUIRHEAD, *REVIEW OF RELATIVE BIOLOGICAL EFFECTIVENESS DEPENDENCE ON LINEAR ENERGY TRANSFER FOR LOW-LET RADIATIONS.* JOURNAL OF RADIOLOGICAL PROTECTION, 2009. **29**(1): P. 5-21.

292. ALPEN, E.L., *PRENTICE HALL BIOPHYSICS AND BIOENGINEERING SERIES RADIATION BIOPHYSICS*. ALPEN, E. L. PRENTICE HALL BIOPHYSICS AND BIOENGINEERING SERIES: RADIATION BIOPHYSICS. XX+392P. PRENTICE HALL: ENGLEWOOD CLIFFS, NEW JERSEY, USA; LONDON, ENGLAND, UK. ILLUS. 1990. XX+392P-XX+392P.

293. *HTTP://WWW.RADIOLOGYSCHOOLS.COM/RADIOLOGY-COURSES/RADBIOL/02BIO/BIO-02-06.HTML*.

294. WEYRATHER, W.K., ET AL., *RBE FOR CARBON TRACK-SEGMENT IRRADIATION IN CELL LINES OF DIFFERING REPAIR CAPACITY.* INTERNATIONAL JOURNAL OF RADIATION BIOLOGY, 1999. **75**(11): P. 1357-1364.

295. WEYRATHER, W.K. AND G. KRAFT, *RBE OF CARBON IONS: EXPERIMENTAL DATA AND THE STRATEGY OF RBE CALCULATION FOR TREATMENT PLANNING.* RADIOTHERAPY AND ONCOLOGY, 2004. **73**: P. S161-S169.

296. BUTTS, J.J. AND R. KATZ, *THEORY OF RBE FOR HEAVY ION BOMBARDMENT OF DRY ENZYMES AND VIRUSES.* RADIATION RESEARCH, 1967. **30**(4): P. 855-&.

297. *HTTP://WWW.TWIV.TV/TWIV197-082612.PDF*.

298. PUCK, T.T. AND P.I. MARCUS, *ACTION OF X-RAYS ON MAMMALIAN CELLS.* JOURNAL OF EXPERIMENTAL MEDICINE, 1956. **103**(5): P. 653-&.

299. BOYD, M., ET AL., *RADIATION QUALITY-DEPENDENT BYSTANDER EFFECTS ELICITED BY TARGETED RADIONUCLIDES.* JOURNAL OF PHARMACY AND PHARMACOLOGY, 2008. **60**(8): P. 951-958.

300. BUFFA, F.M., ET AL., *INCORPORATING BIOLOGIC MEASUREMENTS (SF2, CFE) INTO A TUMOR CONTROL PROBABILITY MODEL INCREASES THEIR PROGNOSTIC SIGNIFICANCE: A STUDY IN CERVICAL CARCINOMA TREATED WITH RADIATION THERAPY.* INTERNATIONAL JOURNAL OF RADIATION ONCOLOGY BIOLOGY PHYSICS, 2001. **50**(5): P. 1113-1122.

301. FOWLER, J.F., *THE LINEAR-QUADRATIC FORMULA AND PROGRESS IN FRACTIONATED RADIOTHERAPY.* BRITISH JOURNAL OF RADIOLOGY, 1989. **62**(740): P. 679-694.

302. BRENNER, D.J., ET AL., *THE LINEAR-QUADRATIC MODEL AND MOST OTHER COMMON RADIOBIOLOGICAL MODELS RESULT IN SIMILAR PREDICTIONS OF TIME-DOSE RELATIONSHIPS.* RADIATION RESEARCH, 1998. **150**(1): P. 83-91.

303. *HTTP://OZRADONC.WIKIDOT.COM/CLINICAL-USE-OF-THE-LINEAR-QUADRATIC-EQUATION*.

304. BEWES, J.M., ET AL., *THE RADIOBIOLOGICAL EFFECT OF INTRA-FRACTION DOSE-RATE MODULATION IN INTENSITY MODULATED RADIATION THERAPY (IMRT).* PHYSICS IN MEDICINE AND BIOLOGY, 2008. **53**(13): P. 3567-3578.

305. YANG, H.J., ET AL., *INVESTIGATION OF RADIATION-INDUCED TRANSCRIPTOME PROFILE OF RADIORESISTANT NON-SMALL CELL LUNG CANCER A549 CELLS USING RNA-SEQ.* PLOS ONE, 2013. **8**(3).

306. GOMEZ-CASAL, R., ET AL., *NON-SMALL CELL LUNG CANCER CELLS SURVIVED IONIZING RADIATION TREATMENT DISPLAY CANCER STEM CELL AND EPITHELIAL-MESENCHYMAL TRANSITION PHENOTYPES.* MOLECULAR CANCER, 2013. **12**.

307. FORAY, N., ET AL., *DOSE-RATE EFFECT ON RADIATION-INDUCED DNA DOUBLE-STRAND BREAKS IN THE HUMAN FIBROBLAST HF19 CELL LINE.* INTERNATIONAL JOURNAL OF RADIATION BIOLOGY, 1996. **69**(2): P. 241-249.

308. BRENNER, D.J., ET AL., *INTERPRETATION OF INVERSE DOSE-RATE EFFECTS FOR MUTAGENESIS BY SPARSELY IONIZING RADIATION.* INTERNATIONAL JOURNAL OF RADIATION BIOLOGY, 1996. **70**(4): P. 447-458.

309. HALL, E.J., *THE DOSE-RATE FACTOR IN RADIATION BIOLOGY.* INTERNATIONAL JOURNAL OF RADIATION BIOLOGY, 1991. **59**(3): P. 595-610.

310. HARRISON, L.B., ET AL., *IMPACT OF TUMOR HYPOXIA AND ANEMIA ON RADIATION THERAPY OUTCOMES.* ONCOLOGIST, 2002. **7**(6): P. 492-508.

311. SHINOHARA, K., ET AL., *EFFECTS OF SINGLE-PULSE (<= 1 PS) X-RAYS FROM LASER-PRODUCED PLASMAS ON MAMMALIAN CELLS.* JOURNAL OF RADIATION RESEARCH, 2004. **45**(4): P. 509-514.

312. WILSON, P., ET AL., *REVISITING THE ULTRA-HIGH DOSE RATE EFFECT: IMPLICATIONS FOR CHARGED PARTICLE RADIOTHERAPY USING PROTONS AND LIGHT IONS.* BRITISH JOURNAL OF RADIOLOGY, 2012. **85**(1018): P. E933-E939.
313. NIAS, A.H.W., ET AL., *SURVIVAL OF HELA CELLS FROM 10 NANOSECOND PULSES OF ELECTRONS.* INTERNATIONAL JOURNAL OF RADIATION BIOLOGY AND RELATED STUDIES IN PHYSICS CHEMISTRY AND MEDICINE, 1970. **17**(6): P. 595-&.
314. TOWN, C.D., *EFFECT OF HIGH DOSE RATES ON SURVIVAL OF MAMMALIAN CELLS.* NATURE, 1967. **215**(5103): P. 847-&.
315. PREMPREE, T., MICHELSE.A, AND T. MERZ, *REPAIR TIME OF CHROMOSOME BREAKS INDUCED BY PULSED X-RAYS OF ULTRA-HIGH DOSE-RATE.* INTERNATIONAL JOURNAL OF RADIATION BIOLOGY AND RELATED STUDIES IN PHYSICS CHEMISTRY AND MEDICINE, 1969. **15**(6): P. 571-&.
316. NIAS, A.H.W., ET AL., *EFFECTS OF PULSES OF RADIATION ON SURVIVAL OF MAMMALIAN CELLS.* BRITISH JOURNAL OF RADIOLOGY, 1969. **42**(499): P. 553-&.
317. BERRY, R.J., ET AL., *SURVIVAL OF MAMMALIAN CELLS EXPOSED TO X RAYS AT ULTRA-HIGH DOSE-RATES.* BRITISH JOURNAL OF RADIOLOGY, 1969. **42**(494): P. 102-&.
318. BERRY, R.J. AND STEDEFOR.JB, *REPRODUCTIVE SURVIVAL OF MAMMALIAN-CELLS AFTER IRRADIATION AT ULTRA-HIGH DOSE-RATES - FURTHER OBSERVATIONS AND THEIR IMPORTANCE FOR RADIOTHERAPY.* BRITISH JOURNAL OF RADIOLOGY, 1972. **45**(531): P. 171-&.
319. LING, C.C., ET AL., *OXYGEN DIFFUSION INTO MAMMALIAN-CELLS FOLLOWING ULTRAHIGH DOSE-RATE IRRADIATION AND LIFETIME ESTIMATES OF OXYGEN-SENSITIVE SPECIES.* RADIATION RESEARCH, 1978. **76**(3): P. 522-532.
320. WATTS, M.E., R.L. MAUGHAN, AND B.D. MICHAEL, *FAST KINETICS OF OXYGEN EFFECT IN IRRADIATED MAMMALIAN-CELLS.* INTERNATIONAL JOURNAL OF RADIATION BIOLOGY, 1978. **33**(2): P. 195-199.
321. PERSSON, L.M., ET AL., *RBE OF 50 MV SCANNED BREMSSTRAHLUNG BEAMS DETERMINED USING CLONOGENIC ASSAY.* INTERNATIONAL JOURNAL OF RADIATION BIOLOGY, 2002. **78**(4): P. 275-284.
322. MA, C.M., ET AL., *ENERGY- AND INTENSITY-MODULATED ELECTRON BEAMS FOR RADIOTHERAPY.* PHYSICS IN MEDICINE AND BIOLOGY, 2000. **45**(8): P. 2293-2311.
323. KOREVAAR, E.W., ET AL., *MIXING INTENSITY MODULATED ELECTRON AND PHOTON BEAMS: COMBINING A STEEP DOSE FALL-OFF AT DEPTH WITH SHARP AND DEPTH-INDEPENDENT PENUMBRAS AND FIAT BEAM PROFILES.* PHYSICS IN MEDICINE AND BIOLOGY, 1999. **44**(9): P. 2171-2181.
324. MOHIUDDIN, M., ET AL., *HIGH-DOSE SPATIALLY-FRACTIONATED RADIATION (GRID): A NEW PARADIGM IN THE MANAGEMENT OF ADVANCED CANCERS.* INTERNATIONAL JOURNAL OF RADIATION ONCOLOGY BIOLOGY PHYSICS, 1999. **45**(3): P. 721-727.
325. GLINEC, Y., ET AL., *RADIOTHERAPY WITH LASER-PLASMA ACCELERATORS: MONTE CARLO SIMULATION OF DOSE DEPOSITED BY AN EXPERIMENTAL QUASIMONOENERGETIC ELECTRON BEAM.* MEDICAL PHYSICS, 2006. **33**(1): P. 155-162.
326. LIM, J.K., ET AL., *ADJUSTABLE, SHORT FOCAL LENGTH PERMANENT-MAGNET QUADRUPOLE BASED ELECTRON BEAM FINAL FOCUS SYSTEM.* PHYSICAL REVIEW SPECIAL TOPICS-ACCELERATORS AND BEAMS, 2005. **8**(7).
327. AUER, S., ET AL., *SURVIVAL OF TUMOR CELLS AFTER PROTON IRRADIATION WITH ULTRA-HIGH DOSE RATES.* RADIATION ONCOLOGY, 2011. **6**.
328. TILLMAN, C., ET AL., *SURVIVAL OF MAMMALIAN CELLS EXPOSED TO ULTRAHIGH DOSE RATES FROM A LASER-PRODUCED PLASMA X-RAY SOURCE.* RADIOLOGY, 1999. **213**(3): P. 860-865.
329. LASCHINSKY, L., ET AL., *RADIOBIOLOGICAL EFFECTIVENESS OF LASER ACCELERATED ELECTRONS IN COMPARISON TO ELECTRON BEAMS FROM A CONVENTIONAL LINEAR ACCELERATOR.* JOURNAL OF RADIATION RESEARCH, 2012. **53**(3): P. 395-403.